AD-A031 658

Investigation of Rotating Stall Phenomena in Axial Flow Compressors Vol I. Basic Studies of Rotating Stall

Calspan Corp Buffalo N Y

Jun 76

314105

ADA031658
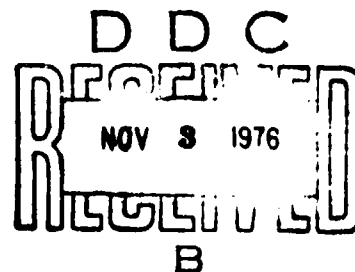
INVESTIGATION OF ROTATING STALL PHENOMENA IN AXIAL FLOW COMPRESSORS
VOLUME I – BASIC STUDIES OF ROTATING STALL

CALSPAN CORPORATION
P.O. BOX 235
BUFFALO, NEW YORK 14221

JUNE 1976

D D C

RECEIVED

NOV 3 1976

B

209

NOTICE

MARVIN A. STIBICH
Project Engineer

FOR THE COMMANDER

MARVIN F. SCHMIDT
Tech Area Manager, Compressors

SECURITY CLASSIFICATION OF THIS PAGE (When Data Entered)

REPORT DOCUMENTATION PAGE		READ INSTRUCTIONS BEFORE COMPLETING FORM
1. REPORT NUMBER AFAPL-TR-76-48 -Volume I	2. GOVT ACCESSION NO.	3. RECIPIENT'S CATALOG NUMBER
4. TITLE (and Subtitle) Investigation of Rotating Stall Phenomena in Axial Flow Compressors Volume I - Basic Studies of Rotating Stall		5. TYPE OF REPORT & PERIOD COVERED Final, May 73 - May 76
		6. PERFORMING ORG. REPORT NUMBER XE-5315-A-12
7. AUTHOR(s) Gary R. Ludwig Joseph P. Nenni John C. Erickson, Jr.		8. CONTRACT OR GRANT NUMBER(s) F33615-73-C-2046
9. PERFORMING ORGANIZATION NAME AND ADDRESS Calspan Corporation P. O. Box 235 Buffalo, New York 14221		10. PROGRAM ELEMENT, PROJECT, TASK AREA & WORK UNIT NUMBERS 30660334
11. CONTROLLING OFFICE NAME AND ADDRESS U.S. Air Force Aero-Propulsion Laboratory Air Force Systems Command Wright-Patterson AFB, Ohio 45433		12. REPORT DATE June 1976
		13. NUMBER OF PAGES 209
14. MONITORING AGENCY NAME & ADDRESS(if different from Controlling Office)		15. SECURITY CLASS. (of this report) Unclassified
		15a. DECLASSIFICATION DOWNGRADING SCHEDULE

16. DISTRIBUTION STATEMENT (of this Report)

Approved for public release; distribution unlimited.

17. DISTRIBUTION STATEMENT (of the abstract entered in Block 20, if different from Report)

18. SUPPLEMENTARY NOTES

19. KEY WORDS (Continue on reverse side if necessary and identify by block number)

Rotating Stall	Fluid Mechanics
Compressor	Jet Engines
Cascade	Acoustics
Control Systems	Noise

20. ABSTRACT (Continue on reverse side if necessary and identify by block number)

This report presents the results of a research program that had two major objectives. The first objective was the development of a prototype rotating stall control system which was tested both on a low speed rig and a J-85-5 engine. The second objective was to perform fundamental studies of the flow mechanisms that produce rotating stall, surge and noise in axial flow compressors and thereby obtain an understanding of these phenomena that would aid attaining the first objective. The work is reported in three separate volumes. Volume I

DD FORM 1JAN 73 1473 EDITION OF 1 NOV 65 IS OBSOLETE

SECURITY CLASSIFICATION OF THIS PAGE (When Data Entered)

20. (Cont'd)

covers the fundamental theoretical and experimental studies of rotating stall; Volume II covers the theoretical and experimental studies of discrete-tone aerodynamic noise generation mechanisms in axial flow compressors; and Volume III covers the development and testing of a prototype rotating stall control system on both the low speed test rig and the J-85-5 engine.

ACCESSION for

NTIS   White Section

DDC   E.: Section

UNANNOUNCED

JUSTIFICATION

BY

DISTRIBUTION/AVAILABILITY CODES

Dist.   AVAIL. and or SPECIAL

FOREWORD

This is the final Technical Report prepared by the Calspan
Corporation. The effort was sponsored by the Air Force Aero-
Propulsion Laboratory, Air Force Systems Command, Wright-Patterson
AFB, Ohio under Contract F33615-73-C-2046 for the period 1 May 1973
to 31 May 1976. The work herein was accomplished under Project 3066,
Task 306603, Work Unit 30660334, "Investigation of Rotating Stall
Phenomena in Axial Flow Compressors," with Mr. Marvin A. Stibich,
AFAPL/TBC, as Project Engineer. Dr. Gary R. Ludwig of the Calspan
Corporation was technically responsible for the work. Other Calspan
personnel were: Joseph P. Nenni, John C. Erickson, John A. Lordi,
Gregory F. Homicz, and Rudy H. Arendt.

ABSTRACT

This report presents the results of a research program that had two
major objectives. The first objective was the development of a prototype
rotating stall control system which was tested both on a low speed rig and a
J-85-5 engine. The second objective was to perform fundamental studies of the
flow mechanisms that produce rotating stall, surge and noise in axial flow
compressors and thereby obtain an understanding of these phenomena that would
aid attaining the first objective. The work is reported in three separate
volumes. Volume I covers the fundamental theoretical and experimental studies
of rotating stall; Volume II covers the theoretical and experimental studies of
discrete-tone aerodynamic noise generation mechanisms in axial flow compressors;
and, Volume III covers the development and testing of a prototype rotating stall
control system on both the low speed test rig and the J-85-5 engine.

Volume I describes the theoretical and experimental investigation of
the influence of distortion on the inception and properties of rotating stall
for an isolated rotor row, and the effects of close coupling of a rotor and
stator row on rotating stall inception. The experiments were conducted in the
Calspan/Air Force Annular Cascade Facility, which is a low speed compressor
research rig. In addition, the previously developed two dimensional stability
theory for prediction of inception conditions was extended to include the
effect of compressibility and the development of a three dimensional theory
was initiated. These studies led to the following key results. The experi-
mental studies of distortion show that for a single blade row the response of
the blade row to the distortion and rotating stall are uncoupled phenomena and
may be explained on the basis of a linearized analysis. The experimental
studies of a closely coupled rotor-stator pair show that the addition of a
closely spaced stator row downstream of a rotor row delays the onset of rotating
stall. Moreover, the corresponding theoretical analysis predicts this trend
although quantitative agreement is hampered by the lack of appropriate steady-
state loss and turning performance for each blade row at the required operating
conditions. The theoretical investigation of the effects of compressibility
for wholly subsonic flows outside the blade rows indicates that the effects of

compressibility do not alter the mechanisms of rotating stall as deduced from the incompressible theory in that the rate of change of the steady state loss curve with inlet swirl is the dominant blade row characteristic affecting its stability. Therefore, if the steady state losses are known for the compressible flow condition, the linearized stability analysis is expected to apply.

Volume II describes a theoretical and experimental study of discrete-tone noise generation by the interaction of a rotor and a stator, and the development of a direct lifting surface theory for an isolated rotor. An approximate model has been developed to predict the sound pressure level and total power radiated at harmonics of the blade passage frequency for a rotor-stator stage. The analysis matches the duct acoustic modes for an annular duct with an approximate representation of the unsteady blade forces which includes compressibility effects. Measurements were made of the sound pressure levels produced on the duct wall of the annular cascade facility by a rotor-stator pair. Predictions which indicated that only the fourth and higher harmonics could be excited at conditions achievable in the facility, were borne out by the experiments. The calculations of the sound pressure levels for the propagating modes were significantly below the measured values. This discrepancy is believed to result from inaccuracies in existing models of rotor wake velocity profiles, which are shown to have a strong influence on predictions of the sound pressure levels of the higher harmonics. Volume II also contains the formulation of a direct lifting surface theory for the compressible, three-dimensional flow through a rotor row in an infinitely long annular duct. A detailed derivation is given for the linearized equations and the corresponding solutions for the blade thickness and loading contributions to the rotor flow field. The governing integral equation for the blade loading in a lifting surface theory is obtained for subsonic flow and progress on its solution is reported.

Volume III describes the development and testing of a prototype rotating stall control system. The control system was tested on the low speed compressor research rig and on a J-85-5 turbojet engine. On the low speed research compressor, the control was tested in the presence of circumferential inlet distortion. These tests were performed to demonstrate the ability of

the control to operate satisfactorily in the presence of inlet distortion and to aid in the selection of stall sensor configurations for the subsequent engine tests. The control system was then installed on a J-85-5 jet engine and its performance was tested under sea level static conditions, both with and without inlet distortion. On the engine, the stall control was installed to override the normal operating schedule of the compressor bleed doors and inlet guide vanes. The J-85-5 was stalled in two ways, first by closing the bleed doors at constant engine speed, and second by decelerating the engine with the bleed doors partially closed at the beginning of the deceleration. A total of 41 compressor stalls were recorded at corrected engine speeds between 48 and 72 percent of the rated speed. In all cases, the control took successful remedial action which limited the duration of the stall to 325 milliseconds or less.

TABLE OF CONTENTS

ILLUSTRATIONS

viii

ILLUSTRATIONS (Cont'd)

x

SYMBOLS

a flow deflection parameter ($\partial \delta_2 / \partial \delta_1$)

a_i sound speed in region i or coefficient in polynomial approximation to stream function

A_{ij} matrix elements defined on pages 64 and 65

A, B constants in solution for total pressure and swirl in three-dimensional theory

A_i, B_i, D_i constants of integration in fundamental disturbance velocity solutions for incompressible flow (additional subscript n refers to nth Fourier component)

b_i coefficients in Equation 77

c complex exponent of disturbance velocity solutions

c_I, c_R imaginary and real part of c respectively

c_1, c_2 constants of integration in three-dimensional theory

$C_{P_{T_i}}$ total pressure coefficient in region i

d_i function defined on page 61

$\mathcal{D}$ function defined on page 52

$\mathcal{D}_i$ function defined page 52

E_i constant in disturbance pressure solution for compressible flow theory

G function expressing flow tuning relationship

G_2 constant used in three-dimensional theory

H total pressure or total pressure divided by density

H_i total pressure in flow region i

I_1 Vorticity integral used in three-dimensional theory

I_i function used in compressible flow theory, see page 65

j $\sqrt{-1}$

k_i coefficient of thermal conductivity in region i for compressible flow theory or constants of integration used in three-dimensional theory

K_i constants of integration in compressible flow theory

$K_i, \mathcal{L}_i,$ solution functions in compressible flow theory
m_i, n_i

L total pressure loss across blade row in three-dimensional theory

m parameter in three-dimensional theory, see page 73

m_i function defined on page 61

M parameter defined on page 75

$\tilde{M}$ parameter defined on page 81

n number of stall cells

SYMBOLS (Cont'd.)

N_i functions defined on pages 64 and 65

p hub-to-tip ratio or pressure

p_i disturbance pressure in region i

P_i mean static pressure in region i

$\ddot{P}_i$ sum of mean and disturbance pressures

q parameter defined on page 51

q_i parameter defined on page 80

q_i, q_o dynamic pressure defined on page 26

Q_i parameter defined on page 75

$\bar{Q}_i, \bar{Q}_j$ parameter defined on page 51

r, θ, z cylindrical coordinate system

r_H hub radius

r_T tip radius

$\mathcal{R}$ gas constant

R_i mean density in region i

S_i absolute swirl in region i

$\mathscr{S}_\iota$ relative swirl in region ι

t time

u_ι axial disturbance velocity in region ι

U, V, W velocities in cylindrical coordinate system

U_ι mean axial velocity in region ι

U_o mean axial velocity far ahead of blade row

$\hat{U}_\iota$ sum of mean and disturbance axial velocities

V_p absolute propagation velocity for rotating stall wave

V_{p_r} relative propagation velocity for rotating stall wave

ω_ι disturbance velocity along cascade axis

ω_b blade velocity

$\overline{W}_b$ mean blade velocity

$\overline{W}_{1_\kappa}$ mean velocity along cascade axis relative to blade row

x, y Cartesian coordinates

Z_1, Z_2 functions defined on page 51

β_ι swirl angle in flow region ι

$\bar{\beta}_\iota$ circumferential average flow angle in region ι

$\bar{\beta}_{\iota_R}$ circumferential average flow angle in region ι relative to blade row

$\bar{\bar{\beta}}_{\iota_R}$ radially averaged value of $\bar{\beta}_\iota$

$\delta_{GV.}$ guide vane stagger angle

δ_{RM} rotor stagger angle

δ_{SM} stator stagger angle

$\Delta \bar{\bar{C}}_{P_T}$ change in averaged total pressure coefficient across blade row

$\Delta \bar{\bar{C}}_{P_{T_\iota}}$ change in total pressure coefficient, see page 26

ΔP_T change in total pressure

$\Delta \theta$ change in azimuthal angle

λ parameter defined on page 51

λ_o parameter defined on page 52

$\hat{\mu}$ mean coefficient of viscosity

ξ_ι functions defined on page 65

ρ density

ϕ flow coefficient

SYMBOLS (Cont'd.)

$\bar{q}$ mean flow coefficient

ϕ disturbance stream function

χ total pressure loss parameter

χ' derivative of χ with respect to δ,

ψ stream function

Ω vorticity

Ω_θ θ component of vorticity

$\bar{\Omega}$ normalized blade velocity

$\bar{\Omega}_i$ normalized blade velocity in region i

ω blade row rotational velocity

SECTION I

INTRODUCTION

The useful operating range of a turbine engine compressor is greatly
influenced by its stalling characteristics. The optimum performance of a
turbo-propulsion system is usually achieved when the compressor is operating
near its maximum pressure ratio. However, this optimum is generally not
attainable because it occurs close to compressor stall and unstable flow con-
ditions. Because of the serious mechanical damage that may result during com-
pressor stall cycles, a factor of safety (stall margin) must be provided
between the compressor operating line and the stall boundary. This is usually
done by prescheduling the primary engine controls. However, the prescheduling
approach can lead to the requirement for a large stall margin in order to keep
the engine from stalling under all possible transient and steady state flight
conditions. It is clear, then, that an engine control system that can sense
incipient destructive unsteady flow in a compressor and take corrective action
would allow for reduced stall margins in the design and thus lead to large
engine performance and/or efficiency gains. Recognition of this fact has been
the motivation for a continuing program of research that the AFAPL has sponsored
at Calspan dating back to 1962.

The work at Calspan has been both theoretical and experimental in
nature and has been aimed at obtaining a sufficient understanding of the rotat-
ing stall phenomena such that its onset and its properties can be predicted
and controlled. The capability of predicting the onset of rotating stall on
isolated blade rows of high hub to tip ratios in low speed flows was demon-
strated in Reference 1. In addition, the basic feasibility of developing a
rotating stall control system was demonstrated in the Calspan/Air Force Annular
Cascade Facility. This present report summarizes the latest three year
research program at Calspan. The specific goals of the present program were
to extend the fundamental studies of rotating stall to consider the effects of
compressibility, blade row interaction and inlet distortion; and to extend the

1

fundamental aerodynamic and acoustic analysis of flow through a compressor. In addition, the rotating stall control system was validated by successful ground tests on a J-85-5 turbojet engine.

The work is reported in three separate volumes. Volume I entitled, "Basic Studies of Rotating Stall", covers the theoretical and experimental work on the effects of distortion and close coupling of blade rows on rotating stall inception and properties. In addition, the theoretical analysis of compressibility is treated in the two-dimensional approximation and the initial development of a three-dimensional theory is given. Volume II entitled, "Investigation of Rotor-Stator Interaction Noise and Lifting Surface Theory for a Rotor", describes the development of a linearized lifting surface theory for the subsonic compressible flow through an isolated rotor row. In addition, a theoretical and experimental study of the noise generated by the interaction of a rotor and stator is described. Volume III entitled, "Development of a Rotating Stall Control System", describes the development and testing of the control system installed on a low speed research compressor and on a J-85-5 turbojet engine.

Volume I has been divided into two main sections which are Experimental Rotating Stall Research and Theoretical Rotating Stall Research. The section on experimental research describes the low speed tests run in the Calspan/Air Force Annular Cascade Facility to investigate the effects of inlet distortion and blade row interference on rotating stall. The section on theoretical research describes the two dimensional stability theory that was developed for correlation with the above experimental data. In addition this section contains the summary of the results of extension of the two dimensional theory to compressible flow and the initial developments of a three dimensional theory.

EXPERIMENTAL ROTATING STALL RESEARCH

As a part of the work under a previous program Contract AF 33(615)-3357, an annular cascade facility was designed and fabricated. Its principal purpose is to provide detailed fundamental experimental data during and prior to the occurrence of rotating stall in order to improve our understanding of the phenomena and for use as a guide in improving the theoretical analysis. The facility has also been used to evaluate the operation of a prototype rotating stall control system and to provide acoustic data for comparison with theory. The acoustic measurements are described in Volume II of this report and the control system tests are described in Volume III. This section presents the fundamental experiments on rotating stall.

In previous programs using the annular cascade facility, rotating stall has been induced on a variety of stator rows with differing geometries and on a rotor row at various stagger angles. The experimental inception conditions and properties of rotating stall were measured. All of these investigations were conducted in the absence of deliberate inlet distortion. We attempted to minimize distortion although some unavoidable radial distortion was present because of the use of inlet guide vanes in most test configurations. The distortion was measured but no attempt was made to vary or investigate the distortion. Since it is known that inlet distortion can influence surge and rotating stall inception, a major portion of the current program was devoted to investigating the effects of circumferential inlet distortion on rotating stall. This study consisted of two parts. In the first part, an isolated rotor was tested in the presence of distortion patterns which were stationary in the laboratory frame of reference. In the second part, one of the distortion patterns was rotated about the compressor axis at a series of angular velocities while the rotor velocity was held fixed. The latter study was designed to determine if the time of passage of a rotor blade through a distortion cell plays a significant role in blade row sensitivity to inlet distortion.

In addition to the inlet distortion studies, the current program included a limited examination of the effects of rotor-stator interference on the inception of rotating stall. The rotor row and stator row chosen for these

experiments had previously been tested in isolation so that the conditions under which the individual rotor row and stator row undergo rotating stall inception were known. Thus the presence of interference effects between the two rows when combined as a rotor-stator stage could be determined by comparison with the individual blade row performances. The results were also used for comparison with the predictions of rotating stall theory for multiple blade rows.

The order of presentation of the experimental program in the remainder of this section is as follows. A description of the annular cascade facility is presented in Section II-A. Section II-B presents the results of the study of rotor-stator interference effects on rotating stall. Section II-C presents the results of the rotating stall experiments in the presence of inlet distortion. This section includes the work on both stationary inlet distortion and on rotating inlet distortion. Finally, in Section II-D, a summary of the experimental program on rotating stall is presented along with those conclusions which can be drawn from inspection of the results.

A.   DESCRIPTION OF ANNULAR CASCADE FACILITY

A detailed description of the annular cascade facility has been presented in Reference 1. Rather than repeat much of this detail, the following description is oriented towards noting changes in the facility made during the current program.

1. General Description

The annular cascade facility consists of a test section built around the outer front casing of a J-79 jet-engine compressor with a Calspan fabricated hub. The facility includes a bell-mouth inlet on the outer casing and a bullet nose on the hub to provide a smooth flow of air to the test section. Outlet ducting is connected to an independently variable source of suction to provide the required flow through the annulus. An electrically powered two-speed axial flow fan is used as the source of suction. Continuous control of

4

the mass flow is achieved through the use of variable inlet guide vanes to the fan and a variable damper in the fan exit flow. Photographs of the complete annular cascade facility and of the test-section portion of the facility are shown in Figures 1 and 2, respectively.

The test section of the annular cascade forms a circular annulus with an outer diameter of 29.35 inches and an inner diameter of 23.35 inches which provides a hub-to-tip ratio of 0.80. The outer casing will accept up to six variable stagger angle stator rows. The hub has provision for two rotor rows at the third- and fifth-stage rotor locations of the J-79 compressor. At present, speed control on each rotor hub is independently variable in either direction of rotation. The overall combination of variable stagger angle stators, independently powered rotors, and independent mass flow control provides exceptional versatility to the complete test rig.

2. Rotating Hub Drive Systems

During the course of the current investigations, two different drive systems were used to power the rotating hubs in the annular cascade facility. The original drive system allowed both rotors to be driven at the same speed or one rotor to be driven while the other was held fixed. All experiments which required the use of only one powered rotor were performed with this drive system. However, the experiments with rotating distortion required each rotor hub to have independent speed control. Thus the rotor drive system was modified to provide this capability. The drive system modification did not alter any dimensions within the circular annulus test section of the facility. Both rotor drive systems are described in the following paragraphs.

Details of the original rotating hub installation in the annular cascade are shown in Figure 3. The main features of the design are as follows. There are two rotor assemblies, one centered at the axial location of the third stage rotor in the J-79 compressor and one centered at the J-79 fifth stage rotor. Both of these rotors are driven by a common drive shaft. However, either rotor can be decoupled from the drive shaft and held stationary

5

while the other rotor is driven. Alternatively, both rotors can be driven, but only at identical velocities in the same direction. Only the rotor assemblies rotate, the outer skin on the hub upstream and downstream of the rotors and between the rotors is held stationary. The drive shaft to the rotors is powered by a 24 horsepower hydraulic motor. Rotational speed is infinitely variable in either direction between zero and approximately 1500 rpm. An external hydraulic pump system powered by a 30 horsepower electric motor is used to provide power for the hydraulic motor.

The modified rotating hub installation is shown in Figure 4. In this design both the third and fifth stage rotor hubs remain in the same axial locations as in Figure 3. The third stage rotor shaft is driven directly by the original drive shaft, hydraulic motor, and hydraulic pump system. The fifth stage rotor is mounted on a concentric drive shaft which is chain driven by a second hydraulic motor. Power for this second hydraulic motor is provided by a separate and larger hydraulic pump system with a 50 horsepower electric motor. With this modified hub, both rotor hubs have completely independent speed controls and can be rotated in either direction. Here again, only the rotor assemblies rotate, the outer skin on the hub upstream and downstream of the rotors and between the rotors is held stationary. Maximum speed capability on the third stage rotor hub is approximately 1500 rpm. Maximum capability on the fifth stage rotor hub has not been tested, but it is   ger than that of the third stage rotor because of the larger hydraulic pump system.

The two rotor hubs have provision for accepting different numbers of rotor blades. The stage 3 rotor hub is designed to accept 36 blades while the stage 5 rotor hub is designed to accept 46 blades. The method of fastening the blades to either hub allows individual adjustment of the stagger angle. Details of the blade fastenings are shown in an insert in Figure 4.

In addition to rotor blades, two symmetric multi-lobe distortion screens were designed for mounting on the third stage rotor hub. The outer edges of the screens are clear of the compressor casing so that they can be

rotated about the compressor axis. The screens are perforated steel plates. The mounting system uses the same holes as the rotor blades. Details of the screen mounting system are shown in an insert in Figure 4. This system allows configuration changes to be made without disassembly of the hub portion of the rotating rig.

3. Rotor and Stator Blading

The tests performed during this program involved either an isolated rotor in the presence of inlet distortion or a closely coupled rotor-stator stage. The fifth stage rotor and stator blades from a J-79 compressor were used in these tests, unmodified except for blade length which was shortened in order to fit into the three-inch annulus of the test rig. In each case, the spanwise portion of the blades closest to the outer compressor casing was used. The set of rotor blades has been designated as Rotor Set No. 1 and the set of stator blades as Stator Set No. 1 in keeping with the nomenclature used in Reference 1. The geometric characteristics of these blades have been presented in Reference 1 along with detailed measurements of turning and loss performance when used as single blade rows in isolation. The extensive performance data are not repeated herein except where they are used for purposes of comparison with the current test results. The blade geometric characteristics are repeated below.

Rotor Set No. 1 has the same number of blades and is at the same axial location as the fifth stage rotor in the original J-79 compressor. These blades have a NACA 65 Series thickness distribution on a circular arc mean line.

The geometric characteristics are listed in TABLE 1.

TABLE I

Geometric Characteristics of Rotor Set No. 1

Blade Length		2.98 inches
Blade Chord		1.448 inches (constant)
Blade Thickness;	Outer Diameter	0.072 inch
	Mid-Annulus	0.086 inch
	Inner Diameter	0.113 inch
Blade Camber Angle (angle between tangents to mean camber line of leading and trailing edges);	Outer Diameter	23.5 degrees
	Mid-Annulus	28.0 degrees
	Inner Diameter	32.7 degrees
Blade Twist		See Below
Number of Blades		46
Solidity at Mid-Annulus		0.805

The blades in Rotor Set No. 1 have a nominal twist of 14.5 degrees over the three inch span. However, measurements showed that in practice, the twist over the center 2-½ inches in these production J-79 blades varied between 10.8 and 14.4 degrees with an average value of 12.9 degrees. The blades were installed in a sequence which distributed the nonuniformities in twist over the complete circumference.

A blade tip clearance problem was encountered on installation of the rotor assembly in the annular cascade. The J-79 compressor outer casing used in the annular cascade is about one-tenth inch out of round with the split line diameter being the largest. In final assembly, the rotor was mounted in the casing with shims along the split line which provided the following tip clearances: 0.030 inch on the top and bottom and 0.046 to 0.048 inch on the sides. Since the stagger angles of the rotor blades are adjustable, the quoted tip clearances apply only to the mid-chord pivot points. Clearance at the blade leading and trailing edges vary slightly with changes in stagger angle from the angle for which the tip contour was determined. The stagger angle used to determine the tip contour was the maximum which was expected to be used. The choice of lower reference stagger angles would have resulted in interference between the blades and outer casing at stagger angles much larger than the reference.

Stator Set No. 1 has the same number of blades and is located at the same axial location as the fifth stage stator row in the original J-79 compressor. Its geometric characteristics are listed in TABLE II.

4. Instrumentation

The outer casing of the annular cascade test section has been modified to allow circumferential and radial traverses with hot-wire and total pressure probes upstream and downstream of the fifth stage location. These traverse locations are shown in Figure 2. Two probes can be accommodated simultaneously in either of these traverse mounts with adjustable circumferential spacing between the two probes. In addition, simple radial traverses can be made at various other locations in the test section.

TABLE II

Geometric Characteristics of Stator Set No. 1

Blade Length		2.98 inches
Blade Chord;	Outer Diameter	1.316 inches
	Inner Diameter	1.290 inches
Blade Thickness;	Outer Diameter	0.152⁴ inch
	Inner Diameter	0.1132 inch

Blade Camber Angle (angle between tangents
to mean camber line of leading and trailing
edges)   35.6 degrees

	Outer Diameter	0 degree
Blade Twist;	Mid-Annulus	0.28 degree
positive twist	Inner Diameter	1.42 degree
reduces stagger		

Number of Blades   54

Solidity at Mid-Annulus   0.85

A linearized two-channel, constant-temperature, hot-wire anemometer system was used in conjunction with a crossed-wire probe for the velocity and swirl angle measurements. Readout for the hot-wire system was made by means of a two-channel integrator-digital voltmeter system. Each linearized hot-wire signal was integrated for 60 seconds and the time average was calculated from the readings on the digital voltmeters.

Total pressure surveys were made through circumferential traverses with a multiple-tube total pressure rake. The total pressure rake was aligned with the flow by using a Conrad arrowhead style yawmeter incorporated on the rake. In all tests, the pressures detected by the rake were photographically recorded from a multitube inclined manometer.

In most cases, rotating stall was detected and the number of cells and propagation velocity were measured by using outer-wall static pressure taps connected to pressure transducers. Two pressure taps at different circumferential locations and at an axial location corresponding to the quarter-chord on the rotor blades were used. In the tests with rotating inlet distortion, rotating stall was detected in several ways. The most informative method consisted of measuring the mid-annulus total pressure fluctuations just upstream of the rotor.

In all of the experiments, mass flow through the test section was determined by measuring the dynamic pressure in the constant-area annulus upstream of the test section.

B.   INVESTIGATION OF EFFECT OF ROTOR-STATOR INTERFERENCE ON ROTATING STALL

Previous studies of rotating stall in the annular cascade facility were concentrated on isolated rows of rotors on stators. Although the stator row studies required the use of upstream guide vanes to generate the swirled flow necessary to provide the conditions for rotating stall, the axial

11

separation between the guide vane row and stator row was large compared to the typical spacing of a rotor-stator pair usually found in a compressor stage. Moreover, in most of these tests, both the guide vane row and the stator row were stationary. Thus the current experiments were undertaken to determine if interference between a closely coupled rotor-stator pair changes the conditions for inception of rotating stall from those which are found on isolated blade rows.

The notation for these experiments is shown in Figure 5 and a sketch of the annular cascade with its geometric dimensions is shown in Figure 6. The rotor-stator stage used in the annular cascade consisted of Rotor Set No. 1 followed by Stator Set No. 1. These are modified blade rows from the fifth stage of a J-79 compressor (See Section II.A.3). The steady state performance of these blade rows had been determined previously (Reference 1) for the conditions near rotating stall inception on each of these blade rows in isolation. In addition, the inception point and properties of rotating stall of each blade row in isolation had also been determined. In the current work, the inception point and properties of rotating stall on the combined blade rows were studied. The techniques used to measure rotating stall properties are the same as those used on the isolated rotor. These have been described in Reference 1.

The tests were performed for one stagger angle setting of the rotor blades (δ_{RM} = 40 degrees) and for four stagger angle settings of the stator blades (δ_{SM} = 28.2, 37.2, 47.2 and 57.2 degrees). Since both rotor and stator blades are twisted, the quoted stagger angles, δ_{RM} and δ_{SM} , correspond to the values at mid-annulus in the annular cascade. In addition to determining the rotating stall inception point, propagation velocity, and number of cells, the static pressure rise across the stage was also measured over a range of rotor rpm's for each of the stator stagger angle settings.

A summary of the inception points found in these tests is presented in Table III along with the isolated rotor results for comparison. In all cases tested, the presence of rotating stall was detectable from signals

12

TABLE III

SUMMARY OF ROTATING STALL INCEPTION POINTS IN PRESENCE OF ROTOR-STATOR INTERACTION

ROTOR SET NO. 1, ROTOR STAGGER ANGLE, δ_{RM} = 40.0 DEG

STATOR SET NO. 1, STATOR STAGGER ANGLE, δ_{SM} VARIABLE

TEST CONFIGURATION	ROTATING STALL INCEPTION POINT WITH INCREASING ROTOR SPEED		ROTATING STALL TERMINATION POINT WITH DECREASING ROTOR SPEED	
	ROTOR RPM	RELATIVE INLET SWIRL ANGLE $\bar{\beta}_{o_R}$ (deg)	ROTOR RPM	RELATIVE INLET SWIRL ANGLE $\bar{\beta}_{o_R}$ (deg)
ISOLATED ROTOR	1000	-62.6	960	-61.6
ROTOR-STATOR, δ_{SM} = 28.2 deg	1070	-64.1	1020	-63.0
ROTOR-STATOR, δ_{SM} = 37.2 deg	1125	-65.2	1080	-64.3
ROTOR-STATOR, δ_{SM} = 47.2 deg	1240	-67.3	1240	-67.3
*ROTOR-STATOR, δ_{SM} = 57.2 deg	$\approx$1275	$\approx$ -67.8	1275	$\approx$ -67.8

NOTE: MEAN AXIAL VELOCITY, U_o = 60 fps FOR ALL TESTS.

*Rotating stall was very irregular for this case making it difficult to determine exact conditions for inception.

generated by pressure transducers installed near the blade tips of both the rotor row and the stator row. Thus, it is not possible to determine absolutely which blade row was responsible for rotating stall when it occurred. However, for the two lowest stator stagger angles, δ_{s_M} = 28.2 and 37.2 degrees, and to a lesser extent for δ_{s_M} = 47.2 degrees, the stall signals displayed character- istics similar to rotating stall on the isolated rotor. At the highest stator stagger angle, the rotating stall signals were very irregular on both blade rows but the general features looked more like those associated with stator stall. In any event, both blade rows in the closely coupled stage appeared to participate strongly in the rotating stall phenomenon.

In Table III, the rotor speed at inception with increasing rotor speed is shown along with the corresponding overall inlet swirl angle $\bar{\beta}_{o_R}$ relative to the rotor. Similar data are shown for the point at w.ich rotating stall dies out as rotor speed i. decreased. The sign convention for angles is given in Figure 5. For all of the cases tested, the addition of a stator row downstream of the rotor row delayed the inception of rotating stall. The delay in inception increased as the stator stagger angle was increased. In terms of rotor speed, the delay in inception was substantial ($\approx 25\%$) at the two highest stator stagger angles. The case with δ_{s_M} = 57.2 degrees is probably not of practical interest since the stator blades were either very lightly loaded or even negatively loaded. Nevertheless, these data could be useful for assessing the validity of the two blade row rotating stall theory under widely varying conditions.

The delay in rotating stall inception to higher rotor speeds on the coupled rotor-stator stage has a large effect on the static pressure rise at- tainable by the stage. Moreover, the behavior of the pressure rise near stall appears to be dependent on the degree of loading of the stator blades. These effects are discussed in the following paragraphs.

The static pressure rise data measured across the isolated rotor and across the rotor-stator stage are shown in Figures 7 and 8 respectively. The data were measured both at the hub and at the tip through pressure taps

14

located on the inner and outer casings of the annular cascade. In these ex-
periments, the pressure rise data were obtained over a range of rotor speeds
with the mean axial flow velocity, U_a, held constant at 60 fps. The pressure
rise has been made dimensionless by dividing by the dynamic pressure correspond-
ing to this value of U_a. On each figure the presence of rotating stall is
indicated by tails on the symbols and the rotor speed at rotating stall in-
ception is indicated. In instances where inception displayed hysteresis,
data are shown both with and without the presence of rotating stall.

As expected, the isolated rotor data in Figure 7 show that the static
pressure rise across the blade row is greater at the tip than at the hub, and
that the difference increases with increasing rotor speed in the unstalled
region. This is in contrast with the pressure rise characteristic for a
stator row which generally displays the greatest static pressure rise at the
hub. See for example Figure 28 of Reference 2. When the rotor and stator are
combined to make a stage, as in Figures 8(a) through 8(d), the difference
between hub and tip static pressure rise on the rotor and stator tend to
cancel provided that the two blade rows are well matched. In these figures,
the data for δ_{SH} = 28.2 degrees provided the closest match between rotor and
stator characteristics. As the stator stagger angle is increased, the blade
row matching deteriorates and the difference between the hub and tip static
pressure rise increases. The data in Figure 8(d) for δ_{SH} = 57.2 degrees is
a particularly bad mismatch. The data for the isolated rotor displays a
greater pressure rise over the full range of rotor speeds tested than the
data for the stage with δ_{SH} = 57.2 degrees. This is true even for the rotor
speed range where the isolated rotor was in rotating stall while the stage
was not.

The stage pressure rise data behave as expected in the rotor speed
range where rotating stall is absent. At any given rotor speed, the highest
pressure rise is attained when the stator row is most highly loaded
(δ_{SH} = 28.2 degrees) and the pressure rise decreases progressively as the
stator row is unloaded (δ_{SH} increasing). However, the pressure rise data
show an interesting feature as inception is approached. The attainable pres-
sure rise just before inception increases in value as the stator row is un-
loaded (except for the badly mismatched case δ_{SH} = 57.2 degrees). Apparently

decreasing the loading on the stator row increases the rotor speed at inception by an amount large enough that the maximum attainable pressure rise is increased before rotating stall occurs.

With the isolated rotor (Figure 7) a small hysteresis in rotating stall inception was observed and the pressure rise curves display a small discontinuity in both magnitude and slope in the hysteretic region. For the stage with δ_{s_M} = 28.2 and 37.2 degrees (Figures 8(a) and 8(b)) rotating stall inception was again hysteretic and the hysteresis was not large in terms of rotor speed. However, the discontinuity in the pressure rise curves is much more pronounced especially for δ_{s_M} = 28.2 degrees. At the two highest stator stagger angles (Figures 8(c) and 8(d)) no hysteresis was observed at inception. In these cases the pressure rise curves show a discontinuity in slope at inception but there does not appear to be a significant discontinuity in magnitude.

The experimentally determined rotating stall propagation velocities and numbers of cells are shown in Figure 9(a) for stator stagger angles of 28.2 and 37.2 degrees and in Figure 9(b) for stator stagger angles of 47.2 and 57.2 degrees. Similar data measured previously on the isolated rotor are shown on each figure for comparison. At the three lowest stator stagger angles the dimensionless propagation velocities relative to the rotor row are substantially higher than those found on the isolated rotor. There also appears to be a small decrease in relative propagation velocity as the stator stagger angle is increased. Near inception, a single stall cell was found to be propagating for stator stagger angles of 28.2, 37.2 and 47.2 degrees as well as for the isolated rotor. After inception, the number of cells remained at one for δ_{s_M} = 28.2 and 37.2 degrees but increased to a maximum of four for δ_{s_M} = 47.2 degrees. The number of stall cells on the isolated rotor increased to two well after inception. Thus for these cases, the number of cells near inception is similar to the isolated rotor and after inception there are some small differences. The characteristics of the pressure signals from the rotating stall sensors looked like those associated with rotating stall on the isolated rotor.

16

At a stator stagger angle of 57.2 degrees, the rotating stall properties changed considerably from those found with the lower stator stagger angles. The relative propagation velocities dropped to values near those found on the isolated rotor and the number of cells increased to between seven and eight. Moreover, as noted previously, the pressure signals from the rotating stall sensors had general features which looked more like those associated with stator stall than with rotor stall.

In summary, the comparison of rotating stall properties observed on the closely coupled stage with those observed on the isolated rotor indicates that the interaction between the blade rows in a stage can have a substantial effect on the inception and properties of rotating stall. The most interesting result was obtained on the stage with the stator stagger angle set at 47.2 degrees. With this configuration, the static pressure rise measured at inception eliminated the sharp drop in pressure rise when rotating stall first occurred. In Section III, the results of preliminary correlations between the predictions of the two-blade row theory and the results of these experiments are presented. These correlations are encouraging in that the theory predicts that blade row coupling does stabilize the stage and appears to provide an accurate quantitative value for the delay in inception for a stator stagger angle of 28.2 degrees. However, the theoretical predictions are based on large extrapolations of the stator steady state turning and loss performance. These extrapolations were necessary because it was found that the data available for Stator Set No. 1 did not fall within the range of inlet conditions which occur when the stators are coupled to Rotor Set No. 1. Moreover, at the larger stator stagger angles tested, the large delay in inception leads to the problem of estimating the steady state losses on the rotor under conditions which normally induce rotating stall on the isolated rotor. Thus it is planned to extend the steady state loss and turning performance measurements on the isolated stator to include the required inlet conditions and also to measure the performance of the rotor row and stator row when combined in a closely coupled stage.

C.   INVESTIGATION OF EFFECT OF STATIONARY AND ROTATING INLET
      DISTORTION ON ROTATING STALL

There have been numerous tests which used circumferential distortion
at the inlet to multistage axial flow compressors. These tests are usually
performed in order to determine the reduction in stall margin of the compres-
sor when subjected to such distortion. In some cases, the compressor appears
to be most sensitive to a particular circumferential extent of the distortion
pattern. In fact, there is evidence that multi-lobe distortion patterns, all
of which have the same total extent, can have different effects on compressor
stall margin (e.g., References 3 and 4). This indicates that the observed
reductions in stall margin could depend on a dimensionless reduced frequency
or Strouhal Number which is formed from the time of passage of a rotor blade
through a distortion pattern, a typical relative flow velocity, and a typical
rotor dimension in the direction of the relative flow. A stall-delay concept
based on the above idea has been recommended recently by Korn[5] for the im-
provement of parallel compressor theories.

Investigations of the above type are very useful for estimating the
effect of inlet distortion on compressors of similar design and for providing
some understanding of the parameters involved. However, they fall short of
providing an understanding which is sufficient to predict the way in which
inlet distortion can initiate rotating stall and surge. For example, it is
possible that the geometry itself, such as the number of lobes, can effect
rotating stall inception independently of the passage time of a rotor blade
through a distortion lobe. Geometry dependent distortion pattern effects
similar to those obtained with the stall delay concept have been proposed in
Reference 6 by considering only the effect of a diffuser downstream of the
compressor.

The work presented in the following paragraphs was designed to
study the effect of circumferential inlet distortion on a simple configuration
consisting of an isolated rotor in a constant area annulus. The configuration
was kept simple in order to facilitate comparison with the theoretical studies

18

of Section III. In addition, these experiments were designed to search for unambiguous evidence that rotating stall inception may be sensitive to a reduced frequency which contains the time of passage of the rotor blades through the distortion pattern. In order to investigate reduced frequency effects, the experimental program consisted of two parts. In the first part, the effect of stationary multi-lobe distortion patterns on rotating stall was studied. Two symmetric multi-lobe distortion patterns were used. Each pattern covered the same total area but one consisted of two lobes and one consisted of four lobes. In he second part, the two-lobe distortion pattern was rotated about the compressor axis at different speeds while holding the rotor speed constant. The latter study allowed variations in the relative reduced frequency seen by the rotor without substantial changes in the geometry of the distortion pattern. Interpretation of changes in rotating stall inception observed in these experiments is subject to less ambiguity than evidence inferred indirectly from multi-lobe distortion investigations in which the geometry of the distortion pattern is changed.

Both the stationary and rotating distortion investigations were performed with Rotor Set No. 1 whose geometric characteristics are described in Section II-A. This rotor set had already been tested as an isolated rotor (Reference 1) so that its performance in isolation was available for purposes of comparison.

The results of the investigation of the effect of circumferential inlet distortion on rotating stall are presented in the following paragraphs. The calibration of the stationary multi-lobe distortion screens is presented first. This is followed by a presentation of the results obtained with stationary distortion. Finally the results of the rotating distortion studies are presented.

1. Calibration of Stationary Distortion Screens

The notation used in the distortion studies is shown in Figure 10 and a sketch of the annular cascade with the appropriate geometric dimensions is given in Figure 11. As discussed in Section II-A-2 and illustrated in

Figure 11, the distortion screens were mounted on the upstream rotor hub so that they could be rotated about the compressor axis. In the tests with stationary inlet distortion, two circumferential distortion screens were used, one with two lobes and one with four lobes. These screens are sketched in Figure 12. Figure 12(a) shows the symmetric two-lobe pattern (Configuration A). Each lobe has a circumferential extent encompassing 60 degrees. Figure 12(b) shows the symmetric four-lobe pattern (Configuration B). Each lobe of this pattern encompasses 30 degrees. T⟨ 1 pressure surveys were made in the wakes of the screens with a small total pressure rake which can be traversed circumferentially over a limited range (approximately 30 degrees), in combination with the various screen locations. The screens could be indexed to any circumferential position. The data were then analyzed as though the screens were held fixed at a reference position and the rake traversed over the complete angular range of interest. Figures 12(a) and 12(b) show the reference locations of the screen elements.

The results obtained from the total pressure surveys downstream of screen configuration A are shown in Figures 13(a) and 13(b) for two different rotor speeds, 500 and 950 rpm respectively. Similar data are shown in Figures 14(a) and 14(b) for screen configuration B. In all of these figures, the total pressure coefficient, $C_{P_{T_i}}(r, \theta)$ is defined as

$$C_{P_{T_i}}(r, \theta) = \frac{H_i - H_o}{\frac{\rho}{2} U_r^2}$$

where H_o is the total pressure upstream of the screen

H_i is the total pressure in the survey plane downstream of the screen (but upstream of the rotor)

U_r is the mean axial velocity measured upstream of the screen

ρ density

Each figure contains circumferential, (θ), surveys for various radial locations. Δr. The origin for the vertical total pressure coordinate is displaced for each Δr in proportion to the value of Δr.

The two rotor rpm's were investigated with each screen to determine
if there was any significant upstream influence from the rotor on the screen
generated distortion patterns. At 500 rpm the rotor was practically unloaded
and at 950 rpm the rotor was loaded nearly to the inception point for rotating
stall. Comparison of Figures 13(a) and 13(b) for configuration A and Figures
14(a) and 14(b) for configuration B indicates that any upstream effect of the
rotor angular velocity on the total pressure was insignificant.

In general, the distortion screens behaved as expected, generating
a relatively sharp edged wake with a total pressure coefficient relatively
close to unity. In all cases, the hub and tip wall boundary layers are evident
in the data for the smallest and the largest values of Δr, where the total
pressure coefficients remain below zero even outside of the screen wakes.

Following the total pressure calibrations, the two distortion screens
were calibrated for swirl angle. All swirl angle measurements were made with
a crossed hot-film probe operated by two Thermo-Systems hot-wire anemometers.
The outputs from the two anemometers were linearized and then integrated for
a period of sixty seconds in order to obtain an accurate time average of the
flow angles. Air temperature variations were corrected for in the initial
calibration procedure prior to a test run. Since each data point in the swirl
angle surveys required a minimum elapsed time greater than sixty seconds, the
swirl angle measurements are more limited in the number of data points gathered
than were the total pressure data.

The results of swirl angle surveys between the rotor and the two-lobe
distortion screen (Configuration A) are shown in Figures 15(a) and 15(b) for
rotor speeds of 500 and 950 rpm respectively. Similar results are shown in
Figures 16(a) and 16(b) for the four-lobe distortion screen (Configuration B).
Each figure contains circumferential (θ) surveys for five different radial
locations (Δr). The sign convention for swirl angle (β) is shown in Figure 10.

The circumferential distributions of swirl angle generated by both
distortion screens are asymmetric, with the data measured near the hub showing
the largest variations. Moreover, unlike the total pressure distributions

21

which were insensitive to rotor speed, the swirl angle distortion increases significantly as rotor speed is increased. Almost all of the increased distortion in swirl angle with increasing rotor speed occurs over the lower half of the screens (the lower edge of the screen is the one with the smallest value of θ). The lar. e variations in swirl angle, between the distortion screens and rotor are similar to those observed under similar conditions in other experiments. For example, see Reference 7 which comments on the results obtained in several experiments. Apparently the swirl angle variations are predicted reasonably well by actuator disc theory and the variations decrease with distance upstream of the rotor.

2. Experiments With Stationary Inlet Distortion

Following the calibration of the two stationary distortion screens, the effect of these inlet distortions on the steady state turning and loss performance of the rotor and their effect on rotating stall was studied. The turning and loss performance of the rotor is presented first.

Total pressure surveys downstream of the rotor were made with both screen configurations for a wide range of rotor rpm and with the mean axial velocity, U_e , held constant at 60 fps. The rotor used in these tests is Rotor Set No. 1 of Reference 1 set at a stagger angle, δ_{RH} of 40 degrees. With screen Configuration A, the rotor rpm's used for the tests were 500, 700, 850, 950, 1000, 1050, and 1150. Rotating stall occurred during the tests at 1050 and 1150 rpm. With screen Configuration B, the rotor rpm's were 500, 700, 850, 950, 1000, 1050, 1150, and 1200 with rotating stall present at the three highest values. These surveys were made with a total pressure rake which spanned approximately one-half of the depth of the annulus. The complete annulus was spanned by taking two sets of data, one with the rake set close to the hub, and one with the rake set close to the tip. The rake incorporated a Conrad arrowhead style yaw meter at its mid-span. This was used to align the rake with the local flow direction. Thus if there were significant deviations in flow angle between the outer and inner portions of the annulus, the two data runs would allow approximate alignment of the rake to account for these deviations.

The results of the total pressure surveys are shown in Figures 17(a) through 17(h) for the two-lobe screen (Configuration A) and in Figures 18(a) through 18(h) for the four-lobe screen (Configuration B). For a given screen configuration, each figure corresponds to a different rotor rpm and the range of rpm's extends from nearly unloaded (500 rpm) to loading beyond the inception point of rotating stall (above 1000 rpm). The total pressure coefficient, $C_{P_{r_2}}(r, \theta)$ is defined as

$$C_{P_{r_2}}(r, \theta) = \frac{H_2 - H_0}{\frac{\rho}{2} U_0^2}$$

where H_0 is the total pressure upstream of the screen

H_2 is the total pressure downstream of the rotor

U_0 is the mean axial velocity measured upstream of the screen

ρ is the air density

Each figure contains circumferential (θ) surveys for various radial locations, Δr. The horizontal reference line for the total pressure coordinate is displaced for each value of Δr in proportion to the value of Δr. Note that these reference lines do not always correspond to $C_{P_r} = 0$. At the higher rotor speeds for each configuration, $C_{P_r} = 1$ was chosen as the reference line in order to maintain the vertical scale ratio for Δr in these figures.

The complete total pressure surveys presented in Figures 17 and 18 show several interesting features. First, the distortion patterns generated by the screens are not completely diffused by the rotor. The wakes are most evident near the hub (small Δr) and tend to be more diffused after rotating stall inception (above 1000 rpm). Second, the data show distinct positive peaks in the total pressure distributions near mid-annulus at a circumferential location, θ, approximately ten degrees less than the location of the lower edge of the screen (the lower edge is the one with the smallest value of θ). The rotor spins in the direction of decreasing θ and any deflection by the rotor of the screen wakes should also occur towards smaller values of θ.

At the smallest rotor speeds, there is evidence of a corresponding negative peak in the total pressure near the upper edge of the screen, but this is small and dies out quickly with increasing rpm. Moreover, the positive peak in the total pressure near the lower edge of the screen dies out after rotating stall inception for both distortion screens. It is possible that the peaks observed in the total pressure distributions are a result of the response of the rotor to the variations in inlet swirl angle generated by the distortion screens. For example, the large negative values of inlet swirl angle shown in Figures 15 and 16 near the lower edges of the screens may be the cause of the positive peaks in downstream total pressure in this same region. The negative swirl angles in this region increase the local angle of attack of the rotor and should increase the work performed by the rotor and thus the downstream total pressure. The converse is true near the upper edges of the screen but the effect is smaller.

Swirl angle distributions were measured downstream of the rotor only for the two-lobe distortion screen (Configuration A). As will be discussed, it was found that there were negligible differences in rotating stall inception and properties after inception for the two distortion screen configurations. This result justified limiting the completion of these tests to one screen configuration. Circumferential surveys were made at five radial locations for each of four different rotor speeds (500, 850, 950 and 1050 rpm). This range of rotor speeds extends from nearly unloaded (500 rpm) to a loading beyond the inception point of rotating stall (above 1000 rpm). The measurement of these swirl angles was accomplished with the hot-film instrumentation described previously.

The results of the swirl angle surveys are presented in Figures 19(a) through 19(d) with each figure corresponding to a different rotor speed. Note that the horizontal reference lines for the swirl angle coordinate do not correspond to zero values of swirl angle, β_2, and that the reference values vary from figure to figure. The variable reference values were selected in order to maintain the same vertical scale ratio for β_2 in these figures.

24

The swirl angles downstream of the rotor vary with circumferential location. The largest deviations from the mean value occur just before rotating stall inception (950 rpm) and decrease after inception (1050 rpm). The extremes of the circumferential variations in downstream swirl angle are approximately half of those observed upstream of the rotor and they do not appear to form a consistent trend which can be associated with the presence of the distortion screen upstream of the rotor.

For each radial location at a given rotor speed, circumferential averages of β_2 have been calculated. Since the data only extend between 24 deg $\leq \theta \leq$ 168 deg, the full 0 to 180 degree circumferential range required for computing circumferential averages (the distortion screen is a symmetric two-lobe pattern) was obtained by assuming a linear variation in β_2 for the region where β_2 was not measured. The resulting circumferential average values of the swirl angle, $\bar{\beta}_2$, are compared in Figure 20 with similar data for the isolated rotor (Ref. 1). In Figure 20, two degrees have been added to the data measured with the screen in place. This has been done in order to allow direct comparison with the shapes of the radial distributions for the isolated rotor. Isolated rotor data are not available for a rotor speed of 850 rpm. Thus a direct comparison for this speed cannot be made. However, the isolated rotor data for rotor speeds of 800 and 900 rpm are shown in the figure to provide an indirect comparison. At 1050 rpm, both the isolated rotor and the rotor with inlet distortion were undergoing rotating stall.

It is evident from inspection of Figure 20 that the radial distributions of $\bar{\beta}_2$ with and without the distortion screen are the same shapes to within the probable experimental accuracy of the data. In addition, it would appear that the radial distributions of $\bar{\beta}_2$ with the screen in place are an almost constant two degrees less than those observed on the isolated rotor. In general, the effect of the distortion screen on the flow turning performance of the rotor is very small. The rotating stall stability theory in Section III requires an overall average, $\bar{\bar{\beta}}_2$, obtained by integrating the circumferential averages $\bar{\beta}_2$ in the radial direction. In view of the constant two degree differences in the circumfereintial averages, it is sufficiently accurate in this

case to assume that the isolated rotor measurements diminished by a constant two degrees can be used for input to the theory.

It is somewhat more difficult to compare the loss performance of the rotor with and without inlet distortion. In principle, such a comparison requires that the radial distributions of total pressure measured in the absolute coordinate system (as in Figures 17 and 18) be converted to a coordinate system relative to the rotor and then integrated radially as in Reference 1. The swirl velocities downstream of the rotor enter into this integration procedure. However in view of the small constant difference in the radial distribution of swirl angle, $\bar{\beta}_2$, observed between the isolated rotor and the rotor with inlet distortion, a valid comparison of rotor loss performance can be made on the basis of the total pressure measurements made in the absolute coordinate system. This has been done and the results are presented in Figure 21.

In Figure 21, the overall total pressure difference across the rotor is plotted in coefficient form as a function of flow coefficient. Both the data for the isolated rotor and for the flows with inlet distortion are shown. The notation in the figure is as follows:

$$\Delta \bar{\bar{C}}_{P_{T_{q_1}}} = -\frac{\bar{\bar{P}}_{2} - \bar{\bar{P}}_{T_1}}{q_1} = \frac{\bar{\bar{P}}_{T_2} - \bar{\bar{P}}_{T_1}}{q_o \left[1 + \left(\frac{\bar{W}_b}{U_o}\right)^2 \right]}$$

$$\phi = \frac{U_o}{\bar{W}_b}$$

where:

q_o = Dynamic pressure corresponding to average axial velocity, $\left(\frac{\rho}{2} U_o^2\right)$

q_1 = Dynamic pressure corresponding to average velocity relative to the rotor, $\frac{\rho}{2} \left(U_o^2 + \bar{W}_b^2\right)$

26

$\bar{P}_{T_1}$ = Area Weighted Average of Total Pressure at Rotor Face
(Measured in absolute coordinate system)

$\bar{P}_{T_2}$ = Area Weighted Average of Total Pressure Leaving Rotor
(Measured in absolute coordinate system)

U_o = Area Weighted Average of Axial Velocity Upstream of Rotor

$\bar{W}_b$ = Area Weighted Average of Rotor Velocity.

The average total pressures were computed by numerically integrating
the measured total pressure data presented in Figures 13, 14, 17 and 18 for
the cases with inlet distortion. These data include the effect of the boundary
layers developed on the hub and outer casing of the annular cascade both up-
stream and downstream of the rotor. The total pressure data for the isolated
rotor (Reference 1) included the wall boundary layers downstream of the rotor
but not upstream of the rotor. In Figure 21, these original data for the
isolated rotor were corrected to include the upstream boundary layers by as-
suming that the dimensionless total pressure data measured between the dis-
tortion screen lobes were representative of the upstream boundary layers on
the isolated rotor. This procedure should be fairly accurate since the geometry
of the annular cascade was identical except for the segments of the distortion
screens. Moreover the data from both screen configurations provided the same
value for the boundary layer correction to the isolated rotor.

It can be seen from Figure 21 that the dimensionless total pressure
differences across the rotor are nearly identical for all of the data except
in the regions where rotating stall is occurring. For application of the ro-
tating stall theory, it is only permissible to use the data measured prior
to rotating stall inception. These regions are labelled "no rotating stall"
in Figure 21 and the small differences in the data are within the range of
the probable experimental scatter. Hence it is concluded that prior to ro-
tating stall inception the average loss performance of the rotor with inlet
distortion was essentially the same as that found on the isolated rotor.
Moreover, as can be seen in Figure 21, rotating stall inception occurred at

almost identical values of flow coefficient, φ, on the isolated rotor and on the rotor with circumferential inlet distortion.

In addition to rotating stall inception points, the numbers of cells and propagation velocities of rotating stall were measured for both distortion screens. These data were obtained through the use of two static pressure taps on the outer casing at the approximate axial location of the rotor quarter-chord. The two static taps were separated by seven rotor blade spaces in the circumferential direction. The rotor contains 46 blades; thus the circumferential separation, $\Delta\theta$, was 54.8 degrees. With the two-lobe distortion screen, data were taken for two different screen circumferential locations with respect to the static pressure taps. This was done in order to determine if the location of the pressure sensors relative to the distortion screen has an effect on the detection of rotating stall inception and its properties after inception. The location of the pressure sensors with respect to the distortion screen had no detectable effect on the inception or properties of rotating stall. However, at rotor rpm's well below rotating stall, the pressure fluctuations due to blade passage were affected by the relative location of the pressure sensors. A pressure sensor in the wake of the distortion screen showed larger blade passage pressure fluctuations than a sensor outside of the screen wake. As rotor speed was increased toward rotating stall inception, the blade passage fluctuations outside of the screen wake increased more rapidly than those inside the wake until, at inception, the blade passage pressure fluctuations were approximately equal inside and outside of the screen wake. Moreover, rotating stall pressure fluctuations were also approximately equal inside and outside of the screen wake.

The measured rotating stall propagation velocities are shown in Figure 22 for both distortion screens. Previously obtained data (Reference 1) for the rotor with no inlet distortion are shown for comparison. Note that the propagation velocities, V_{P_R} are presented in a coordinate system fixed to the rotor blades and also that the propagation velocities have been made dimensionless by the mean inlet swirl velocity, $\bar{W}_{f_R}$, relative to the rotor.

28

The absolute rotating stall propagation velocity is related to the relative velocity by $V_{P_R}/\bar{W}_{,_R} = 1-(V_P/W_P)$ where V_P is the absolute propagation velocity and W_P is the rotor velocity. The horizontal coordinate of Figure 22 is the overall inlet swirl angle, $\bar{\bar{\beta}}_{,_R}$, relative to the rotor. The value of $\bar{\bar{\beta}}_{,_R}$ was calculated as in Reference 1(Equation 10) and assumes that local deviations in the relative inlet swirl angle due to the presence of the distortion screens integrate to zero around the annulus. The number of stall cells are indicated in Figure 22 by the numbers near the data points.

The data presented in Figure 22 show only minor differences in the inception and properties of rotating stall with and without inlet distortion. In all cases, rotating stall inception was slightly hysteretic, that is as rotor rpm was increased ($\bar{\bar{\beta}}_{,_R}$ increasing) rotating stall occurred at a hi. ·r value of rpm than the value at which it disappeared on decreasing the rotor rpm ($\bar{\bar{\beta}}_{,_R}$ decreasing). With both distortion screen configurations, inception occurred at the same value of $\bar{\bar{\beta}}_{,_R}$ and this value was less than one degree larger than the value of $\bar{\bar{\beta}}_{,_R}$ at inception with no distortion screen. The numbers of stall cells observed were similar in all cases, with the changeover from one to two cells occurring at identical values of $\bar{\bar{\beta}}_{,_R}$. With the distortion screens in place, relative propagation velocities were slightly higher than those observed with no distortion but the overall scatter in the data is larger than the apparent differ-nces i.1 propagation velocity. In general it can be stated that the presence of the distortion screens had a negligible effect on the inception of rotating stall and on its properties after inception.

In summary, the comparisons of steady state turning and loss performance and of rotating stall inception and properties on a rotor with and without circumferential inlet distortion has shown only very small differences in all quantities The largest difference is a small constant difference in flow turning performance between the isolated rotor and the rotor with inlet distortion. The nearly identical steady state turning and loss performance of the rotor with and without inlet distortion may be fortuitous. However, given these steady state performance similarities, it is worth noting that

rotating stall inception and its proper*ies after inception were also similar
with and without inlet distortion. The implications of these results are
discussed in Section III where the experimental results are compared to the-
oretical predictions.

3. Experiments With Rotating Distortion

The final tests performed in these studies of rotating stall were
designed to investigate whether there is a difference in rotating stall in-
ception conditions when a circumferential inlet distortion pattern rotates
at different speeds about the compressor axis. The multi-lobe distortion in-
vestigations mentioned previously (Reference 3 and 4) have suggested that
inception may be sensitive to a dimensionless reduced frequency based upon
the time of passage of a rotor blade through the distortion pattern. If this
is true, it should be possible to observe changes in the inception point on
a given rotor subjected to a given inlet distortion pattern which has different
rotational speeds about the compressor axis. The changes will arise because
the passage time of a rotor blade through the lobes of the distortion pattern
will change as the distortion pattern changes speed. Evidence obtained in
this way would be subject to less ambiguity than that inferred from the multi-
lobe distortion investigations because the circumferential extent of the dis-
tortion pattern will remain essentially unchanged.

These tests were performed with Rotor Set No. 1 and the two-lobe
distortion screen (Configuration A) sketched in Figure 12(a). The configura-
tion of the annular cascade was the same as that used for the tests with
stationary distortion (Figure 11). The procedure used in these tests was to
hold the rotor speed constant at 1000 rpm and study rotating stall inception
at a series of distortion screen rotational speeds. At each distortion screen
speed, inception was incurred by gradually reducing the mass flow through the
rotor from a high value to a low value.

Several methods for detecting the presence of rotating stall were
investigated. The most informative data were obtained by recording the unsteady
total pressure fluctuations at mid-annulus immediately upstream of the rotor.

50

These records display the distortion screen wakes with the fluctu-
ations due to rotating stall superimposed upon them. It is these total
pressure records which are used in the following presentation.

The experimental results are presented as a series of Brush Recorder
strips in Figures 23 through 27. Each individual record is composed of two
recorder strips. The upper strip shows the dynamic pressure, q_o , measured
in the constant area annulus well upstream of the distortion screen. (Sta-
tion 0 in Figure 11). The mean axial velocity, U_o , through the test section
is proportional to the square root of q_o . The value of q_o , at rotating stall
inception in combination with the constant rotor speed (1000 rpm) is suffi-
cient to define the flow coefficient, φ , at inception. The lower strip
shows the total pressure difference, ΔP_T between two probes, one mounted at
mid-annulus well upstream of the distortion screen (Station 0 in Figure 11)
and one mounted at mid-annulus just upstream of the rotor (Station 1 in
Figure 11). The connection between the pressure transducer and the total
pressure probe at Station 1 was kept as short as possible to obtain a good
frequency response. The frequency response was not measured but the results
indicate that it was sufficient to display the distortion screen wakes and
fluctuations due to rotating stall.

In each of Figures 23 through 27, the vertical scale factors for
q_o and ΔP_T are shown on the right side of the appropriate record strips.
The scale factor for q_o is the same in all records (0.4 to 1.4 inches of
water). Two different scale factors were used for the total pressure dif-
ference, ΔP_T . The first experiments, which were performed with the rotor
and screen rotating in opposite directions, used a full scale range from 0 to
-2 inches of water. (Negative values indicate a total pressure drop across
the distortion screen.) In later tests with the rotor and screen rotating in
the same direction, this range was found to be too small. Thus the full
scale range for ΔP_T was changed to 0 to -5 inches of water. This change in
scale should be kept in mind when inspecting the ΔP_T records. In all cases,
time is increasing from left to right and its magnitude is given between the
q_o and ΔP_T record strips. Changes in time scale during a record are also
indicated.

The first set of records, shown in Figure 23, illustrate rotating stall inception with the distortion screen stationary. These records correspond to the test conditions used in the stationary distortion screen experiments described in Section II-C-2. The measurements made during the stationary screen experiments were more comprehensive and used rotating stall detection techniques which have been proven in past studies. Thus it is of interest to compare results obtained from Figure 23 with the results of the stationary distortion screen experiments. This is done in the following discussion.

Figure 23(a) was obtained with the downstream total pressure probe (Station 1) in the free-stream area between the two distortion screen lobes. Figure 23(b) was obtained with the same total pressure probe in the wake of one of the distortion screen lobes. The presence of rotating stall is obvious in both the q_o and the ΔP_T record strips. The steady total pressure drop in the distortion screen wake prior to rotating stall inception can be seen on the far left side of Figure 23(b). The flow coefficient ϕ defined in Section II-A-2 can be calculated from the rotor speed and the value of q_o at inception. These calculated values of ϕ are 0.509 and 0.496 for Figures 23(a) and 23(b) respectively. These values compare well with the stationary distortion data shown in Figure 21.

The expanded time portions of the ΔP_T records on the right side of Figure 23 show that with stationary distortion rotating stall is highly regular with a frequency of 8 Hz. This corresponds to one stall cell moving at an absolute propagation velocity of 48 percent of the rotor speed or a relative velocity of 52 percent of the rotor speed. The relative value falls within the range of values observed in the earlier tests with stationary distortion. (Figure 22, Configuration A). The main difference between the total pressure records in Figures 23(a) and 23(b) is that the distortion screen wake is evident both before and after rotating stall inception in Figure 23(b).

In view of the good agreeme between the results for rotating stall inception inferred from the data presented in Figure 23 and the results obtained in the more comprehensive measurements presented in Section II-A-2 for stationary distortion, it is concluded that the technique used to generate Figure 23 can be used to study the effect of rotating distortion on inception of rotating stall. The results obtained with rotating distortion are presented in the following paragraphs.

Figure 24 presents a series of Brush record strips taken with the distortion screen rotating in the direction opposite that of the rotor. Parts a, b and c of Figure 24 show the results obtained at three different rotational speeds of the distortion screen. The full series of tests covered the range of screen rpm's between 0 and -1000 in increments of 100 rpm. As with the stationary screen, inception of rotating stall is obvious in both the ΔP_T and the q_o record strips.

The left side of Figure 23 shows conditions prior to inception. The ΔP_T records indicate that the magnitude of the defect in the wakes of the rotating screen increased with increasing screen rpm. This effect will be illustrated more clearly in later figures where the average value of q_o was held constant. In this figure q_o was varied in order to induce inception. The q_o records prior to rotating stall also show fluctuations at the passage frequency of the distortion screen lobes. This indicates that the screen generated disturbances extend well upstream of the rotating screen. The magnitude of these q_o fluctuations are probably larger than those in the record strips since the q_o transducer was connected to the upstream total and static pressure probes by long tubing. For the purpose of these experiments, only the time average value of q_o is required at rotating stall inception. This was obtained by numerically averaging the fluctuating q_o records at inception.

Inspection of the expanded time scale records on the right of Figure 24 suggests that rotating stall is almost completely independent of the distortion screen disturbances. This is particularly apparent at the two lower screen η 's where the ΔP_T signals from rotating stall are easily

distinguishable from the screen wakes because the stall signals are substantially larger than the wake signals. The rotating stall signals show the same characteristics as those obtained with the stationary screen (Figure 23). The screen wake signals are simply superimposed on the rotating stall signals. Moreover, the fluctuating q_e records show that the stall frequency is nearly independent of screen rpm. This frequency decreased a very small amount with increased screen rpm, from 8 Hz at 0 screen rpm (0 Hz) to 5.8 Hz at -800 screen rpm (26.7 Hz).

Inspection of the inlet dynamic pressure, q_e, records at rotating stall inception shows that as negative screen rotation increased, the average value of q_e, and hence the average flow coefficient $\bar{\phi}$, increased by a small amount. The quantitative effect of screen rotation on the average flow coefficient at inception will be presented shortly along with results obtained with positive screen rotation. At this point it is sufficient to note that the rotating stall inception points defined by q_e and also the frequencies of rotating stall after inception were almost independent of distortion screen rotation in a direction opposite that of the rotor.

Sample records obtained with the distortion screen rotating in the same direction as the rotor are shown in Figure 25. Note that the ΔP_r records have a different full scale range than those shown in Figure 24. As with the negative screen rotation, the full series of tests covered the complete range of screen rpm's between 0 and 1000 in increments of 100 rpm. Additional results were recorded at 50 and 550 rpm on the screen because of some interesting features in the overall results.

Prior to inception of rotating stall, the q_e and ΔP_r records in Figure 25 show screen generated fluctuations similar to those observed at negative screen rotations. However the average value of q_e at inception varies considerably with positive screen rotation. The complete set of records taken with positive screen rotation showed that there is a large peak in the inception values of q_e. This peak is centered about a screen speed

34

of approximately 550 rpm. At lower and higher screen speeds the inception
values of q_o decrease. This result is different from that obtained with
negative screen rotational speeds where the value of q_o at inception was
almost independent of screen speed.

After stall inception, the ΔP_T records display a variable behavior.
At low screen speeds (Figure 25(a)) the rotating screen wakes appear to inter-
fere destructively with rotating stall, limiting the occurrence of large
amplitude stall to intermittent intervals in time. This destructive inter-
ference appeared to reach a maximum at a screen speed of approximately
300 rpm (Not shown). At screen rotational speeds near 500 rpm, (Figure 25(b))
the screen generated disturbances become nearly in phase with rotating stall
and appear to reinforce the occurrence of rotating stall. The stall frequency
under these conditions appears to double, corresponding to a two cell ro-
tating stall pattern appropriate to the two lobe rotating distortion screen.
At screen speeds well above 500 rpm, destructive interference begins to occur
again (Figure 25(c)).

The screen speeds at which rotating stall is reinforced correspond
to the peak values of q_o measured at inception while the destructive inter-
ference corresponds to decreasing values of q_o at inception. In the regions
of destructive interference, it is possible to distinguish the occurrence of
a small amplitude and a large amplitude rotating stall at different values of
q_o, with the small amplitude inception occurring at higher values of q_o.
These inception points have been labeled in Figure 25 in cases where they are
distinguishable. It is worth noting that the results obtained with negative
screen rotation (Figure 24) showed only large amplitude stall inception,
while the stationary screen (Figure 23) showed small amplitude inception which
rapidly changed to large amplitude without a change in q_o.

In summary, the results presented in Figure 24 and 25 for negative
and positive values of distortion screen rotational speeds suggest that ro-
tating stall displays an effect similar to resonance with the maximum effect

centered at a screen speed of approximately 550 rpm (55 percent of the rotor speed). In a rotor fixed coordinate system this corresponds to a speed ratio of 0.45 which agrees very well with the natural rotating stall propagation speeds observed on the isolated rotor and on the rotor with stationary distortion Configuration A (See Figure 22).

Some additional records which display the similarity to resonance are shown in Figures 26 and 27. In these figures the average inlet dynamic pressure was held constant at one inch of water and a series of records were obtained for fine increments in screen rotational speed. Rotor speed was held constant at 1000 rpm. The result is somewhat similar to inspecting the amplitude versus frequency response of a forced resonant system while holding the forcing amplitude nearly constant. The correspondence is not exact since the forcing function amplitude, ΔP_T , increased with increasing screen speed and the response depends on the constant value of q_a selected. In this case, q_a was selected to be above the value required for rotating stall inception except in the region of the resonant peak.

The records obtained with negative screen speeds are shown in Figure 26. Rotating stall was not occurring in any of these records. The main feature to be observed is the increase in amplitude of the total pressure defect, ΔP_T , as screen speed is increased. This occurred even though the value of q_a was held constant. It is believed to be a result of increasing swirl angle relative to the screen as the screen speed is increased. The screen is composed of flat plates with holes drilled through them to attain the required porosity. In this type of structure, changing the flow angle from a direction normal to its face results in increased losses due to changes in leading edge separation on the holes. The effect should be independent of the direction of rotation. Similar results have been observed on honey comb structures. In any event, as noted previously the increase in ΔP_T amplitude with negative screen speed did not have much influence on rotating stall inception or on its properties after inception.

The records obtained with positive screen rotational speeds are shown in Figure 27. At screen rpm's of 300 and less (Figures 27(a), (b) and (c)) rotating stall did not occur while at 400 rpm there is evidence of an occasional small amplitude rotating stall in the ΔP_T record (Figure 27(d)). At 500 and 550 rpm (Figures 27(e) and (f)), large amplitude rotating stall occurs regularly and is nearly in phase with the screen generated disturbances. At rotational speeds above 550 rpm, rotating stall becomes intermittent and of smaller amplitude until at 800 rpm, detectable rotating stall has disappeared. In the absence of rotating stall, the screen generated disturbances in ΔP_T increase with screen speed in approximately the same fashion as observed with negative screen speeds (Note the change in full scale range of the ΔP_T records between Figures 26 and 27.) At high positive screen speeds, the expanded time records for ΔP_T display a change in shape but no significant changes in amplitude. These changes may be due to an interaction between the distortion and the rotor as the distortion speed approaches the rotor speed. However, they are definitely not evidence of large amplitude rotating stall and are not believed to be evidence of small amplitude rotating stall.

As noted previously, quantitative values for the average flow coefficient, $\bar{\phi}$, at rotating stall inception can be calculated from the average value of q_o at inception. This has been done for all of the records. The results are shown in Figure 28 plotted as a function of distortion screen rpm divided by the rotor rpm. When presented in this way, the resulting curve is similar to that of a damped harmonic oscillator with its fundamental frequency occurring at a screen/rotor velocity ratio of about 0.55. There are no data available to define the peak of the resonant curve because the maximum flow coefficient attainable in the annular cascade was reached before rotating stall disappeared in this region. The maximum attainable value of $\bar{\phi}$ is shown as a heavy dashed line in Figure 28. Points A and B in the peak region were obtained at the maximum attainable $\bar{\phi}$ rather than at inception. The corresponding notes for A and B are included to describe the rotating stall characteristics at this maximum value of $\bar{\phi}$. The data presented in Figures 26 and 27 for constant average q_o correspond to a constant average flow coefficient, $\bar{\phi}$, of 0.586 in Figure 28. Thus Figures 27(e), (f) and (g)

37

display large amplitude rotating stall at screen/rotor velocity ratios of 0.5, 0.55, and 0.6 respectively, while Figures 27(d) and (h) display small amplitude rotating stall for screen/rotor velocity ratios of 0.4 and 0.7 respectively.

In previous experiments, the propagation velocities of rotating stall on the isolated rotor and on the rotor with stationary inlet distortion were measured. The results obtained for these naturally occurring rotating stalls have been presented in Figure 22 for a frame of reference fixed to the rotor. The range of these natural stall propagation speeds are shown in Figure 28 in the stationary coordinate system appropriate to this figure. Note that the peak in the rotating stall inception curve occurs at screen/ rotor speed ratios which agree almost exactly with the natural rotating stall propagation speed.

The general characteristics for the rotating stall inception data shown in Figure 28 agree with the observations made previously regarding the characteristics of rotating stall when it does occur. These may be summarized as follows. At negative and zero screen/rotor velocity ratios, rotating stall amplitude and frequency are almost completely independent of screen velocity. At low positive screen/rotor velocity ratios there is destructive interference between the distortion and the rotating stall. Rotating stall becomes inter- mittent and occurs as a small amplitude stall followed by a larger amplitude stall at a lower value of $\bar{Q}$. The maximum destructive interference was ob- served with a screen/rotor velocity ratio of 0.3. The same value shows the maximum delay in inception of large amplitude rotating stall (lowest value of $\bar{Q}$). Near the peak of the inception curve, rotating stall becomes large in amplitude and approximately in phase with the distortion screen wakes. Moreover the rotating stall frequency doubles from its previous nearly constant value. This indicates that the number of stall cells has changed from one to two in correspondence with the number of lobes on the distortion screen. At screen/rotor velocity ratios larger than the value at the peaks of the in- ception curve, rotating stall again becomes intermittent and the amplitude decreases. Here again, large amplitude rotating stall is preceded by small

amplitude rotating stall and the flow coefficient at inception decreases
with increasing distortion screen speed.

The above observations on destructive interference and reinforce-
ment and the resonant-like peak response of the inception curve contradict
the hypothesis that there is a minimum time required to stall the rotor
blades, and thus that the time required for a rotor blade to pass through a
distortion cell will have a significant influence on rotating stall. If
the hypothesis were valid, rotating stall inception would occur at increasingly
larger values of flow coefficient as the screen speed approached the rotor
speed. Instead the data show a decrease in flow coefficient near a screen/
rotor speed ratio of one. Moreover, the destructive interference observed
in the data cannot be reconciled with the time to stall hypothesis.

In many ways the results obtained in the rotating distortion ex-
periments are similar to the results observed in the damping experiments of
Reference 1. In those experiments a disturbance was generated by rotating
a small flat plate about a radial axis. The plate was situated between two
of the blades in a stator row. It was found that rotating stall is almost
completely independent of the disturbance excitation frequency unless the
disturbance frequency and the frequency of naturally occurring rotating stall
were closely matched. A small amount of destructive interference between
the forcing disturbance and rotating stall was also observed at disturbance
generator frequencies removed from the natural rotating stall frequency.

Thus both the previous damping experiments and the current rotating
distortion experiments suggest that the response of a blade row to circum-
ferential distortion and the occurrence of rotating stall on that blade row
are uncoupled phenomena except under conditions where the disturbance velocity
approaches the propagation speed of naturally occurring rotating stall.
This matching of distortion and stall propagations speeds is not likely to
be attained in a typical compressor since the distortion is usually stationary
while rotating stall propagates at some fraction of the rotor speed. The
observed dependence of stall inception on the extent of stationary distortion

39

cells (References 3 and 4) would appear to be a result of phenomena other than the time to stall argument (Reference 5). The dependence may be due to the effects of a downstream diffuser such as studied in Reference 6.

E.   CONCLUDING REMARKS

The results of two separate experimental investigations of rotating stall have been presented in Section II. In the first investigation, Section II-B, the experiments were designed to investigate whether interference between a rotor and a stator has an effect on the conditions for inception of rotating stall. The rotor row and the stator row used in these experiments had previously been tested in isolation so that the conditions under which the individual blade rows undergo inception were known. Thus the presence of interference effects between the two rows when combined to form a compressor stage could be determined by comparison with the individual blade row performances. In the second investigation, Section II-C, the effects of circumferential inlet distortion on the inception and properties of rotating stall on a rotor were studied. These tests were performed both with the distortion pattern stationary in the laboratory frame of reference and with the distortion pattern rotating about the compressor axis at various speeds. The rotating distortion experiments were undertaken to determine if the time of passage of a rotor blade through a distortion cell has an influence on the inception of rotating stall. As with the blade row interference studies, the rotor used in these tests had been tested previously in isolation so that the conditions which cause rotating stall on the rotor with uniform inflow were available for comparison.

In all of the rotor-stator interference experiments of Section II-B, the inlet flow conditions relative to each blade row were such that in the absence of interference, rotating stall would occur first on the rotor. These studies were performed at a fixed setting of the rotor blade stagger angle, but with four different settings of the stator blade stagger angle. The combined results showed an increasingly larger delay in rotating stall

40

inception in comparison to the isolated rotor as the stator stagger angle was increased, that is as the stator row was unloaded. Thus it is concluded that rotor-stator interference does have an effect on rotating stall inception and that the magnitude of the effect depends on the loading of the blade row which would be unstalled in the absence of interference. The results of these experiments are compared with the predictions of two-blade row rotating stall theory in Section III.

The studies of rotating stall on a rotor in the presence of stationary circumferential inlet distortion, Section II-C-2, used two symmetric multi-lobe distortion screens. Each screen covered the same total area but one consisted of two lobes and one consisted of four lobes. The screens produced square wave circumferential inlet distortion patterns with a total pressure drop of approximately 1.1 times the dynamic pressure far upstream. Comparison of the steady state turning and loss performance of the rotor with and without inlet distortion showed only very small differences in these performances. The largest difference was a small constant difference in flow turning performance between the isolated rotor and the rotor with inlet distortion. Similar comparisons of rotating stall inception conditions and of the numbers of cells and propagation velocities after inception showed negligible differences between the distorted and undistorted flow results. Rotating stall inception and its properties after inception appeared to be almost completely independent of the presence of stationary inlet distortion.

The studies of rotating stall in the presence of rotating inlet distortion, Section II-C-3, were performed with the two-lobe distortion screen from the preceding tests. In these tests the distortion screen was rotated about the compressor axis at various angular velocities, both in the direction of the rotor velocity and in a direction opposite that of the rotor velocity. The maximum screen rpm in both directions was equal to the magnitude of the rotor rpm. For zero and negative screen rpm's (screen rotating in a direction opposite that of the rotor), rotating stall inception and its properties after inception appeared to be almost completely independent of

41

the presence of inlet distortion. However the results obtained with positive
screen rpm were greatly dependent on screen rotation. When the screen was
rotated at a velocity near that of the propagation speed of rotating stall
on the isolated rotor, inception occurred considerably earlier and rotating
stall appeared to occur in phase with the distortion screen disturbances.
At screen speeds other than that corresponding to the natural stall propaga-
tion speed, rotating stall inception was delayed relative to the in-phase
value. When the compressor flow coefficient at inception is plotted as a
function of screen/rotor speed ratio, the resulting curve is similar in shape
to the amplitude versus frequency curve of a damped harmonic oscillator with
its resonant frequency at the natural propagation speed of rotating stall.

The overall results of the studies with stationary and rotating
inlet distortion suggest that rotating stall inception is significantly in-
fluenced by circumferential inlet distortion only when the distortion dis-
turbances are nearly in phase with the rotating stall which would occur
naturally on the same rotor. This matching of distortion and rotating stall
is not likely to occur in a typical compressor with stationary inlet dis-
tortion. Experiments which display a dependence of stall inception conditions
on the circumferential extent of stationary distortion require an explanation
other than the hypothesis that rotating stall depends on the rotor blade pas-
sage time through a distortion cell. Such dependence may be a direct result
of the geometry of the distortion pattern in combination with the presence of
a diffuser downstream of the compressor (Reference 6). In the current studies,
diffuser effects were minimized by extending the constant area annulus far
downstream of the rotor and terminating the constant area annulus with an
annular honeycomb structure.

In addition to the results discussed above, the experimental in-
vestigations provided qualitative and quantitative data which are valuable
for guidance of the theoretical development and for assessing the success
of the theoretical predictions by comparison with experimental results. (See
Section III).

SECTION III
THEORETICAL ROTATING STALL RESEARCH

A.   INTRODUCTION

The primary questions that have been addressed by the theoretical
studies are the effects of distortion, close coupling of blade rows and
compressibility on the inception conditions for rotating stall. The previous
program at Calspan (reported in Reference 1) showed that a two-dimensional
small disturbance stability theory was capable of adequately predicting
inception conditions for isolated blade rows of high hub-to-tip ratio in low
speed flows. Consequently, the major portion of effort during the present
program was concerned with extending this theory to include the above mentioned
effects. In addition, the development of a three dimensional rotating stall
theory was initiated and its present state of development is reported here.

The analysis of distortion has been treated by an extension of the
small disturbance stability theory given in Reference 1. This strictly limits
considerations to small distortions of the mean flow, but proves adequate to
explain the qualitative trends found in the experiments reported in Section II
where the distortion was not small. The distortion analysis is presented in
Section III-B.

The two-dimensional stability theory had been formulated for a two
blade row configuration in Reference 1. A limited amount of correlation of the
two blade row theory was also given there but the spacing between blade rows
for the configurations analyzed was evidently so large that no significant
effects of spacing on rotating stall inception were found. The primary effect
found for those configurations was that the blade row spacing determined the
number of stall cells that occurred at inception, but the relative swirl angle
for inception was essentially unaltered from the isolated blade row case. The
results of the present study of closely coupled blade rows drastically alter
this second conclusion. The present results indicate that for a normal type of

43

closely coupled rotor-stator stage, the inlet swirl to the rotor at which
rotating stall occurs is considerably higher than for the case of the rotor
alone. The analysis for blade-row interference is presented in Section III-C.

The previously developed stability theory[1] for incompressible flow
has also been extended to consider the case for wholly subsonic flow external
to the blade row. The extension proves to be straightforward and does not turn
up any new mechanisms that influence the onset of rotating stall. Namely, the
slope of the loss curve as a function of inlet swirl is still the dominant blade
row characteristic that influences the stability of a given flow configuration.
As such, the theory is expected to give an adequate prediction of the rotating
stall boundary provided that the appropriate loss characteristics of the
blade row in compressible flow are available. This analysis is presented in
Section III-D.

Although a two dimensional theory has proved adequate to describe the
rotating stall phenomena that have been observed in the Calspan/Air Force Annular
Cascade Facility (a low speed test rig of high hub-to-tip ratio) there are
many practical configurations where this situation does not obtain. In particular,
the first stages of many actual jet engine compressors are of relatively low
hub-to-tip ratio where three dimensional effects may be important. For this
reason, the development of a three dimensional stability theory was initiated
under the present program. The overall format of the theory will be the same
as in the two-dimensional case in that the stability of a basic mean flow to
unsteady perturbations will be studied. The first task in developing such a
theory is to obtain a realistic but tractable representation for the mean
steady three dimensional flow through a blade row such that the perturbation
analysis does not become so complex as to obscure the physics of the flow
process. A simplified actuator-disc model has been developed as a viable
candidate for this required mean flow representation. The model is not limited
to small turning through the blade row and uses two-dimensional blade row loss
and turning performance (such as would be available from conventional cascade
tests) in a strip theory fashion. This analysis for three dimensional flow is
presented in Section III-E.

44

B.   EFFECTS OF INLET DISTORTION

The analysis of inlet distortion has been made within the framework
of a two-dimensional incompressible flow model. It was shown in Reference 1
that this type of analysis was adequate for high hub-to-tip ratio configurations.
Strictly interpreted, the two-dimensional assumption restricts the analysis to
consideration of distortion patterns that have only circumferential variation.
However, it was found in Reference 1 that some radial variations in flow
quantities can be handled by using appropriate radial averages. Presumably,
this would also be true for the distortion problem.

The flow model employed is similar to that used in the small disturbance
stability theory of Reference 1. We briefly restate the basic assumptions that
are inherent in this type of modeling:

1.   The flow is incompressible (low speed)
2.   The blade row has high hub-to-tip ratio
3.   The annular area is constant
4.   The flow disturbances have wave lengths in the circumferential
      direction (Y-direction) which are large compared to either the
      blade spacing or chord.
5.   The local performance of the blade row is only a function of the
      local inlet swirl and dynamic pressure and may be obtained in a
      quasi-steady fashion from the steady state performance data.

Assumption 4 in conjunction with 5 implies that the admissible dis-
turbances have a low reduced frequency based upon the velocity relative to the
blade and the blade chord length. This is consistent with our previous results.

It has been suggested[5] that the phenomenon of "stall delay" is im-
portant to the fashion in which inlet distortion influences the stall boundary
of a compressor stage. In reality, this is the same phenomenon that was referred

45

to as a boundary layer lag time for separation in the early rotating stall works. The basic idea is that when an airfoil (or blade row) has its angle of attack (inlet swirl) suddenly increased to a condition where the airfoil would normally be stalled then the boundary layer does not respond immediately to the new conditions but requires some time to adjust. During this adjustment period, the airfoil (blade row) may exceed its normal steady state performance limits. It was found in Reference 1 that the occurrence of this phenomenon was not essential to the development of a rotating stall; consequently, it has not been considered in the ensuing analysis of distortion.

In addition to the previously mentioned restrictions on the flow model, the following analysis will be limited to the case where the distortion is a small perturbation on the mean steady flow. It was found necessary to limit the theory in this respect in order to obtain analytical results. Moreover, the use of this assumption and the theory of linear systems would allow us to immediately state the results; however, since the linearized theory adequately explains many of the experimental observations given in Section II-C, the formal development will be presented in detail.

The flow through an isolated blade row in incompressible flow is considered. A finite thickness two-dimensional actuator as shown in Figure 29 is used to model the blade row. Also, an arbitrary, but prescribed, distortion in total pressure and/or velocity is indicated ahead of the blade row. Subscripts o's indicate quantities in a blade fixed coordinate system. The transformation between blade fixed coordinates and the laboratory fixed system is given by:

$$x_o = x$$

$$y_o = y - W_b t$$

$$t_o = t$$

where W_b is the blade velocity in the laboratory fixed system. The conditions upstream of the blade row are denoted by a subscript 1 while conditions downstream of the blade row are denoted by a subscript 2. The mean flows upstream and downstream of the blade row are uniform but of different swirl angles. The

46

mean absolute swirl in each flow region is denoted by S_i and is equal to W_i/U_i. The blade row is moving with an absolute velocity W_b and the non-dimensional blade velocity is given by $\bar{\Omega} = W_b/U_1$. The relative swirl with respect to the blade row is denoted by $\not{S}_i$ and is given by $\not{S}_i = S_i - \bar{\Omega}$. The total flow quantities which are denoted by a hat are decomposed in steady and unsteady parts as:

$$\hat{W}_i = W_i + \omega_i\,(x,y,t)$$

$$\hat{U}_i = U_i + u_i\,(x,y,t)$$

$$\hat{H}_i = H_i + h_i\,(x,y,t)$$

where H is the total pressure.

It is assumed that the steady state performance of the blade row is known in the following form:

The turning performance of the blade row is given by
$$\not{S}_2 = G(\not{S}_1)$$
and the losses through the blade row are given by
$$H_{o_2} = H_{o_1} - \frac{1}{2}\,\chi\,\rho\,(U_{o_1}^2 + W_{o_1}^2)$$
where $\chi = \chi(\not{S}_1)$ is known.

By the quasi-steady assumption, the instantaneous values of $\hat{\not{S}}_2$ or $\hat{H}_{o_i}$ in unsteady flow are obtained by inputing the required instantaneous values of $\hat{\not{S}}_i$, $\hat{U}_{o_1}$, and $\hat{W}_{o_1}$ in the above functions. We assume that the distortion wave does not alter the mean part of these quasi-steady relations. In the actual use of these relations, they will be linearized about their steady state values.

We start by considering the distortion pattern. Clearly, the distortion pattern must satisfy the equations of motion. Since the flow is incompressible, the distortion pattern may be described by a stream function

$\psi(x, y, t)$ which is related to the velocity components by $\hat{U} = \partial\psi/\partial y$ and $\hat{w} = -\partial\psi/\partial x$. The equation for the stream function is

$$\frac{\partial \Omega}{\partial t} - \frac{\partial \psi}{\partial y}\frac{\partial \Omega}{\partial x} - \frac{\partial \psi}{\partial x}\frac{\partial \Omega}{\partial y} = 0$$

(1)

where $\Omega = -\nabla^2\psi$ and is the vorticity. We should note that Equation 1 is <u>not</u> limited to small disturbances, and applies to a general rotational unsteady flow. Now we are interested in solutions of Equation (1) that represent wave like patterns superimposed on a uniformly swirled steady mainstream. That is, we seek solutions of the form

$$\psi = U_i y - W_i x + \alpha e^{j(ax + by + ct)} + \beta e^{j(\ell x + my + nt)}$$

(2)

T   st two terms represent the mean flow with swirl $\phi_i = \frac{W_i}{U_i}$ and the
.ecu.. two terms correspond to unsteady waves of arbitrary amplitude α and β respectively. The a, b, c, ℓ, m and n are complex constants. Now it may be verified by substitution that Equation (1) has solutions of the desired form provided that the following conditions hold:

$$c + U_i a + W_i b = 0$$

(3)

$$n + U_i \ell + W_i m = 0$$

(4)

$$(ma - b\ell)\{a^2 + b^2 - (m^2 + \ell^2)\} = 0$$

(5)

Conditions (3) and (4) indicate that the waves are convected in the mean flow direction. Since these conditions do not involve the wave amplitude, α and β, we arrive at the very important conclusion that with regard to solution forms of the type (2) the flow acts as a linear system. It is not demonstrated here, but these types of relations generalize to an arbitrary number of waves superimposed on the mean flow. Moreover, it may be shown that waves which are different harmonics of the same fundamental frequency satisfy Equation (5). It should also be noted that the disturbance stream functions employed in Reference 1 are of the form considered here.

These results have the following significance for the present analysis.

1) The analysis is limited to small distortion because the blade
   row performance is linearized about its mean value not because
   of the type of velocity perturbations considered.

2) The usual methods of Fourier analysis may be used to build up an
   arbitrary distortion wave ahead of the blade row. In the
   following work, we will consider a single arbitrary Fourier
   component of distortion ahead of the blade row.

3) The usual method of studying the stability of a flow is to
   perturb the flow with a small periodic disturbance and determine
   under what conditions the disturbance is damped or amplified.
   When the basic flow is time dependent as in the present case,
   this type of analysis can become quite complicated. However,
   since the perturbations to be considered are of the same form as
   the basic Fourier component of the distortion wave and we have
   just shown that they do not interact, and since the blade row
   (actuator) performance is linearized about its mean performance
   point, we may formally split the problem into two parts. The
   first part turns out to be the stability analysis of the mean
   flow without the distortion wave. This is precisely the problem
   considered in Reference 1. The second part of the problem is
   the response of the blade row to the distortion wave. Since
   the first part of the problem is adequately treated in Reference 1
   we will concentrate on the second part in the following work.
   Of course, the same split up of the problem can be accomplished
   by a formal linearization procedure whereby we would consider
   the stability of small periodic disturbances superimposed upon
   a small distortion wave. However, the present discoveries
   allow this split up without recourse to arguments that involve
   the relative orders of smallness of these disturbances.

In the following analysis, we will consider the response of the blade row to a distortion wave. It suffices to consider the velocities associated with a distortion wave since if they are known, the definition of total pressure may be used to calculate the corresponding total pressure variation of the wave. The distortion problem has many similarities to the stability problem considered in Reference 1. Namely, the solutions for the disturbance velocities upstream and downstream of the blade row are of the same general form and contain three undetermined constants. These constants are determined by applying the same matching conditions across the blade row. The notation of Reference 1 will be followed as closely as possible.

It is sufficient to consider the response of the blade row to a single, arbitrary, Fourier component of an upstream distortion wave. The perturbation stream function in each flow region is readily available from the work of Reference 1 as

$$\psi_{i_n}(x, y, t) = \left\{ A_{i_n} e^{-\frac{n x}{r}} + B_{i_n} e^{\frac{n x}{r}} + D_{i_n} e^{-i \frac{n x}{r}(\frac{cr}{n U_o} + S_i)} \right\} e^{i(ct + \frac{n y}{r})} \qquad (6)$$

where the A_{i_n}, B_{i_n}, D_{i_n} are constants in each flow region i and the subscript n denotes that we are considering the nth Fourier component. Prescribing the distortion is equivalent to specifying D_{i_n} and since the system is linear and is being forced at a prescribed frequency, the response will occur only at this prescribed frequency. Hence, we need only consider the single Fourier component in each flow region that corresponds to this forced frequency. Since the Fourier component of the distortion is specified, then c is also specified as opposed to being a free parameter in the stability analysis. Furthermore, c will be all real, otherwise the specified distortion wave would grow or die out exponentially with time. Then, the overall problem will be to solve for the response, i.e., A_{i_n}, B_{i_n} and D_{i_n} for a specified input, D_{i_n}, and determine conditions for the response to become unbounded.

The remaining boundary conditions and matching conditions will be those used in the analysis of Reference 1. In the following analysis, the subscript for Fourier component number will be dropped. The condition of boundedness at upstream and downstream infinity requires $A_i = B_4 = 0$. Then

50

assuming that the distortion, i.e., D_1, is prescribed, the analysis on pp. 46-53 of Reference 1 can be extended to include the D_1 terms. Again, three equations are required to determine B_1, A_2 and D_2 in terms of D_1. The same three matching conditions; namely, mass flow conservation, vorticity compatibility, and the flow deflection relation, are used. With these, the homogeneous system of equations in the stability theory, Equation (26) of Reference 1,[*] is replaced by the corresponding inhomogeneous system of equations of inlet distortion response theory; namely,

$$
\begin{bmatrix}
1 & -e^{\bar{Q}_1} & -e^{\bar{Q}_3} \\
-j\lambda(1+q)-z_1 & -j\lambda e^{\bar{Q}_1} & -[(\lambda+\vartheta_2)\vartheta_2+1]e^{\bar{Q}_3} \\
a(1+j\vartheta_1) & (1-j\vartheta_2)e^{\bar{Q}_1} & j\lambda e^{\bar{Q}_3}
\end{bmatrix}
\begin{bmatrix}
B_1/D_1 \\
A_2/D_1 \\
D_2/D_1
\end{bmatrix}
=
\begin{bmatrix}
-1 \\
z_2(X-1)+\dfrac{X'(1+\vartheta_1^2)\lambda}{2}+j\lambda q \\
j a \lambda
\end{bmatrix}
$$

(7)

where

$$z_1 = (1+j\vartheta_1)\left[\tfrac{1}{2}(1+\vartheta_1^2)X'+X\right]$$

$$z_2 = 1+\vartheta_1(\lambda+\vartheta_1)$$

$$\lambda = \frac{cr}{nU_0} + \Omega$$

$$q = \frac{dn}{r}\,\sec\delta$$

$$\bar{Q}_1 = -\frac{nx_{01}}{r} + j\frac{an}{r}\sin\delta$$

$$\bar{Q}_3 = j\left[\frac{an}{r}\sin\delta - \frac{nx_{02}}{r} + \vartheta_2\right]$$

$$X = \frac{jX}{j\vartheta_1}$$

$$a = \frac{j\vartheta_2}{j\vartheta}$$

_____

[*] Equation 26 of Reference 1 contains a typographical error. The bracket

$$\begin{bmatrix} B_1 \\ A_2 \\ D_2 \end{bmatrix}$$ in Reference 1 should read $$\begin{bmatrix} B_1 \\ A_2 \\ D_2 \end{bmatrix}$$

Equation (7) is a system of three simultaneous linear equations in B_1/D_1, A_2/D_1 and D_2/D_1. The solutions are

$$B_1/D_1 = \mathscr{D}_1/\mathscr{D} \tag{9}$$

$$A_2/D_1 = \mathscr{D}_2/\mathscr{D} \tag{10}$$

$$D_2/D_1 = \mathscr{D}_3/\mathscr{D} \tag{11}$$

where the determinants are

$$\mathscr{D} = \begin{vmatrix} 1 & -e^{\tilde{a}_1} & -e^{\tilde{a}_3} \\ -j\lambda(1+q)-z_1 & -j\lambda e^{\tilde{a}_1} & -\left[(\lambda+\delta_2)\delta_2+1\right]e^{\tilde{a}_3} \\ a(1+j\delta_1) & (1-j\delta_2)e^{\tilde{a}_1} & j\lambda e^{\tilde{a}_3} \end{vmatrix} \tag{12}$$

$$\mathscr{D}_1 = \begin{vmatrix} -1 & -e^{\tilde{a}_1} & -e^{\tilde{a}_3} \\ z_2(X-1)+\dfrac{X'(1+\delta_1^2)\lambda}{2}+j\lambda q & -j\lambda e^{\tilde{a}_1} & -\left[(\lambda+\delta_2)\delta_2+1\right]e^{\tilde{a}_3} \\ j a\lambda & (1-j\delta_2)e^{\tilde{a}_1} & j\lambda e^{\tilde{a}_3} \end{vmatrix} \tag{13}$$

$$\mathscr{D}_2 = \begin{vmatrix} 1 & -1 & -e^{\tilde{a}_3} \\ -j\lambda(1+q)-z_1 & z_2(X-1)+\dfrac{X'(1+\delta_1^2)\lambda}{2}+j\lambda q & -\left[(\lambda+\delta_2)\delta_2+1\right]e^{\tilde{a}_3} \\ a(1+j\delta_1) & j a\lambda & j\lambda e^{\tilde{a}_3} \end{vmatrix} \tag{14}$$

$$\mathscr{D}_3 = \begin{vmatrix} 1 & -e^{\tilde{a}_1} & -1 \\ -j\lambda(1+q)-z_1 & -j\lambda e^{\tilde{a}_1} & z_2(X-1)+\dfrac{X'(1+\delta_1^2)\lambda}{2}+j\lambda q \\ a(1+j\delta_1) & (1-j\delta_2)e^{\tilde{a}_1} & j a\lambda \end{vmatrix} \tag{15}$$

The determinant $\mathscr{D}$ can be expanded out and written in the form

$$\mathscr{D} = (2+q)e^{\tilde{a}_1+\tilde{a}_3}\left[\lambda+j+\delta_2\right]\left[\lambda-\lambda_0\right] \tag{16}$$

where

$$R.P.(\lambda_0) = -\frac{1}{(2+q)}\left\{\frac{1}{2}+\delta_1^2 X+\delta_1 X+a(\delta_1-\delta_2)\delta_1\right\} \tag{17}$$

$$I.P.(\lambda_0) = \frac{1}{(2+q)}\left\{X+\delta_1^2+a(1-\delta_1\delta_2)-\frac{\delta_1}{2}+\delta_1^2 X\right\} \tag{18}$$

Now examining these results, it can be concluded that B_1, D_1 and A_1 will be finite unless $\mathcal{B} \neq 0$. From Equation 16 this can only occur if $\lambda = -(\mathcal{S} + \frac{1}{\lambda})$ or $\lambda = \lambda_0$. The first case is impossible since, as noted previously, C is completely real for specified inlet distortion. The second case would require

$$I.P.(\lambda_0) = 0 \tag{19a}$$

and
$$R.P.(\lambda_0) = \lambda \equiv \frac{cr}{nU_0} \tag{19b}$$

But, the condition described by Equation (19a) can only occur if the inlet conditions to the blade row are such that the blade row is on the rotating stall boundary with no distortion present and Equation (19b) requires that the prescribed distortion have the propagation speed for the self excited rotating stall wave. Hence, we find that the distortion will have no effect on the flow unless the undistorted flow conditions would produce rotating stall and the distortion has a Fourier component corresponding to a natural rotating stall wave under those conditions. In effect, the system is then in resonance, that is, we are then forcing a linear system at its natural frequency. Of course, in the vicinity of resonance, we expect the velocity perturbations to become so large that the linearization is no longer valid. In this region, the nonlinearities will take over to limit the amplitudes of the motion. Then, based upon the linear analysis, we expect that distortion will not affect the rotating stall boundary unless the blade row is near stall and the distortion has a Fourier component which would correspond to the natural rotating stall mode of the blade row. Comparison with the results of the experiments with a rotating distortion screen (see Figure 28) show that this is the case.

It should be pointed out that a linearized small perturbation analysis would result in a similar conclusion for more complex flow situations such as multiple blade rows and variable annulus area. Namely, that the distortion would not affect the stall line unless the distortion put the system in resonance. That is, once the linearized stability boundary has been determined for a given flow case (using the proper blade row performance and boundary conditions for that case), the addition of small distortion to the flow in the fashion done here will only result in unbounded blade row response if the

53

distortion wave has a Fourier component corresponding to the natural rotating stall mode for that particular case.

It should be reemphasized that the foregoing analysis and conclusions assumed that the distortion wave did not influence the mean steady performance of the blade row and the blade row performance was linearized about its mean steady operating point. Some effort was spent upon trying to remove this assumption from the analysis and thus arrive at a nonlinear stability theory. Unfortunately, this type of analysis cannot proceed very far without resulting in the requirement for numerical solutions. The analysis, however, did reveal the following points which aid in the understanding of how distortion affects the stability of the flow.

1. For nonlinear blade row performance we cannot formally split the problem into two parts, i.e., the stability and response problems cannot be treated separately.

2. In the nonlinear case the response of the actuator contains all the Fourier components in the upstream and downstream disturbance velocities. This results in the distortion wave interacting with the blade row to produce a perturbation of the mean steady swirl upstream and downstream of the blade row. This perturbation dies out exponentially with distance from the blade row; but in effect, results in the blade row seeing a different mean inlet swirl and producing different mean performance curves for the blade row. In the real nonlinear case then, each individual distortion wave will produce new mean flow conditions for the blade row which are dependent upon the type of distortion being considered

On the basis of the theoretical analysis performed, we were unable to draw any general conclusions about the interaction of the distortion wave and the mean flow, but on the basis of the experimental results it would appear that these effects are only important near resonance

54

C. THEORY FOR CLOSELY-COUPLES BLADE ROWS

In a typical compressor stage, the spacing between blade rows is less than a chord length. The effect of this close spacing has been investigated experimentally in the annular cascade facility using a stage consisting of Rotor Set No. 1 followed by Stator Set No. 1. The experiments are described above in Section II. Here, we will discuss the corresponding theoretical calculations.

The two blade row stability theory was developed and applied to four cases in Reference 1. These cases were Stator Sets Nos. 1, 4 and 5, each in conjunction with the stationary inlet guide vanes, and Stator Set No. 6, in conjunction with the rotating inlet guide vanes. The spacing between blade rows was large (several chord lengths) in all of these cases to corresponds to the experimental arrangement. The predicted results generally agreed well with the experiments. One case was run with the spacing halved and the results were presented in Figure 51 of Reference 1. Unfortunately, there were no data for comparison.

In the present study, one of the computer programs developed to implement the two blade row analysis of Reference 1 has been modified to handle the input in the form in which it is available for the stage consisting of Rotor Set No. 1 and Stator Set No. 1. The turning and loss data for Rotor Set No. 1 operating in isolation are given in Figures 35 to 37 of Reference 1. These data are used as before, except for the correction of some errors in data reduction. In particular, the last two installed data points for the overall total pressure loss coefficient $\bar{\omega}_{2_e}$, in Figure 37 of Reference 1 are too large. The corrected data are given in Figure 36. Thus, the corrected data have a decreased slope of the loss curve in the vicinity of rotating stall.

Unfortunately, the turning and loss data that are available for Stator Set No. 1 operating in isolation (Figures 11 and 14 of Reference 1) are limited in relative inlet swirl angles to the range of angles near which rotating stall occurred on this set. The relative inlet swirl angles to

55

Stator Set No. 1 in the present experiments are those corresponding to the outlet swirl of Rotor Set No. 1 and are considerably smaller than those for which Stator Set No. 1 data exist. Therefore, extrapolations of the data were necessary. The way in which the data have been extrapolated is described in the next paragraphs.

The Stator Set No. 1 flow turning data in Figure 11 of Reference 1 were obtained for inlet swirl angles, $\vec{\beta}_1$, greater than 53 degrees because it was in this range that rotating stall occurred on this blade row. For the present calculations these data must be extrapolated down to $\vec{\beta}_1$ values of about 20 degrees. The extrapolation was done as follows. First, the flow turning data for Rotor Set No. 1 were examined because they had been obtained over a wide range of operation (Figure 36 of Reference 1). Those data were recast in the form of total flow turning angle $|\vec{\beta}_{1_R}| - |\vec{\beta}_{2_R}|$ versus mean angle of attack $|\vec{\beta}_{1_R}| - |\delta_{R_M}|$, where $\vec{\beta}_{1_R}$ and $\vec{\beta}_{2_R}$ are the inlet and outlet flow angles relative to the blades, respectively, and δ_{R_M} is the rotor stagger angle. The results are plotted in Figure 31 (without denoting the individual data points), for δ_{R_M} values of 30, 40 and 50 degrees. These data collapse quite well into a single curve, particularly at angles of attack below 10 degrees. The main discrepancies are at the higher angles of attack for each δ_{R_M}.

Next, the Stator Set No. 1 flow turning data (Figure 11 of Reference 1) were recast in the same form of $|\vec{\beta}_1| - |\vec{\beta}_2|$ vs $|\vec{\beta}_1| - |\delta_{S_M}|$, where δ_{S_M} is the stator stagger angle, and are plotted in Figure 32 for $\delta_{S_M} = 28.2, 37.2,$ and 57.2 degrees. A single correlation curve has been drawn on Figure 32 to pass approximately through the data points and to have the same behavior at the lower angles of attack that the Rotor Set No. 1 data had in Figure 31. This correlation curve in Figure 32 was then used to generate the desired extrapolations for each of the δ_{S_M} values. The operating range of Stator Set No. 1, when used in conjunction with Rotor Set No. 1, includes conditions for which $\vec{\beta}_1$ is less than δ_{S_M}. For these conditions, the flow turning is assumed to be symmetrical about $\vec{\beta}_1 = \delta_{S_M}$. The final extrapolations so generated are shown in Figure 33, where the actual data points are indicated by the symbols.

56

The extrapolation method for the loss data could not be established on such a firm basis. No loss correlations analogous to those of Figure 31 could be found for the data of Rotor Set No. 1 (Figure 30). Instead, those data could be used only as a guide for the extrapolations for Stator Set No. 1, which are presented in Figure 34. In particular, the minimum value of the total pressure loss coefficient, $\Delta \bar{C}_{P_T}$, was taken as 0.2 for $\delta_{sM} = 28.2$ and 37.2 degrees, as was measured for Rotor Set No. 1 at the two lower stagger angles. A larger value of the $\Delta \bar{C}_{P_T}$ minimum was used for $\delta_{sM} = 57.2$ degrees, analogous to the rotor result for $\delta_{sM} = 50$ degrees. The loss data also were assumed to be symmetrical about $\bar{\beta}_1 = \delta_{sM}$, just as for the flow turning extrapolations of Figure 33. It is unfortunate that a better loss data extrapolation could not be found because, as discussed in Reference 1, the slope of the loss curve is the key parameter in the stability analysis.

Numerical calculations based on the two blade row stability theory were carried out for the stage consisting of Rotor Set No. 1 followed by Stator Set No. 1 using the extrapolations. The rotor stagger angle was $\delta_{sM} = 40$ degrees to correspond to the experiment. The computed damping factor for the stage is plotted as a function of the relative inlet swirl to the rotor, β_1, in Figure 35a both for the rotor alone and for the rotor with the stator at $\delta_{sM} = 28.2$ degrees. Rotating stall inception occurs when the damping factor first goes to zero and the experimental inception points are shown for comparison. Rotating stall occurred with one stall cell both experimentally and theoretically. The presence of the stator delays stall both in theory and experiment by roughly the same amount.

The computed propagation velocity of the one-cell rotating stall pattern is plotted, in the absolute coordinate system, in Figure 35b as a function of β_1, again for the rotor alone and with the stator at $\delta_{sM} = 28.2$ degrees. The computed curve is dashed beyond the theoretical inception point to indicate that the theory is not strictly applicable beyond initial inception. The experimental propagation velocities at inception are shown as well in Figure 35b.

Numerical calculations were also carried out at stator stagger angles of 37.2 and 57.2 degrees. At δ_{SM} = 37.2 degrees, there was a slight additional delay in the predicted rotating stall inception point, but not as much as was found experimentally. The predicted absolute propagation velocity decreased still further which is counter to the experimental results. However, the loss data at δ_{SM} = 37.2 degrees is much more limited than at δ_{SM} = 28.2 degrees, see Figure 34, so that there is not as much confidence in the extrapolation. At δ_{SM} = 57.2 degrees, there is only a small range over which the extrapolated stator data overlaps with the rotor data of Figure 30. These rotor data were obtained at rotor speeds up to 1200 rpm. Since rotating stall inception occurred experimentally on the isolated rotor at 1000 rpm, all the performance data between 1000 and 1200 rpm were measured with rotating stall present and so include very high losses. For numerical calculations at δ_{SM} = 57.2 degrees with the two blade row stability theory, the rotor performance data in rotating stall were used between 1000 and 1200 rpm. The discontinuity in a loss curve at inception was faired out for this purpose. Rotating stall inception on the stage with δ_{SM} = 57.2 degrees was not predicted up to the 1200 rpm limit. This agrees with the experiments where inception did not occur until a rotor speed of 1275 rpm was reached.

The results for a closely coupled rotor-stator row are encouraging since the basic trends of a delay in rotating stall inception and a reduction in the stall propagation velocity are predicted qualitatively. However, the large extrapolations which were necessary in the steady-state loss and turning data, make quantitative comparisons of limited value. More significant correlations must await the acquisition of steady-state loss and turning data on the isolated stator row at the required inlet conditions as well as the measurement of the performance of the rotor row and stator row when combined in a closely coupled stage.

D.   EFFECTS OF COMPRESSIBILITY

The flow model and overall method of analysis employed in the stability theory treatment of compressible flow through a blade row are quite similar to

the incompressible analysis. The major differences are the introduction of
one more dependent variable, the density, and a corresponding additional
matching condition across the actuator which is derived from the energy
equation. The flow model is shown in Figure 36 where again the blade row is
modeled by a finite thickness actuator. The flow region upstream of the
blade row is noted as region 1 and that downstream as region 2. The mean
swirls upstream and downstream are constant but of different values. Quantities
in a blade fixed coordinate system are denoted with a subscript o. The trans-
formation between blade fixed and duct fixed corrdinates is given by

$$x_o = x$$
$$y_o = y - W_b t$$
$$t_o = t$$

where W_b is the blade velocity in the duct fixed system. This velocity is
given in non-dimensional form by $\bar{\Omega}_i = \dfrac{W_b}{U_i}$ where i denotes the flow region and
U_i is the mean axial flow in region i. The mean absolute swirl angle in
each region is denoted as $\bar{\beta}_i$ and the tangent of $\bar{\beta}_i$ is defined as S_i the
absolute swirl. The relative swirl with respect to the blade row is given by
$\beta_i = S_i - \Omega_i$.

Following References 1 and 2, all of the total flow quantities, which
are denoted by a hat, are decomposed into steady and unsteady parts as

$$\hat{U}_i = U_i + u_i(t)$$
$$\hat{W}_i = w_i + w_i(t)$$
$$\hat{P}_i = P_i + p_i(t)$$
$$\hat{\rho}_i = \bar{\rho}_i + \rho_i(t)$$

where $\hat{P}$ and $\hat{\rho}$ are the pressure and density, respectively, and the i denotes
the flow region. The assumptions on the unsteady flow are basically the same
as in the incompressible case, i.e., the flow between blade rows is considered
inviscid, so that frictional and heat conduction effects are neglected.
Generally, however, the flow will be rotational to reflect the losses in-
curred in the blade row. The unsteady disturbance quantities are assumed to
be much smaller than the steady quantities so that the equations of motion can
be linearized about the steady flow.

The resulting linearized equations of motion are those of continuity, x- and y- momentum and energy; namely,

$$\frac{\partial \rho_i}{\partial t} + U_i \frac{\partial \rho_i}{\partial x} + W_i \frac{\partial \rho_i}{\partial y} + R_i \left[\frac{\partial u_i}{\partial x} + \frac{\partial w_i}{\partial y} \right] = 0 \qquad (20)$$

$$\frac{\partial u_i}{\partial t} + U_i \frac{\partial u_i}{\partial x} + W_i \frac{\partial u_i}{\partial y} + \frac{1}{R_i} \frac{\partial p_i}{\partial x} = 0 \qquad (21)$$

$$\frac{\partial w_i}{\partial t} + U_i \frac{\partial w_i}{\partial x} + W_i \frac{\partial w_i}{\partial y} + \frac{1}{R_i} \frac{\partial p_i}{\partial y} = 0 \qquad (22)$$

$$\frac{\partial (p_i - a_i^2 \rho_i)}{\partial t} + U_i \frac{\partial (p_i - a_i^2 \rho_i)}{\partial x} + W_i \frac{\partial (p_i - a_i^2 \rho_i)}{\partial y} = 0 \qquad (23)$$

where the speed of sound a_i is given by $a_i^2 = \gamma P_i / R_i$ and is constant in each flow region; γ is the ratio of specific heats. It will be observed that ρ_i and p_i are coupled with the velocity components. This is in contrast to the incompressible case where ρ_i is zero and p_i decouples. In the incompressible case, a stream function can be defined and the equation solved for it, whereupon u_i, w_i and p_i can be evaluated. A stream function does not exist in unsteady compressible flow, but Equations (20) to (23) can be solved by assuming solutions of the form

$$u_i(x, y, t) = q_i(x) e^{j(ct + \frac{ny}{r})} \qquad (24)$$

$$w_i(x, y, t) = l_i(x) e^{j(ct + \frac{ny}{r})} \qquad (25)$$

$$p_i(x, y, t) = m_i(x) e^{j(ct + \frac{ny}{r})} \qquad (26)$$

$$\rho_i(x, y, t) = n_i(x) e^{j(ct + \frac{ny}{r})} \qquad (27)$$

Here $c = c_R + j c_i$, and n is the number of stall cells and r is the mean radius of the blade row. The resulting disturbance is spatially periodic in the y direction with period $2\pi n r$. The flow is neutrally stable if $c_i = 0$, unstable if $c_i < 0$ and stable if $c_i > 0$.

If Equations (24) to (27) are substituted into Equations (20) to (23), four coupled linear ordinary differential equations in $\hat{x}$, $\mathscr{L}_i$, $\mathfrak{M}_i$ and $\mathfrak{N}_i$ are obtained. These have been solved and the results are

$$u_i(x, y, t) = D_i \, \exp j\left[-m_i x + ct + \frac{ny}{r}\right]$$

$$- \frac{A_i\left(j m_i M_i^2 - \frac{nd_i}{r}\right)}{R_i U_i \left(j m_i - \frac{nd_i}{r}\right)} \, \exp j\left[\frac{m_i M_i^2 + j \frac{nd_i}{r}}{1 - M_i^2} x + ct + \frac{ny}{r}\right]$$

$$- \frac{B_i\left(j m_i M_i^2 + \frac{nd_i}{r}\right)}{R_i U_i \left(j m_i + \frac{nd_i}{r}\right)} \, \exp j\left[\frac{m_i M_i^2 - j \frac{nd_i}{r}}{1 - M_i^2} x + ct + \frac{ny}{r}\right] \quad (28)$$

$$w_i(x, y, t) = \frac{r m_i D_i}{n} \, \exp j\left[-m_i x + ct + \frac{ny}{r}\right]$$

$$- \frac{j \frac{n}{r} A_i (1 - M_i^2)}{R_i U_i \left(j m_i - \frac{nd_i}{r}\right)} \, \exp j\left[\frac{m_i M_i + j \frac{nd_i}{r}}{1 - M_i^2} x + ct + \frac{ny}{r}\right]$$

$$- \frac{j \frac{n}{r} B_i (1 - M_i^2)}{R_i U_i \left(j m_i + \frac{nd_i}{r}\right)} \, \exp j\left[\frac{m_i M_i^2 - j \frac{nd_i}{r}}{1 - M_i^2} x + ct + \frac{ny}{r}\right] \quad (29)$$

$$p_i(x, y, t) = A_i \, \exp j\left[-\frac{m_i M_i^2 + j \frac{nd_i}{r}}{1 - M_i^2} x + ct + \frac{ny}{r}\right]$$

$$+ B_i \, \exp j\left[\frac{m_i M_i^2 - j \frac{nd_i}{r}}{1 - M_i^2} x + ct + \frac{ny}{r}\right] \quad (30)$$

$$\rho_i(x, y, t) = \frac{1}{a_i^2} p_i(x, y, t) + E_i \, \exp j\left[-m_i x + ct + \frac{ny}{r}\right]$$

$$(31)$$

where A_i, B_i, D_i, E_i are constants to be determined by the boundary conditions and the matching conditions, the axial Mach number is $M_i = U_i/a_i$, $m_i = (c + \frac{n}{r} V_i)/U_i$, and $d_i = \left[1 - M_i^2 \left(1 + \frac{r^2 m_i^2}{n^2}\right)\right]^{1/2}$.

Equations 28 to 31 reduce to the incompressible solution of Reference 1 if M_x is set equal to zero and the δ disturbance is neglected. However, the notation is different from that of Reference 1. So in the compressible case, just as in the incompressible case, there are irrotational disturbances (terms proportional to A_i and B_i) and vorticity waves convected along the mean flow streamlines (term proportional to D_i). In addition, for the compressible flow case, the term proportional to E_i represents an entropy wave convected along the mean flow streamline.

There are eight constants to be determined from the boundary conditions. The boundary conditions at upstream and downstream infinity allow the immediate determination of four of these constants. Requiring irrotational isenstropic flow upstream of the blade row gives $D_i \cdot E_i = 0$. Requiring bounded solutions at upstream and downstream infinity gives $A_i \cdot B_2 = 0$. The four remaining constants are determined by the matching conditions across the actuator; namely, the conservation of mass flow, conservation of vorticity, flow turning relation and conservation of energy. The first three of these matching conditions are similar to the incompressible case, with consideration for variable density, and the fourth is new for the compressible flow case.

These matching conditions will be outlined in the following. The conservation of mass flow across the actuator is

$$ U_1 \, \rho_1 + u_1 R_1 - U_2 \, \rho_2 - u_2 R_2 + \cos\delta \, \frac{\partial}{\partial t} \int_0^d \rho \, ds = 0 \tag{32} $$

In vector form, the vorticity compatability condition is

$$ \frac{\partial}{\partial t} \oint \vec{V} \cdot d\vec{s} - \oint (\vec{V} \times \vec{\Omega}) \cdot d\vec{r} = -\oint \left(\frac{\hat{p}}{\rho_1} \nabla \hat{\rho}\right) \cdot d\vec{s} + \oint \vec{F} \cdot d\vec{s} \tag{33} $$

where the line integrals are taken around the countour indicated in Figure 36 and $\vec{F}$ indicates the frictional forces. Introducing the total pressure loss coefficient χ as defind in Section IIIB and taking the limit as side 2 approaches side 4 Equation 33 becomes:

$$\frac{1}{\partial t_o} \cdots \cdots \sec\delta \frac{1}{\partial t_o} \cdots \frac{\partial \cdots}{\partial \eta} \cdots$$

$$\cdots \left\{ \left[\lambda + \frac{J}{2} \cdots J^2 \right) \cdots \frac{\partial \cdots}{\partial \eta} - \left(J \cdots \frac{\cdot}{2} \cdots J^2 \right) \cdots \frac{\partial \cdots}{\partial \eta} \right\} = 0 \qquad 34$$

where $\chi = \partial\chi/\partial\xi$ and all quantities with a subscript 1 are evaluated at x_{o_1} and y_{o_1}, while all quantities with a subscript 2 are evaluated at x_{o_2} and y_{o_2}. For adiabatic flow through the blade row the energy equation may be put in the form

$$\int_o^{\cdot} m_{tr} \, dS + \frac{\bar{\mu}}{a^2} \int_o^{\cdot} \phi_{tr} + \frac{q_{tr}}{a^2 \cos\delta} = 0 \qquad 35$$

where

$$m_{tr} = \frac{\cdot}{\gamma - 1} \left[\frac{\partial \rho}{\partial t} + J \frac{\partial \rho}{\partial x} + n \frac{\partial \rho}{\partial y} \right] - \frac{\cdot}{a^2(\gamma - 1)} \left[\frac{\partial \sigma}{\partial t} + J \frac{\partial \sigma}{\partial x} + w \frac{\partial \sigma}{\partial y} \right]$$

$$\phi_{tr} = \frac{\theta}{3} \frac{\partial U}{\partial x} \frac{\partial u}{\partial x} - \frac{4}{3} \frac{\partial}{\partial x} \frac{\partial w}{\partial y} + 2 \frac{\partial W}{\partial x} \frac{\partial w}{\partial x} + 2 \frac{\partial W}{\partial x} \frac{\partial u}{\partial y}$$

$$q_{tr} = \frac{k_2}{R\,R_2} \left(\frac{\partial p_2}{\partial x_o} - \frac{\rho_2}{R_2} \frac{\partial \rho_2}{\partial x_o} \right) - \frac{k_1}{R\,R_1} \left(\frac{\partial p_1}{\partial x_o} - \frac{\rho_1}{R_1} \frac{\partial \rho_1}{\partial x_o} \right)$$

where k_i is the coefficient of thermal conductivity in region i. R is the gas constant and a_i is the sound speed in region i. In the above expressions the integrals appearing are calculated assuming that the functions appearing in the integrand have a linear variation between blade row inlet and outlet conditions. The turning relation is of exactly the same form as in the incompressible case, Equation (25) Reference 1. Substituting Equation (28) through (31) into those matching conditions results in the following homogenious set of equations.

$$\left[A_{ij} \right] \begin{bmatrix} B_1 \\ D_2 \\ B_2 \\ E_2 \end{bmatrix} = 0 \qquad (36)$$

$$i, j = 1, 2, 3, 4$$

$$A_{11} = \ldots \frac{1}{2} \frac{n}{r} l\, w_1^2 \cos\ldots - w_2^2 \cdot \frac{\cdot}{\cdot_2}$$

$$A_{12} = \frac{R_1 U_1^2}{U_2}$$

$$A_{13} = M_2^2 \frac{U_1}{U_2} \cdot \nleftarrow \wedge w_2^2 \left(\frac{\cdot_1}{a_2}\right)^2 \frac{n}{r} l \cos\delta - \frac{U_1 \cdot_1}{U_2 \cdot_2}$$

$$A_{14} = U_1 U_2 \left(1 + \nleftarrow \frac{\lambda}{2} \frac{U_1}{U_2} \frac{n}{r} l \cos\delta\right)$$

$$A_{21} = \frac{a\, U_2}{U_1 I_2} \left\{\nleftarrow(1 - M_1^2) - \mathcal{J}_1 \cdot_2\right\}$$

$$A_{22} = R_1 U_1 \left(\xi_2 - \mathcal{J}_2\right)$$

$$A_{23} = \frac{1}{I_4}\left\{\mathcal{J}_2 I_3 - \nleftarrow(1 - M_2^2)\right\}$$

$$A_{24} = 0$$

$$A_{31} = \frac{1}{I_4}\left\{\left(\nleftarrow\left[\chi - \frac{\mathcal{J}_1}{2}\left(1 + \mathcal{J}_1^2\right)\chi'\right] - \frac{\lambda}{2}\frac{n}{r} l \sec\delta\right) I_1\right.$$
$$\left. - \left(1 - M_2^2\right)\left[\lambda + \chi\mathcal{J}_1 + \frac{1}{2}\left(1 + \mathcal{J}_1^2\right)\chi'\right]\right\}$$

$$A_{32} = R_1 U_1 \lambda\left(i\,\xi_2 + \frac{1}{2}\frac{n}{r} l \sec\delta\right) - \nleftarrow \frac{U_2}{U_1}\left(1 + \xi_2^2\right) R_1 U_1$$

$$A_{33} = \frac{\lambda}{I_4}\left\{\left(1 - M_2^2\right) - \frac{1}{2}\frac{n}{r} l \sec\delta\, I_3\right\}$$

$$A_{34} = 0$$

$$a_{41} = \frac{\cdots}{a^2 \cdot_2} \left\{ 1 \; \frac{4 U_2}{3 U_1} \frac{\left(\frac{\cdots}{U_2} \cdot\right)}{\cdots U_2} \; \frac{\bar{u}}{a} \; \frac{(1 \cdots)}{U_1 \, l \sec \delta} \cdots \right.$$

$$\cdot \; \frac{2 U_2}{U_1} \left(\delta_1 - \frac{J}{U_2} \delta_1 \right) \frac{\bar{u}}{a_1} \frac{(1 \cdots)}{U_1 \, l \sec \delta} \cdots \cdot 1 \frac{2 U_2}{3 U_1} \frac{\cdots U^2 \frac{\cdots}{U_1} \cdots \dot{u} \, 1 \cdots}{a \cdots \sec \delta}$$

$$A_{42} = \frac{2 \, U_1}{a^2} \left\{ \mu U_2 \left(\delta_1 - \frac{U_1}{U_2} \delta_1 \right) \frac{(1 \cdots)}{U_1 \, l \sec \delta} \right.$$

$$\cdot \; \frac{\xi_2 \, 2 \mu U_2 \left(\frac{U_2}{U_2} \cdot \right)(1 \cdots)}{U_1 \, l \sec \delta} - \xi_2^2 \mu U_2 \left(\delta_1 \cdot \right) \qquad \frac{(1 \cdots)}{l \, l \sec \delta} \right\}$$

$$A_{43} = \frac{1}{a_1^2} \left\{ \lambda N_1 \cdot 1 \, N_2 I_3 \cdot N_3 - \frac{1}{I_4} \left(1 \, N_4 I_3^2 \cdot N_5 \cdots \cdot 1 \, N_6 \right) \right\}$$

$$A_{44} = \frac{\lambda}{2} - \xi_2 \left\{ \frac{2 \cdot \frac{U_1}{U_2}}{6 \; \frac{U_1}{U_2}} - \frac{(1 \cdots)}{U_1 \, l \sec \delta \, \delta} \left(\frac{k_1}{R \, R_1} \right) \frac{\rho_1}{\rho} \frac{k_2}{k_1} \left(\frac{U_1}{U_1} \right) \right\} \cdot \frac{\frac{U_1}{U_2} \delta_1 \cdot 2 \, \delta_1}{6 \; \frac{U_1}{U_2}}$$

$$I_1 = j \, M_1^2 \, \xi_1 \cdot \left[1 - M_1^2 \left(1 + \xi_1^2 \right) \right]^{1/2}$$

$$I_2 = j \, \xi_1 \cdot \left[1 - M_1^2 \left(1 + \xi_1^2 \right) \right]^{1/2}$$

$$I_3 = j \, M_2^2 \, \xi_2 - \left[1 - M_2^2 \left(1 + \xi_2^2 \right) \right]^{1/2}$$

$$I_4 = j \, \xi_2 - \left[1 - M_2^2 \left(1 + \xi_2^2 \right) \right]^{1/2}$$

$$\xi_1 = \lambda + \delta_1$$

$$\xi_2 = \frac{U_1}{U_2} \lambda + \delta_2$$

$$\lambda = \frac{c r}{n U_0} + \bar{\Omega}_1$$

$$N_1 = \frac{1}{2} \left(\frac{a_1^2}{a_2^2} - 1 \right)$$

$$N_2 = \frac{1}{U_1}\left\{ \frac{2 - \frac{c}{U_1}}{1 - \frac{c}{U_1}} - \frac{a_2^2}{a_1^2} - \frac{\gamma}{U_1 \, l \sec \delta}\, \frac{\bar{\mu}}{2R_1} \left(1 - \frac{\frac{2}{3} a_2^2}{\gamma \frac{U_2}{U_1} a_1^2} \right) \right\}$$

$$N_3 = \left(\frac{a_2^2}{a_1^2} \right) \cdot \frac{\frac{U_2}{U_1}\, \delta_1 + \delta_2}{1 - \frac{c}{U_2}}$$

$$N_4 = \frac{1}{1 - M_2^2}\, \frac{4}{\gamma \frac{U_2}{U_1}}\, \frac{\left(\frac{c}{U_1} - 1\right)}{R_1}\, \mu\, \frac{(\gamma - 1)}{U_1 \, l \sec \delta}$$

$$N_5 = \frac{2 U_2}{U_1} \left(\delta_2 - \frac{U_1}{U_2}\, \delta_1 \right) \frac{\bar{\mu}}{R_1}\, \frac{(\gamma - 1)}{U_1 \, l \sec \delta}$$

$$N_6 = \frac{(1 - M_1^2)^2}{1 - M_2^2}\, \frac{2}{3} \left(1 - \frac{U_2}{U_1} \right) \frac{\bar{\mu}}{R_1}\, \frac{(\gamma - 1)}{U_1 \, l \sec \delta}$$

$$M_1 = \frac{U_1}{a_1}$$

$$M_2 = \frac{U_2}{a_2}$$

The characteristic equation is then

$$|A_{ij}| = 0 \tag{37}$$

which gives the allowable values of λ (or C) for self excited disturbance waves.

Equation (37) is not a simple polynomial as was the case for incompressible flow, hence we cannot make an analytical comparison with that case. However, Equation (37) has been solved numerically for several cases and the calculations for Stator Set No. 4 (from Reference 1) at a stator stagger angle of 28.2 degrees are presented in Figure 37 as being representative of the cases examined. In these calculations, the experimental low speed turning and loss performance (given in Figures 12 and 15 of Reference 1) have been used as the required inputs to the theory. This data was used for two reasons.

66

First, appropriate blade row performance data under compressible flow conditions
was not available. Secondly, use of the low speed data allows a direct com-
parison with the results of the incompressible theoretical results and there-
by isolate the effects of compressible flow alone on the stability boundary.
Figure 37 indicates that compressible flow outside the blade row has a slight
destabilizing effect on rotating stall inception but results in a sizeable
increase in the stall propagation velocity relative to the blade row. The
slight effect on inception conditions would indicate that compressibility does
not significantly alter the flow mechanism involved in rotating stall. More-
over the slope of the loss curve with inlet swirl still appears to dominate
the stability of a given flow configuration.

The present results suggest the possibility that the stability of
a compressible flow configuration may be approximated by using the compressible
flow blade row performance in the incompressible theory. Concrete proof of
this contention would require using compressible flow blade row performance in
both theories and comparison of the results.

E.   THREE-DIMENSIONAL THEORY

Although the various versions of the two-dimensional small disturbance
stability theory have been reasonably successful in predicting the rotating
stall boundaries for the configurations tested in the Calspan/Air Force Annular
Cascade facility, there are many practical compressor designs of low hub-to-
top ratio where the two-dimensional assumptions are not expected to be valid.
This has been the motivation for the three-dimensional theoretical studies.
However, the overall approach of studying the stability of small disturbances
superimposed on a mean steady flow that was used in the two-dimensional case
appears to be substantiated by the correlations with experiment and will serve
as the basis for the three-dimensional analysis. The first step in this approach
for the three-dimensional case is the development or selection of an appropriate
analysis for the mean steady portion of the flow. Once this portion of the
flow model is available, an appropriate stability analysis may be performed.

67

Several methods of predicting the steady flow through a blade row available in the literature were surveyed but none were found satisfactory, for various reasons, and therefore, an appropriate approximate method was developed. A brief review of the requirements of the steady flow model and of models already available will precede the description of the approximate model developed under the present program.

It is required that the model for the mean flow be capable of representing the losses and large turning that occur across a blade row when it is near the rotating stall boundary. This essentially limits consideration to some sort of actuator disk model where empirical turning and loss data may be introduced. Although three-dimensional inviscid calculations through a blade row using finite difference schemes have been developed by Rae[8,9], it is not yet possible to introduce viscous or separation losses in these calculation procedures. As such, the flow through the blade passages cannot be calculated in detail but must be modeled by an actuator. The overall approach then consists of developing axisymmetric solutions for the flow upstream and downstream of the blade row and matching them with the appropriate conditions across the actuator much in the same fashion that was employed in the two-dimensional theory.[1] Such a model was developed by Marble[10] but unfortunately this model is limited to small turning through the actuator. Actuator models allowing for large turning through the blade row have been developed by Wu[11] and Oates.[12] These works, however, use an eigen function expansion procedure which result in analytical expressions for the steady velocity components which are too complicated to allow for a stability analysis for the unsteady flow. In addition, these approaches, as currently formulated, are limited to flows in constant area annuli. Eigen function expansion solutions were also given for unsteady perturbations superimposed on free vortex and wheel swirled flows in constant area annuli by Kerrebrock.[13] This work only considers the propagating wave forms that occur in such flows and does not include the decaying modes that would, in general, be required to represent a blade row. Also, this work suffers the limitation to constant area annuli. Oates and Knight[14] and Oates and Carey[15] have developed a fairly general calculation procedure using the

method of finite elements. These methods would be technically suitable for the present purposes except that the numerical calculations involved were beyond the scope of the present program. The actual method developed may be considered as a simplified version of the finite element approach.

1. **General Theory**

The present analysis considers the steady flow of an incompressible fluid through a blade row in a constant area annulus. The methods employed, however, will leave open the options for extending the analysis to compressible flow through a variable area annulus. The actuator will be considered as infinitely thin, since, the extension to finite thickness, is not considered difficult. The basic idea of the present analysis is to represent the flow quantities in the regions upstream and downstream of the actuator, by polynomials in the radial variable with coefficients that are functions of the axial variable. These coefficients will then be determined by satisfying the equations of motion in an integrated or average sense.

The basic system of momentum and continuity equations for steady axisymmetric flow are

$$V \frac{\partial V}{\partial r} + U \frac{\partial V}{\partial z} - \frac{W^2}{r} = - \frac{1}{\rho} \frac{\partial P}{\partial z} \tag{38a}$$

$$V \frac{\partial U}{\partial r} + U \frac{\partial U}{\partial z} = - \frac{1}{\rho} \frac{\partial P}{\partial z} \tag{38b}$$

$$V \frac{\partial W}{\partial r} + U \frac{\partial W}{\partial z} + \frac{VW}{r} = 0 \tag{38c}$$

$$\frac{1}{r} \frac{\partial}{\partial r} (rV) + \frac{\partial U}{\partial z} = 0 \tag{38d}$$

69

The coordinate system is indicated in the following sketch
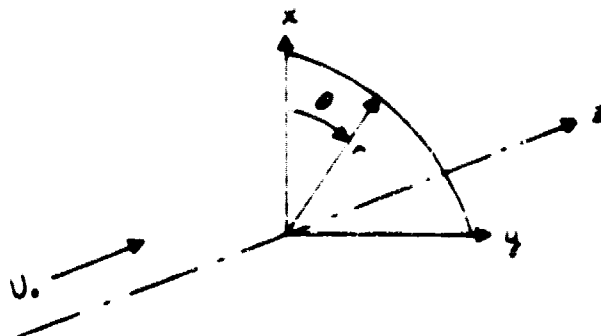
The velocities in the r, θ and z direction are denoted as V, W and U respectively. The static pressure is denoted as P. The actuator is located at $z = 0$. The annulus of constant area has an inner radius denoted by r_H and an outer radius denoted by r_T. The boundary conditions are:

- No flow through the annulus walls

$$V = 0 \quad at \quad r = r_T , r_H \tag{39}$$

- Uniform flow at upstream infinity

$$U \rightarrow U_o \quad , \quad V, W \rightarrow 0 \quad ; \quad z \rightarrow -\infty \tag{40}$$

- All quantities bounded at downstream infinity

- Flow turning and loss relationships specified through the actuator

- The U and V velocity components are continuous through the actuator

Instead of working directly with the velocity components and pressure as dependent variables, it was found to be more convenient to work with the following defined quantities:

70

- A stream function ψ defined such that

$$W = -\frac{1}{r} \psi_z$$

$$U = \frac{1}{r} \psi_r$$

then Equation (38d) is satisfied identically

- The total pressure divided by density

$$H = \frac{p}{\rho} + \frac{1}{2} (U^2 + V^2 + W^2)$$

- The product rW

- The θ component of vorticity

$$\Omega_\theta = \frac{\partial V}{\partial z} - \frac{\partial U}{\partial r}$$

Substituting these definitions into Equation (38) and using the definition of vorticity, the governing equations for these quantities become:

$$\psi_{rr} + \psi_{zz} - \frac{1}{r} \psi_z = -r \Omega_\theta \tag{41}$$

$$\frac{\partial H}{\partial r} + \frac{V_r}{r} \Omega_\theta - \frac{rw}{r^2} \frac{\partial}{\partial r} (rw) = 0 \tag{42}$$

$$\frac{\partial H}{\partial z} + \frac{V_z}{r} \Omega_\theta - \frac{rw}{r^2} \frac{\partial}{\partial z} (rw) = 0 \tag{43}$$

$$\psi_r \frac{\partial}{\partial z} (rw) - \psi_z \frac{\partial}{\partial r} (rw) = 0 \tag{44}$$

Upstream of the blade row we must have $\Omega_\theta = 0$, $H =$ constant and $W =$ constant $= 0$, and the only unknown flow quantity is ψ which is determined by the homogeneous version of Equation (41). Now ψ is to be approximated by a polynomial in r and it has been found that a three term polynomial is the lowest order polynomial that may be used without resulting in a trivial solution. Hence, for the initial stages of the analysis, we consider only a three term polynomial approximation for the flow quantities with the understanding that no steps in the analysis will be used that would prevent generalization to higher order polynomials.

71

We first define a perturbation stream function by

$$\psi = \frac{1}{2} U_\infty r^2 + \phi$$

Then we find that ϕ satisfies the following equation.

$$\phi_{rr} + \phi_{zz} - \frac{1}{r} \phi_r = 0 \tag{45}$$

The appropriate ϕ will be of form

$$\phi = a_o(z) + a_1(z) r + a_2(z) r^2 \tag{46}$$

The a_i are to be determined by satisfying Equation (45) on an integrated basis. Namely, we require that

$$\int_{r_H}^{r_T} r^j \left(\phi_{rr} + \phi_{zz} - \frac{1}{r} \phi_r \right) dr = 0 \tag{47}$$

for $j = 0, 1, \ldots$

Sufficient values of j are used to provide a number of equations equal to the number of unknown functions. Using the wall boundary condition, Equation (39) we find that

$$a_o = K_o a_2 + k_o$$

$$a_1 = K_1 a_2 + k_1$$

where

$$K_o = r_T r_H$$

$$K_1 = -(r_H + r_T)$$

and k_o and k_1 are constants to be determined. This effectively leaves only one unknown function, a_2, so that only the $j = 0$ version of Equation (47) is needed. This becomes an ordinary differential equation with constant coefficients for a_2 viz.

$$A_1 a_2'' + A_2 a_2 = k_1 A_3 \tag{48}$$

72

where
$$A_1 = -\frac{(r_T - r_H)^3}{6}$$

$$A_2 = K_1 \ln \frac{r_H}{r_T}$$

$$A_3 = \ln \frac{r_T}{r_H}$$

and the primes denote differentiation with respect to $\bar{z}$. The general solution of Equation (48) is

$$a_2 = k_1 \frac{A_0}{A_2} + C_1 e^{-mz} + C_2 e^{mz} \tag{49}$$

where $m = \left(\frac{-A_3}{A_1}\right)^{1/2}$ and is real. Application of the upstream boundary condition gives

$$k_0 = k_1 = C_1 = 0$$

and C_2 remains unknown at this stage. C_2 is renamed G_2 for convenience of the following analysis. To this stage of the analysis, we have then

$$a_0 = K_0 G_2 e^{mz} \tag{50a}$$

$$a_1 = K_1 G_2 e^{mz} \tag{50b}$$

$$a_2 = G_2 e^{mz} \tag{50c}$$

Now proceeding to the downstream flow, we will denote ϕ downstream of the actuator by ϕ^* and, in general, all downstream quantities will be denoted by a star. The partial differential equation for ϕ^* is

$$\phi^*_{rr} + \phi^*_{zz} - \frac{1}{r} \phi^*_r = -r \Omega^*_\theta \tag{51}$$

Using the polynomial approximation for ϕ^* we let

$$\phi^* = a^*_0 + a^*_1 r + a^*_2 r^2 \tag{52}$$

The wall boundary conditions again give

$$a_o^* = \kappa_o a_2^* + k_o$$

$$a_1^* = \kappa_1 a_2^* + k_1$$

so that a_2^* is the only remaining unknown function and is found by satisfying the integrated version of Equation (47); namely,

$$A_1 a_2^{*''} + A_2 a_2^* = k_1 A_3 + I_1 \tag{53}$$

where

$$I_1 = -\int_{r_r}^{r_w} r \, \Omega_\theta^* \, dr$$

Before proceeding to solve this equation, a better representation of I_1 is necessary. The first step in obtaining this representation is accomplished by multiplying Equation (42) by ψ_z^* and subtracting Equation (43) multiplied by ψ_r^*. The result is

$$\psi_r^* \frac{\partial H^*}{\partial z} - \psi_z^* \frac{\partial H^*}{\partial r} = 0 \tag{54}$$

or $H^* = H^*(\psi^*)$ and consistent with the polynomial approximation procedure

$$H^* = A \psi^* + D_1 \tag{55}$$

where A and D_1 are constants.

Also from Equation (44) we have

$$r w^* = F(\psi^*) = B \psi^* + D_2 \tag{56}$$

where B and D_2 are constants.

Substituting Equations (56) and (55) into either Equations (42) or (43), results in

$$\Omega_\theta^* = \frac{B^2}{r} \psi^* + D_2 \frac{B}{r} - r A \tag{57}$$

74

Using this equation to evaluate I_1, gives

$$I_1 = 2m^2 A_1 Q_1 - B^2 A_1 a_2^*$$ (58)

where

$$Q_1 = \frac{1}{2m^2 A_1}\left\{A \frac{r_T^3 - r_H^3}{3} - B^2 \frac{U_\infty}{6}(r_T^3 - r_H^3) - D_2 B(r_T - r_H)\right\}$$

Then using Equation (58) in Equation (53), we obtain

$$a_2^{*''} - M^2 a_2^* = k \frac{A_3}{A_2} + 2m^2 Q_1$$ (59)

where

$$M^2 = m^2 - B^2$$

The general solution to this equation is

$$a_2^* = b_1 e^{-Mz} + b_2 e^{Mz} - \frac{2m^2}{M^2} Q_1 - k_1 \frac{A_3}{A_1 M^2}$$ (60)

where $b_2 = 0$ to keep ϕ^* bounded at infinity downstream. The continuity of U and V across the actuator is equivalent to keeping ϕ and ϕ' continuous across the actuator or

$$\phi(o) = \phi^*(o)$$ (61a)

and

$$\phi'(o) = \phi^{*'}(o)$$ (61b)

which give

$$k_1 = k_2 = 0$$

$$b_1 = \frac{2m^2 Q_1}{M^2(M+m)}$$

and

$$G_2 = \frac{-2m^2 Q_1}{M(M+m)}$$

Thus far, we have

$$a_2^* = \frac{2Q_1 m^2}{M^2}\left(\frac{m}{M+m} e^{-Mz} - 1\right)$$ (62)

$$a_2 = \frac{-2m^2 Q_1}{m(M+m)} e^{m z} \tag{63}$$

$$\psi = \frac{1}{2} U_0 r^2 + (K_0 + K_1 r + r^2) a_2 \tag{64}$$

$$\psi^* = \frac{1}{2} U_0 r^2 + (K_0 + K_1 r + r^2) a_2^* \tag{65}$$

so that the steady velocity field is known up to the four constants A, D_1, B and D_2 (appearing in Q_1 and M) which are associated with the steady turning and loss performance of the blade row. In the previously mentioned actuator disk theories,[10-15] the turning (W component of velocity) and the total pressure are considered as specified at the outlet of the blade row (actuator sheet) which is equivalent to specifying these four constants. In fact, for the present purposes, they could be chosen so as to agree with the annular cascade measurements. However, for the unsteady perturbation analysis that will employ this model for the mean flow, the blade row performance as a function of local inlet swirl will have to be used. Therefore, we will develop the steady analysis using the appropriate form of matching conditions derived from the local blade row performance data. Before presenting an example calculation, a few comments concerning the form of the solution, Equations (63) through (65) are in order.

There is no tangential velocity perturbation transmitted upstream of the blade row. There is, however, an axial velocity and a radial velocity perturbation upstream of the blade row. This is to be contrasted with the two-dimensional steady case where no disturbances are transmitted upstream of the blade row. This feature of the three dimensional theory is expected to be very significant in considering blade row interactions that are currently not explainable by two-dimensional theories. It is noted that for the specific polynomial form used here, a single linear differential equation is obtained for the coefficients. If a higher order polynomial had been used, the result would be a system of differential equations, but the system would still be

76

linear. Also, the restriction to constant annulus area results in a system
of equations with constant coefficients. Consideration of variable area
annuli will result in a linear system with non-constant coefficients.

2. Example Calculations

As an example of the above theory, the turning and loss performance
of the stationary guide vane row of the Calspan/Air Force Annular Cascade has
been estimated. The blade row turning and loss performance required by the
theory were obtained from two-dimensional cascade data given in Reference 16.
The data are applied in a strip-wise fashion at each radial station assuming
that the outlet conditions to the blade row are only a function of the local
inlet swirl and dynamic pressure at the given radial location. The local
inlet conditions are not those corresponding to the undisturbed flow far ahead
of the blade row, but are calculated as part of the solution.

The turning and loss relations across the blade row will be given for
the general case first and then specialized to the guide vane case. These
relations are applied in a coordinate system fixed to the blades. Denote
conditions immediately upstream of the blade row by a subscript 1 and those
immediately downstream by a subscript 2. Then at any radial station, the total
pressure change normalized by the density is

$$H_2 - H_1 = r\omega (W_2 - W_1) - \frac{L}{\rho}$$

(66)

where ω is the blade row rotational velocity and L represents the losses
and it is assumed that they are given by

$$L = \frac{1}{2} \chi \rho \left\{ U_1^2 + (W_1 - r\omega)^2 \right\}$$

The total pressure loss coefficient, χ , is defined as in the previous section
of this report and it is assumed that it is available from two-dimensional
cascade data as a function of solidity, stagger angle, inlet swirl and airfoil
section shape. Since these parameters may vary along the span of a blade, χ
will in general be a function of r . Equation (66) is merely the Euler turbine
equation with the added consideration of losses.

77

Since the upstream total pressure is constant and assumed known, the previous results for H_2 and W_2 may be substituted into Equation (66) to give

$$A \psi^*(o) + D_1 - H_1 = \omega (B \psi^*(o) + D_2) - \frac{L}{\rho} \tag{67}$$

where

$$\frac{L}{\rho} = \frac{1}{2} \chi \left[\left(\frac{1}{r} \psi_r^*(o) \right)^2 - r^2 \omega^2 \right] \tag{68}$$

Equation (67) may be differentiated with respect to r to give

$$A \psi_r^*(o) = \omega B \psi_r^*(o) - \frac{\partial L}{\partial r} \tag{69}$$

which really represents the vorticity compatability relation for three-dimensional flow.

Let the local relative swirl ahead of and behind the actuator be denoted by $\mathcal{S}_i$ so that

$$\mathcal{S}_i = \frac{W_i - r\omega}{U_i}$$

It is then assumed that the turning performance of the blade row is available from two-dimensional cascade tests so that $\mathcal{S}_2$ is known by

$$\mathcal{S}_2 = G(\mathcal{S}_1) \tag{70}$$

where G is also a function of solidity, stagger angle and airfoil shape, which in general will vary along the blade span. Using the previous forms of the solution obtained, Equation (70) may be written as

$$B \psi^*(o) + D_2 = r^2 \omega + \psi_r^*(o) G \tag{71}$$

differentiating this with respect to r gives

$$B \psi^*(o) = 2 r\omega + \psi_{rr}^*(o) G + \psi_r^*(o) G_r \tag{72}$$

78

Now integrating Equations (67), (69), (71) and (72) between r_T and r_H gives a system of four algebraic equations for the four unknown constants

The solution of this system will be demonstrated for the case of the fixed guide vane row used in the Calspan/Air Force Annular Cascade Facility. This blade row has a hub to tip ratio of 0.8, a constant solidity of 1.17 along the span and untwisted blades. The stagger angle is constant along the span and is variable approximately from 18° to 52°. The guide vanes had an NACA 63- $(24A_4 K_6)$ 10 guide vane profile which is 10 percent thick. These parameters do not correspond to those tested in Reference 16; the solidity falls within the test range but all the tests results are for a 6 percent thick section. Corrections could have been applied to the turning performance, however, there was no reliable method to correct the loss data. In addition, preliminary comparison of the loss data presented in Reference 16 with that measured in the annular cascade facility indicated a large descrepancy in levels. This is presumably due to the large differences in Reynolds number between the two tests as well as the thickness differences. The Reynolds number in the annular cascade facility was 9.5×10^4 where as those in Reference 16 were approximately 2.5×10^5. It was realized at the outset that these differences in loss level would lead to poor correlation between the present theory and the annular cascade data, but the numerical calculations were continued in order to check that the theory was completely formulated and would give the right trends. The experimental loss and turning data corresponding to a solidity ratio of 1.0 were used in the theory.

For this particular case with $\omega = 0$ and $W_t = 0$ there is no relative swirl ahead of the guide vane row. In addition, the constant blade row geometrical properties along the span greatly simplify the application of the matching conditions and the integrated forms of Equations (72) and (71) become respectively:

$$B = 2G \frac{1 + 2q_1}{r_T + r_H} \tag{73}$$

79

and

$$\frac{D_2}{U_o} = G\left(R_3 + R_4 q_1 + R_5 q_1^2\right) \tag{74}$$

where

$$q_1 = \frac{-2 m^2 Q_1}{U_o M(M+m)}$$

$$R_3 = \frac{r_H + r_T}{2} - \frac{1}{3} \frac{(r_T^3 - r_H^3)}{(r_T^2 - r_H^2)}$$

$$R_4 = \frac{1}{3} \left\{ \frac{(r_T - r_H)^2}{r_T + r_H} - 2 \frac{(r_T^3 - r_H^3)}{r_T^2 - r_H^2} \right\}$$

$$R_5 = \frac{2}{3} \frac{(r_T - r_H)^2}{r_T + r_H}$$

The integration of Equation (69) and (67) give respectively

$$\frac{A}{U_o} = - \frac{\chi}{2} \frac{(r_H + r_T)^2}{r_H^2 r_T^2} q_1 \tag{75}$$

and

$$\frac{D_1 - H_1}{U_o} = - \frac{1}{2} \chi + \chi \left(R_1 q_1 + R_2 q_1^2\right) \tag{76}$$

where

$$R_1 = \frac{1}{12} \frac{(r_T + r_H)^2 (r_T^3 - r_H^3)}{r_H^2 r_T^2 (r_T - r_H)} - \frac{K_1}{r_T - r_H} \ln \frac{r_T}{r_H} - 2$$

$$R_2 = - \frac{1}{2} \left\{ \frac{K_1^2}{r_T r_H} + 2 K_1 \ln \frac{r_T}{r_H} + 4 + \frac{(r_H + r_T)^2 (r_H - r_T)^2}{6 r_H^2 r_T^2} \right\}$$

Substitution of Equations (73) - (76) into the definition of q_1 give a single algebraic equation for q_1 namely,

$$q_1 = - \frac{1}{\tilde{M}(\tilde{M}+1)} \left\{ b_1 + b_2 q_1 + b_3 \left(q_1^2 + q_1^3\right) \right\} \tag{77}$$

80

where

$$\tilde{M} = \frac{M}{m} = \left\{ 1 - \frac{4G^2(1+2q_1)^2}{m^2 r_r^2(1+p)} \right\}^{1/2}$$

$$m^2 r_r^2 = -6 \frac{(1+p)}{(1-p)^3} \ln p$$

$$b_1 m^2 r_r^2 = \frac{6G^2}{(1-p)^2}$$

$$b_2 m^2 r_r^2 = \chi \frac{(1+p)(1-p^3)}{(1-p)^3 p^2} + G^2\left[\frac{4}{(1+p)^2} + \frac{12}{(1+p^2)}\right]$$

$$b_3 m^2 r_r^2 = \frac{16G^2}{(1+p)^2}$$

and $p = \frac{r_H}{r_T} = .8$ for this case. Equation (77) has been solved numerically and has been found to possess only one real root. The required G and χ functions at each guide vane stagger angle were obtained from Reference 16 as previously explained. In terms of these parameters, the overall average total pressure loss coefficient for the blade row is

$$\bar{\bar{C}}_{P_r} = A \frac{r_T^2}{U_o} \left\{ \frac{1+p^2}{2} - q_1 \frac{(1-p^2)}{3} \right\} + \frac{2(D_1 - H_1)}{U_o^2} \tag{78}$$

This expression is plotted as a function of stagger angle in Figure 38 where the corresponding experimental measurements are also shown. As previously explained because of the difference in loss levels, poor quantitative agreement was expected. However, throughout most of the stagger angle range the theory has the proper trend. Comparison of the theoretical results with the two-dimensional cascade data of Reference 16 also shown in Figure 38, indicates that the theory is predicting the induced drag on the blade row correctly. The reason for the abnormally high loss prediction at a stator stagger angle of 48° is not clear. Perhaps a three term polynomial is inadequate to represent the large radial variations that occur under these high loss conditions.

81

The theoretical prediction of turning performance is compared with the experiment in Figure 39. The theory is about four degrees low throughout the stagger angle range. This is easily explained by the difference in solidity and thickness between the annular cascade and the data used from Reference 16. Overall then, it is seen that the theory predicts the qualitative trends correctly. The absolute level of the predictions is off because the two-dimensional cascade data was not strictly appropriate for the annular cascade guide vane geometry. Moreover, better agreement of the levels of turning and loss performance between theory and experiment may be forced by empirical specification of the four unknown constants A, B, D_1 and D_2. Therefore, the present theory should serve as an adequate representation of the mean flow upon which we can perform an unsteady stability analysis.

F.   CONCLUDING REMARKS ON THEORETICAL INVESTIGATIONS

During this program, the two-dimensional stability theory was extended to consider inlet distortion for incompressible flows and compressible flows without inlet distortion. The analyses show that the principal effects of distortion occur when the distortion wave corresponds to the natural rotating stall mode for the system. The two-dimensional theory was also used to examine the stability of the case of two closely coupled blade rows in a rotor-stator stage. The theory indicates that blade row interference for this configuration has a large stabilizing effect on the stall boundary. The correlations with experiments verify this trend but are hampered because of lack of appropriate steady blade row performance data.

In addition to these two-dimensional analysis, the initial development of a three-dimensional theory is reported. An approximate three-dimensional analysis for the steady flow through a blade row is given. This model is to serve as the basis of a stability analysis to predict the rotating stall boundary.

82

SECTION IV
SUMMARY AND CONCLUSIONS

A combined experimental and theoretical research program on rotating stall in axial flow compressors has been conducted. The primary topics addressed in this report are the effects of stationary and moving distortion on the rotating stall boundary for an isolated rotor row and the effects on the boundary of close coupling of the blade rows in a rotor-stator stage.

The tests on stationary distortion effects on a rotor row included both a two lobed and a four lobed distortion pattern. Although the total pressure distortions were quite high for both patterns, they did not significantly affect the rotating stall boundary or the rotating stall properties after inception. Similarly, measurements of averaged blade row loss and turning data showed little influence of the distortion. The tests with moving distortion were performed by rotating the two lobed pattern about the compressor axis both in the direction of blade row rotation and opposite to it. It was generally found that the rotating distortion pattern either had little effect on or else destructively interfered with rotating stall formation except when the pattern was rotated at speeds near the natural stall propagation velocity for undistorted flow. Under these latter conditions, the rotor incurred rotating stall at much higher flow coefficients than for the undistorted flow case. These results contradict the "time to stall" arguement that has been used in several instances to explain the effects of multilobe distortion patterns on compressor stall boundaries. The theoretical analysis are in general agreement with the experimental findings. The theory concludes that distortion will not influence the rotating stall boundary unless the distortion pattern contains a Fourier component which corresponds to the natural rotating stall mode for the system.

The experiments on the effect of close coupling on the rotating stall boundary for a rotor-stator stage show that the blade row interference results in a significant delay in rotating stall inception. The rotor-stator stage

83

stalls at a much larger inlet swirl than the isolated rotor. The theoretical results also show this delay, but the numerical predictions of the theory are generally inaccurate due to lack of the steady state performance data for the isolated blade rows in the swirl angle ranges needed. The theory requires these steady state data as inputs.

In addition to the above mentioned theoretical studies, which were performed with an incompressible two-dimensional small disturbance stability theory, studies were performed to extend the two-dimensional theory to include compressibility and to initiate the development of a three-dimensional theory. The theory for compressible flow, which assumes that the flow is subsonic everywhere, indicates that the slope of the loss curve as a function inlet swirl still controls the stability of a given flow configuration. The three-dimensional theory has not been completed at this time, but the development to date is given in this report.

2 SPEED FAN

TEST SECTION
(J-79 COMPRESSOR CASING)

INLET GUIDE
VANES

OUTLET DAMPER
VANES
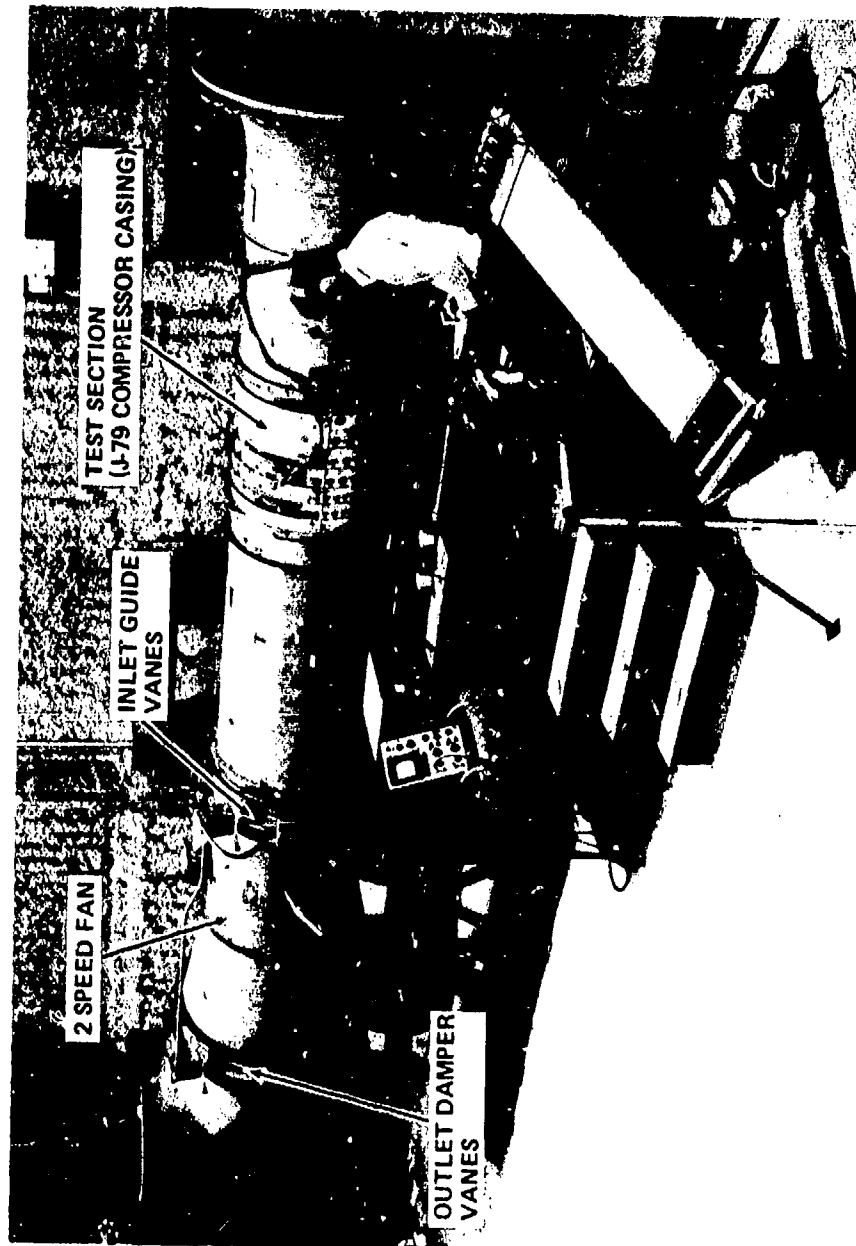
Figure 1   OVERALL VIEW OF ANNULAR CASCADE FACILITY

85

STAGE 3
ROTOR
LOCATION

STAGE 5
ROTOR
LOCATION

STAGE 5
STATOR
LOCATION

CIRCUMFERENTIAL
TRAVERSE
LOCATIONS
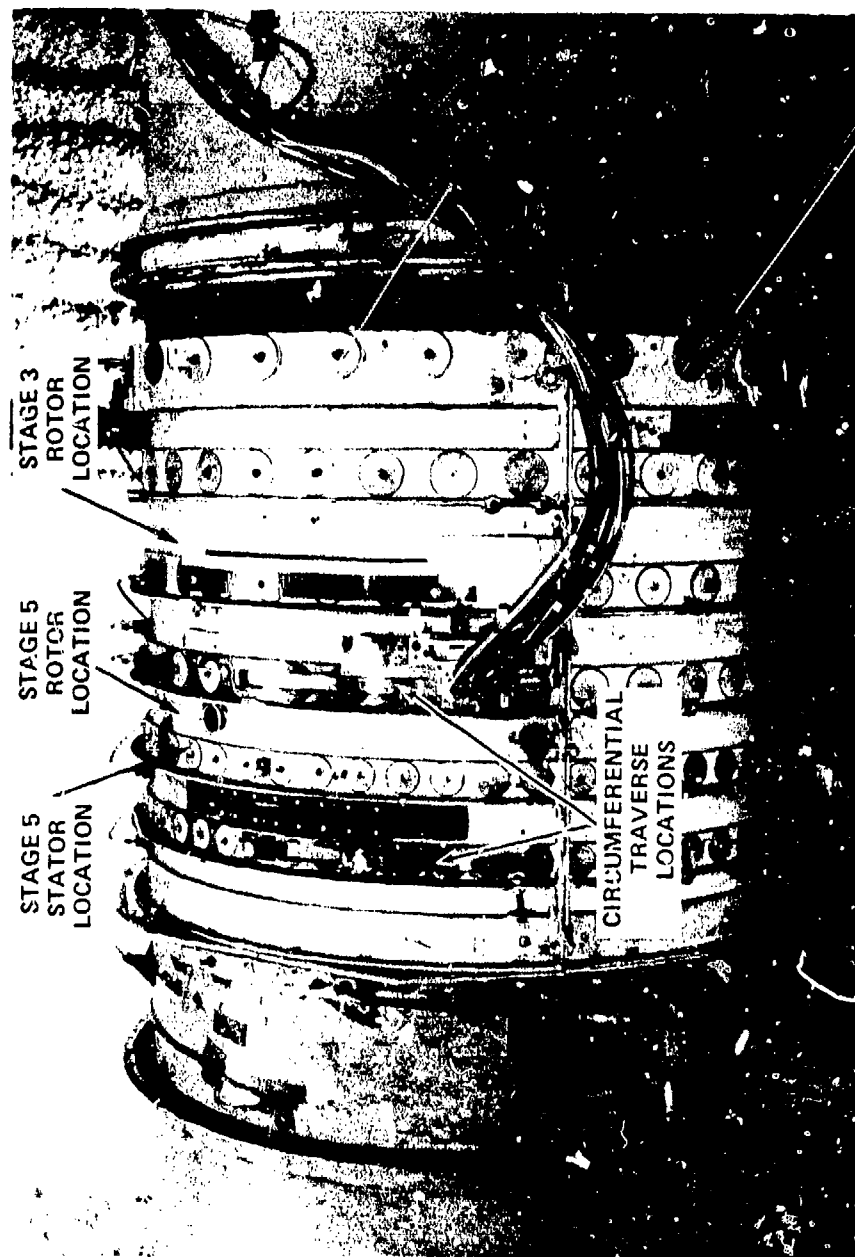
Figure 2   VIEW OF ANNULAR CASCADE TEST SECTION

DETAILS OF ORIGINAL ROTATING HUB CONFIG-
URATION IN ANNULAR CASCADE FACILITY
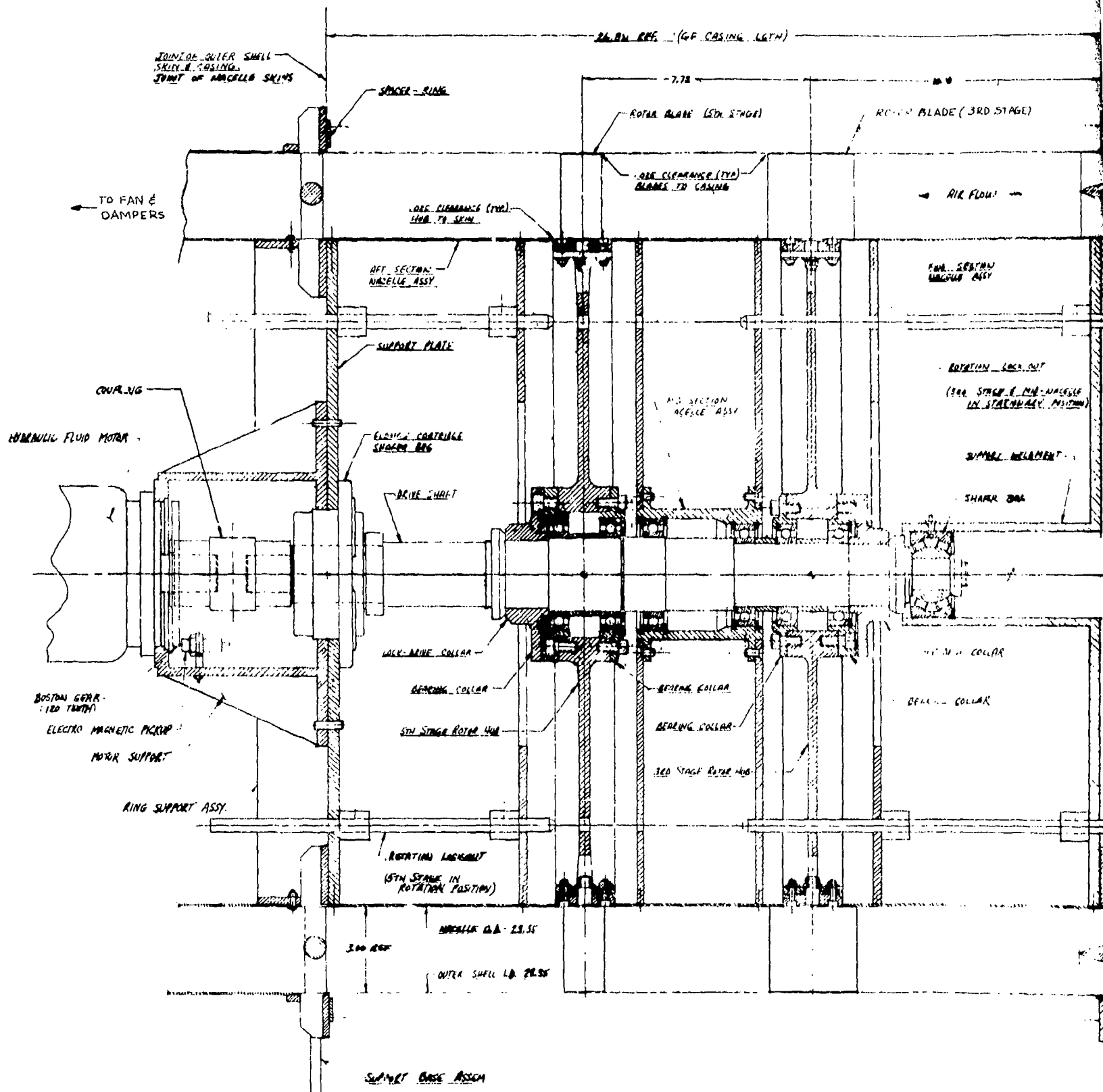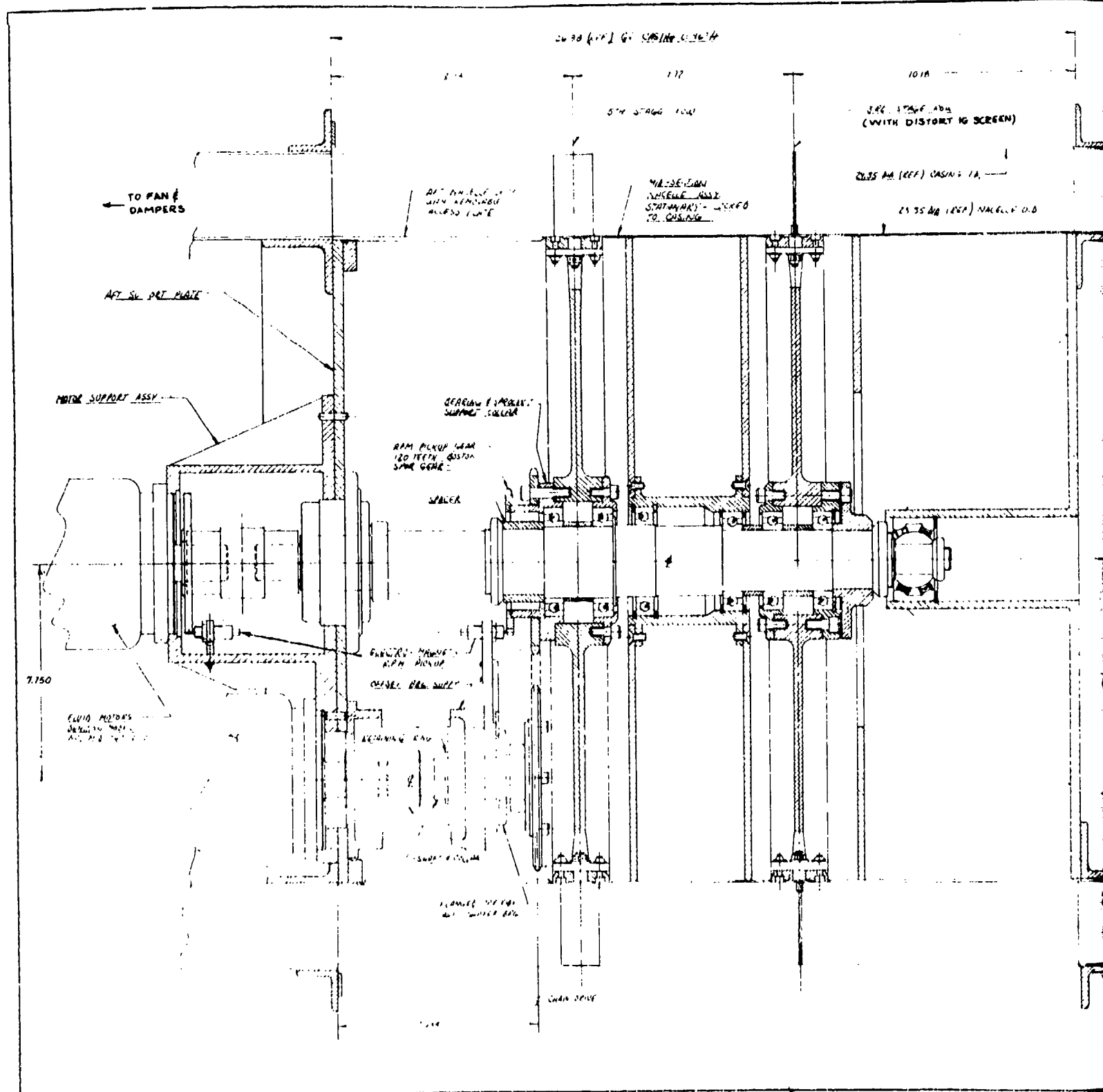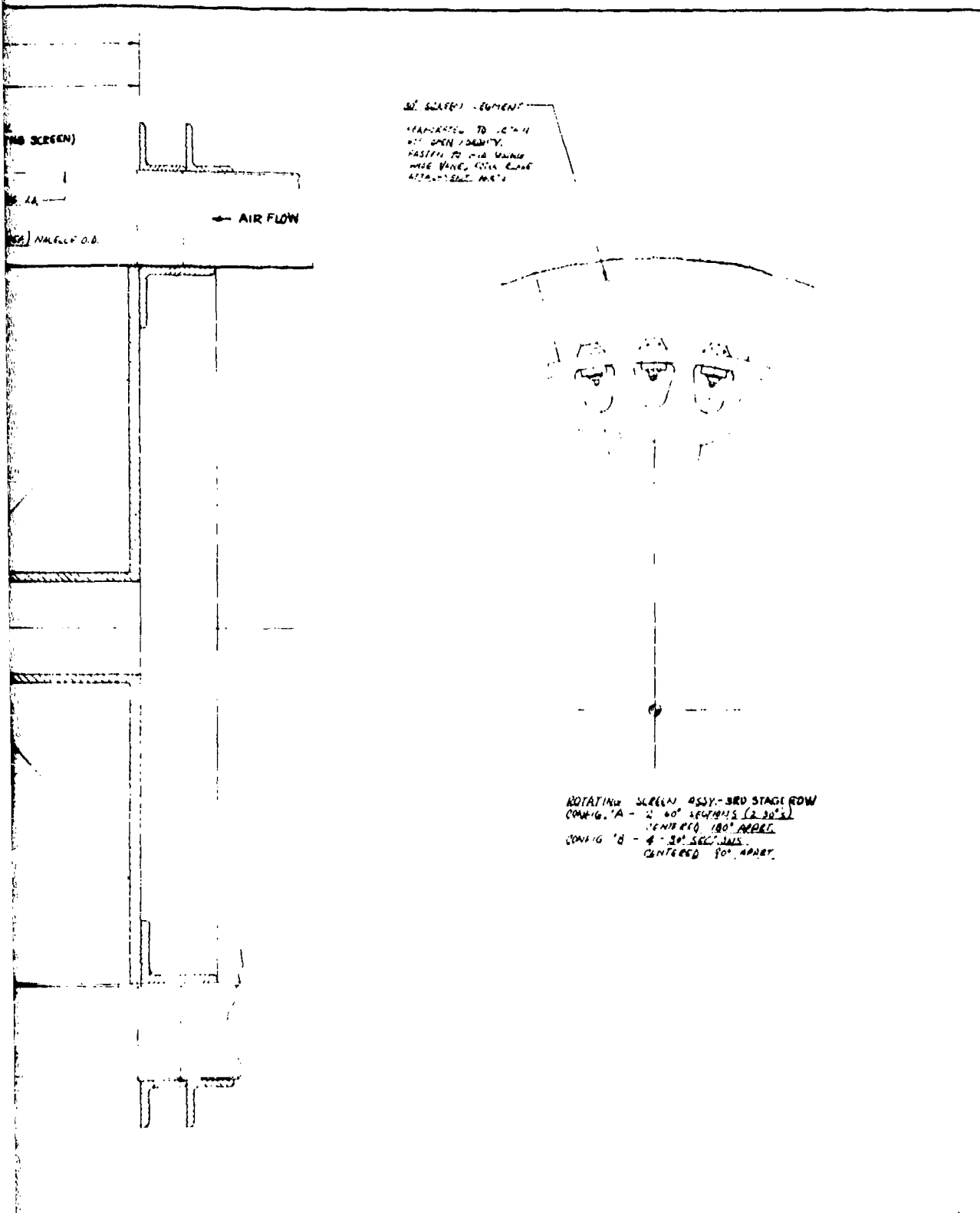
Figure 3

Figure 4

ROTATING HUB CONFIGURATION MODIFIED
TO PROVIDE INDEPENDENT ROTATION OF
TWO ROTOR ROWS

88
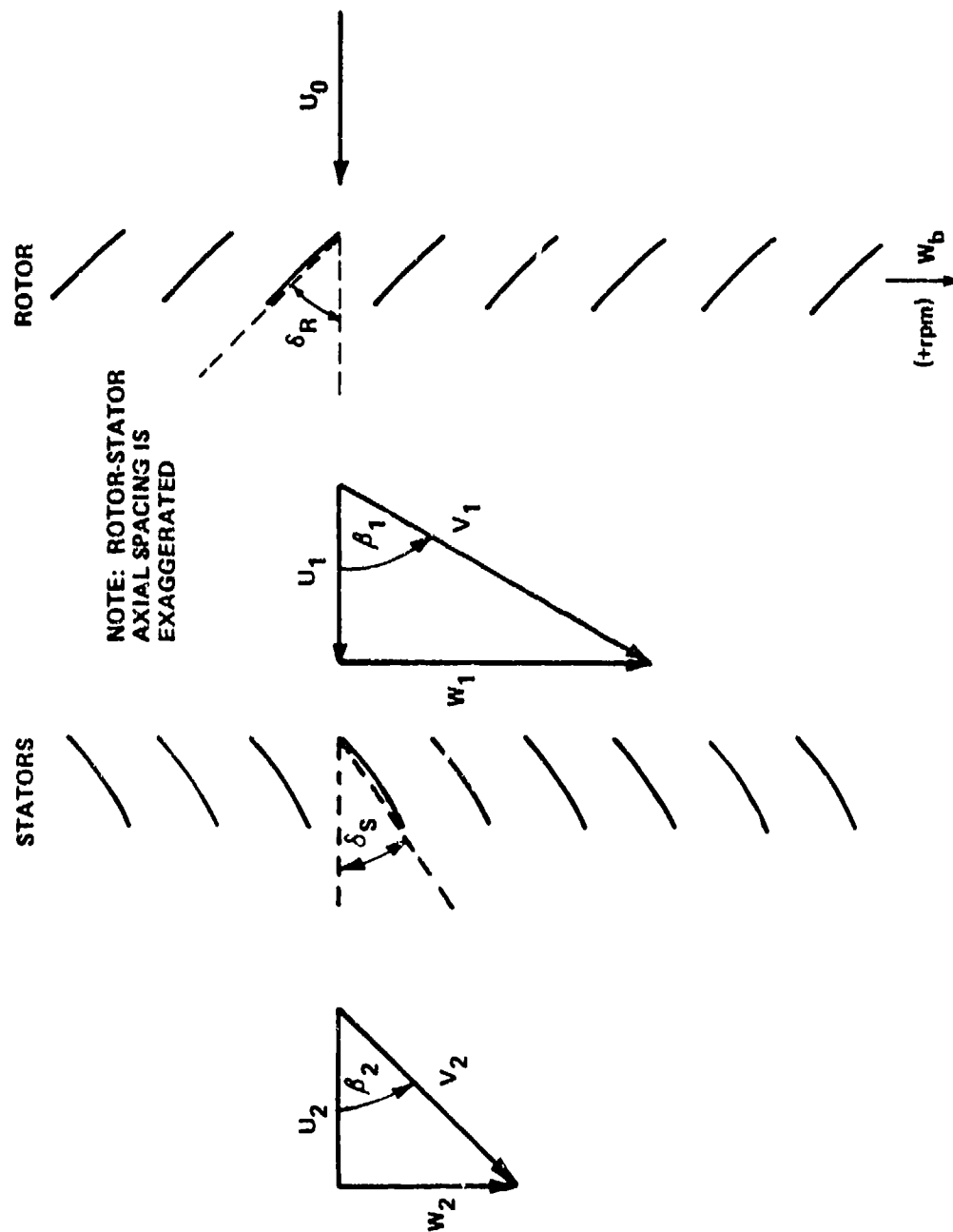
Figure 5   NOTATION FOR ANNULAR CASCADE WITH ROTOR-STATOR STAGE
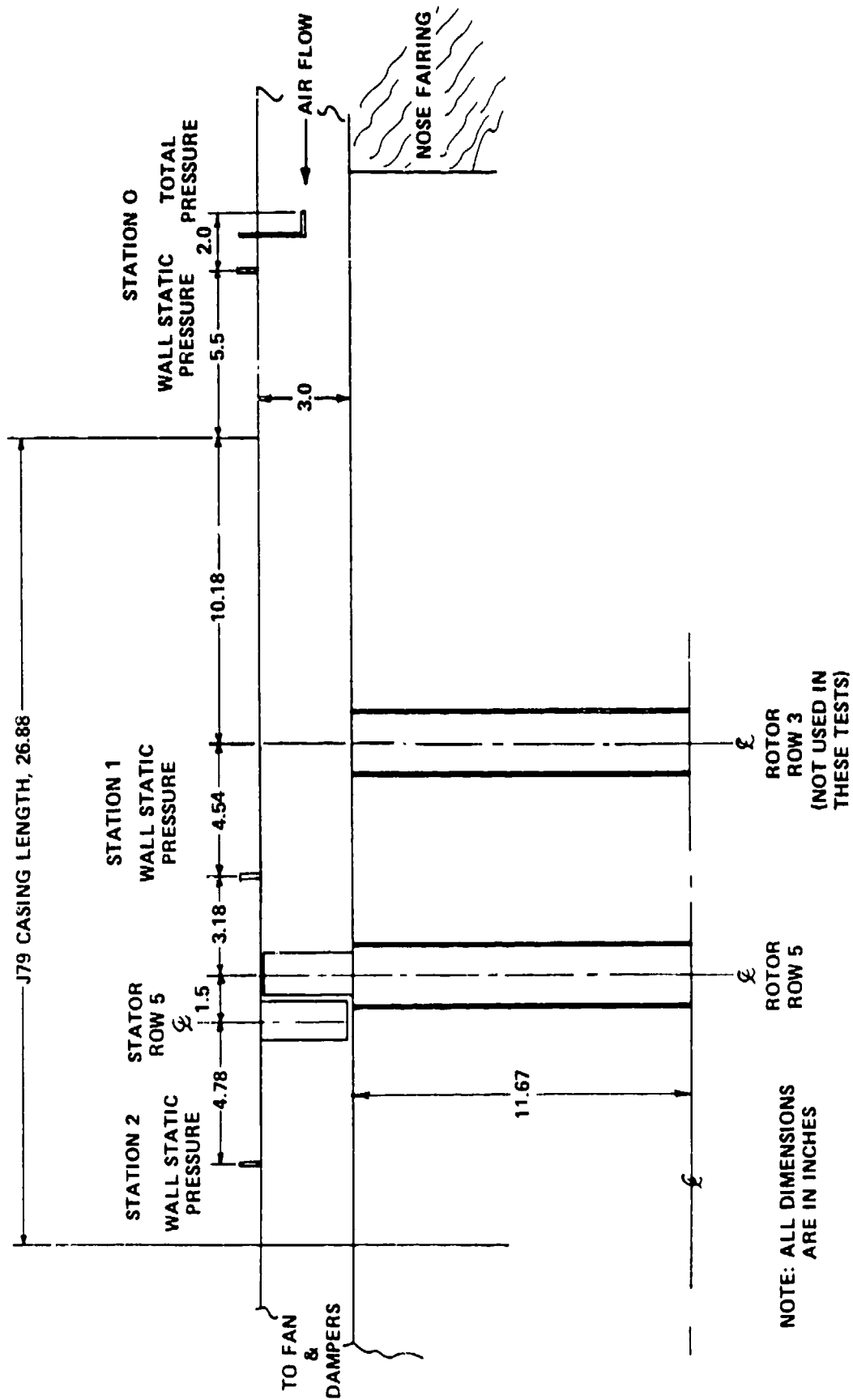
Figure 6   ANNULAR CASCADE CONFIGURATION USED FOR ROTATING STALL STUDIES ON ROTOR–STATOR STAGE
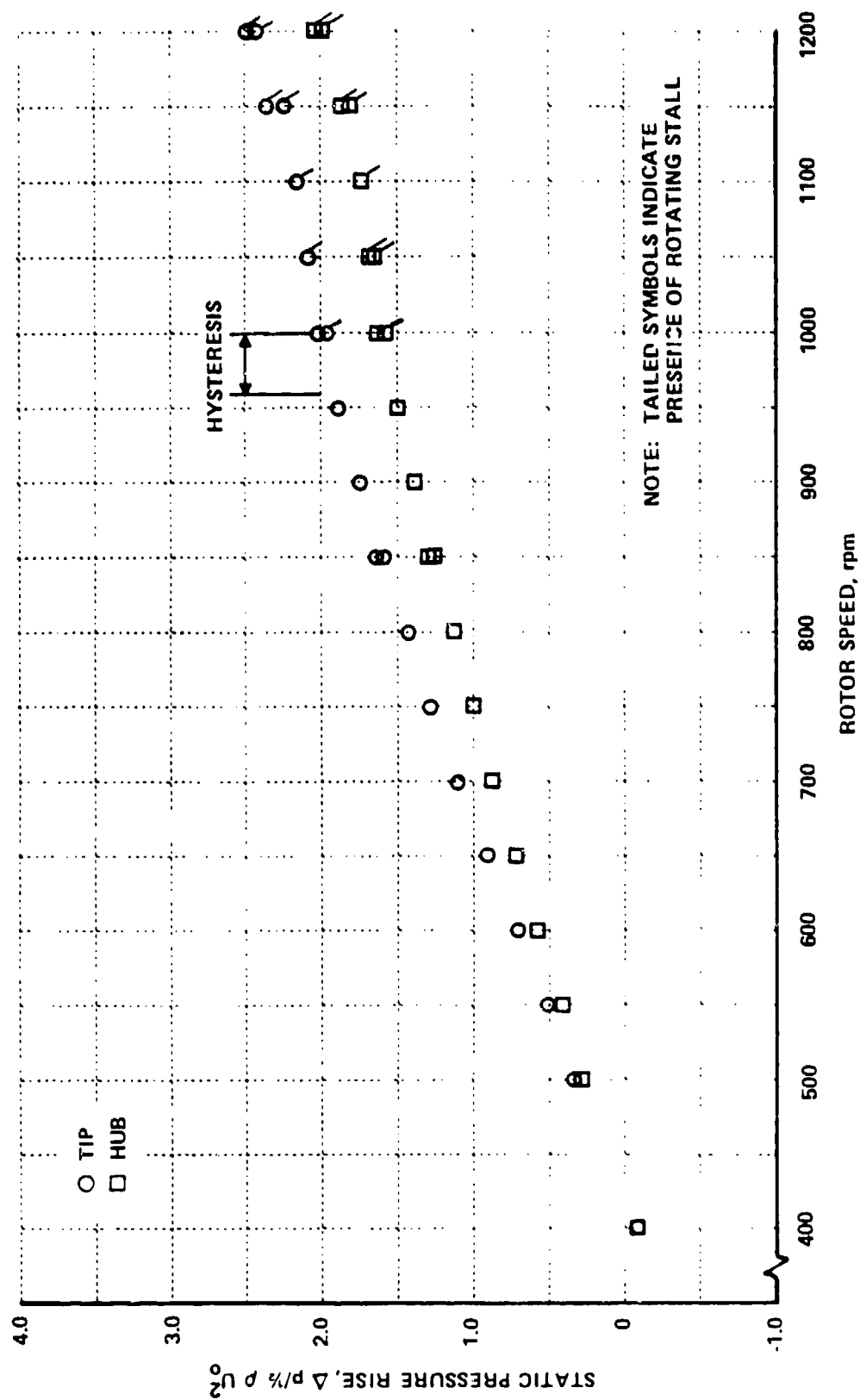
Figure 7   STATIC PRESSURE RISE ACROSS ROTOR SET NUMBER 1 —
ROTOR STAGGER ANGLE, $\delta_{RM} = 40°$
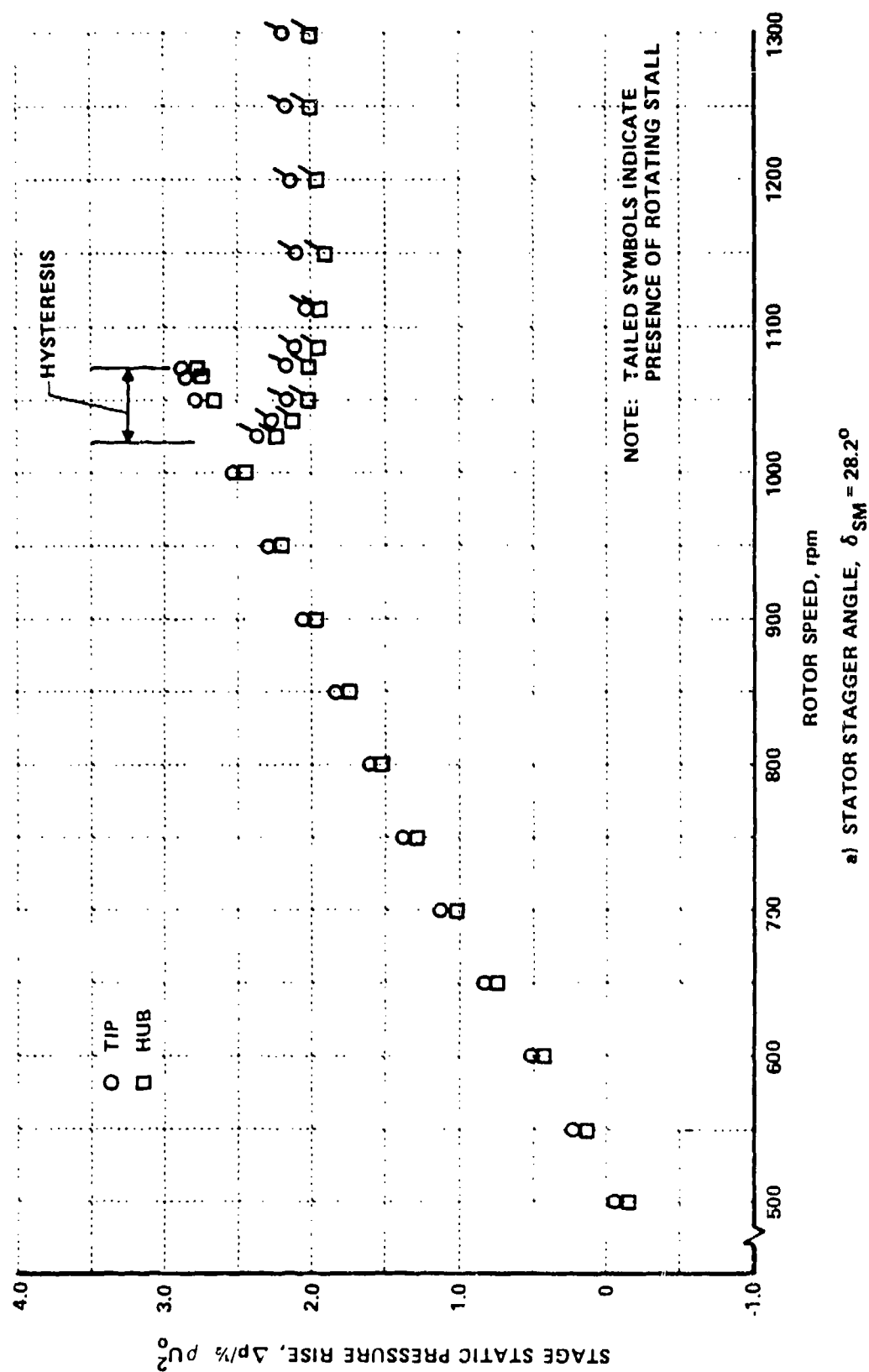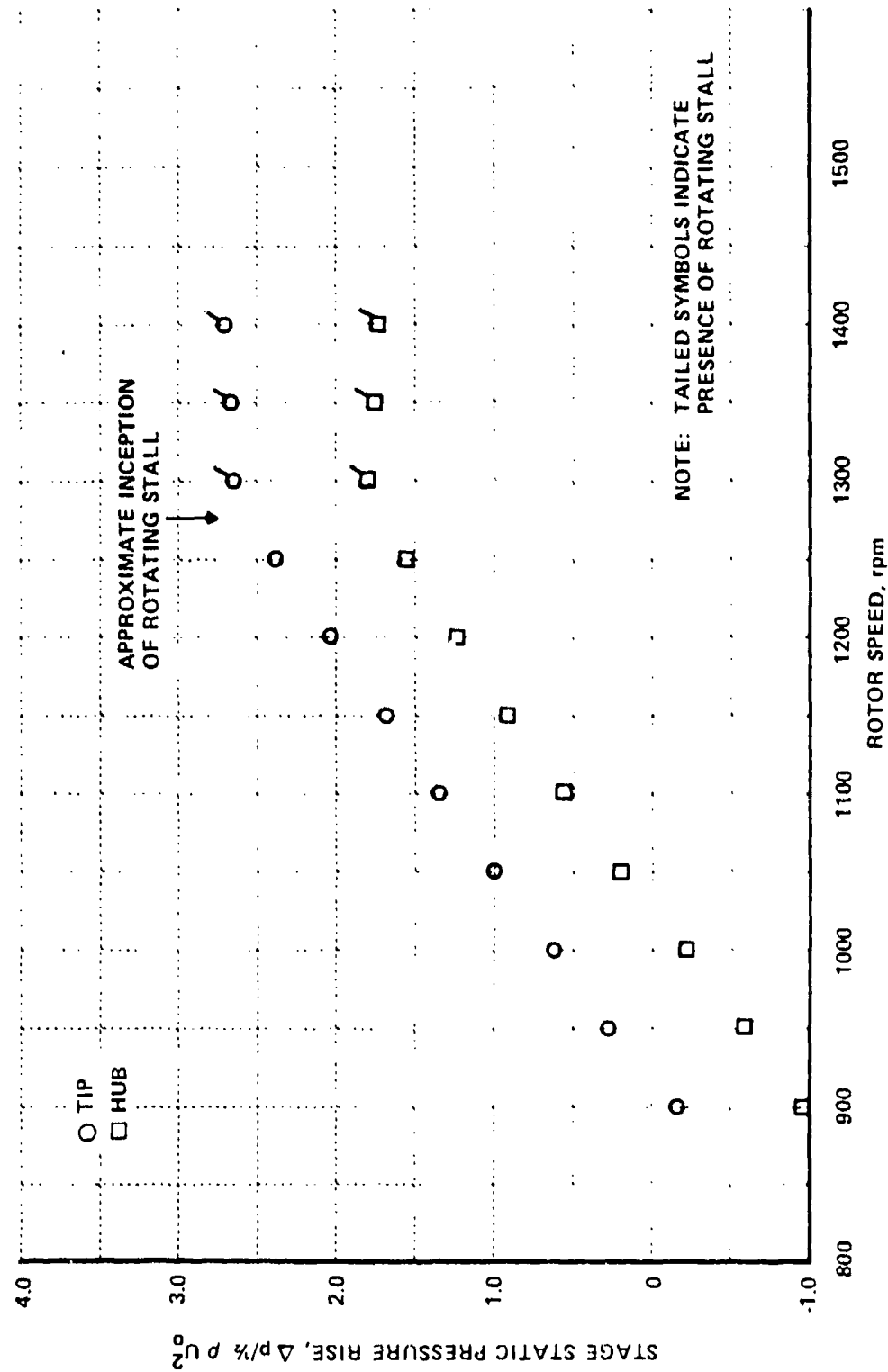
Figure 8 STATIC PRESSURE RISE ACROSS ROTOR-STATOR SET NUMBER 1 –
ROTOR STAGGER ANGLE, $\delta_{RM} = 40^{\circ}$

a) STATOR STAGGER ANGLE, $\delta_{SM} = 28.2^{\circ}$

NOTE: TAILED SYMBOLS INDICATE
PRESENCE OF ROTATING STALL

Figure 8 (Cont.) STATIC PRESSURE RISE ACROSS ROTOR-STATOR SET NUMBER 1 —

b) STATOR STAGGER ANGLE, $\delta_{SM} = 37.2°$ ROTOR STAGGER ANGLE, $\delta_{RM} = 40°$

NOTE: TAILED SYMBOLS INDICATE PRESENCE OF ROTATING STALL

93

c) STATIC PRESSURE RISE ACROSS ROTOR-STATOR SET NUMBER –
   STATOR STAGGER ANGLE, $\delta_{SM} = 47.2^0$
   ROTOR STAGGER ANGLE, $\delta_{RM} = 40^0$

Figure 8 (Cont.)   STATIC PRESSURE RISE ACROSS ROTOR-STATOR SET NUMBER –
                    STATOR STAGGER ANGLE, $\delta_{SM} = 47.2^0$
                    ROTOR STAGGER ANGLE, $\delta_{RM} = 40^0$

94

Figure 8 (Cont.) STATIC PRESSURE RISE ACROSS ROTOR-STATOR SET NUMBER 1 — ROTOR STAGGER ANGLE, $\delta_{RM} = 40^{\circ}$

d) STATOR STAGGER ANGLE, $\delta_{SM} = 57.2^{\circ}$

NOTE: TAILED SYMBOLS INDICATE PRESENCE OF ROTATING STALL

95

Figure 9   ROTATING STALL PROPAGATION VELOCITY AND NUMBER OF CELLS
FOR ISOLATED ROTOR AND FOR ROTOR-STATOR STAGE, COORDINATE
SYSTEM RELATIVE TO ROTOR
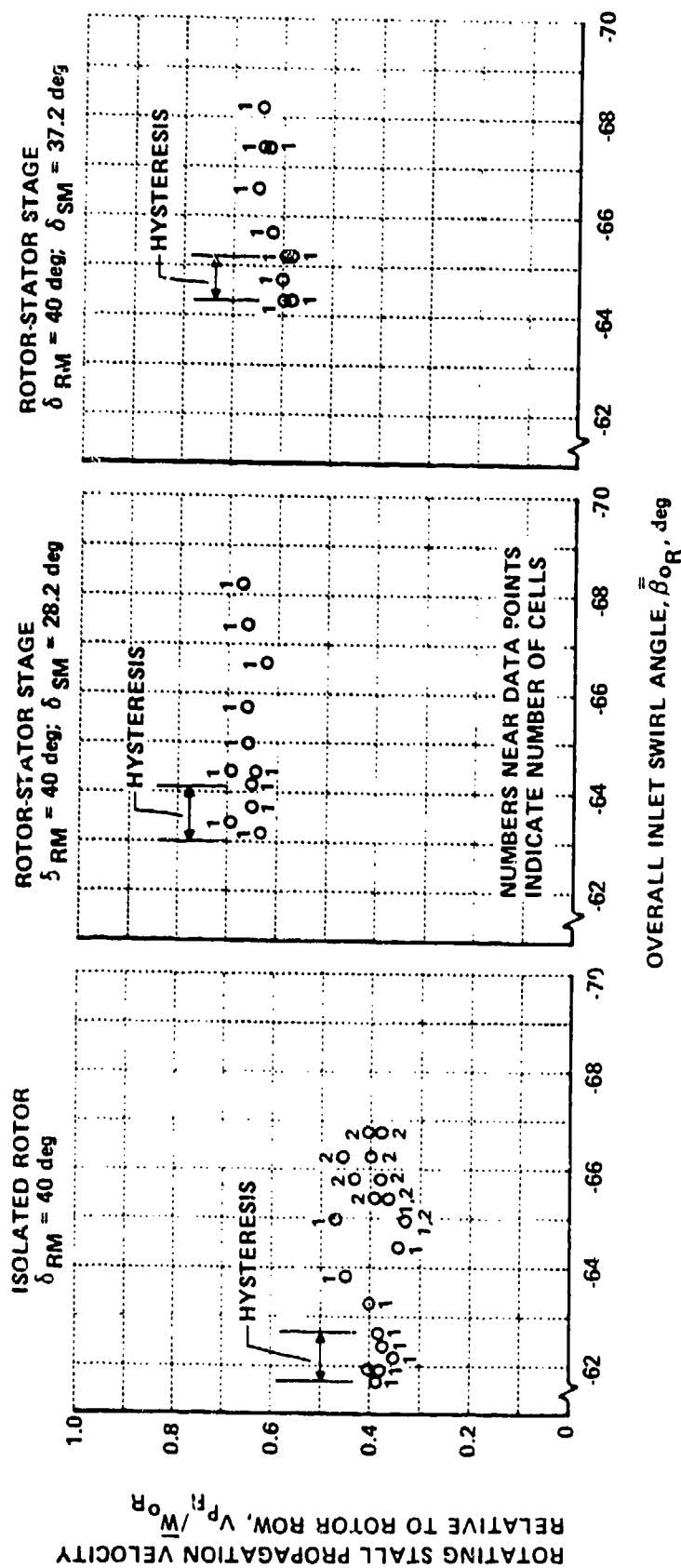
a) STATOR STAGGER ANGLES, $\delta_{SM} = 28.2$ AND 37.2 deg
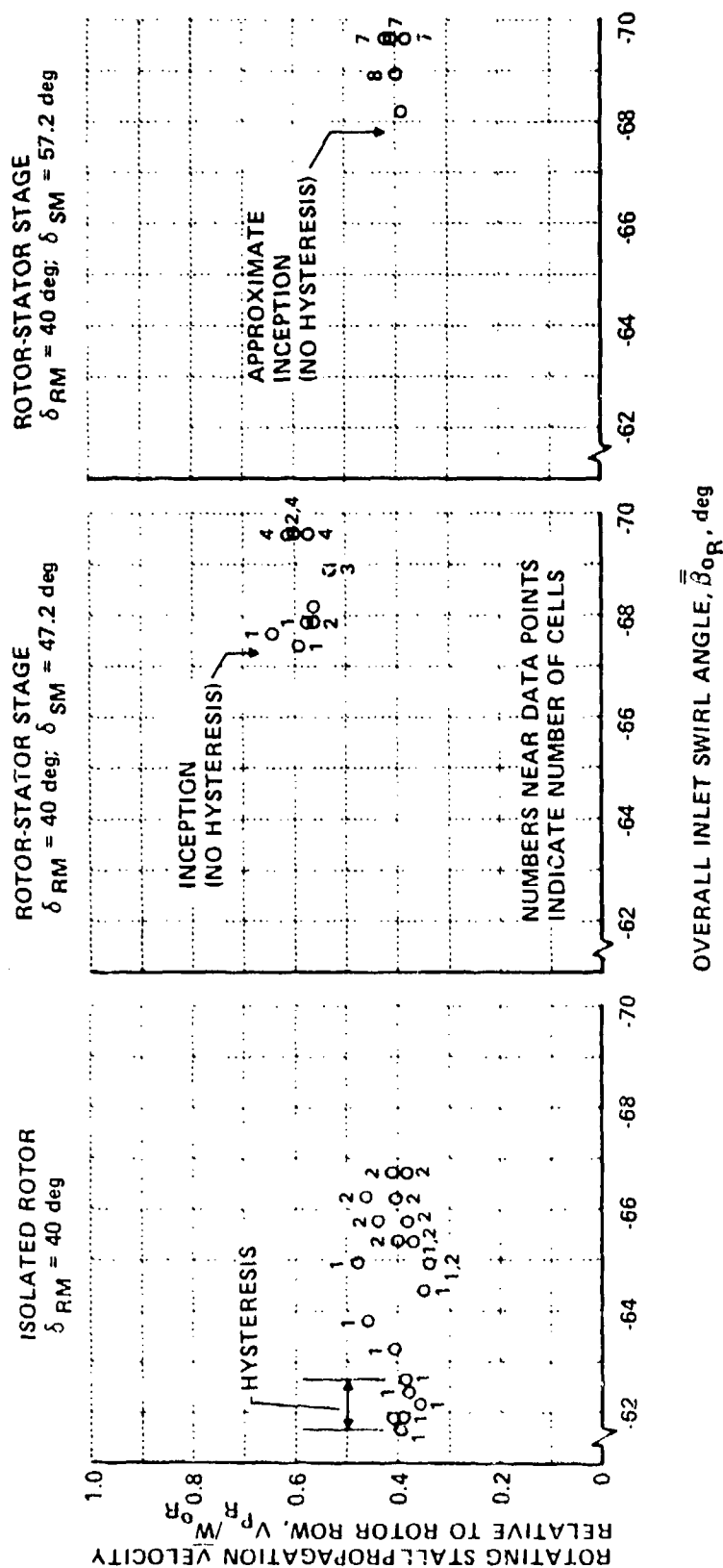
b) STATOR STAGGER ANGLES, δ_{SM} = 47.2 AND 57.2 deg

Figure 9 (Cont.) ROTATING STALL PROPAGATION VELOCITY AND NUMBER OF CELLS FOR ISOLATED ROTOR AND FOR ROTOR-STATOR STAGE, COORDINATE SYSTEM RELATIVE TO ROTOR

97
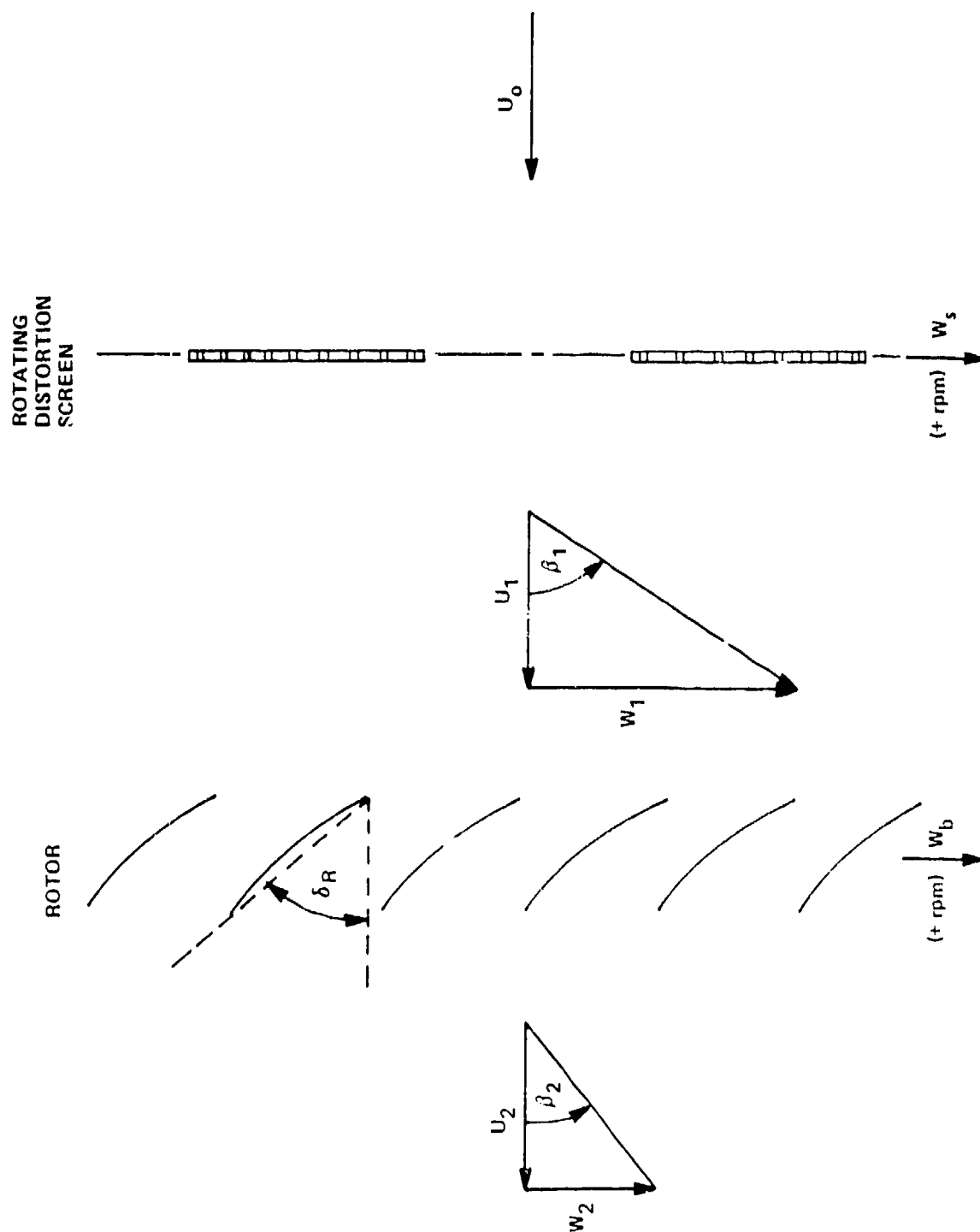
Figure 10 NOTATION FOR ANNULAR CASCADE WITH ROTATING DISTORTION SCREEN
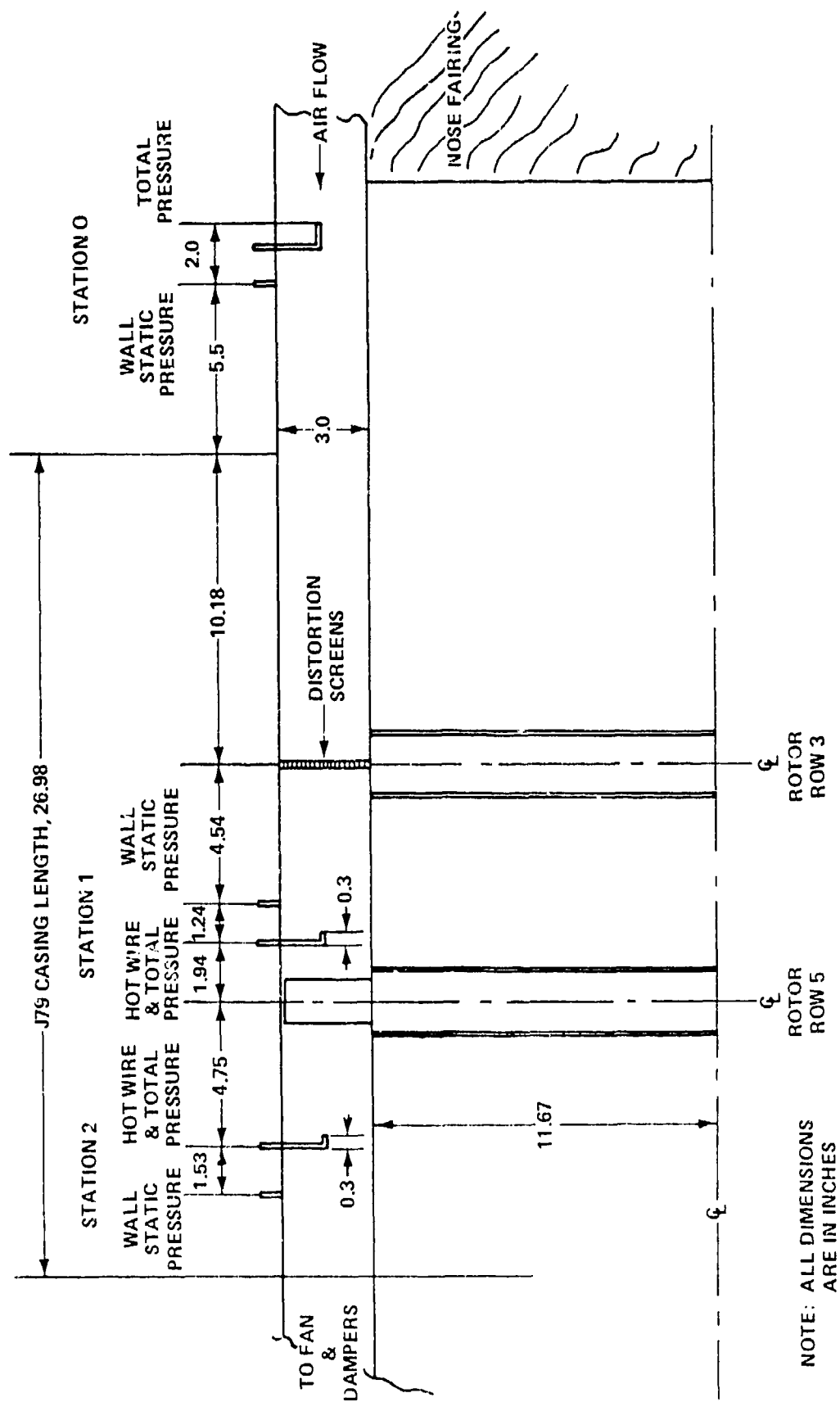
Figure 11   ANNULAR CASCADE CONFIGURATION USED FOR ROTATING STALL STUDIES WITH STATIONARY AND ROTATING INLET DISTORTION
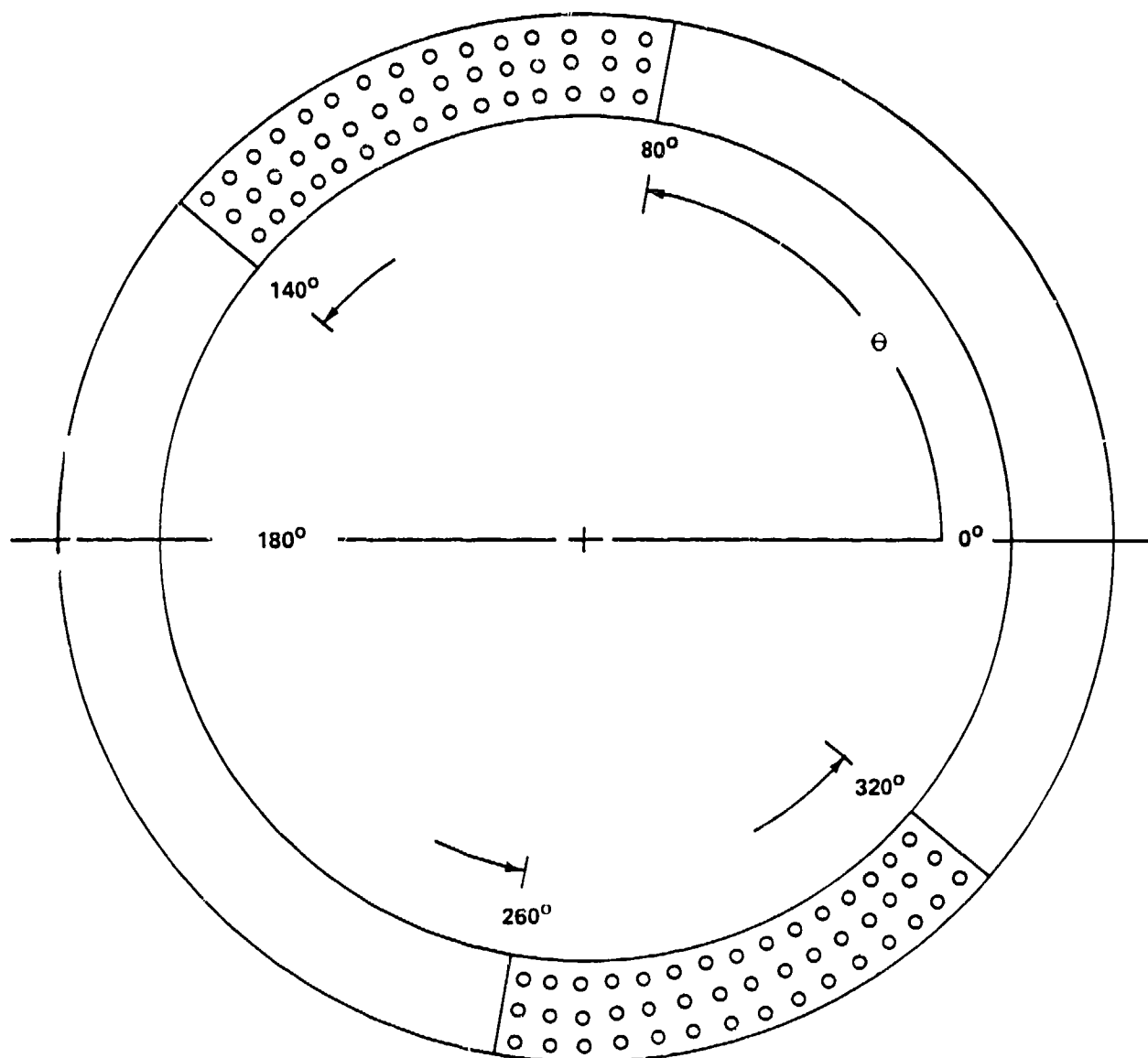
a) CONFIGURATION A

Figure 12 GEOMETRY OF STATIONARY DISTORTION SCREEN (LOOKING UPSTREAM)

100
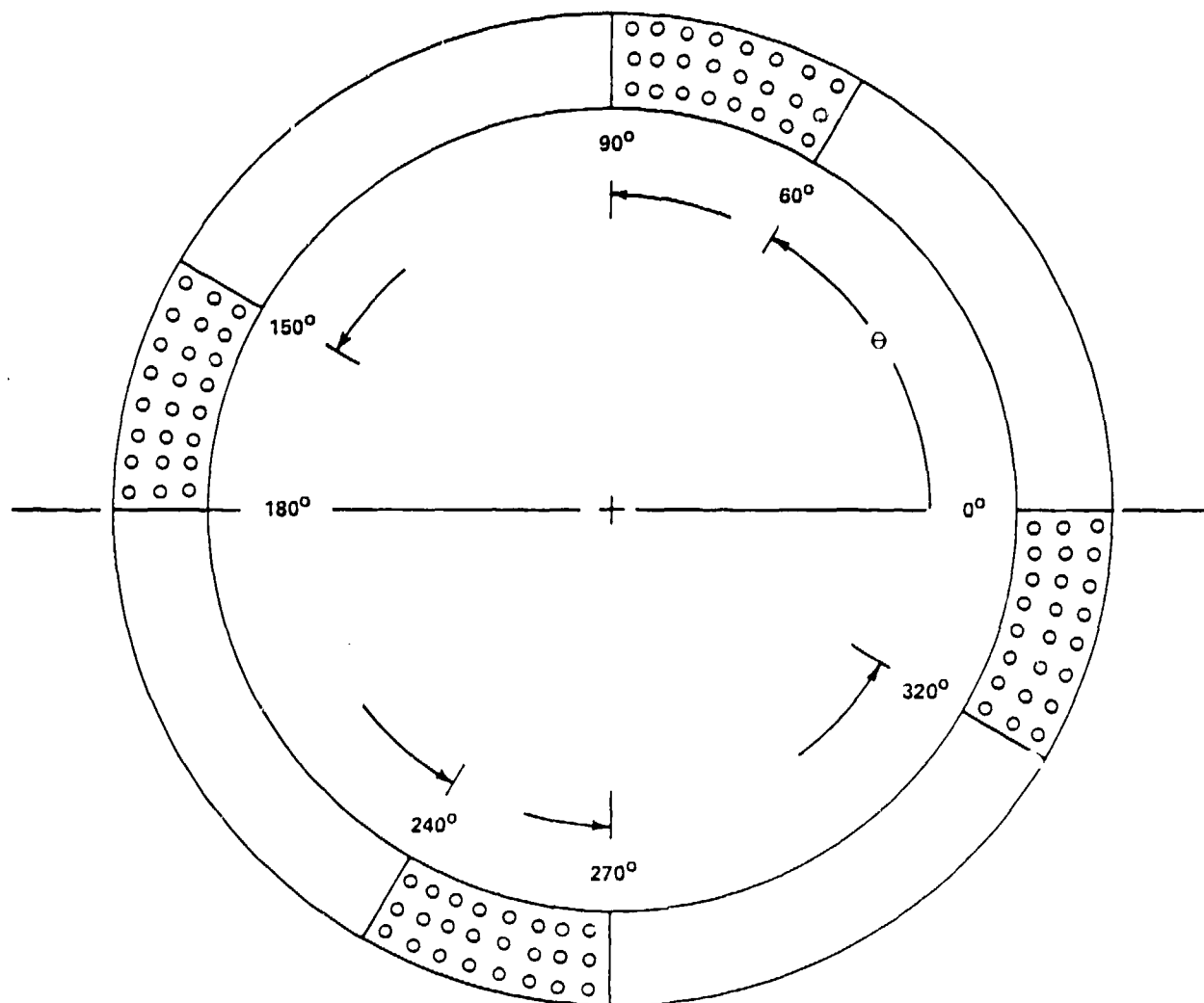
b) CONFIGURATION B

Figure 12 (Cont.) GEOMETRY OF STATIONARY DISTORTION SCREEN (LOOKING UPSTREAM)

DISTANCE FROM HUB

Δr = 2.96 in.
Δr = 2.83 in.
Δr = 2.58 in.
Δr = 2.33 in.
Δr = 2.08 in.
Δr = 1.83 in.
Δr = 1.58 in.
Δr = 1.33 in.
Δr = 1.08 in.
Δr = 0.83 in.

SCREEN POSITION

TOTAL PRESSURE COEFFICIENT, $C_{p_{T_1}}$ (r, θ)

0   -1.0   0   -1.0   0   -1.0   0   -1.0   0   -1.0   0   -1.0   0   -1.0   0   -1.0   0   -1.0   0
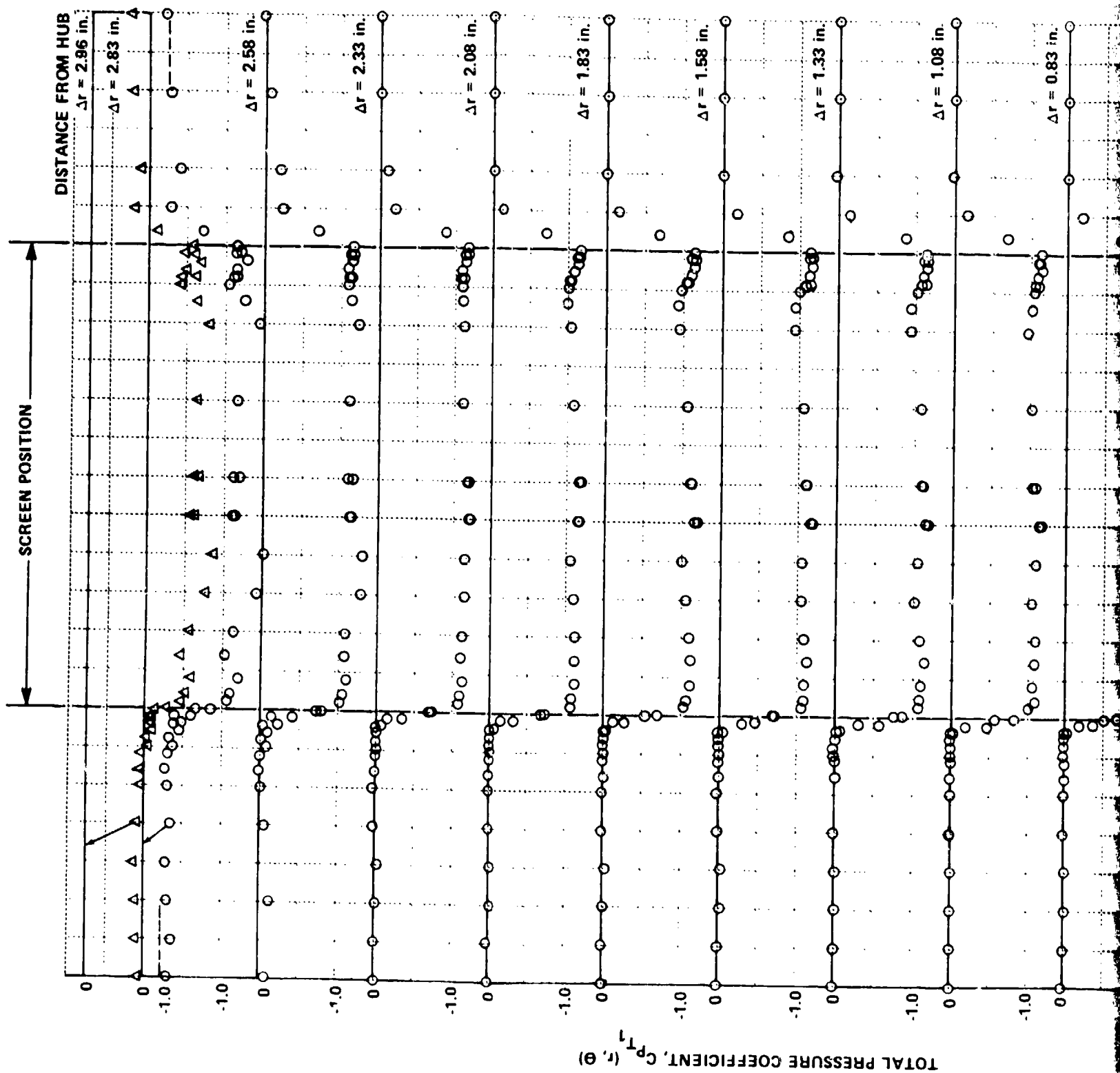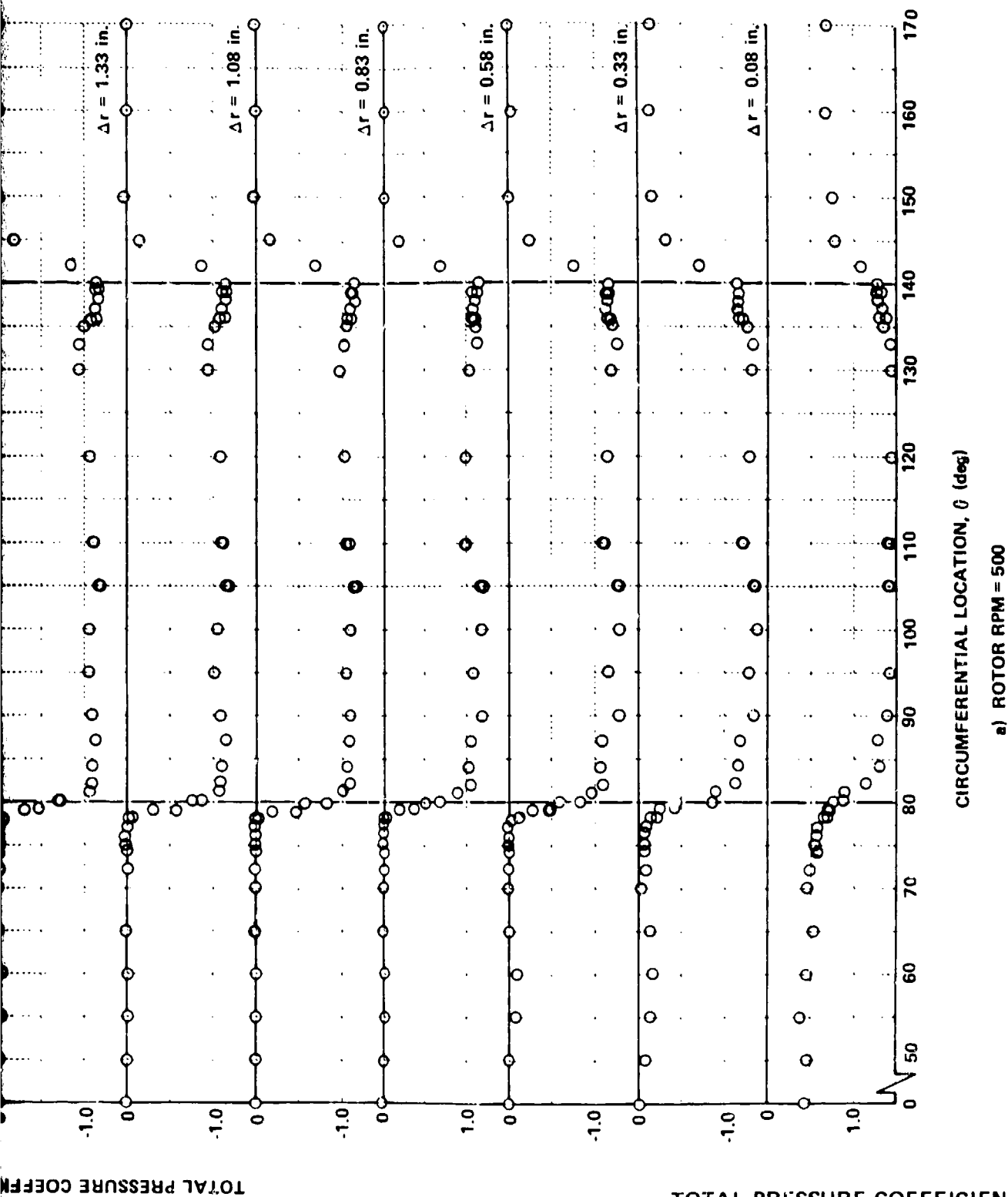
Figure 13

TOTAL PRESSURE COEFFICIENTS, $C_{P_{T_1}}$ (r, Θ),

DOWNSTREAM OF DISTORTION SCREEN
CONFIGURATION A

DISTANCE FROM HUB,

Δr = 2.96 in.

Δr = 2.83 in.

Δr = 2.58 in.

Δr = 2.33 in.

Δr = 2.08 in.

Δr = 1.83 in.

Δr = 1.58 in.

Δr = 1.33 in.

Δr = 1.08 in.

Δr = .083 in.

SCREEN POSITION

TOTAL PRESSURE COEFFICIENT, $C_{P_{T_1}}$ (r, θ)
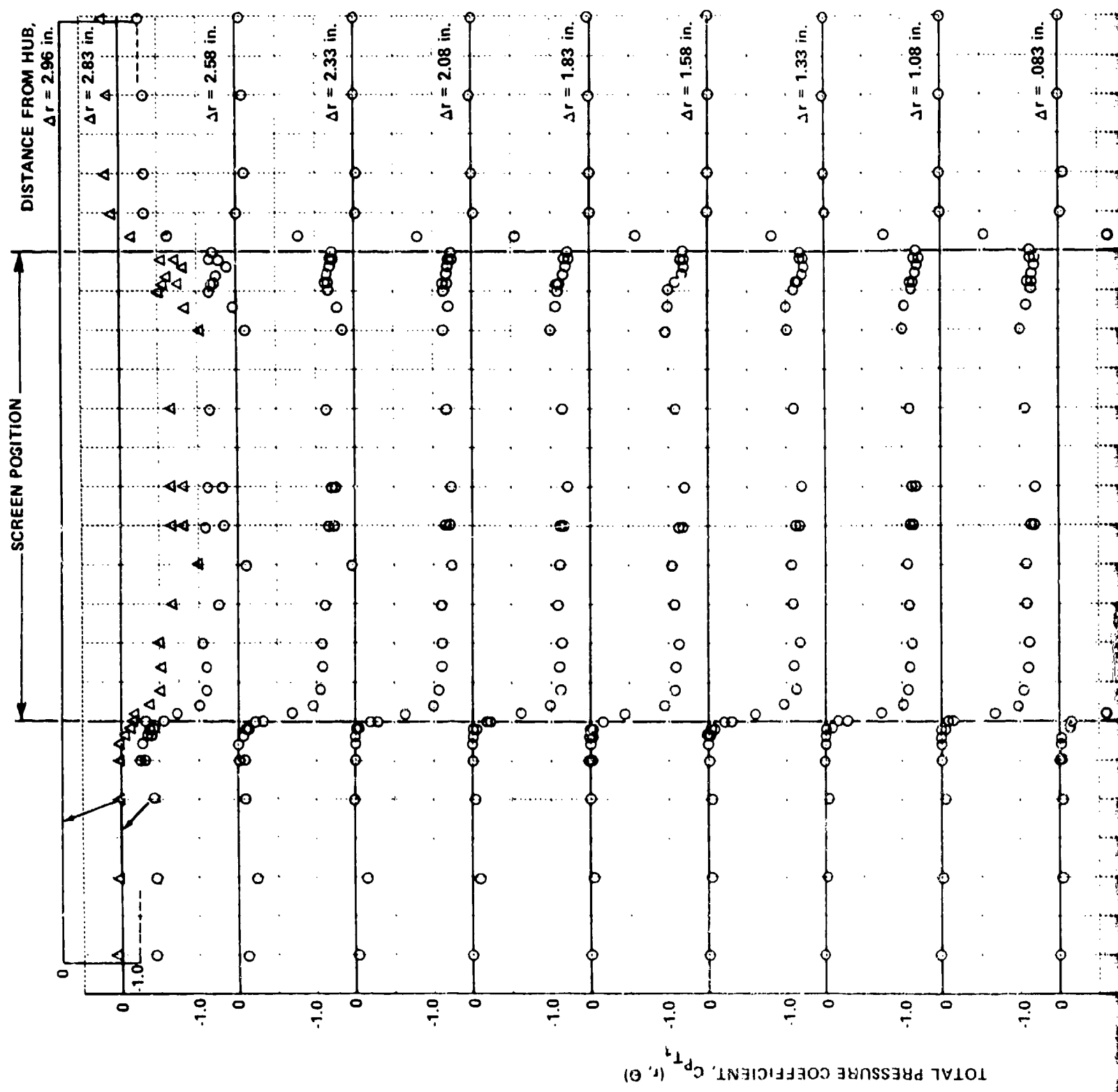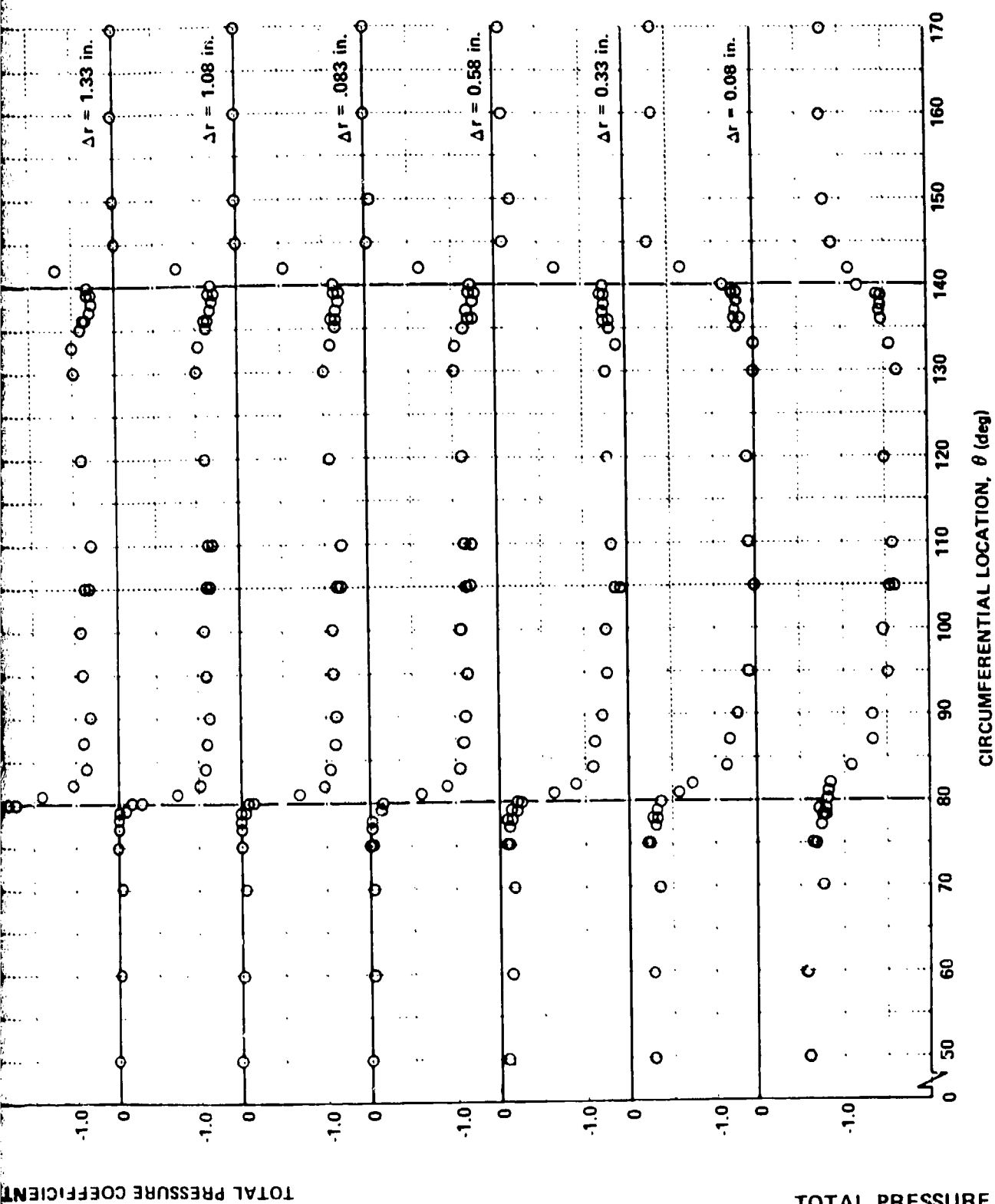
Figure 13 (Cont.)

TOTAL PRESSURE COEFFICIENTS, $C_{P_{T_1}}$ (r, Θ), DOWNSTREAM OF DISTORTION SCREEN CONFIGURATION A

TOTAL PRESSURE COEFFICIENT, C_{P_1} (r, θ)
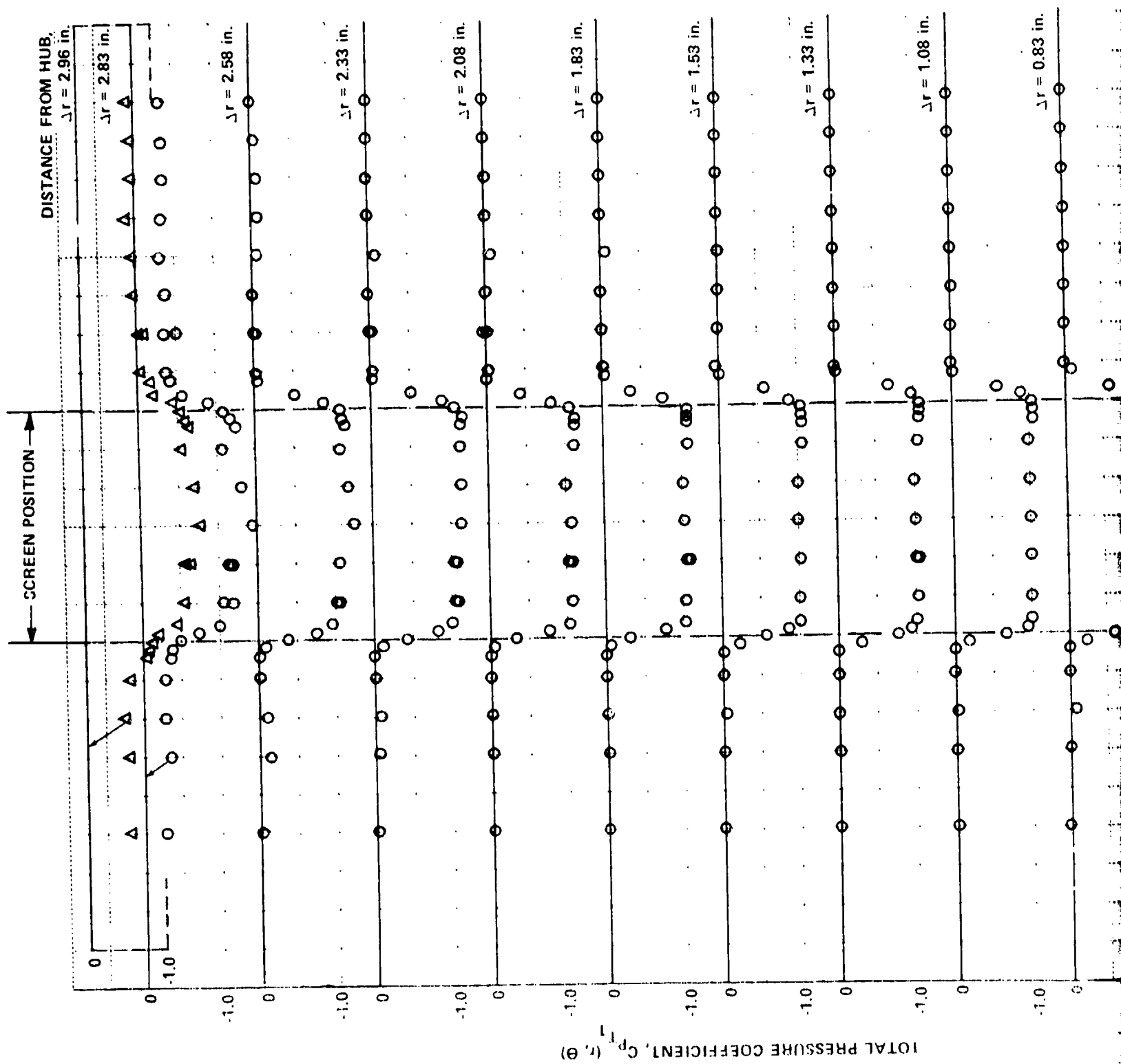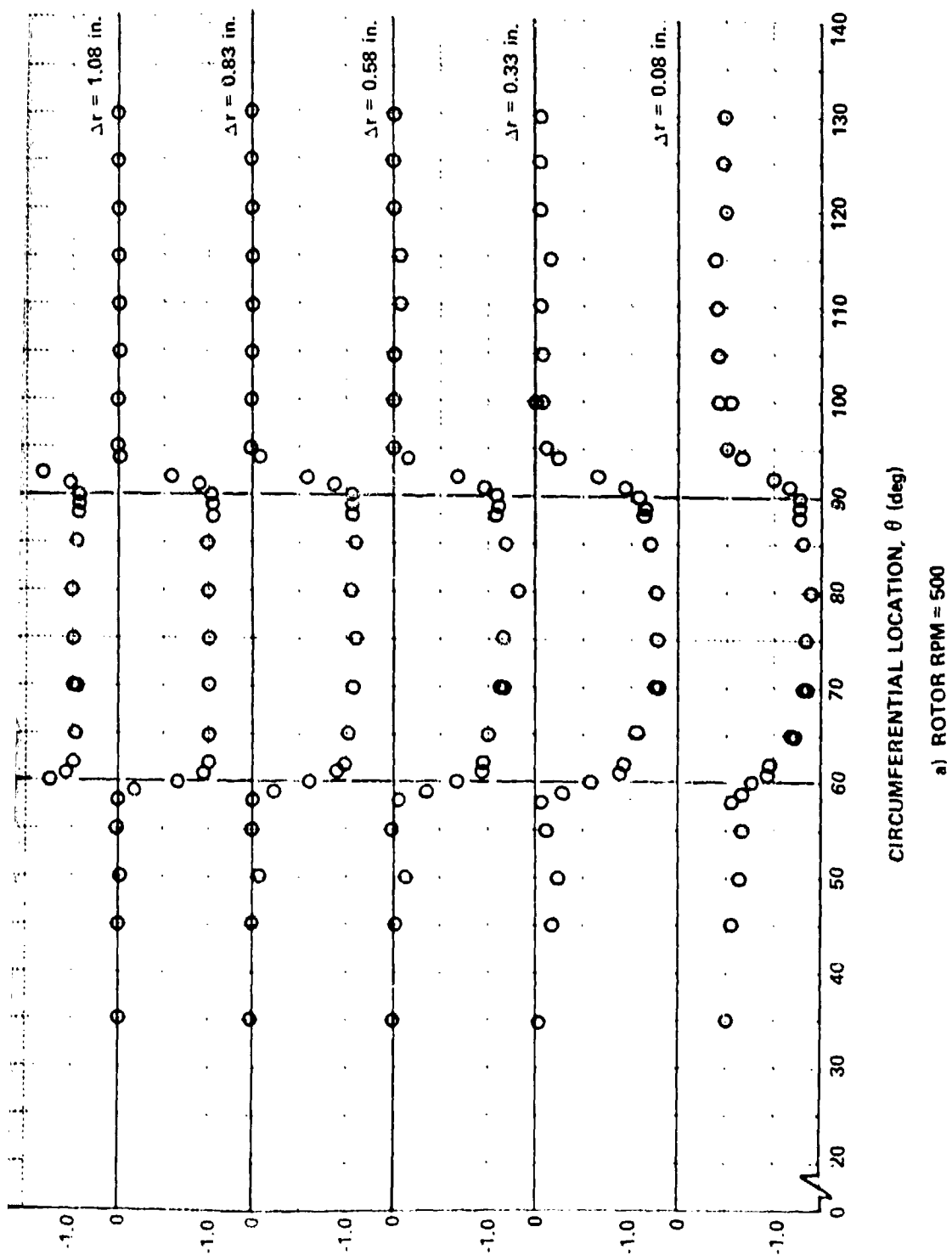
Figure 14

TOTAL PRESSURE COEFFICIENTS, $C_{P_{T_1}}$ (r, Θ), DOWNSTREAM OF DISTORTION SCREEN CONFIGURATION B

DISTANCE FROM HUB,
Δr = 2.96 in.

Δr = 2.83 in.

Δr = 2.58 in.

Δr = 2.33 in.

Δr = 2.08 in.

Δr = 1.83 in.

Δr = 1.58 in.

Δr = 1.33 in.

Δr = 1.08 in.

Δr = 0.83 in.

SCREEN POSITION

TOTAL PRESSURE COEFFICIENT, $C_{P_{T_1}}(r, \theta)$
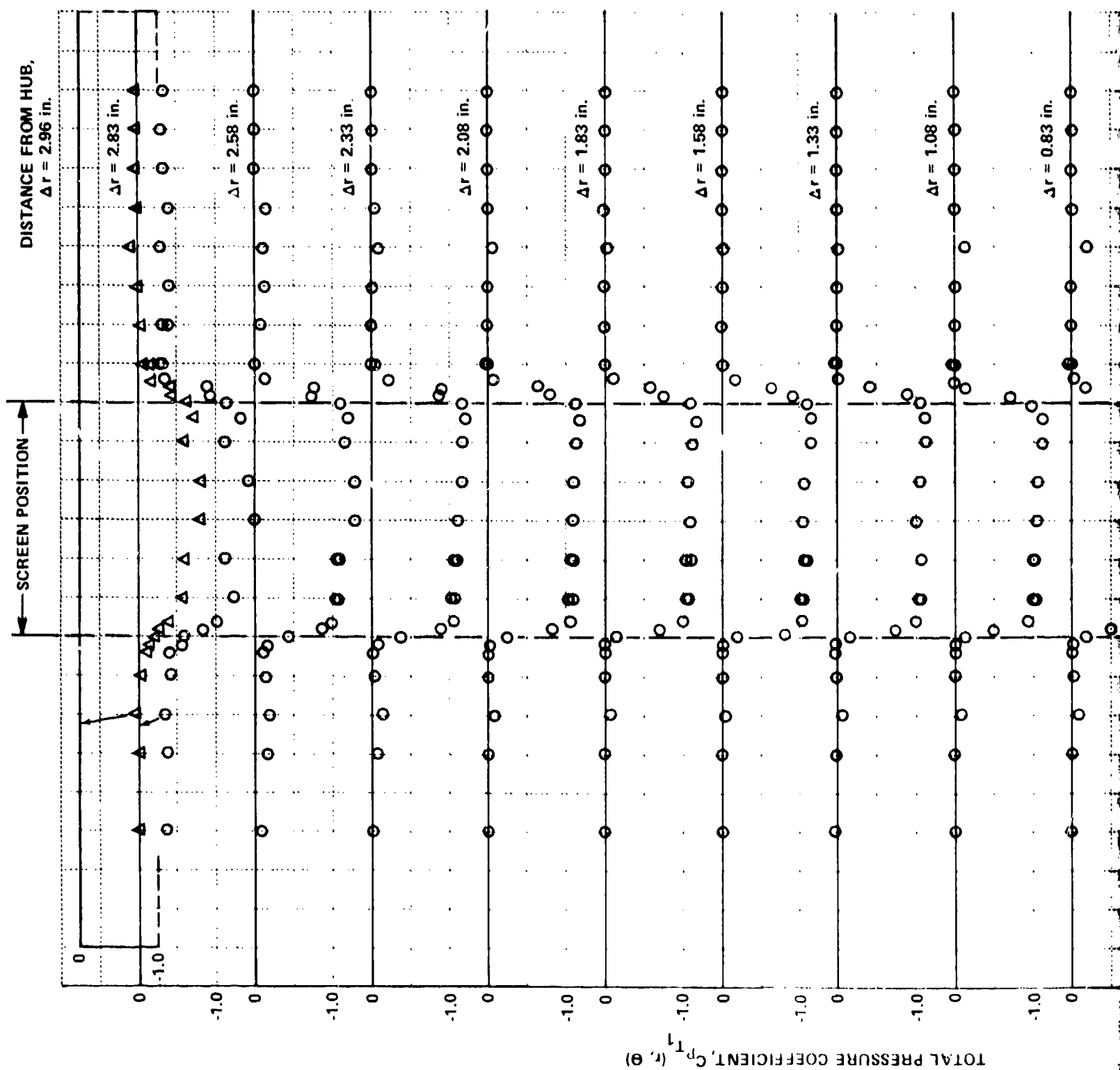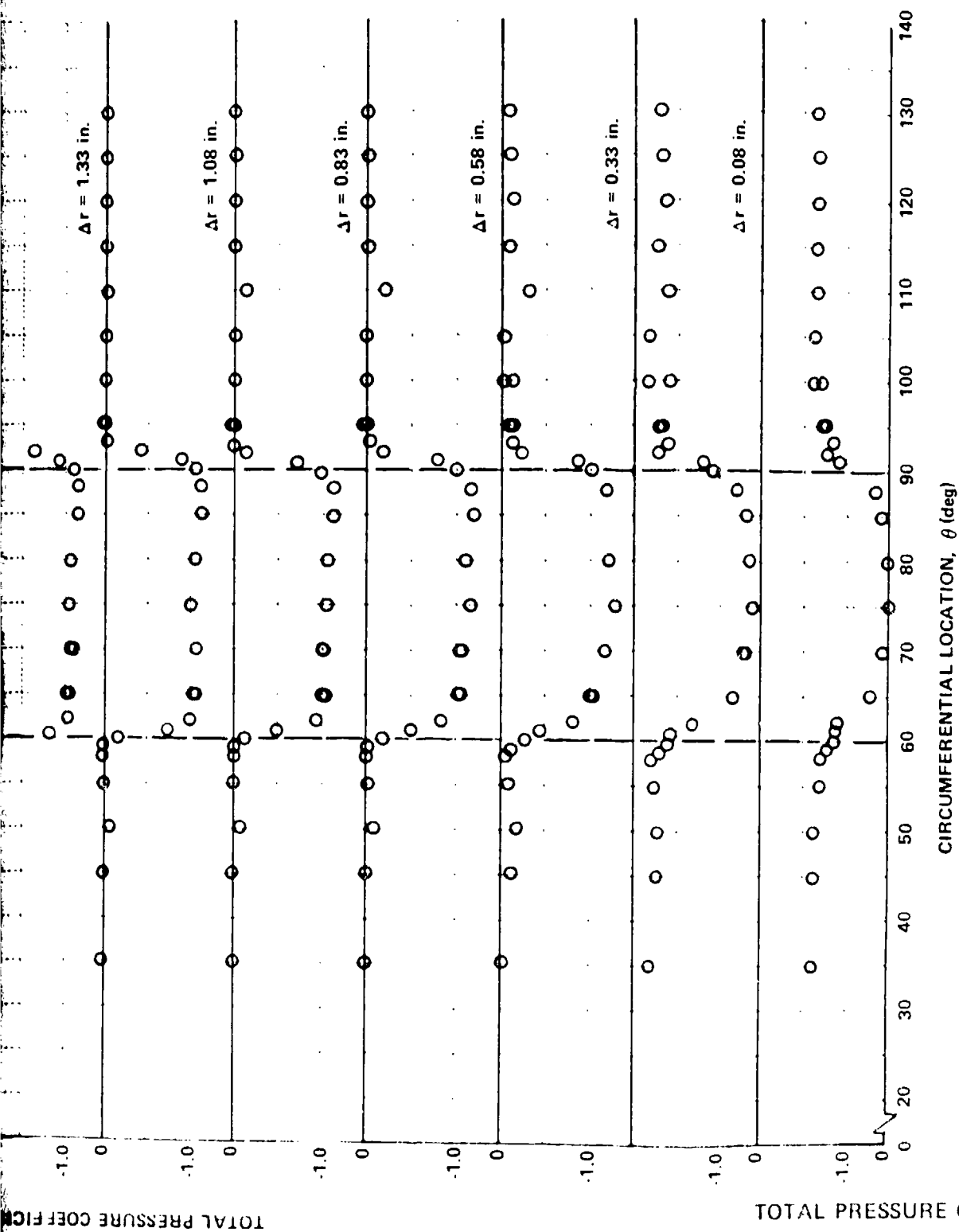
Figure 14 (Cont.)

TOTAL PRESSURE COEFFICIENTS, $C_{P_{T_1}}$ (r, Θ),
DOWNSTREAM OF DISTORTION SCREEN
CONFIGURATION B

135
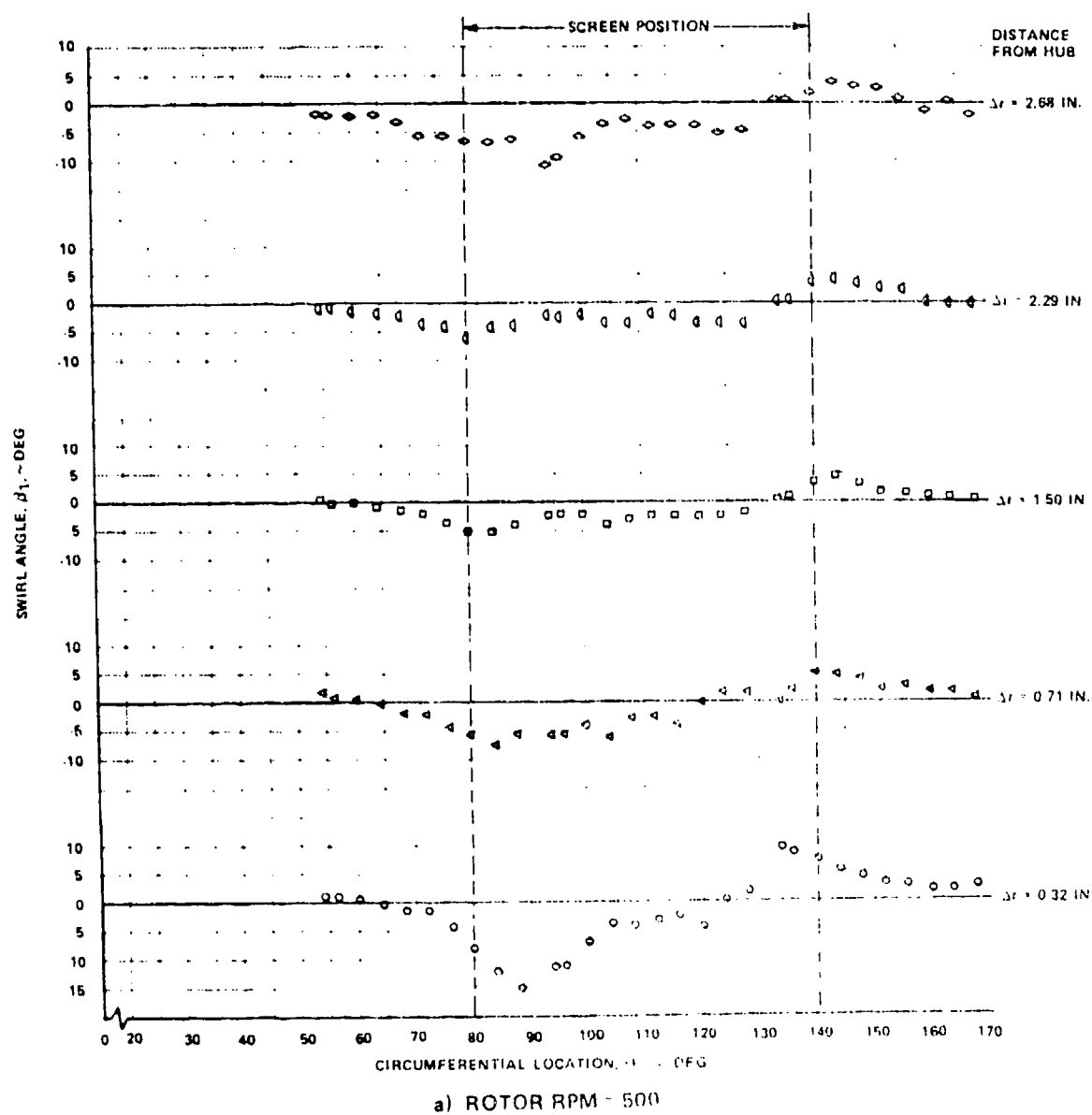
Figure 15   CIRCUMFERENTIAL DISTRIBUTIONS OF SWIRL ANGLE, β_1, BETWEEN DISTORTION
SCREEN AND ROTOR, SCREEN CONFIGURATION A
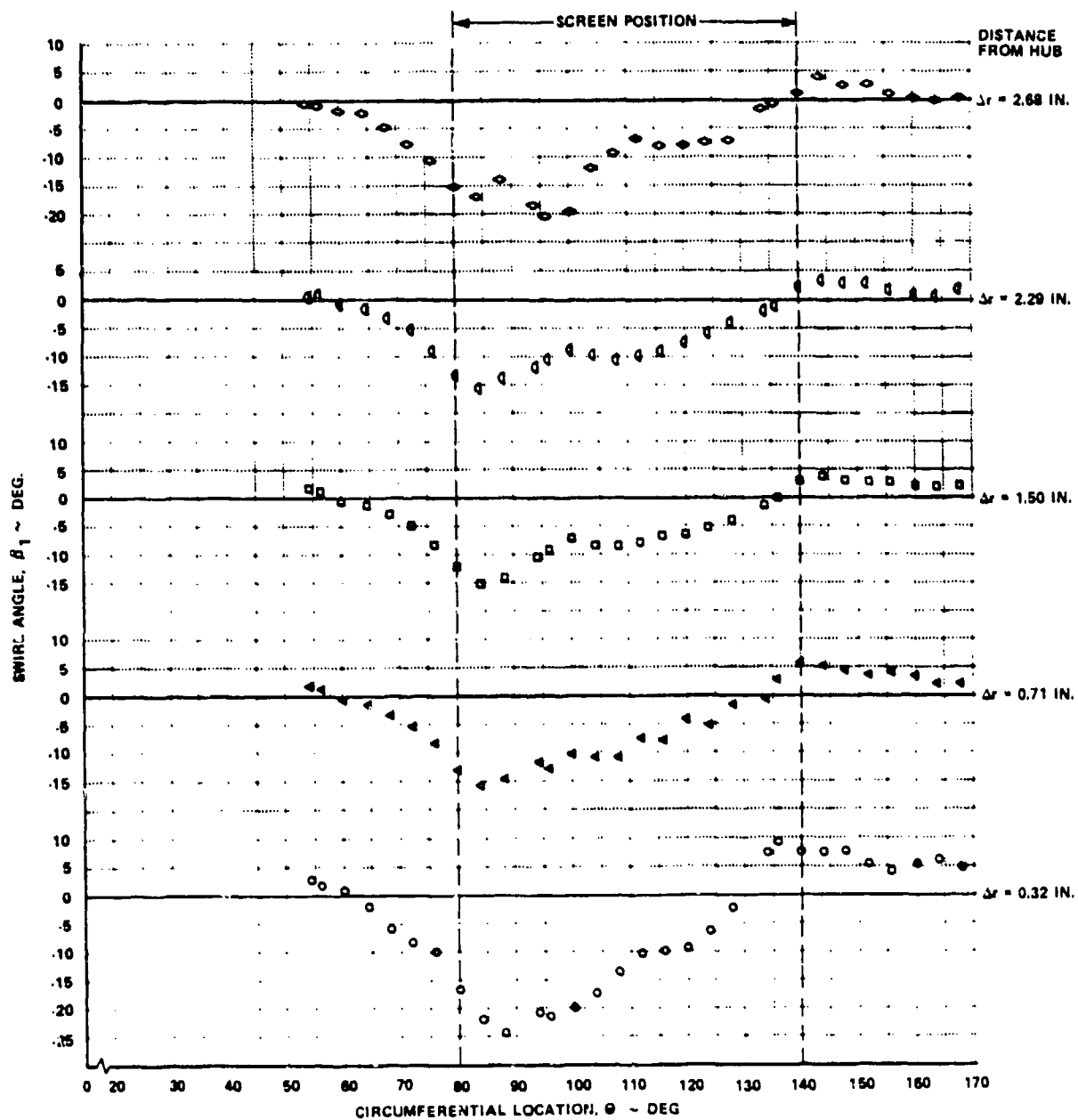
b) ROTOR RPM = 950

Figure 15 (Cont.)   CIRCUMFERENTIAL DISTRIBUTIONS OF SWIRL ANGLE, β_1, BETWEEN DISTORTION SCREEN AND ROTOR, SCREEN CONFIGURATION A

107
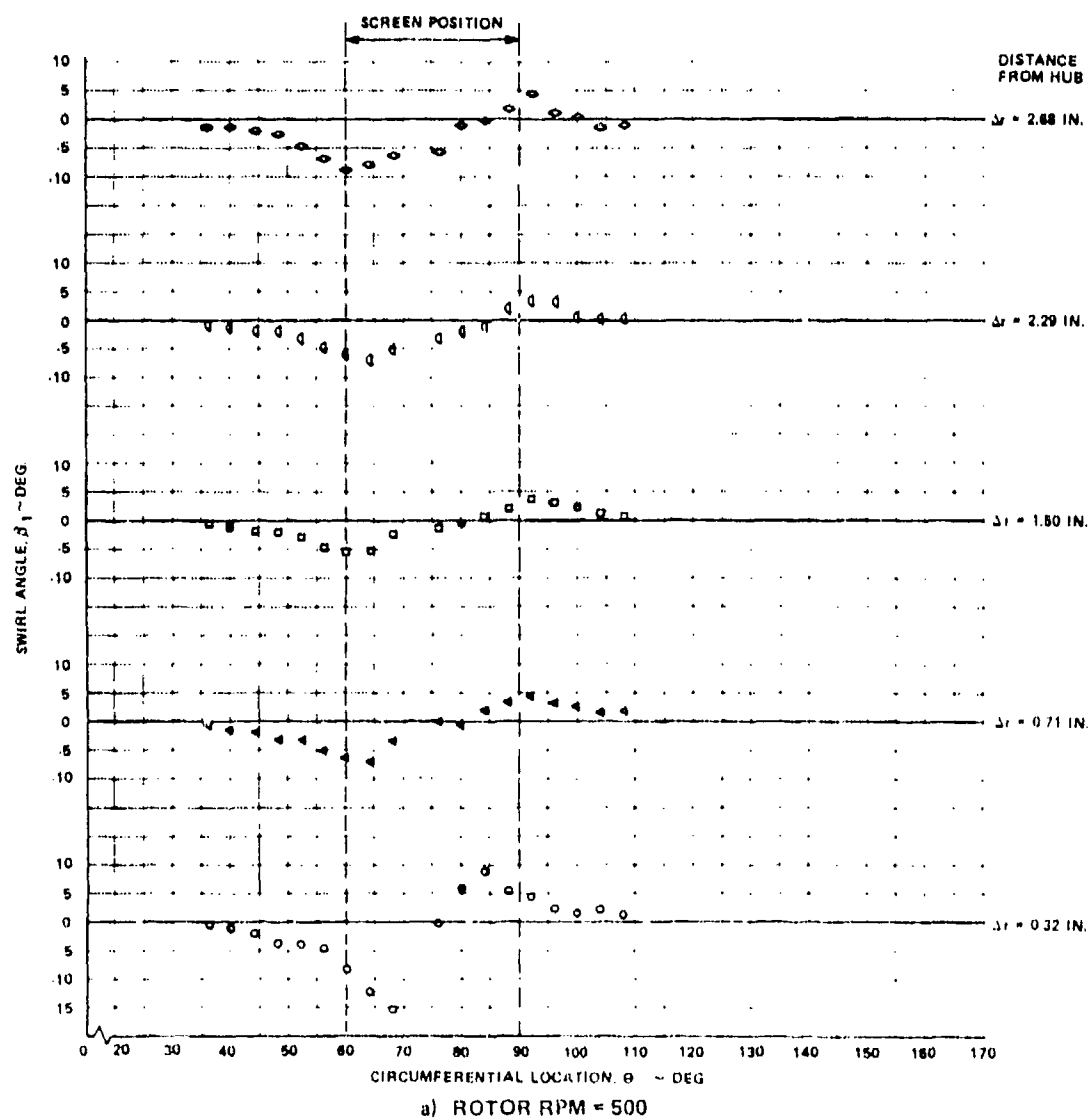
Figure 16 CIRCUMFERENTIAL DISTRIBUTIONS OF SWIRL ANGLE, β_1, BETWEEN DISTORTION SCREEN AND ROTOR, SCREEN CONFIGURATION B

b) ROTOR RPM = 950
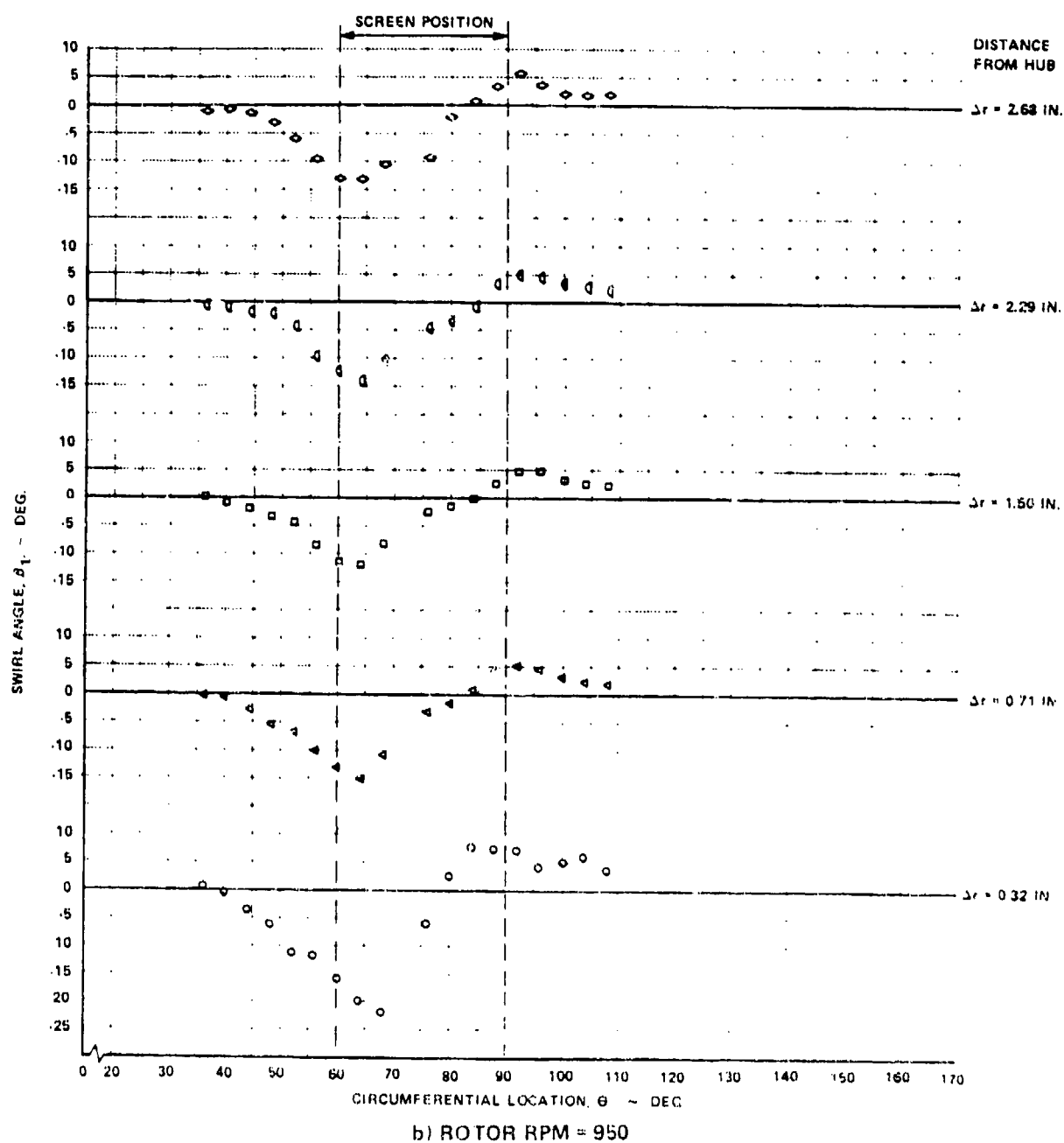
Figure 16 (Cont.) CIRCUMFERENTIAL DISTRIBUTIONS OF SWIRL ANGLE, β_1, BETWEEN DISTORTION SCREEN AND ROTOR, SCREEN CONFIGURATION B

TOTAL PRESSURE COEFFICIENT, $C_{p_{T_2}}(r, \theta)$

DISTANCE FROM HUB.

$\Delta r = 2.97$ in.

$\Delta r = 2.72$ in.

$\Delta r = 2.47$ in.

$\Delta r = 2.22$ in.

$\Delta r = 1.97$ in.

$\Delta r = 1.72$ in.

$\Delta r = 1.53$ in.
$\Delta r = 1.47$ in.

$\Delta r = 1.28$ in.

$\Delta r = 1.03$ in.

$\Delta r = 0.78$ in.

$\Delta r = 0.53$ in.

$\Delta r = 0.28$ in.

SCREEN POSITION

CIRCUMFERENTIAL LOCATION, θ (deg)

a) ROTOR RPM = 500
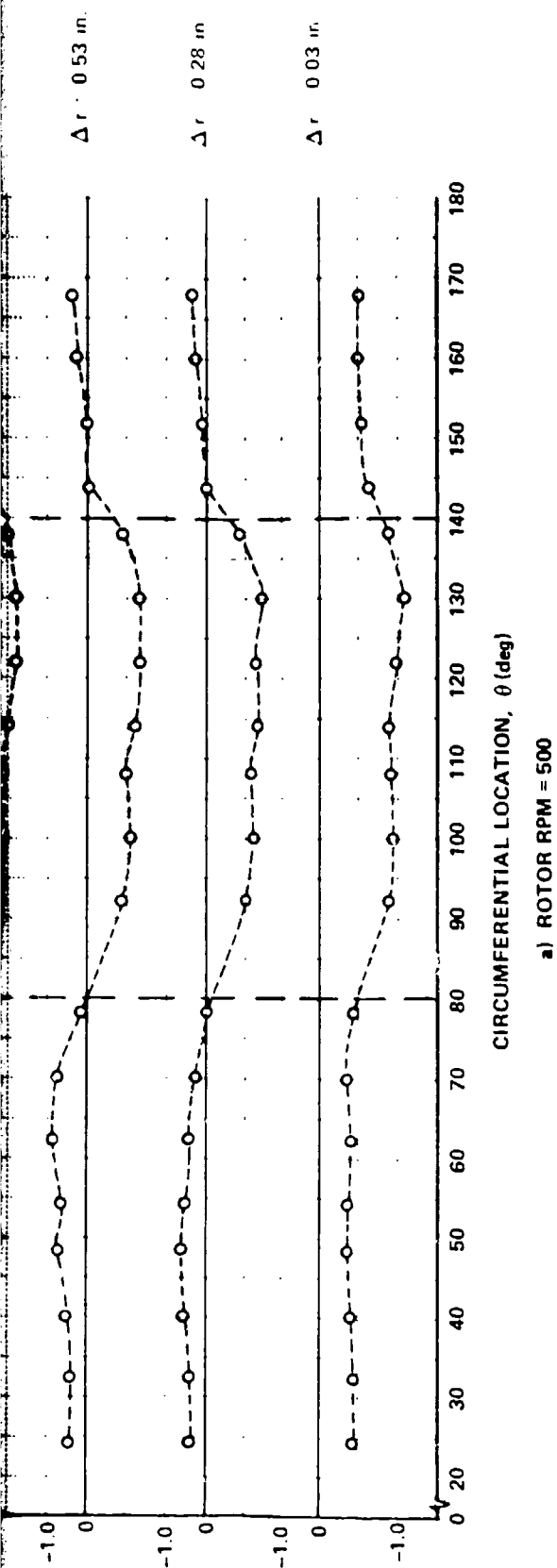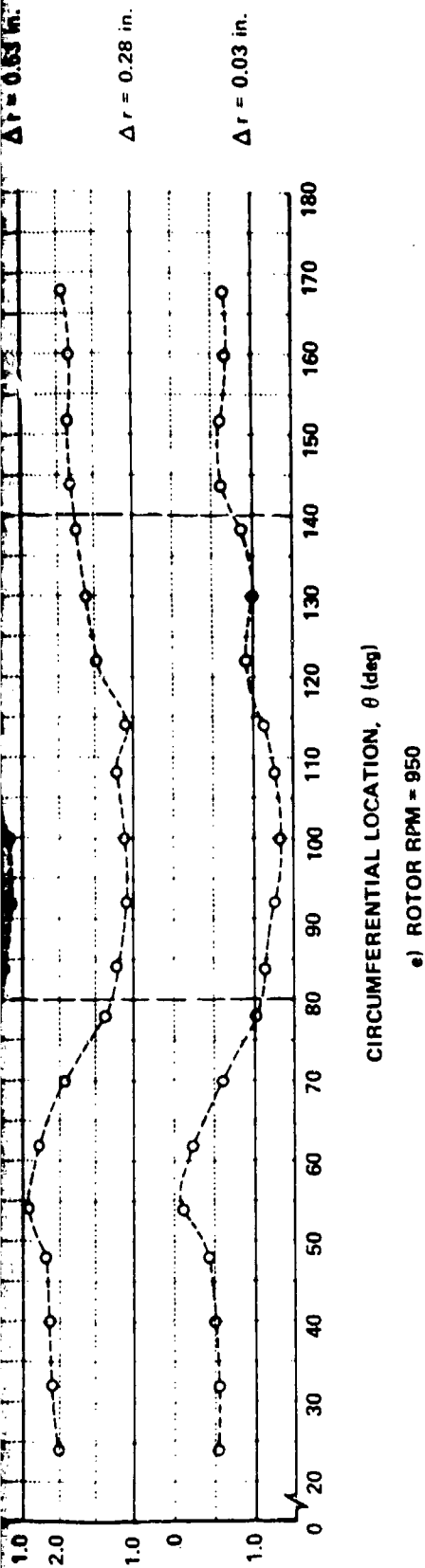
Figure 17

TOTAL PRESSURE COEFFICIENTS DOWNSTREAM
OF ROTOR, DISTORTION SCREEN
CONFIGURATION A

DISTANCE FROM HUB.
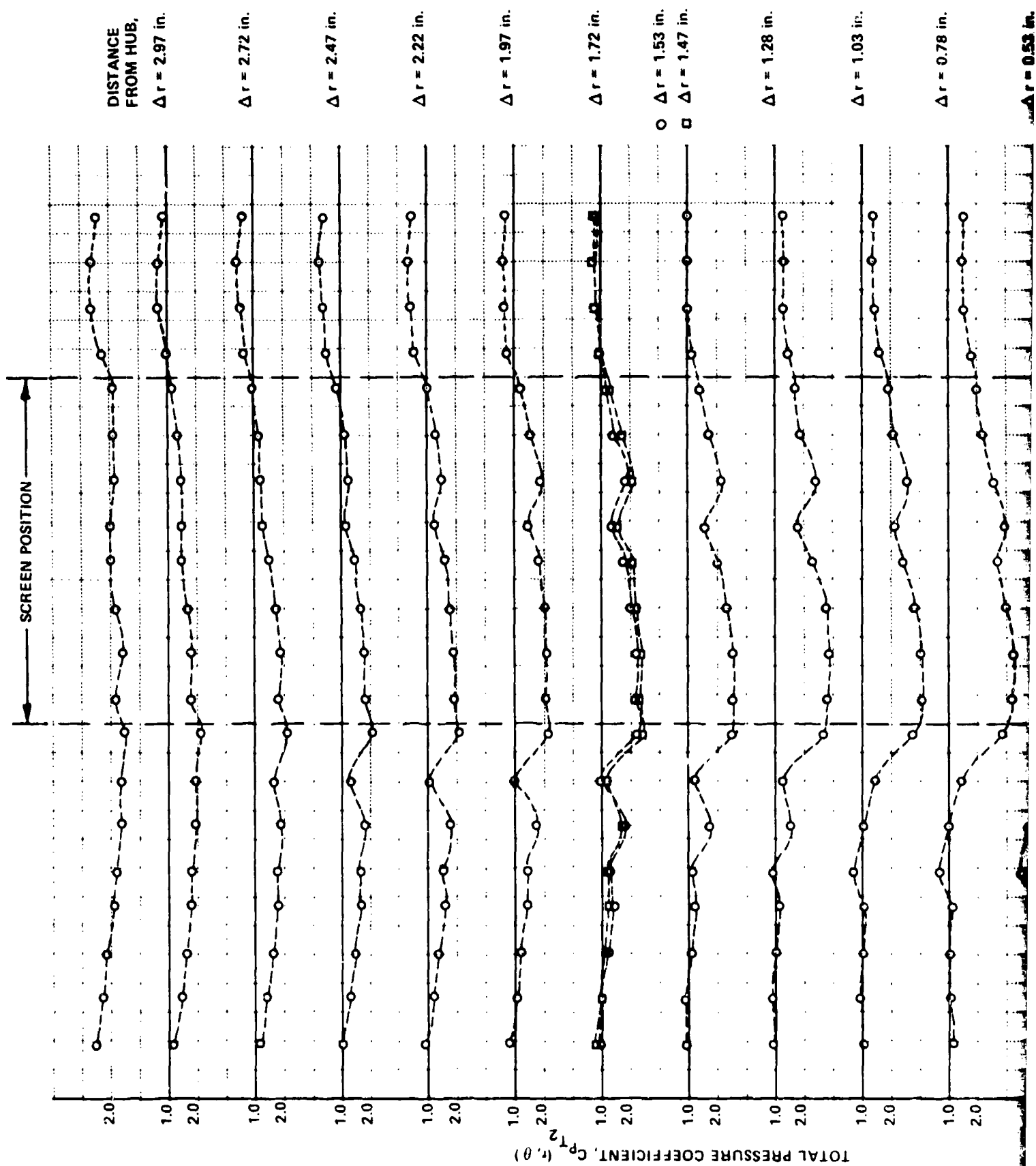
Δr = 2.97 in.

Δr = 2.72 in.

Δr = 2.47 in.

Δr = 2.22 in.

Δr = 1.97 in.

Δr = 1.72 in.

○ Δr = 1.53 in
□ Δr = 1.47 in.

Δr = 1.28 in.

Δr = 1.03 in.

Δr = 0.78 in.

Δr = 0.53 in.

Δr = 0.28 in.

SCREEN POSITION

TOTAL PRESSURE COEFFICIENT, $c_{p_{T_2}}(r, \theta)$

CIRCUMFERENTIAL LOCATION θ (deg)

b) ROTOR RPM = 700

$\Delta r = 0.78$ in.

$\Delta r = 0.53$ in.

$\Delta r = 0.28$ in.

$\Delta r = 0.03$ in.

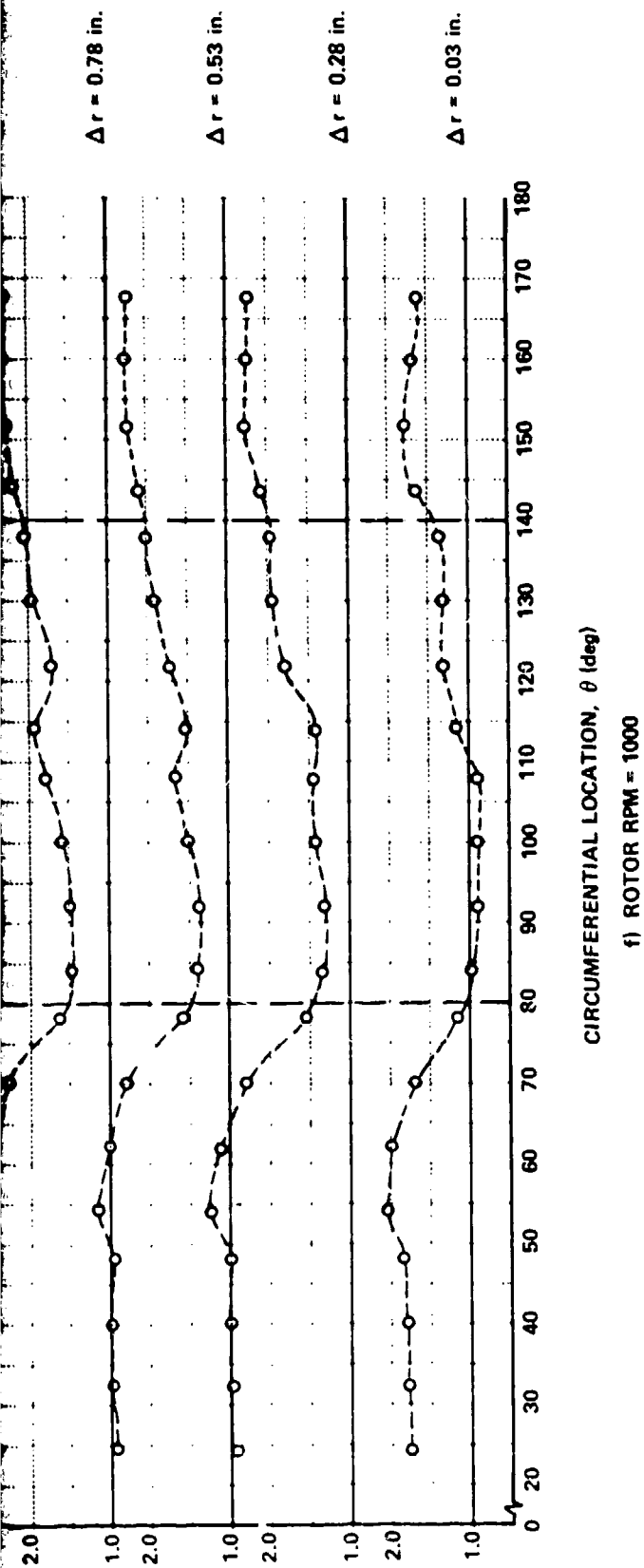Figure 17 (Cont.)

TOTAL PRESSURE COEFFICIENTS DOWNSTREAM
OF ROTOR, DISTORTION SCREEN
CONFIGURATION A

111

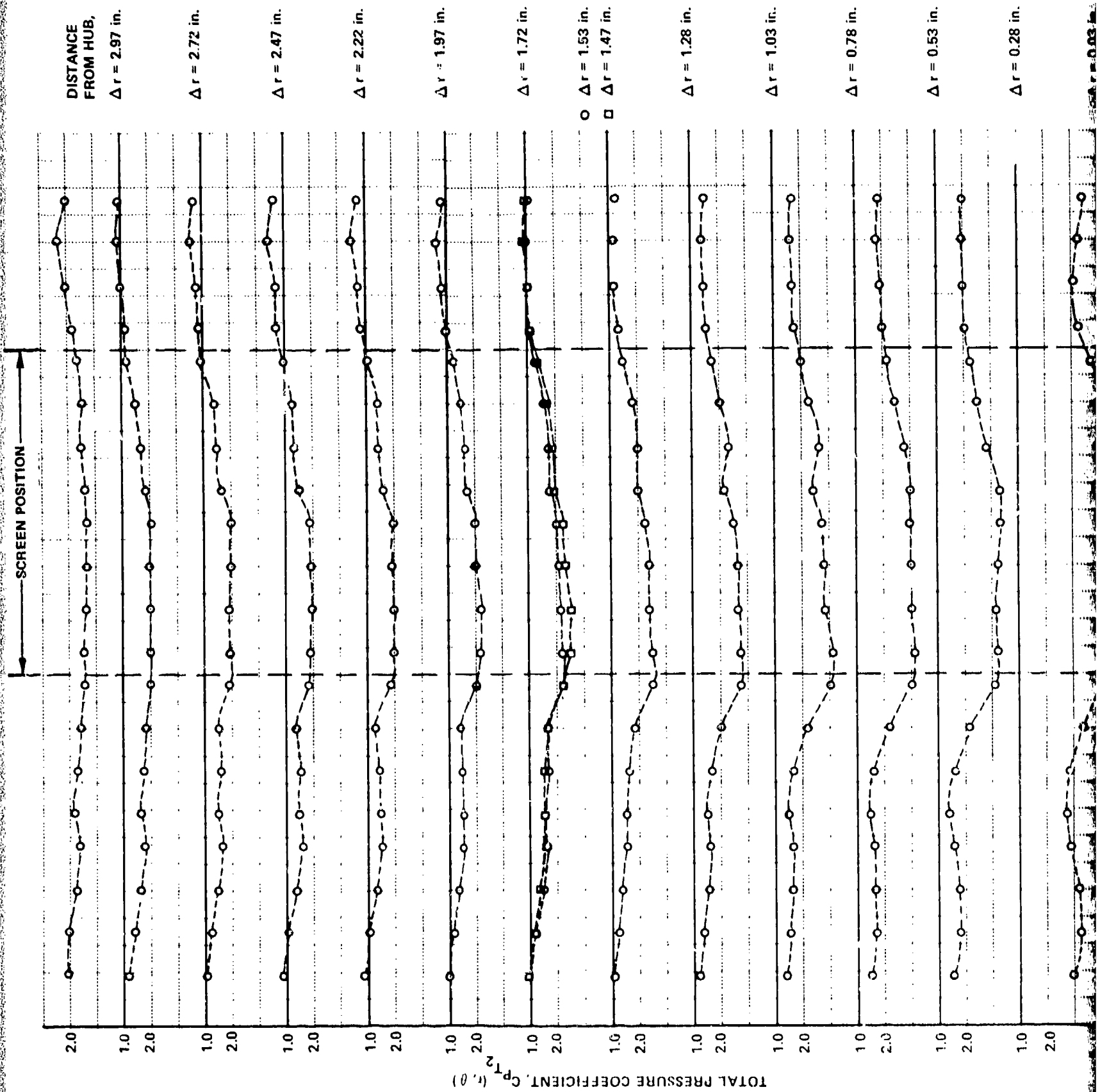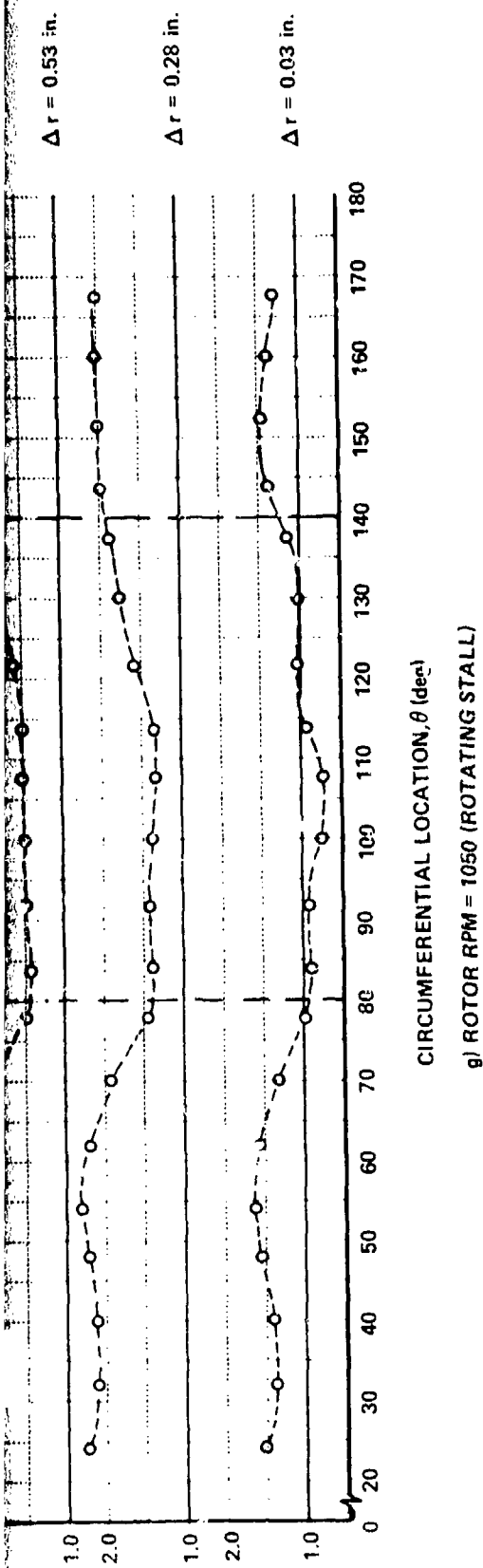DISTANCE
FROM HUB.

Δr = 2.97 in.

Δr = 2.72 in.

Δr = 2.47 in.

Δr = 2.22 in.

Δr = 1.97 in.

Δr = 1.72 in.

Δr = 1.53 in.
Δr = 1.47 in.

Δr = 1.28 in.

Δr = 1.03 in.

Δr = 0.78 in.

Δr = 0.53 in.

Δr = 0.28 in.

SCREEN POSITION

TOTAL PRESSURE COEFFICIENT, $C_{P_{T_2}}$ (r, θ)

Figure 17 (Cont.)

TOTAL PRESSURE COEFFICIENTS DOWNSTREAM
OF ROTOR, DISTORTION SCREEN
CONFIGURATION A

112

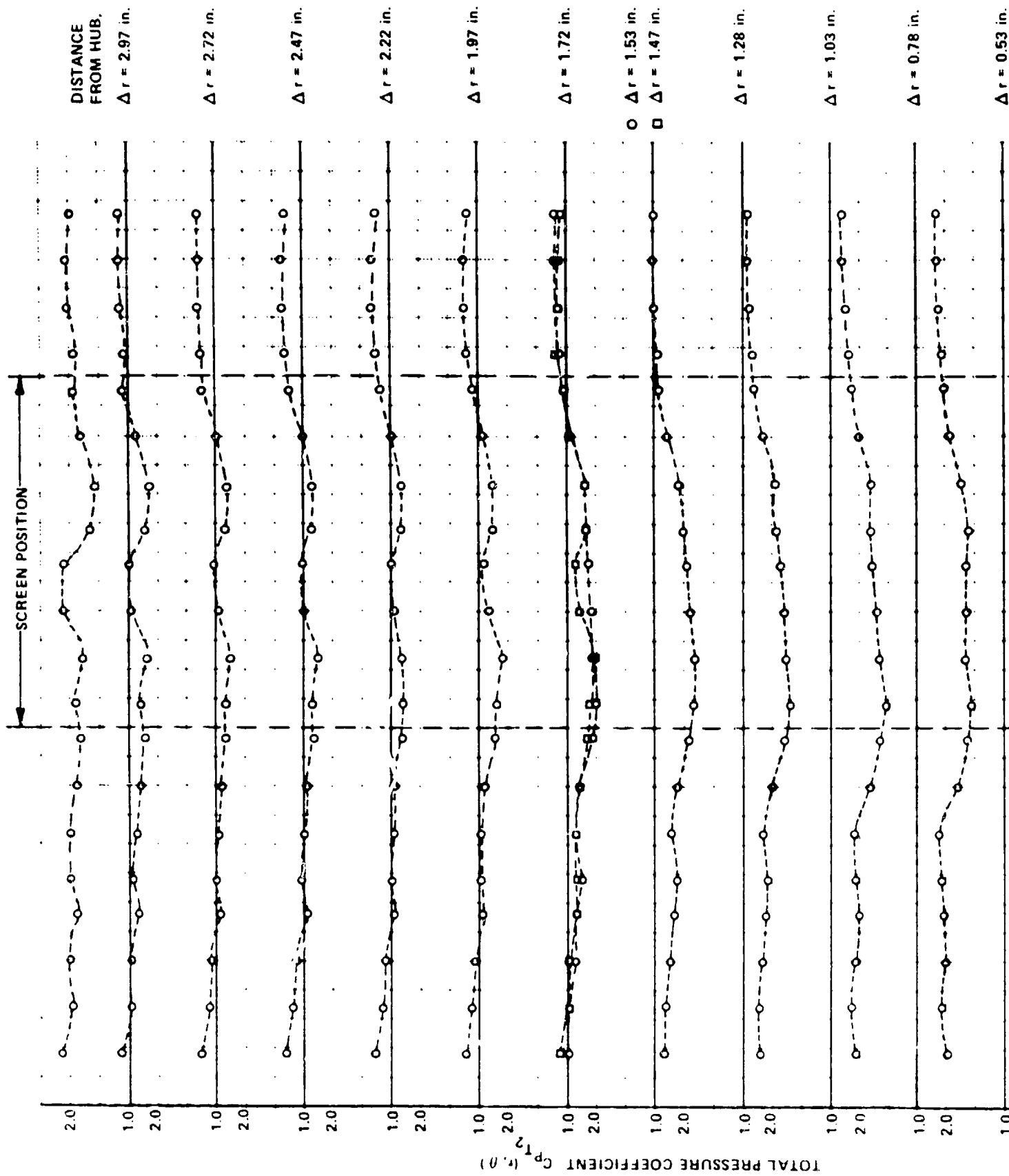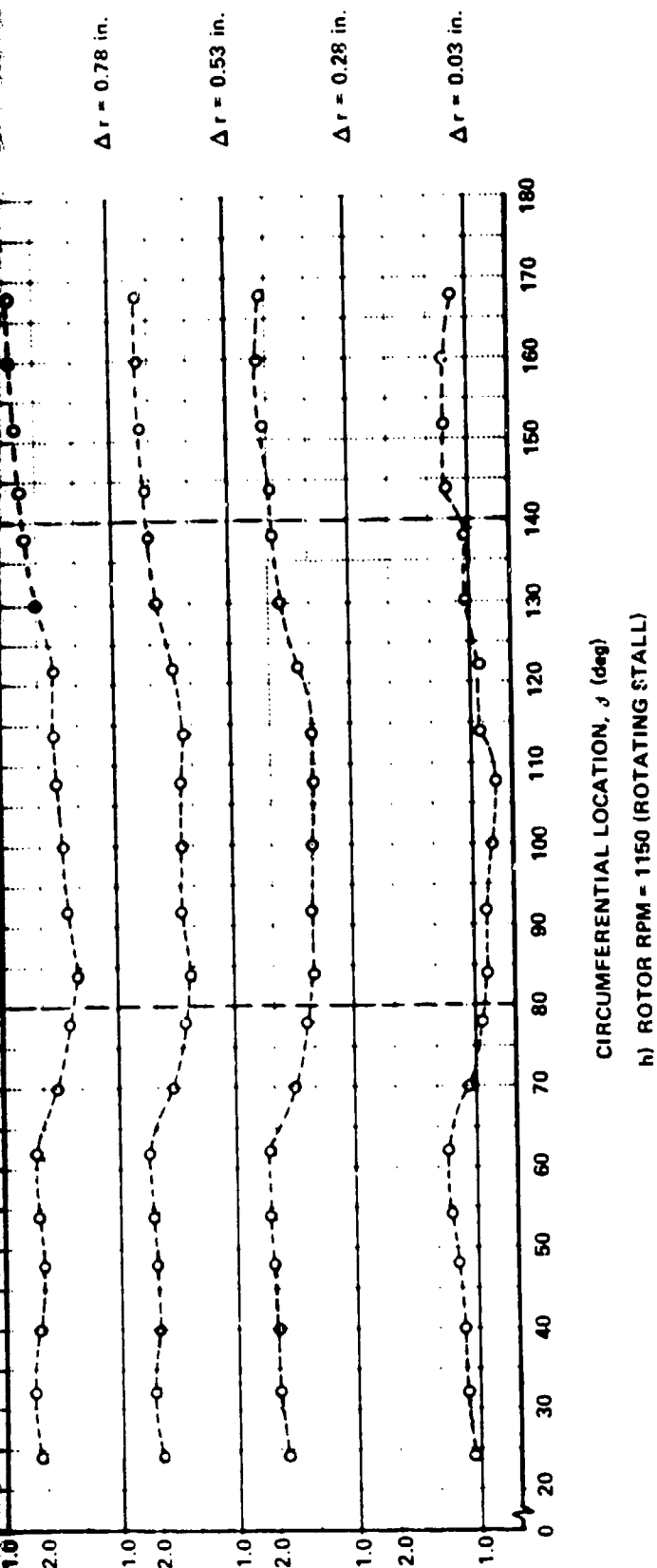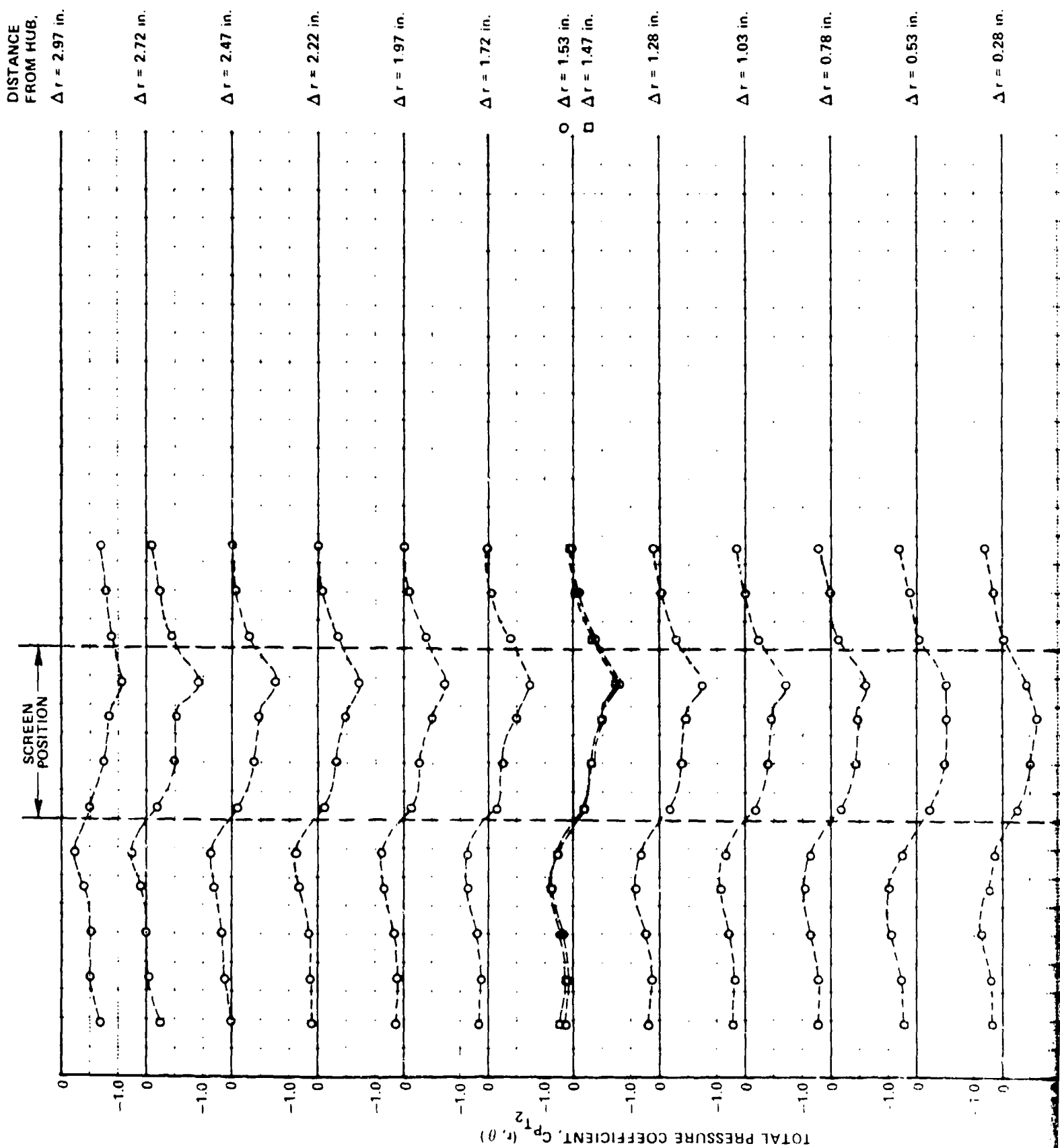DISTANCE FROM HUB,

Δr = 2.97 in.

Δr = 2.72 in.

Δr = 2.47 in.

Δr = 2.22 in.

Δr = 1.97 in.

Δr = 1.72 in.

○ Δr = 1.53 in.
□ Δr = 1.47 in.

Δr = 1.28 in.

Δr = 1.03 in.

Δr = 0.78 in.

Δr = 0.53 in.

Δr = 0.28 in.

SCREEN POSITION

TOTAL PRESSURE COEFFICIENT, Cp_{T_2} (r, θ)

2.0 1.0 2.0 1.0 2.0 1.0 2.0 1.0 2.0 1.0 2.0 1.0 2.0 1.0 2.0 1.0 2.0 1.0 2.0 1.0 2.0 1.0 2.0 1.0 2.0

$\Delta r = 0.78$ in.

$\Delta r = 0.53$ in.

$\Delta r = 0.28$ in.

$\Delta r = 0.03$ in.

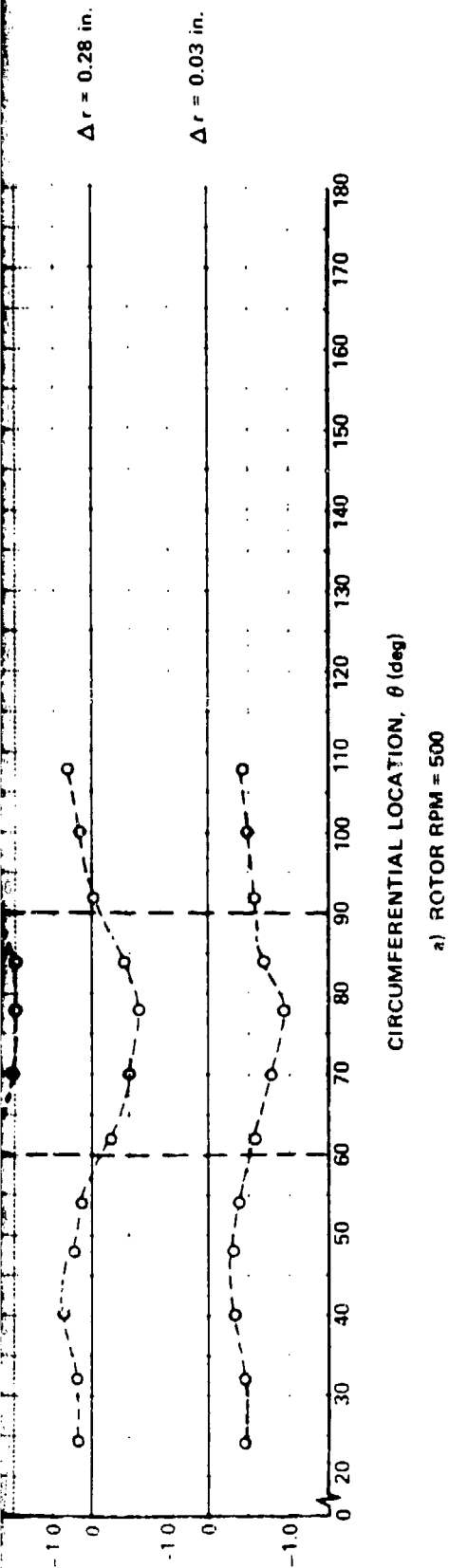CIRCUMFERENTIAL LOCATION, θ (deg)

d) ROTOR RPM = 900

Figure 17 (Cont.)

TOTAL PRESSURE COEFFICIENTS DOWNSTREAM
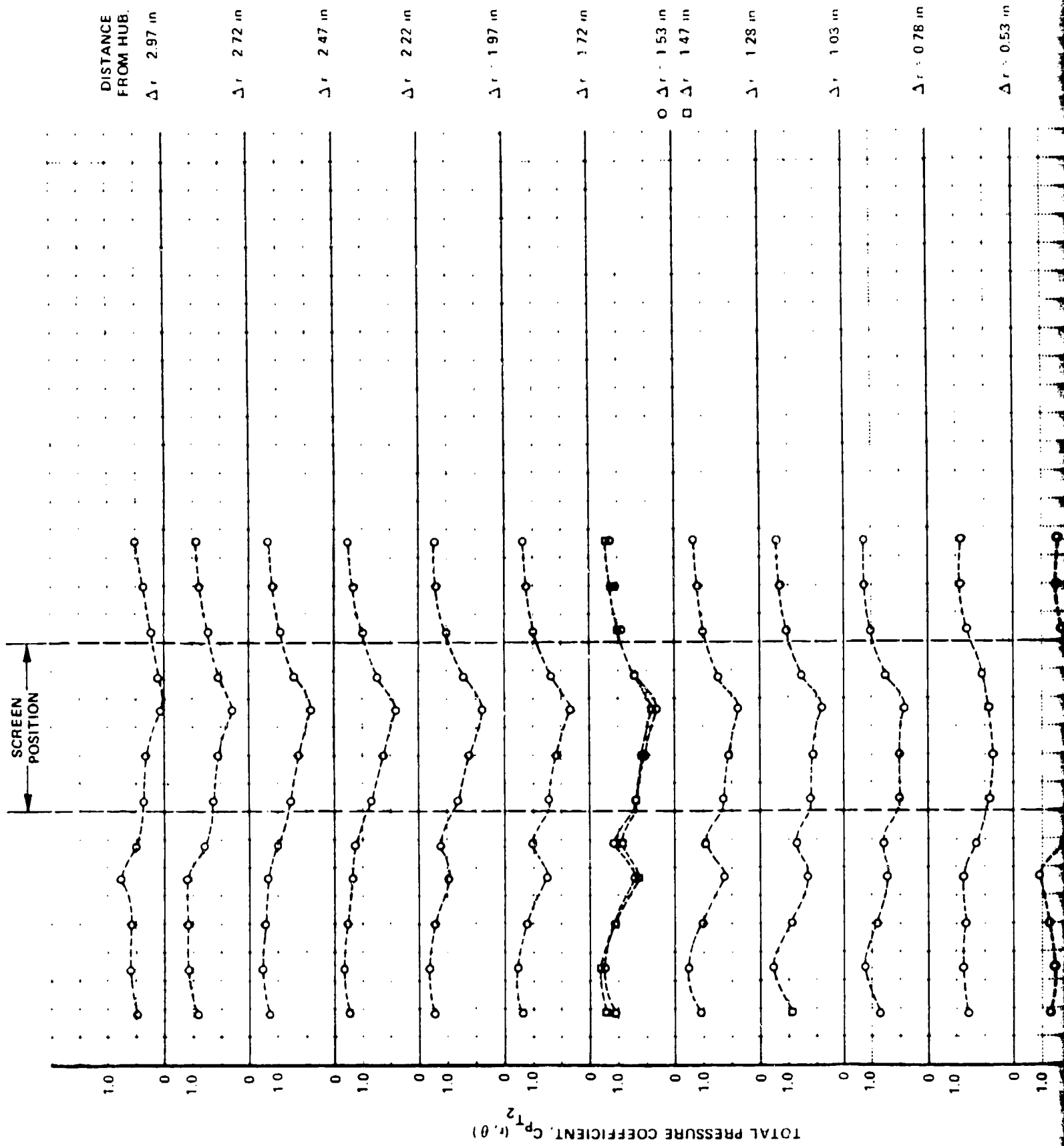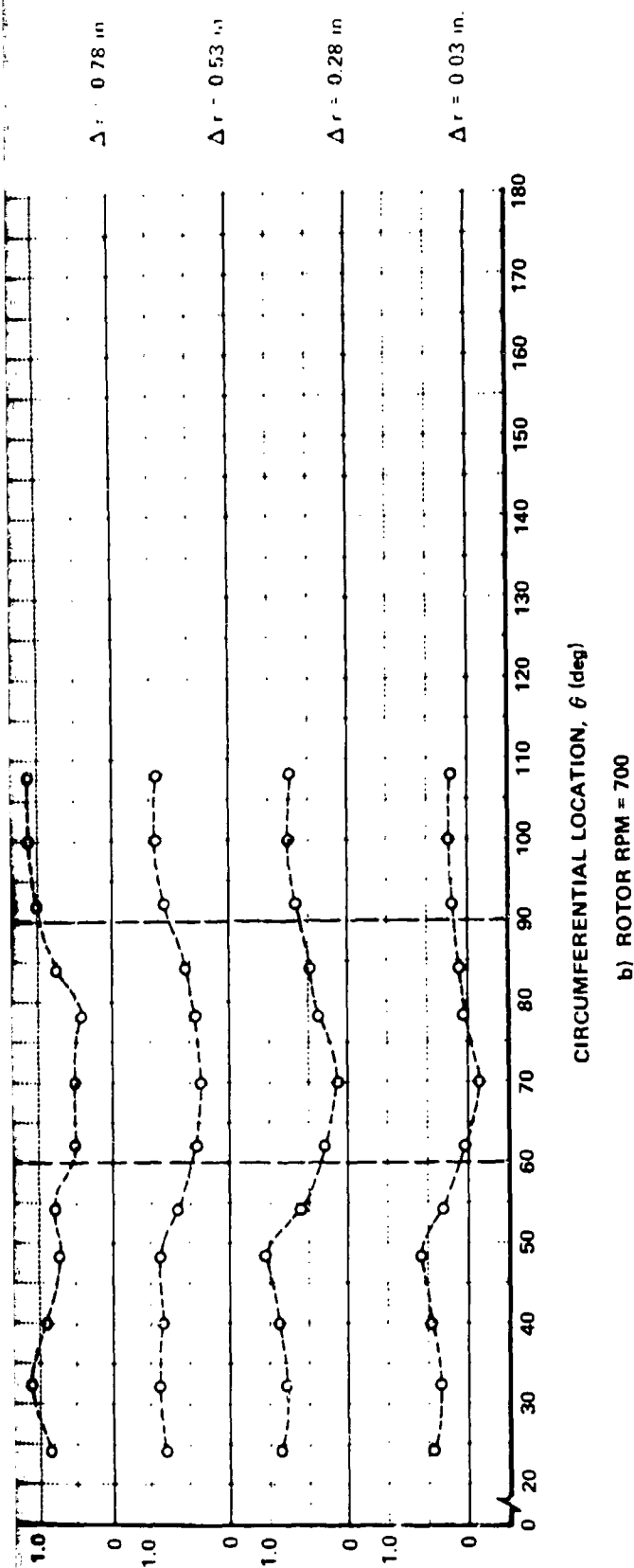OF ROTOR, DISTORTION SCREEN
CONFIGURATION A

113

DISTANCE
FROM HUB,

$\Delta r = 2.97$ in.

$\Delta r = 2.72$ in.

$\Delta r = 2.47$ in.

$\Delta r = 2.22$ in.

$\Delta r = 1.97$ in.

$\Delta r = 1.72$ in.

○ $\Delta r = 1.53$ in.
□ $\Delta r = 1.47$ in.

$\Delta r = 1.2b$ in.

$\Delta r = 1.03$ in.

$\Delta r = 0.78$ in.

$\Delta r = 0.53$ in.

$\Delta r = 0.28$ in.

SCREEN POSITION

2.0
1.0
2.0
1.0
2.0
1.0
2.0
1.0
2.0
1.0
2.0
1.0
2.0
1.0
2.0
1.0
2.0
1.0
2.0
1.0
2.0
1.0
2.0
1.0
2.0

TOTAL PRESSURE COEFFICIENT, $C_{P_{T_2}} (r, \theta)$

e) ROTOR RPM = 950

CIRCUMFERENTIAL LOCATION, θ (deg)

Figure 17 (Cont.)

TOTAL PRESSURE COEFFICIENTS DOWNSTREAM
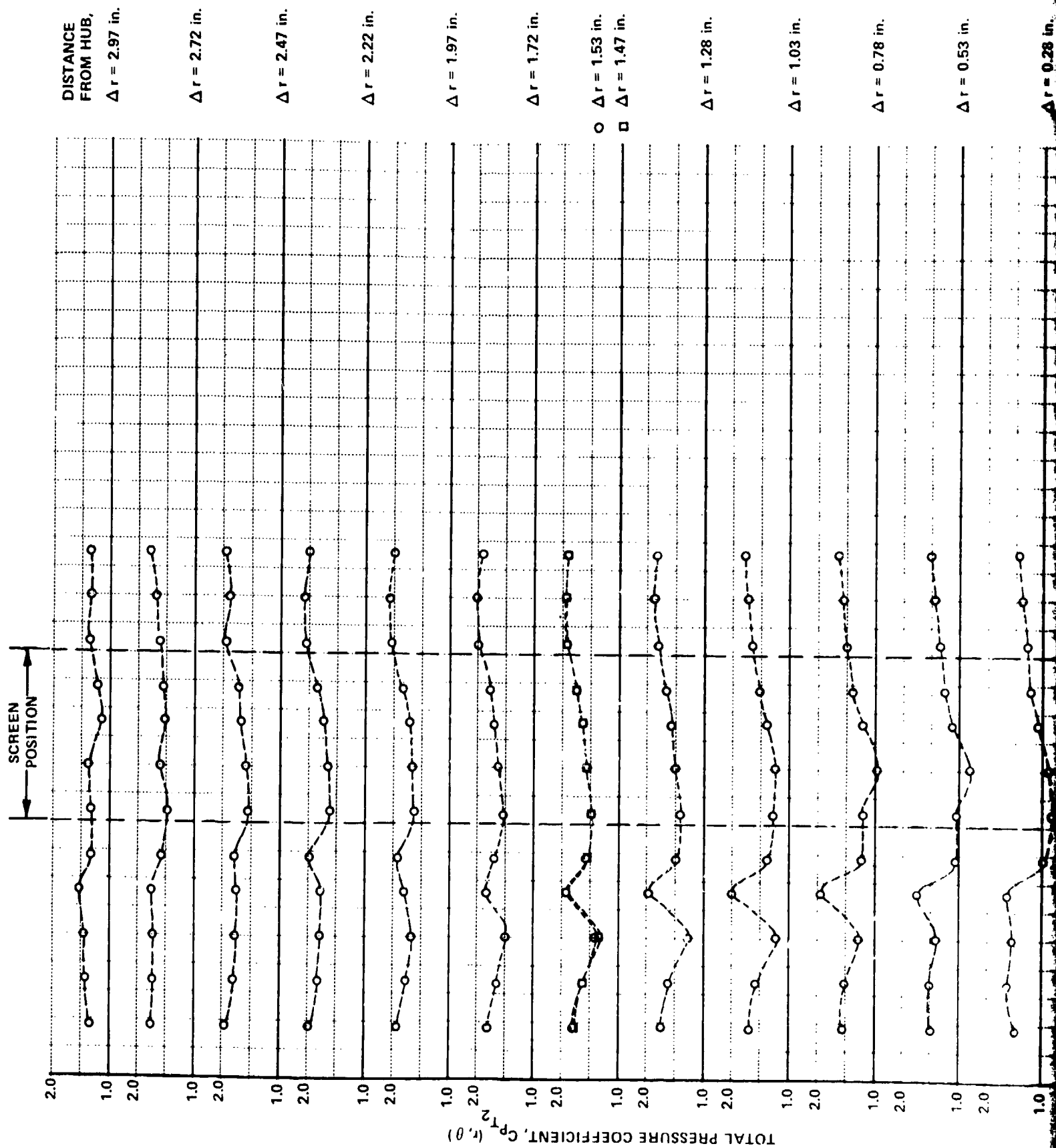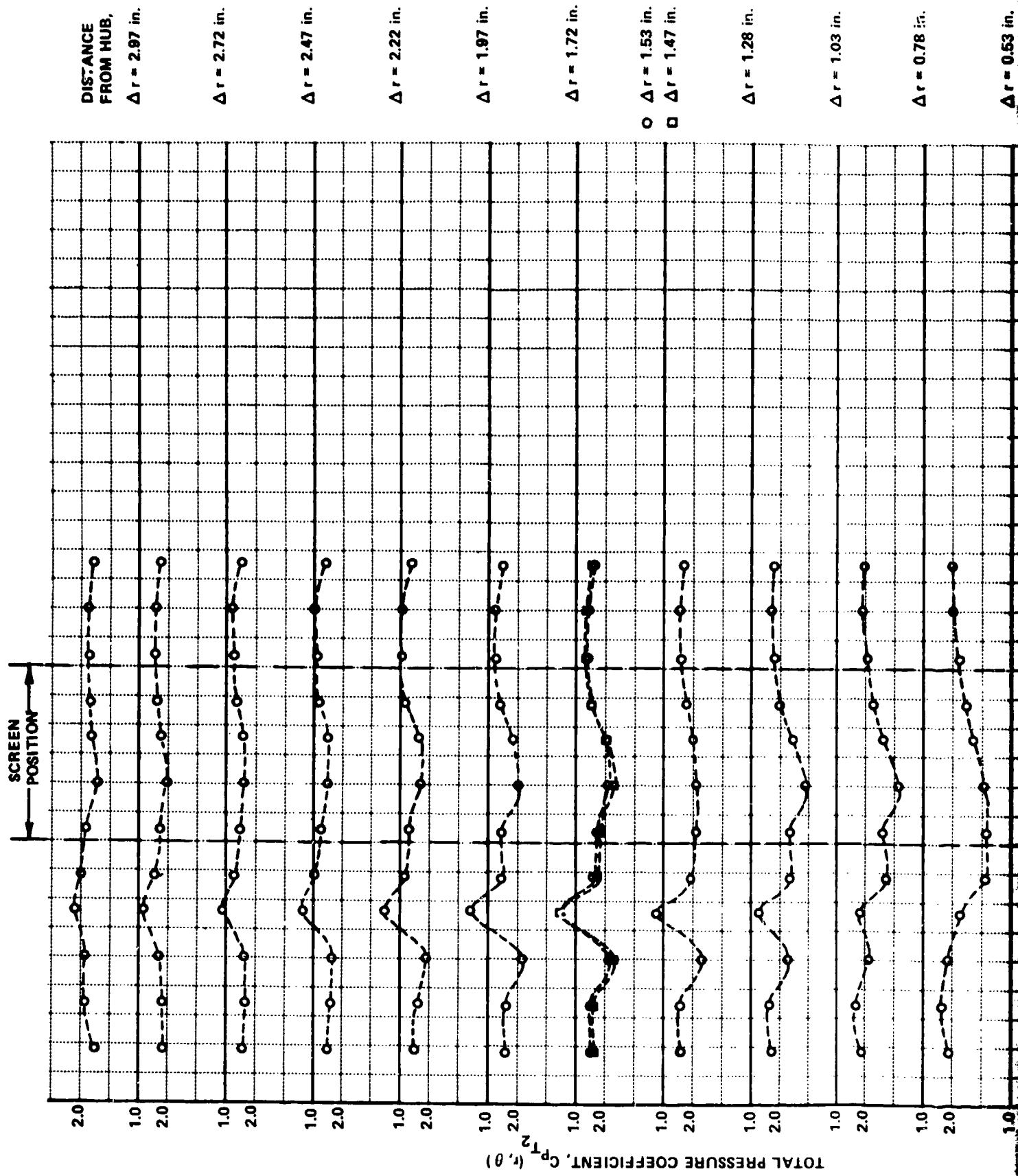OF ROTOR, DISTORTION SCREEN
CONFIGURATION A

114

DISTANCE
FROM HUB,

Δr = 2.97 in.

Δr = 2.72 in.

Δr = 2.47 in.

Δr = 2.22 in.

Δr = 1.97 in.

Δr = 1.72 in.

○ Δr = 1.53 in.
□ Δr = 1.47 in.

Δr = 1.28 in.

Δr = 1.03 in.

Δr = 0.78 in.

Δr = 0.53 in.

SCREEN POSITION

TOTAL PRESSURE COEFFICIENT, Cp_{T_2} (r, θ)

CIRCUMFERENTIAL LOCATION, θ (deg)

f) ROTOR RPM = 1000

Δr = 0.78 in.

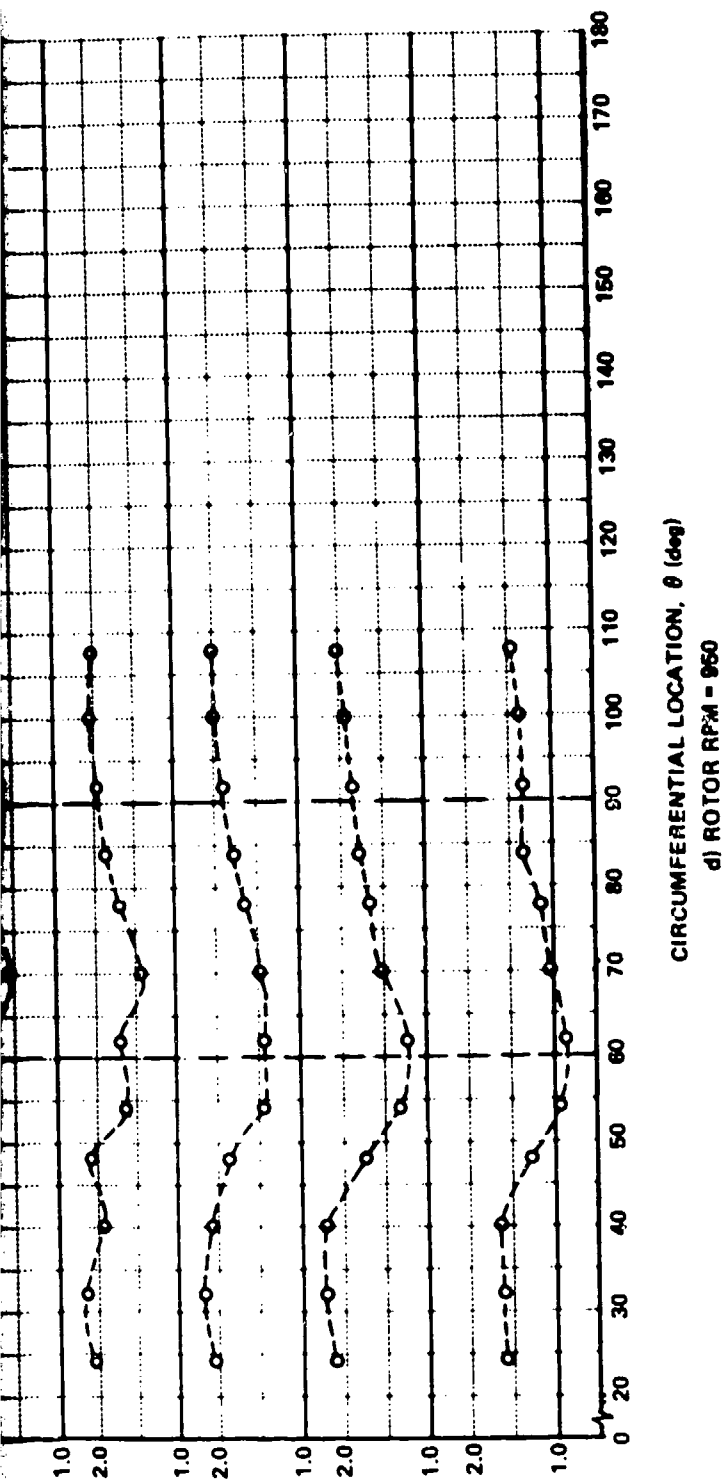Δr = 0.53 in.

Δr = 0.28 in.

Δr = 0.03 in.

Figure 17 (Cont.)

TOTAL PRESSURE COEFFICIENTS DOWNSTREAM
OF ROTOR, DISTORTION SCREEN
CONFIGURATION A

115

DISTANCE FROM HUB,

Δr = 2.97 in.

Δr = 2.72 in.

Δr = 2.47 in.

Δr = 2.22 in.

Δr = 1.97 in.

Δr = 1.72 in.

○ Δr = 1.53 in.
□ Δr = 1.47 in.

Δr = 1.28 in.

Δr = 1.03 in.

Δr = 0.78 in.

Δr = 0.53 in.

Δr = 0.28 in.

SCREEN POSITION

TOTAL PRESSURE COEFFICIENT, $C_{p_{T_2}}(r, \theta)$

CIRCUMFERENTIAL LOCATION, θ (deg)

g) ROTOR RPM = 1050 (ROTATING STALL)

$\Delta r = 0.53$ in.

$\Delta r = 0.28$ in.

$\Delta r = 0.03$ in.

Figure 17 (Cont.)

TOTAL PRESSURE COEFFICIENTS DOWNSTREAM
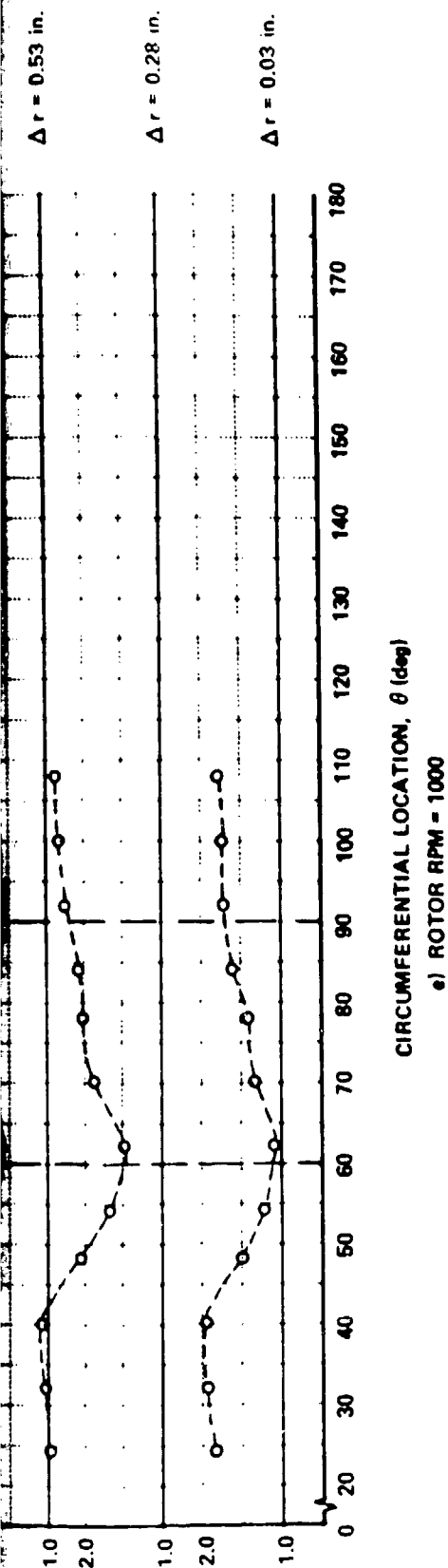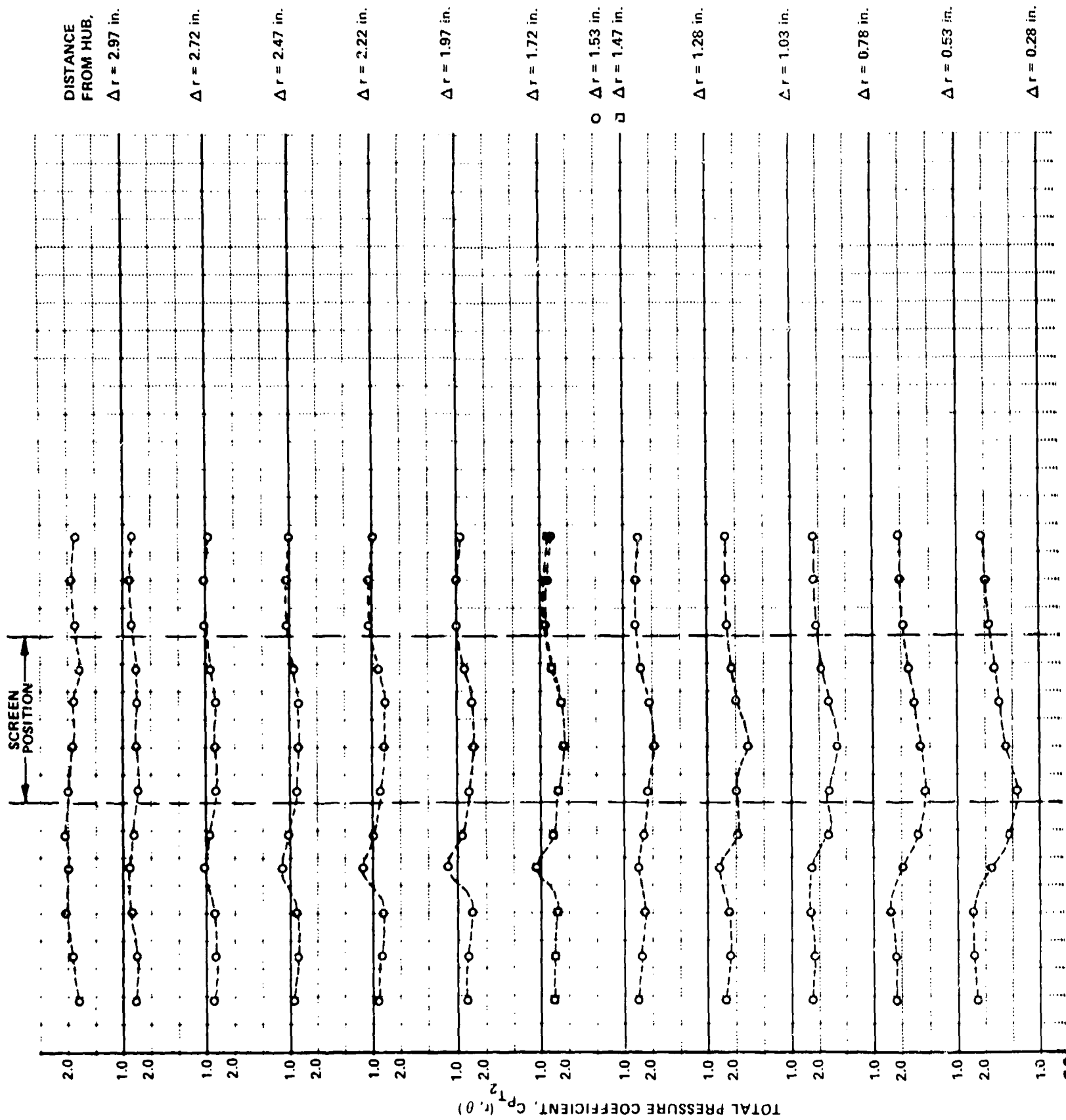OF ROTOR, DISTORTION SCREEN
CONFIGURATION A

116

DISTANCE
FROM HUB.

Δr = 2.97 in.

Δr = 2.72 in.

Δr = 2.47 in.

Δr = 2.22 in.

Δr = 1.97 in.

Δr = 1.72 in.

○ Δr = 1.53 in.
□ Δr = 1.47 in.

Δr = 1.28 in.

Δr = 1.03 in.

Δr = 0.78 in.

Δr = 0.53 in.

SCREEN POSITION

TOTAL PRESSURE COEFFICIENT $C_{P_{T_2}}(r, \theta)$

2.0 1.0 2.0 1.0 2.0 1.0 2.0 1.0 2.0 1.0 2.0 1.0 2.0 1.0 2.0 1.0 2.0 1.0 2.0 1.0 2.0 1.0 2.0

Figure 17 (Cont.)

TOTAL PRESSURE COEFFICIENTS DOWNSTREAM
OF ROTOR, DISTORTION SCREEN
CONFIGURATION A

117

DISTANCE FROM HUB.

$\Delta r = 2.97$ in.

$\Delta r = 2.72$ in.

$\Delta r = 2.47$ in.

$\Delta r = 2.22$ in.

$\Delta r = 1.97$ in.

$\Delta r = 1.72$ in.

O $\Delta r = 1.53$ in.
□ $\Delta r = 1.47$ in.

$\Delta r = 1.28$ in.

$\Delta r = 1.03$ in.

$\Delta r = 0.78$ in.

$\Delta r = 0.53$ in.

$\Delta r = 0.28$ in.

SCREEN POSITION

TOTAL PRESSURE COEFFICIENT, $C_{p_{T_2}}(r, \theta)$

CIRCUMFERENTIAL LOCATION, θ (deg)

a) ROTOR RPM = 500

$\Delta r = 0.28$ in.

$\Delta r = 0.03$ in.

Figure 18

TOTAL PRESSURE COEFFICIENTS DOWNSTREAM
OF ROTOR, DISTORTION SCREEN
CONFIGURATION B

TOTAL PRESSURE COEFFICIENT, $C_{p_{T_2}}(r, \theta)$

$\Delta r = 0.78$ in

$\Delta r = 0.53$ in

$\Delta r = 0.28$ in

$\Delta r = 0.03$ in

CIRCUMFERENTIAL LOCATION, θ (deg)

b) ROTOR RPM = 700

Figure 18 (Cont.)

TOTAL PRESSURE COEFFICIENTS DOWNSTREAM
OF ROTOR, DISTORTION SCREEN
CONFIGURATION B

119

CIRCUMFERENTIAL LOCATION, θ (deg)

c) ROTOR RPM = 850
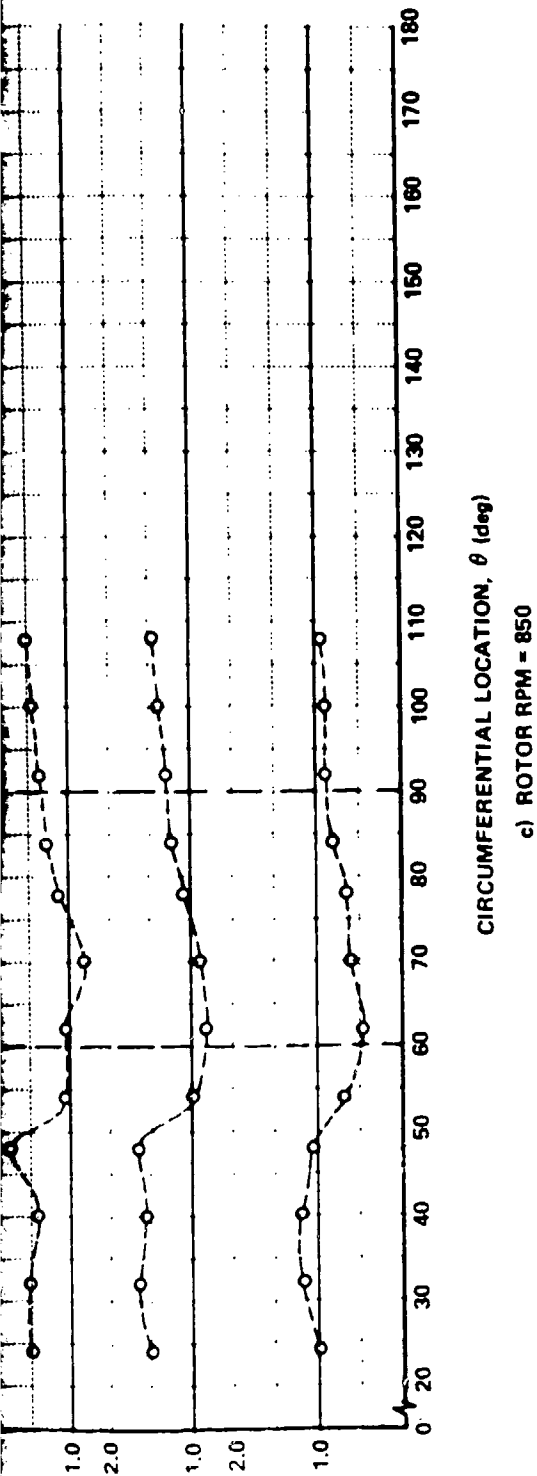
Δr = 0.53 in.

Δr = 0.28 in.

Δr = 0.03 in.

Figure 18 (Cont.)

TOTAL PRESSURE COEFFICIENTS DOWNSTREAM
OF ROTOR, DISTORTION SCREEN
CONFIGURATION B

TOTAL PRESSURE COEFFICIENT, $C_{P_{T_2}}(r, \theta)$

DISTANCE FROM HUB,

Δr = 2.97 in.

Δr = 2.72 in.

Δr = 2.47 in.

Δr = 2.22 in.

Δr = 1.97 in.

Δr = 1.72 in.

○ Δr = 1.53 in.
□ Δr = 1.47 in.

Δr = 1.28 in.

Δr = 1.03 in.

Δr = 0.78 in.

Δr = 0.53 in.

SCREEN POSITION

CIRCUMFERENTIAL LOCATION, θ (deg)
d) ROTOR RPM = 950

Figure 18 (Cont.)

TOTAL PRESSURE COEFFICIENT
DOWNSTREAM OF ROTOR, DIS-
TORTION SCREEN CONFIGURATION B
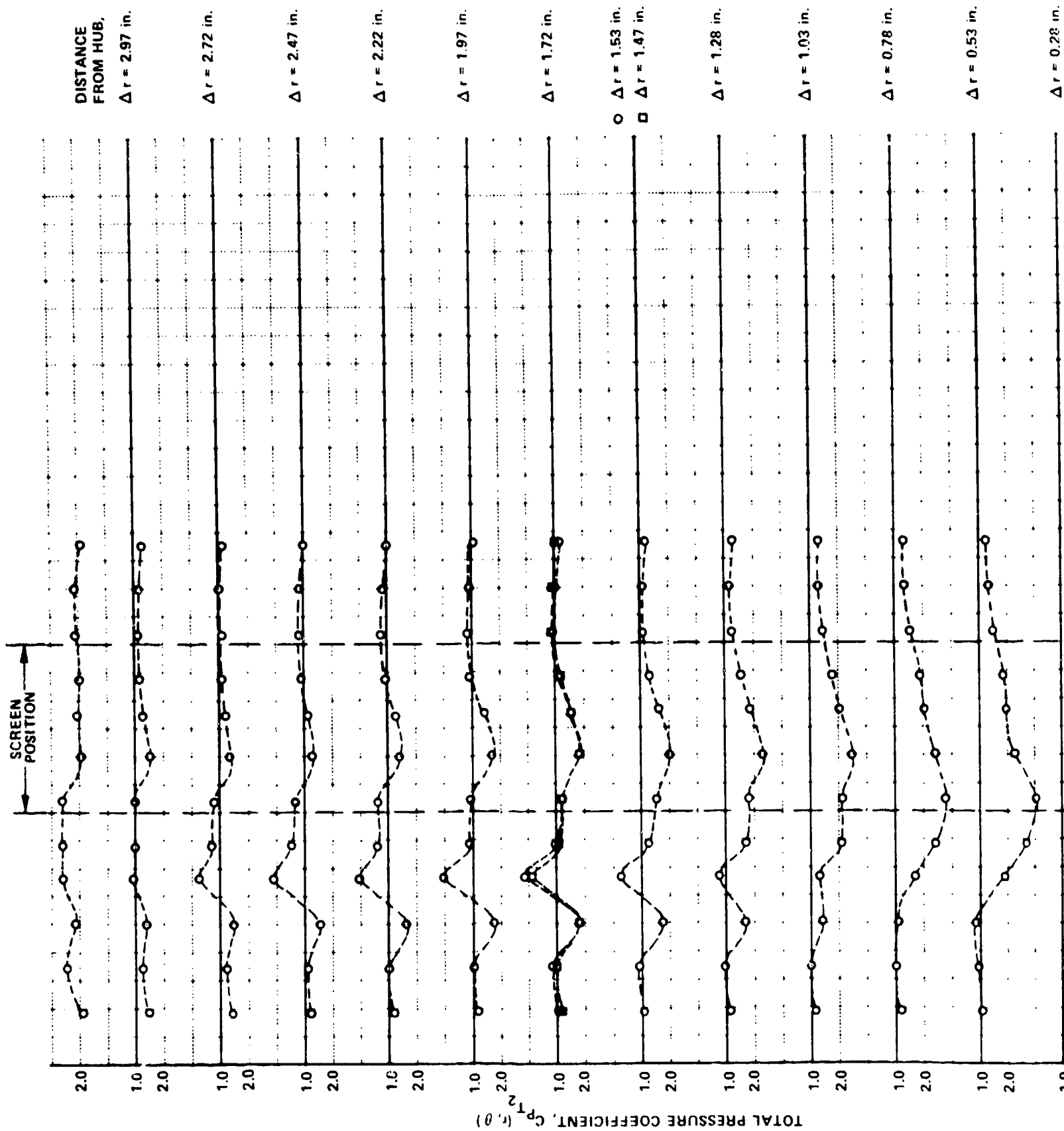
DISTANCE FROM HUB.

Δr = 2.97 in.
Δr = 2.72 in.
Δr = 2.47 in.
Δr = 2.22 in.
Δr = 1.97 in.
Δr = 1.72 in.
○ Δr = 1.53 in.
□ Δr = 1.47 in.
Δr = 1.28 in.
Δr = 1.03 in.
Δr = 0.78 in.
Δr = 0.53 in.
Δr = 0.28 in.

SCREEN POSITION

TOTAL PRESSURE COEFFICIENT, $C_{P_{T_2}}(r, \theta)$

Figure 18 (Cont.)
TOTAL PRESSURE COEFFICIENTS DOWNSTREAM
OF ROTOR, DISTORTION SCREEN
CONFIGURATION B

122

DISTANCE
FROM HUB.

$\Delta r = 2.97$ in.

$\Delta r = 2.72$ in.

$\Delta r = 2.47$ in.

$\Delta r = 2.22$ in.

$\Delta r = 1.97$ in.

$\Delta r = 1.72$ in.

$\circ$ $\Delta r = 1.53$ in.
$\square$ $\Delta r = 1.47$ in.

$\Delta r = 1.28$ in.

$\Delta r = 1.03$ in.

$\Delta r = 0.78$ in.

$\Delta r = 0.53$ in.

$\Delta r = 0.28$ in.
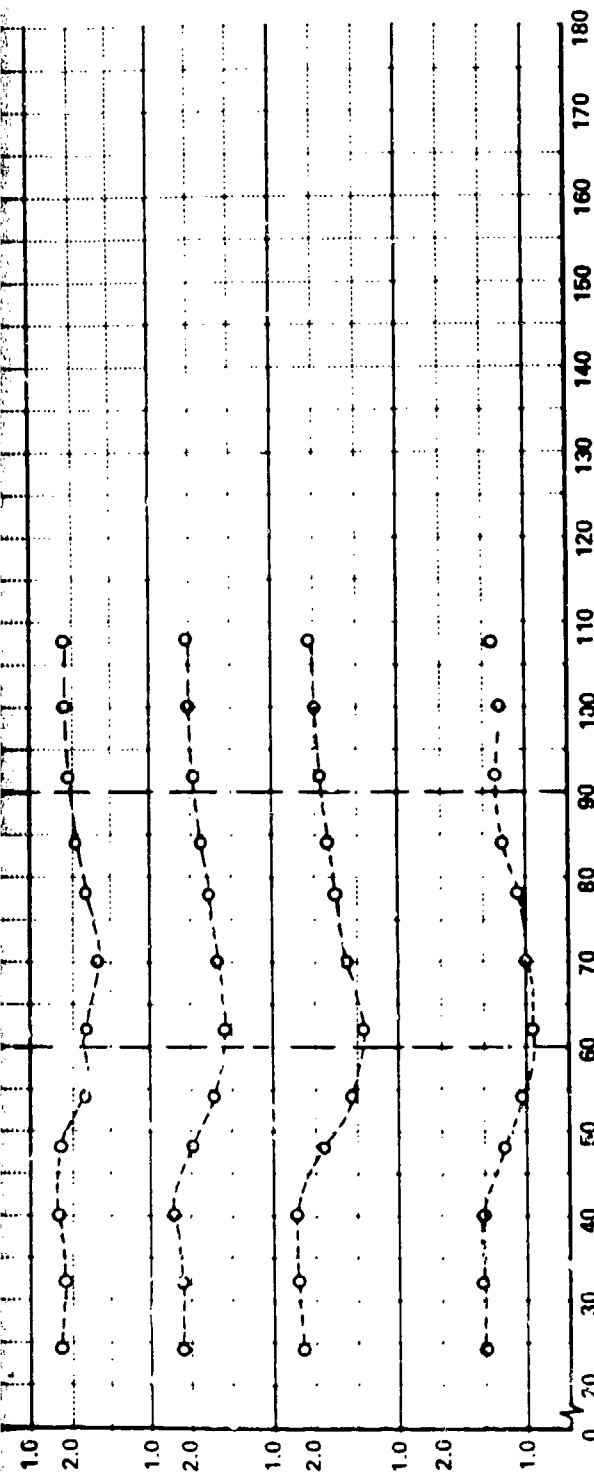
SCREEN
POSITION

TOTAL PRESSURE COEFFICIENT, $c_{p_{T_2}}(r, \theta)$

Figure 18 (Cont.)

TOTAL PRESSURE COEFFICIENTS DOWNSTREAM
OF ROTOR, DISTORTION SCREEN
CONFIGURATION 8
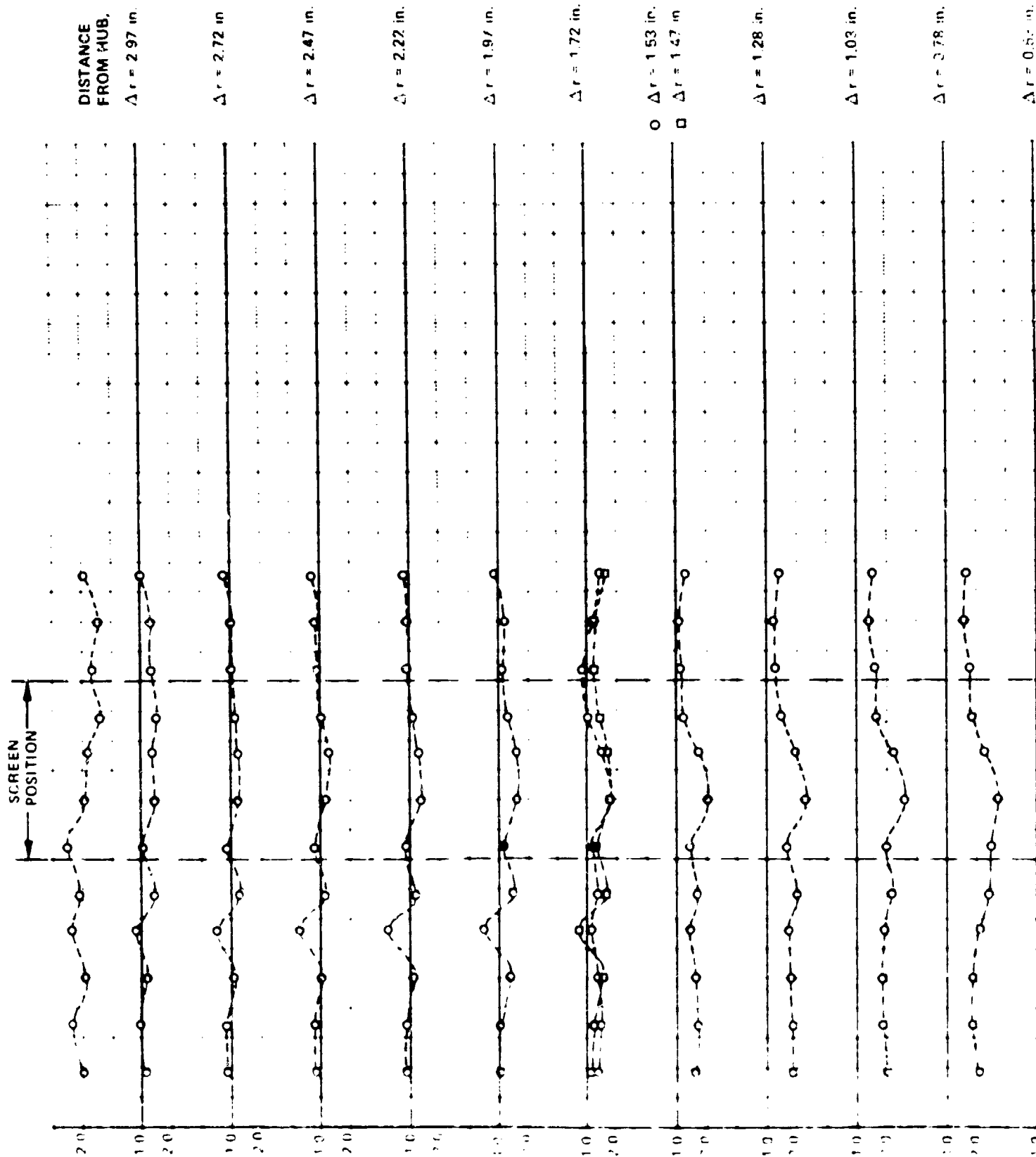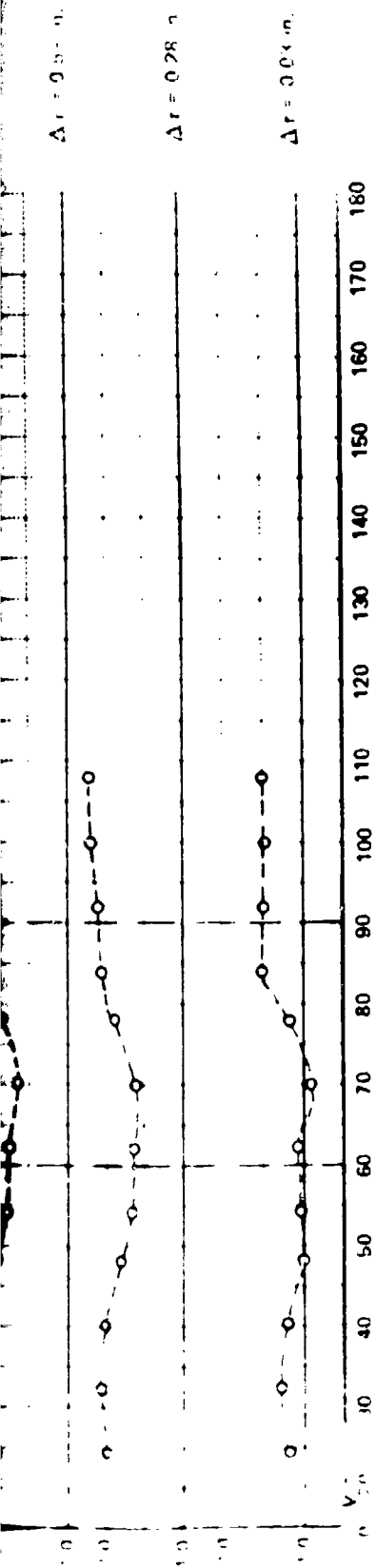
CIRCUMFERENTIAL LOCATION, θ (deg)

a) ROTOR RPM = 1100 (ROTATING STALL)

Figure 18 (Cont.)

TOTAL PRESSURE COEFFICIENTS DOWNSTREAM
OF ROTOR DISTORTION SCREEN
CONFIGURATION B

DISTANCE FROM HUB,

Δr = 2.97 in.

Δr = 2.72 in.

Δr = 2.47 in.

Δr = 2.22 in.

Δr = 1.97 in.

Δr = 1.72 in.

○ Δr = 1.53 in.
□ Δr = 1.47 in.

Δr = 1.28 in.

Δr = 1.03 in.

Δr = 0.78 in.

Δr = 0.53 in.

SCREEN POSITION
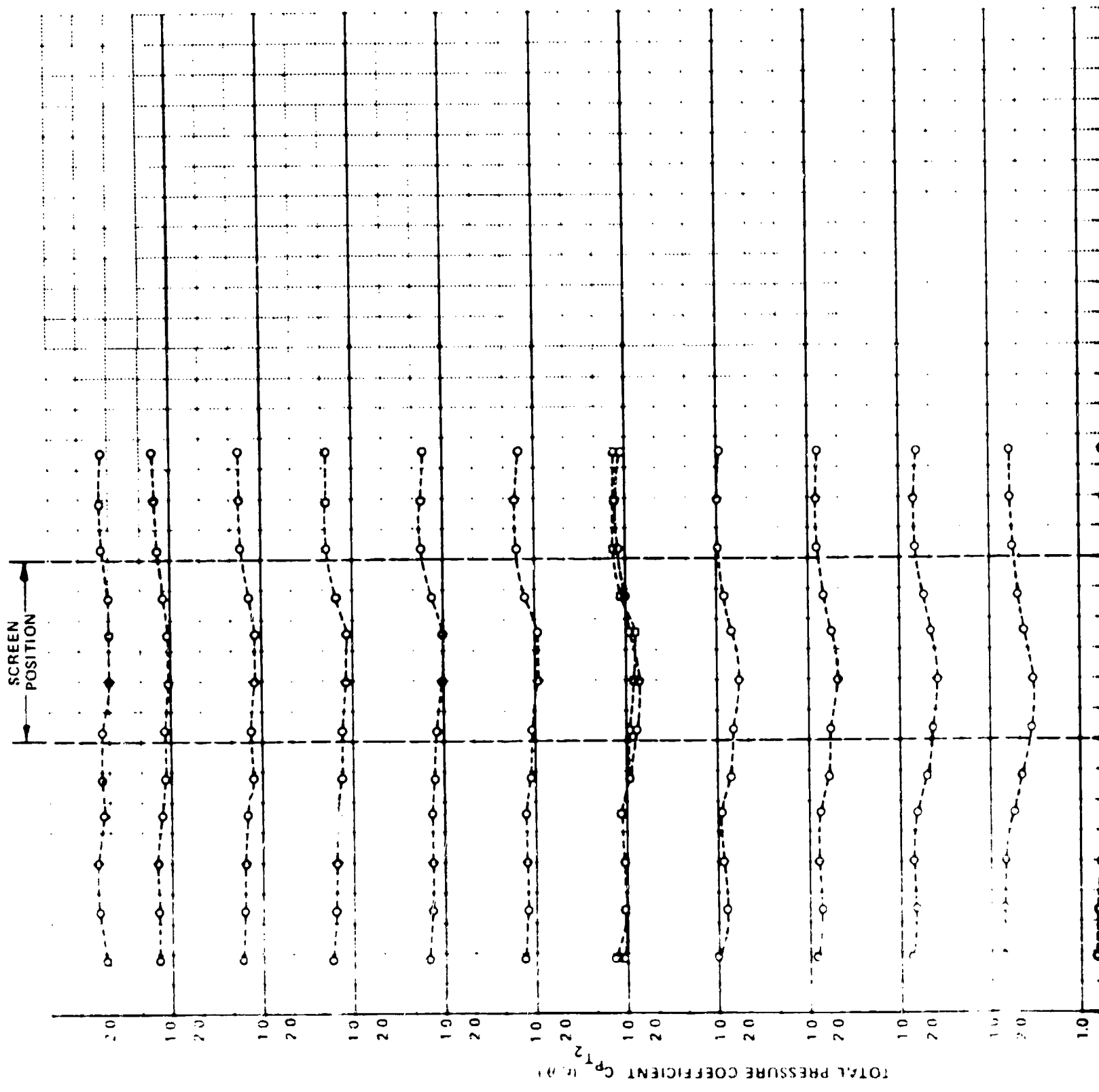
TOTAL PRESSURE COEFFICIENT $C_{P_{T_2}}$ (r, θ)
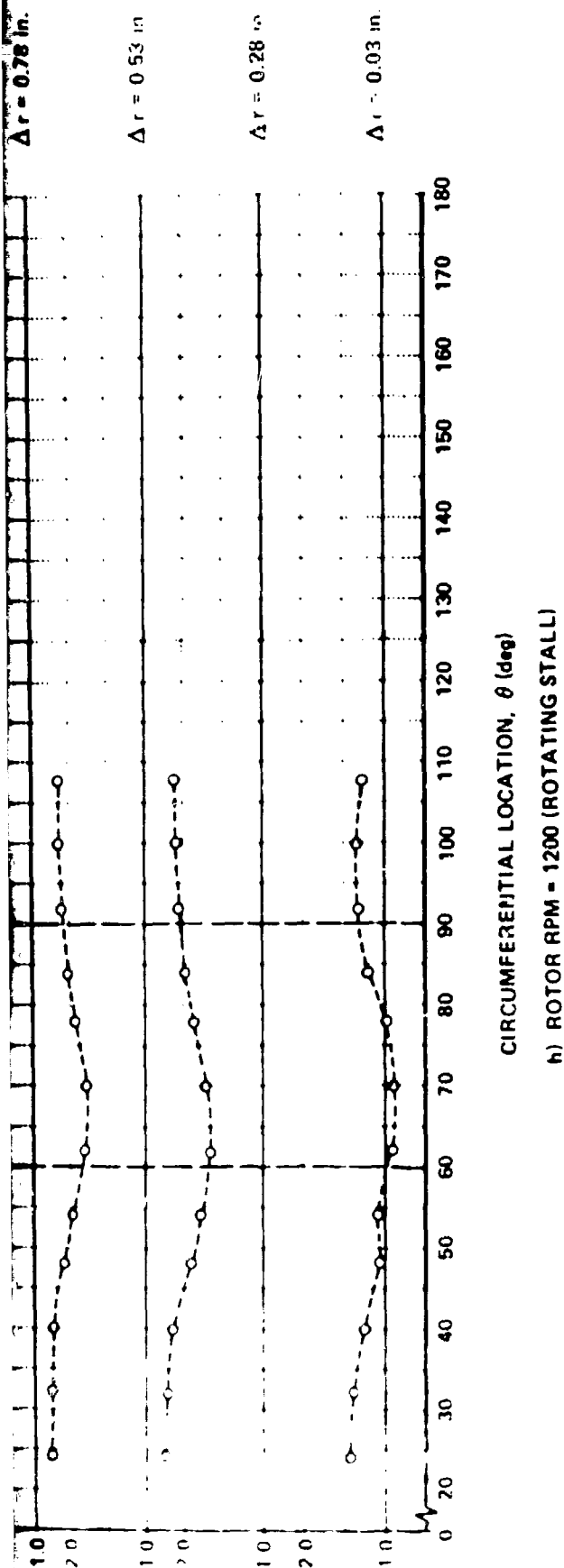
CIRCUMFERENTIAL LOCATION, θ (deg)

h) ROTOR RPM = 1200 (ROTATING STALL)

Figure 18 (Cont.)

TOTAL PRESSURE COEFFICIENTS DOWNSTREAM
OF ROTOR DISTORTION SCREEN
CONFIGURATION B
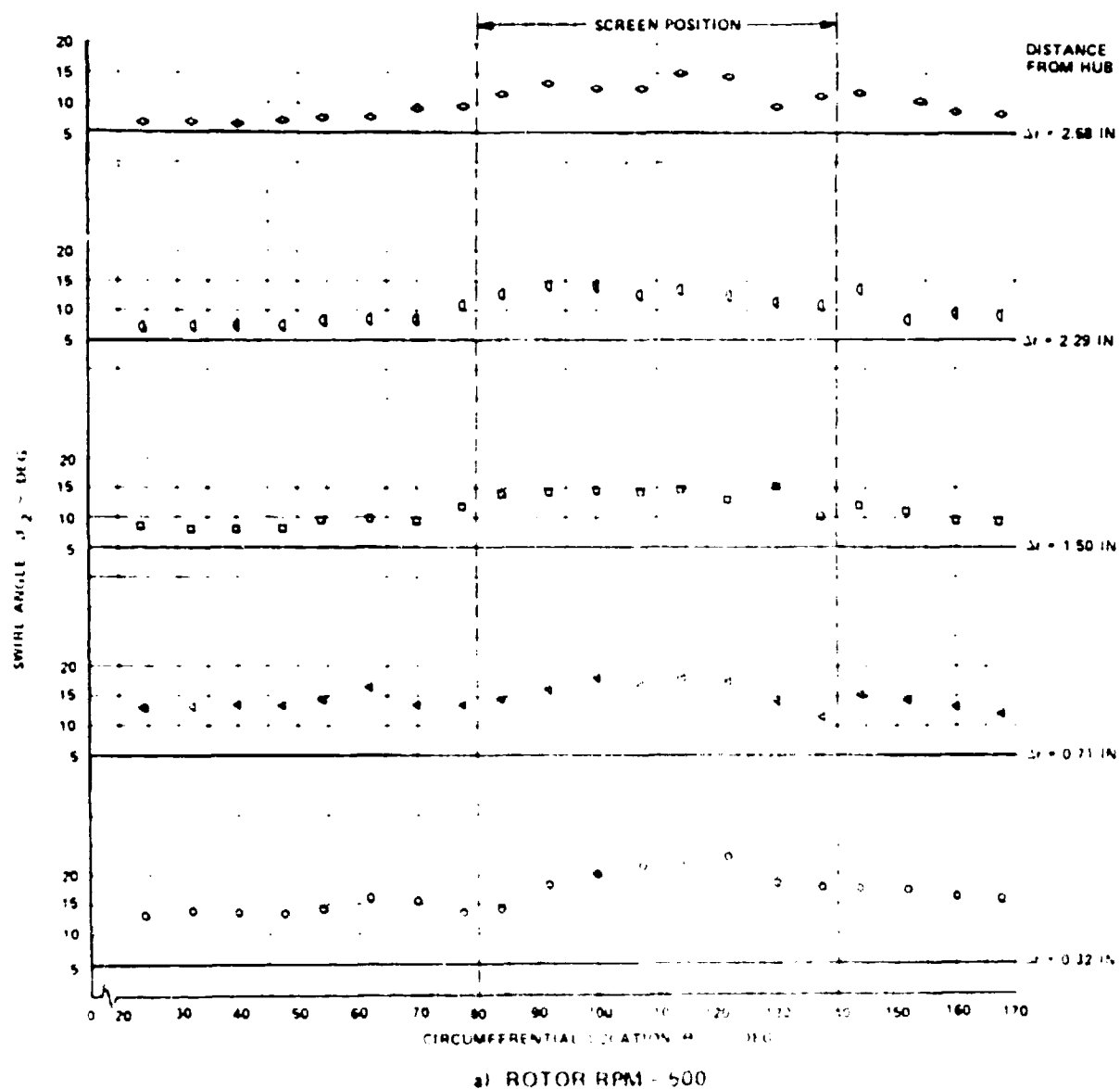
Figure 19   CIRCUMFERENTIAL DISTRIBUTION OF SWIRL ANGLE β_2, DOWNSTREAM OF ROTOR SCREEN CONFIGURATION A
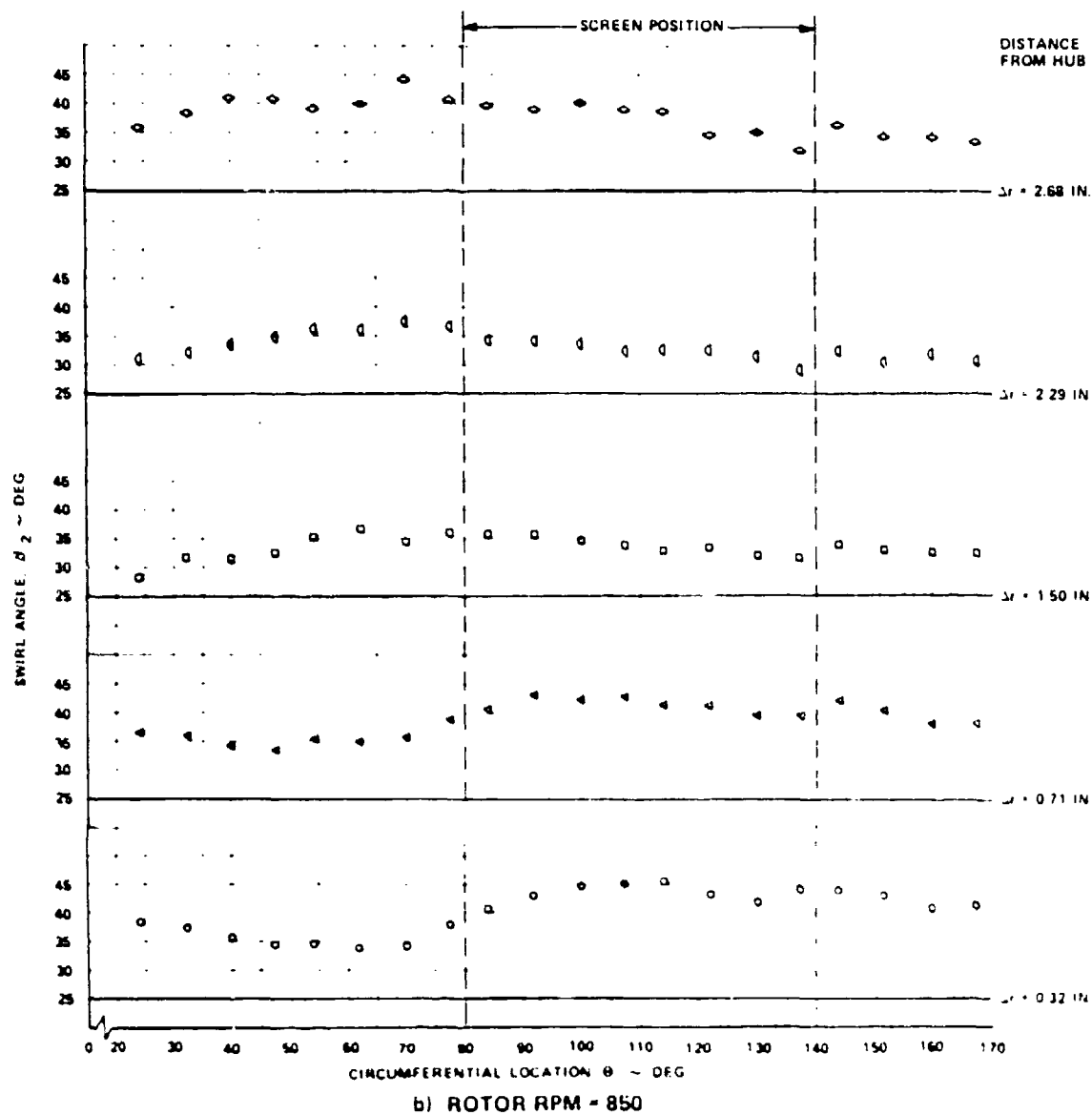
Figure 19 (Cont.)   CIRCUMFERENTIAL DISTRIBUTION OF SWIRL ANGLE, β_2, DOWNSTREAM OF ROTOR SCREEN CONFIGURATION A
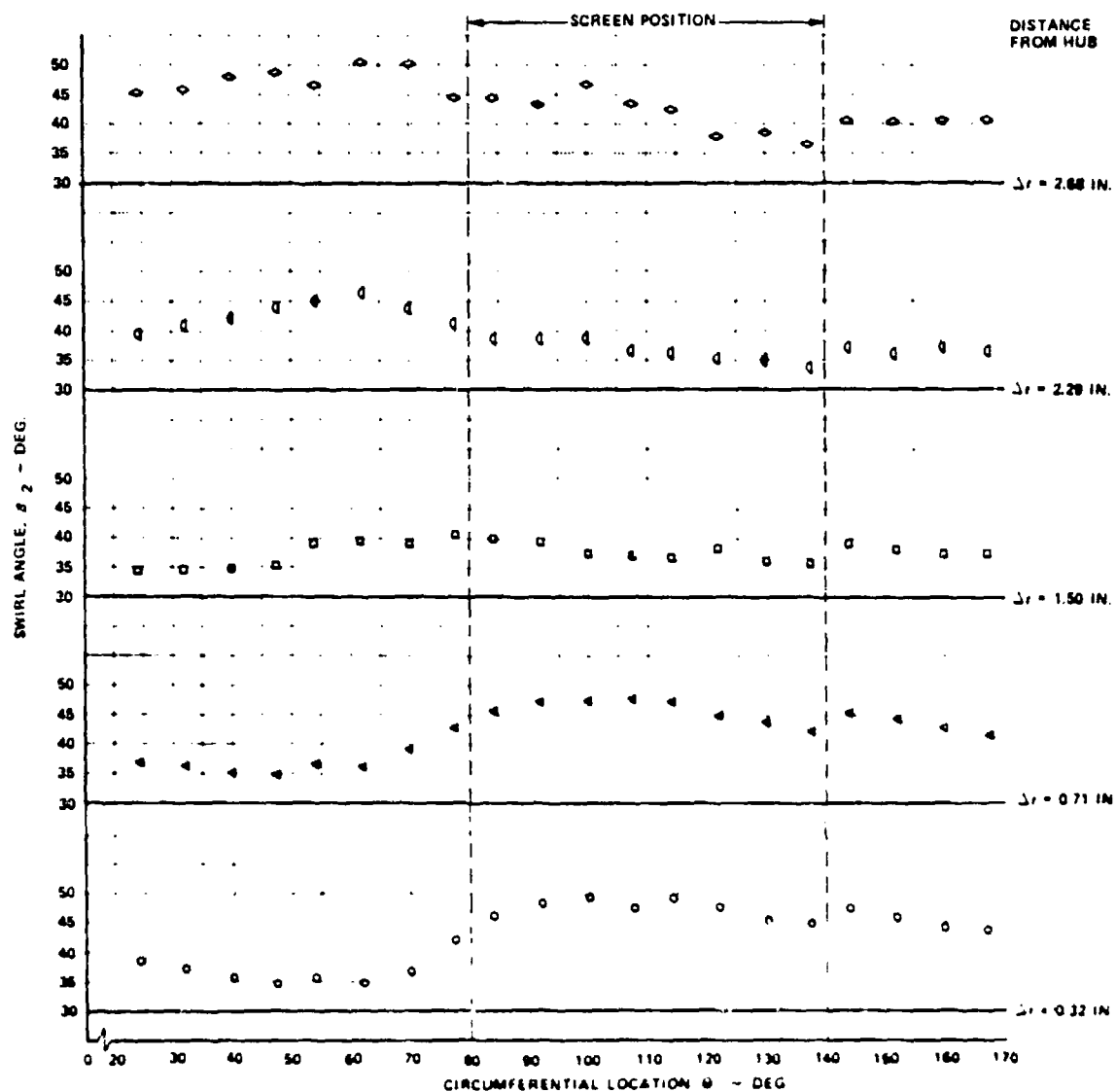
Figure 19 (Cont.) CIRCUMFERENTIAL DISTRIBUTION OF SWIRL ANGLE, β_2, DOWNSTREAM OF ROTOR, SCREEN CONFIGURATION A
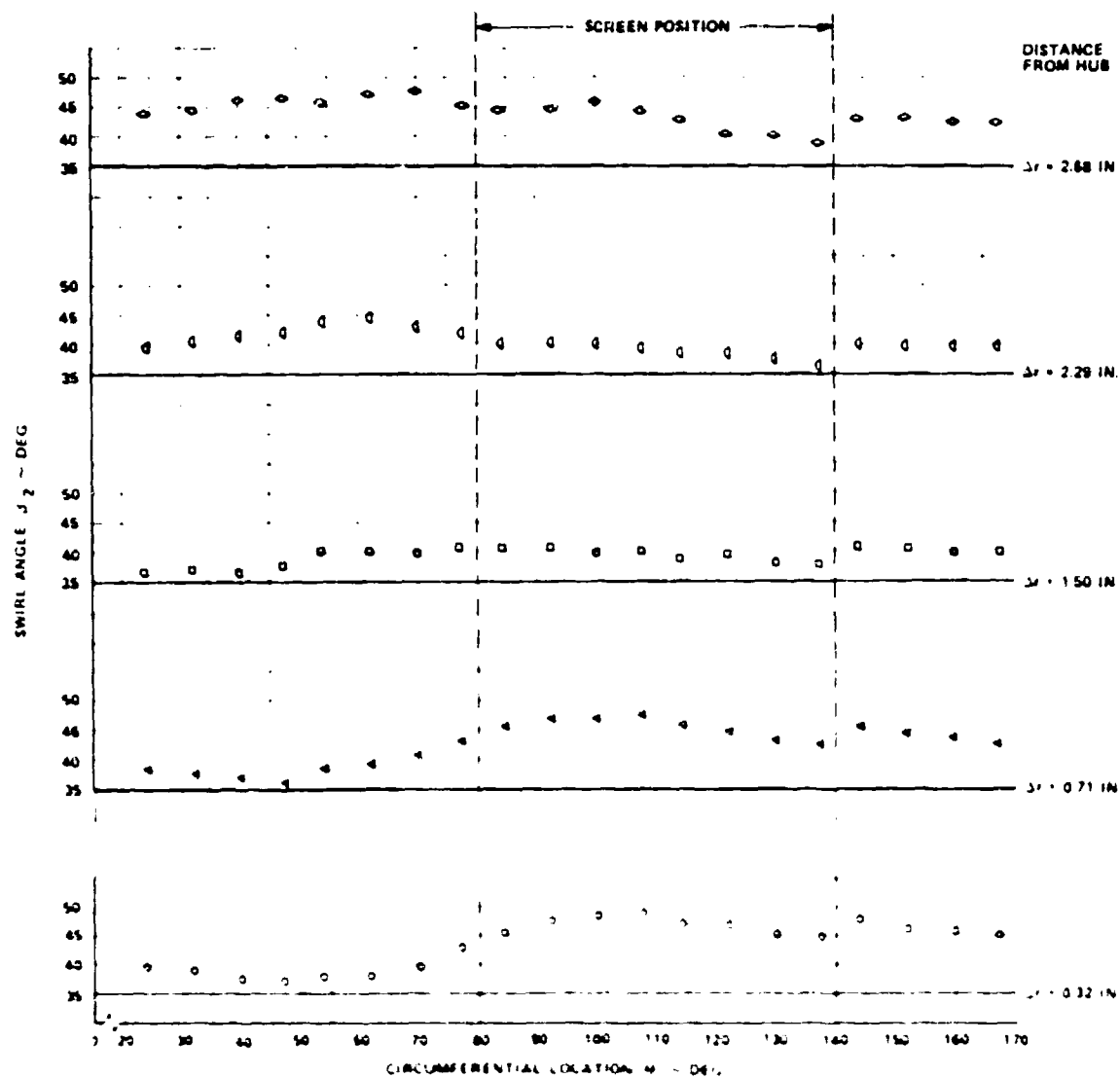
d) ROTOR RPM = 1050 (ROTATING STALL)

Figure 19 (Cont.) CIRCUMFERENTIAL DISTRIBUTION OF SWIRL ANGLE, β_2, DOWNSTREAM OF ROTOR SCREEN CONFIGURATION A
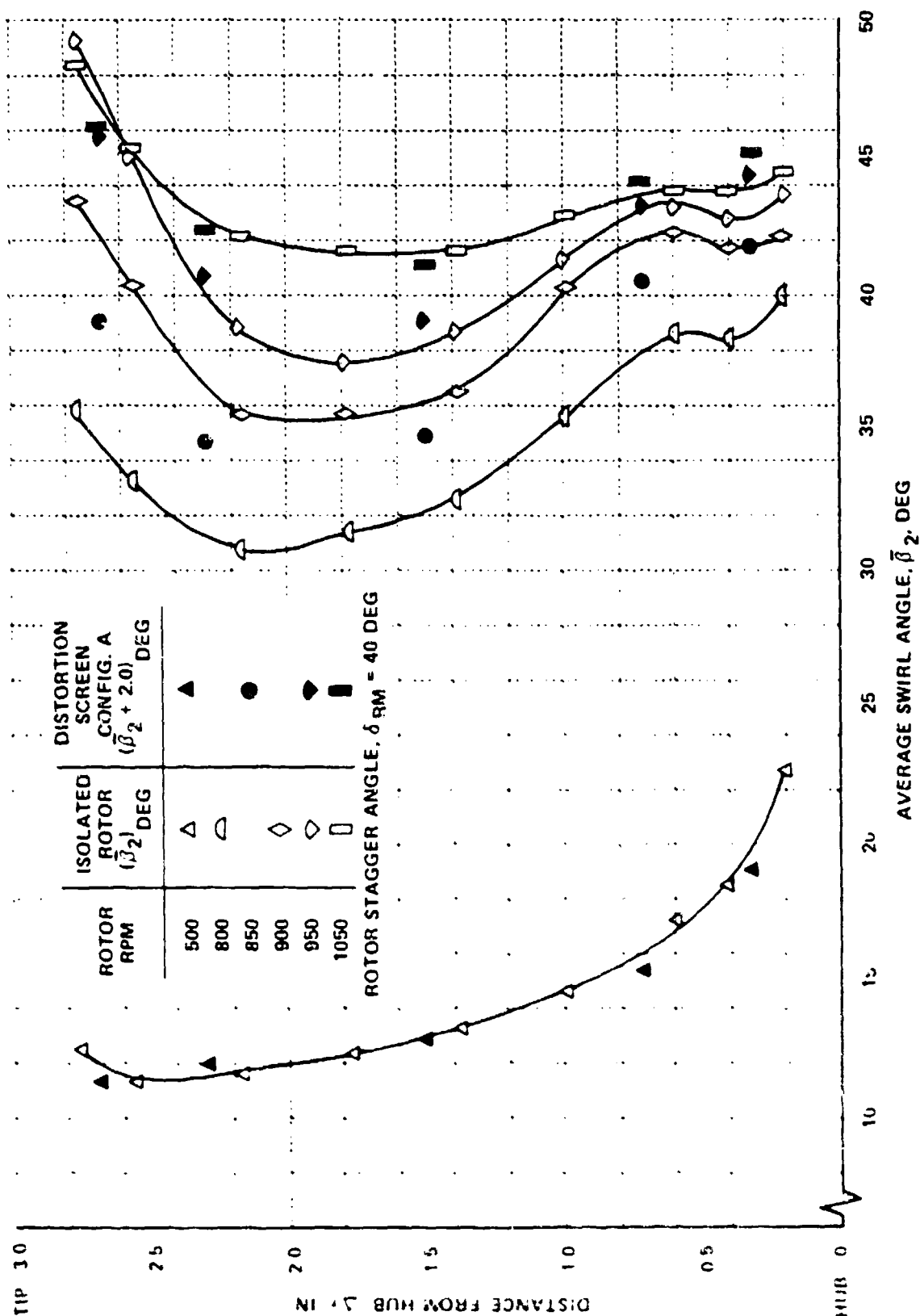
Figure 20   EFFECT OF DISTORTION SCREEN CONFIGURATION A ON AVERAGE SWIRL ANGLES DOWNSTREAM OF ROTOR SET NO. 1, ABSOLUTE COORDINATE SYSTEM
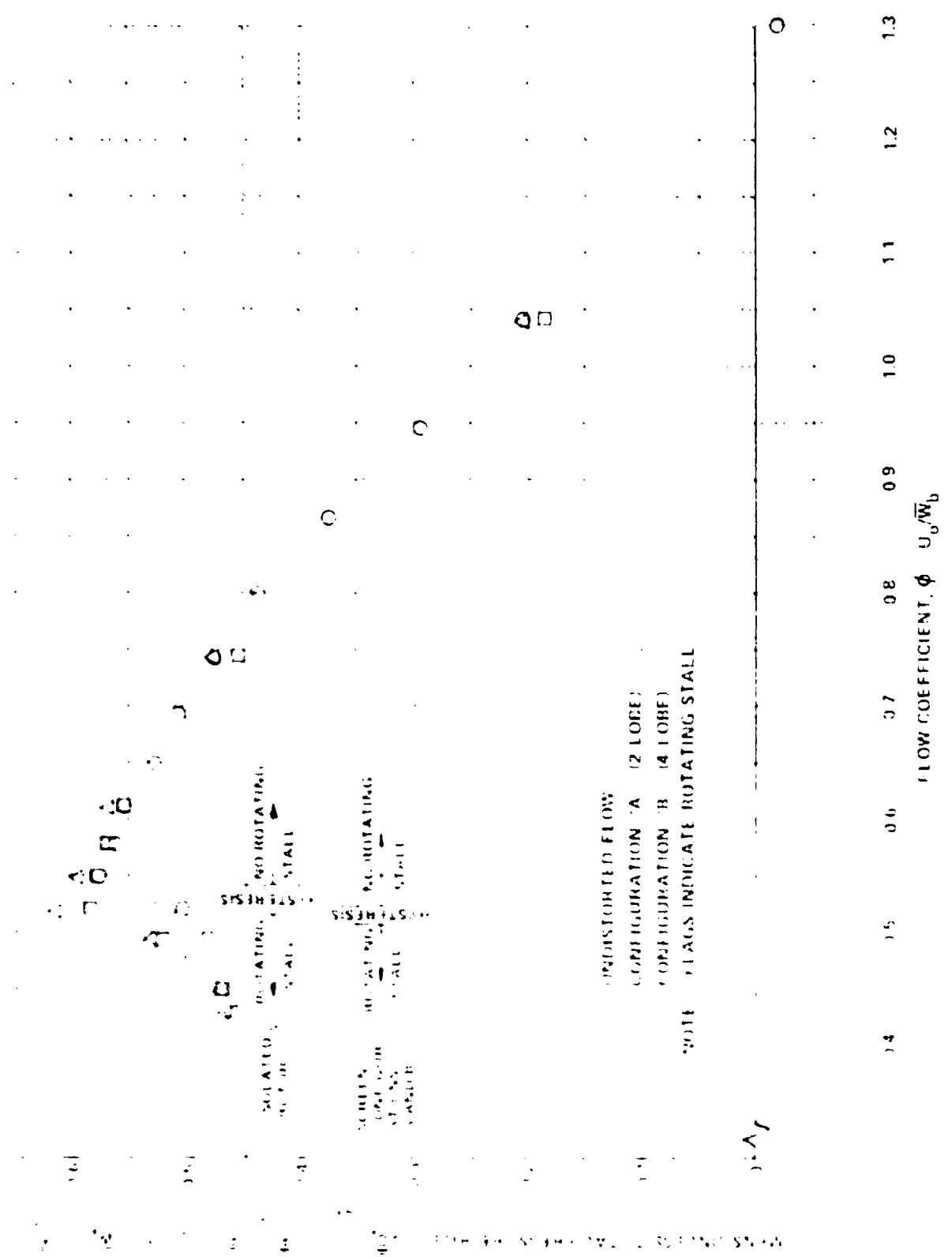
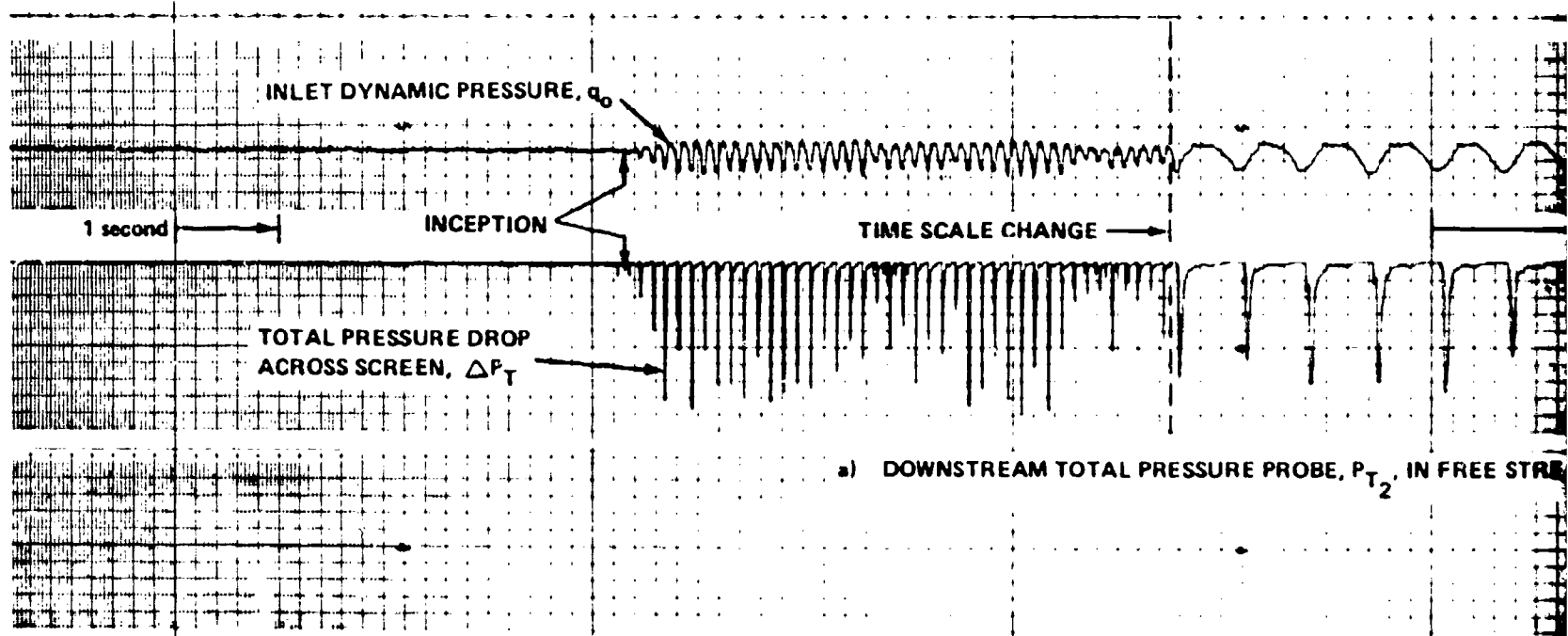Figure 21. EFFECT OF DISTORTION SCREENS ON TOTAL PRESSURE RISE OF ROTOR SET NO. 1
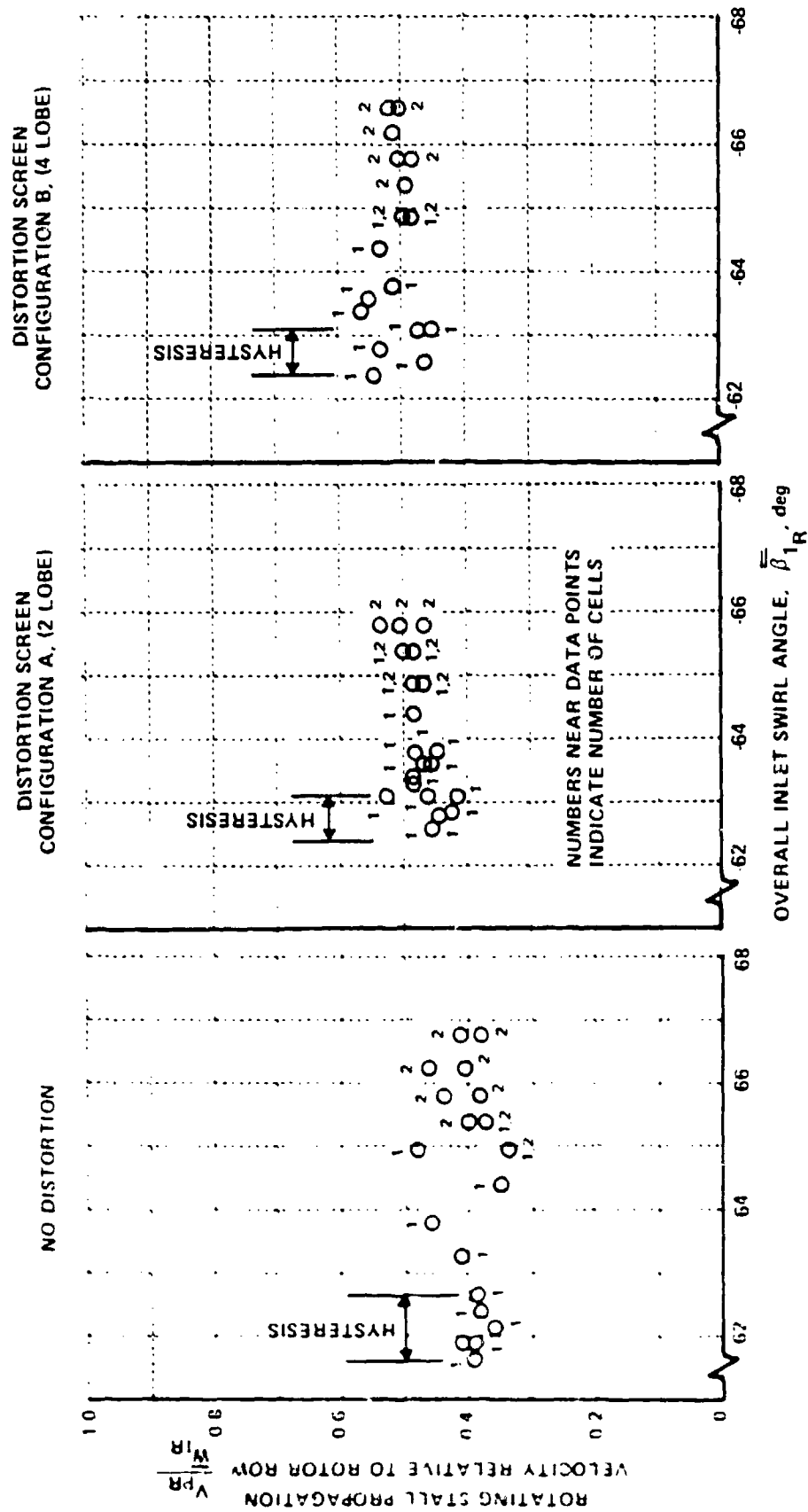
Figure 22   ROTATING STALL PROPAGATION VELOCITY AND NUMBER OF CELLS FOR ROTOR SET NO. 1 WITH AND WITHOUT UPSTREAM DISTORTION, COORDINATE SYSTEM RELATIVE TO ROTOR
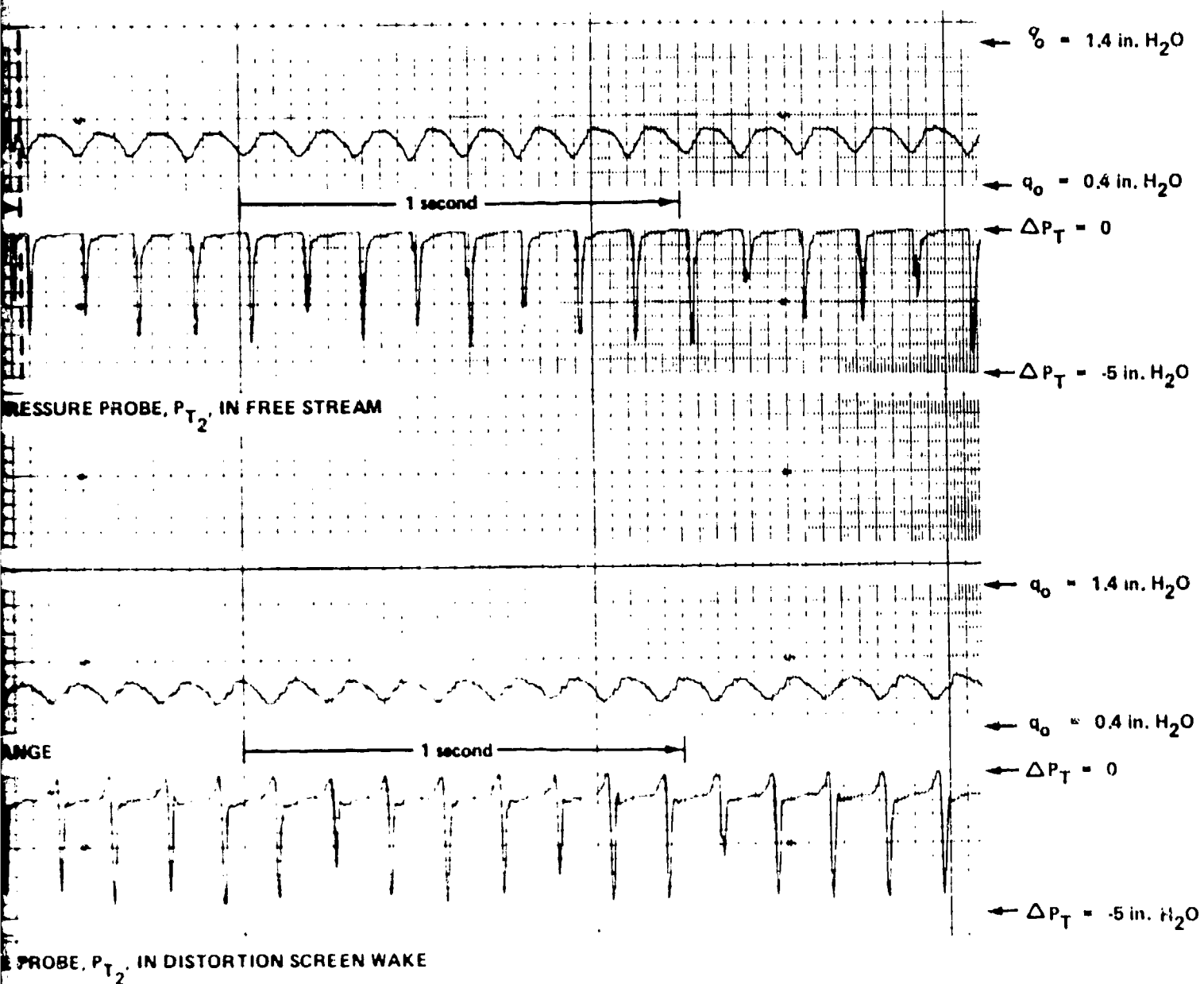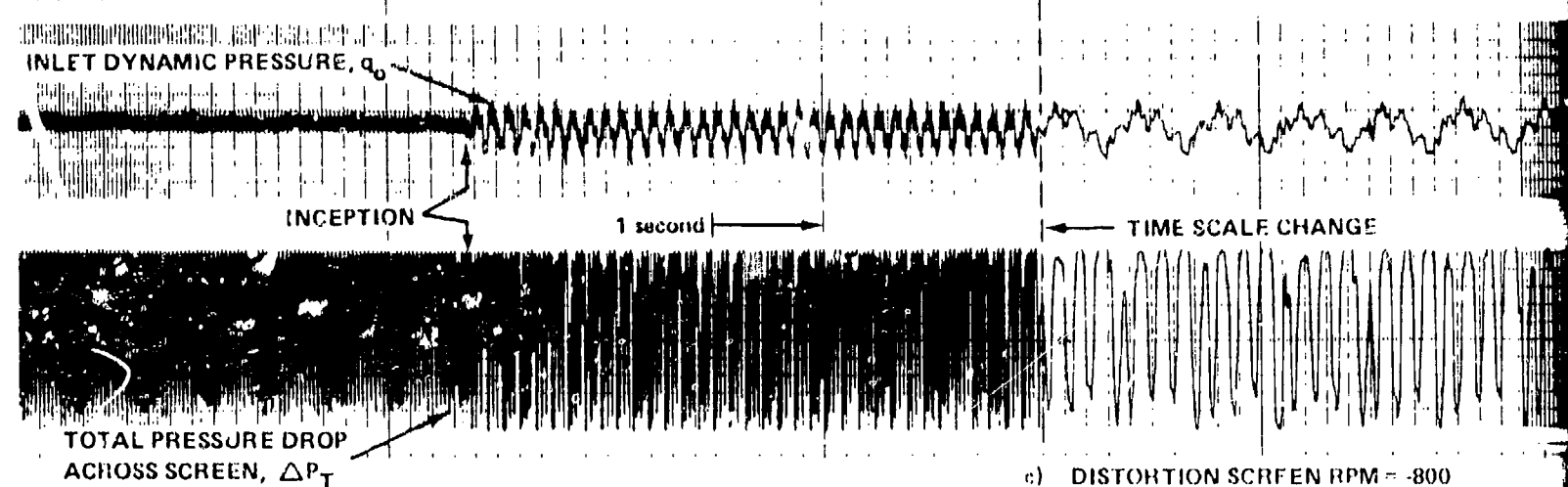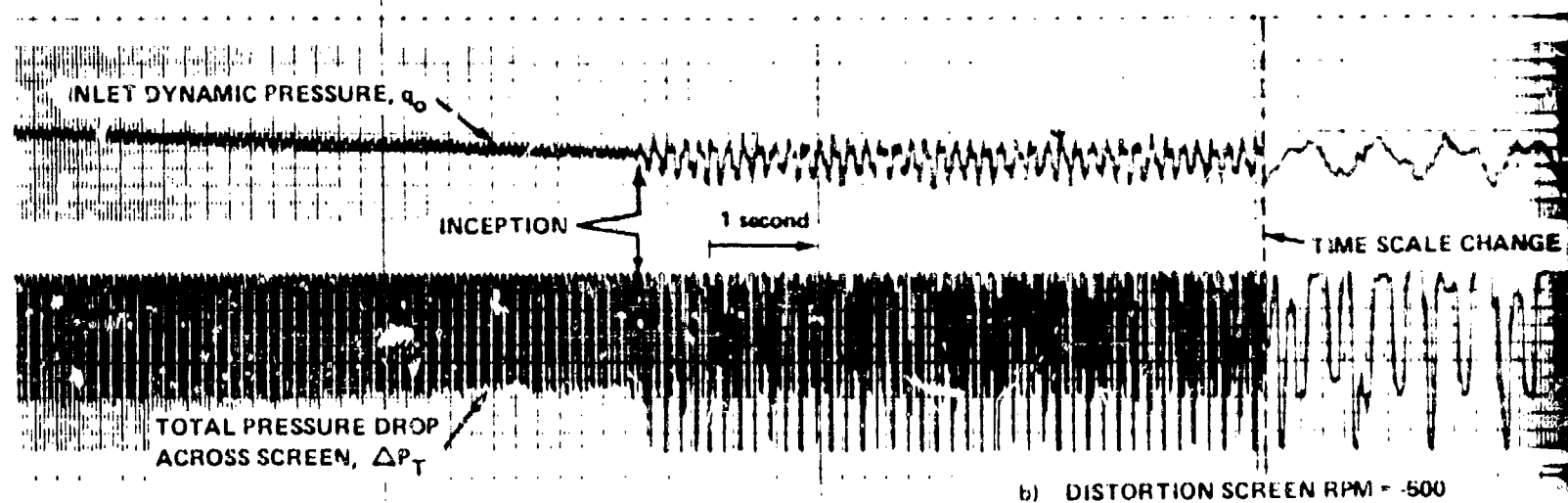
INLET DYNAMIC PRESSURE, q_o

INCEPTION

TIME SCALE CHANGE

1 second

TOTAL PRESSURE DROP ACROSS SCREEN, ΔP_T

a) DOWNSTREAM TOTAL PRESSURE PROBE, P_{T_2}, IN FREE STREAM

INLET DYNAMIC PRESSURE, q_o

INCEPTION

1 second

TIME SCALE CHANGE

TOTAL PRESSURE DROP ACROSS SCREEN, ΔP_T

b) DOWNSTREAM TOTAL PRESSURE PROBE, P_{T_2}, IN DISTORTION SCREEN

PRESSURE PROBE, P_{T_2}, IN FREE STREAM

$q_0 = 1.4$ in. H_2O

$q_0 = 0.4$ in. H_2O

$\Delta P_T = 0$

$\Delta P_T = -5$ in. H_2O

$q_0 = 1.4$ in. H_2O

$q_0 = 0.4$ in. H_2O

$\Delta P_T = 0$

$\Delta P_T = -5$ in. H_2O

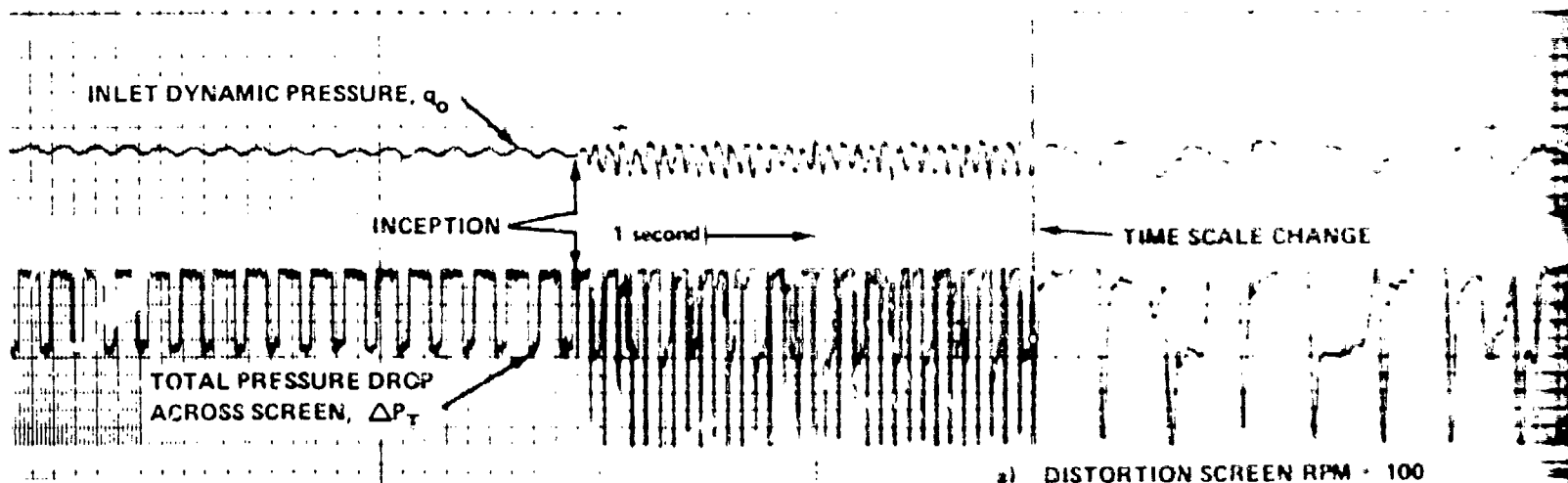PROBE, P_{T_2}, IN DISTORTION SCREEN WAKE

Figure 23

INCEPTION OF ROTATING STALL WITH DECREASING
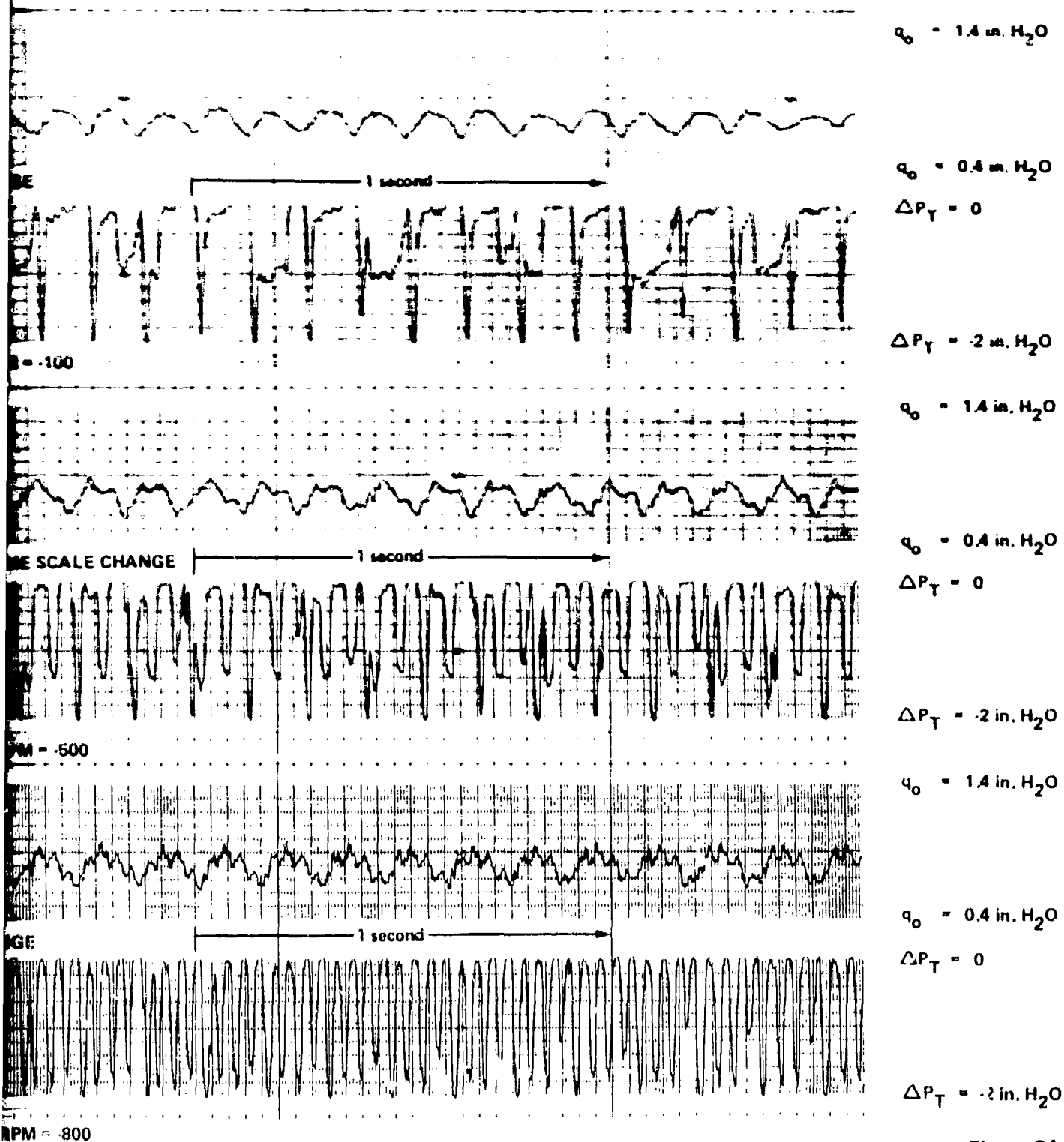INLET DYNAMIC PRESSURE
STATIONARY DISTORTION, ROTOR RPM = 1000

INLET DYNAMIC PRESSURE, q_0
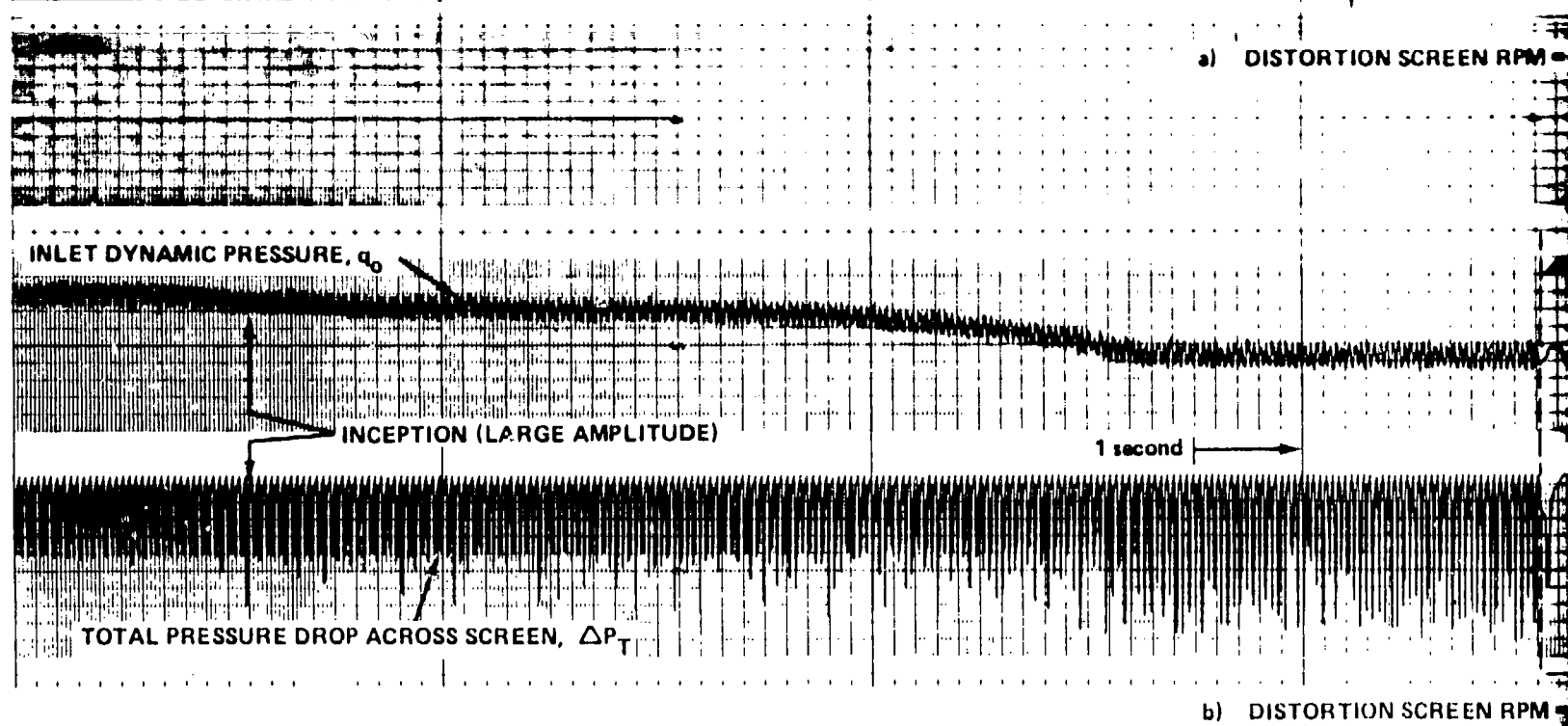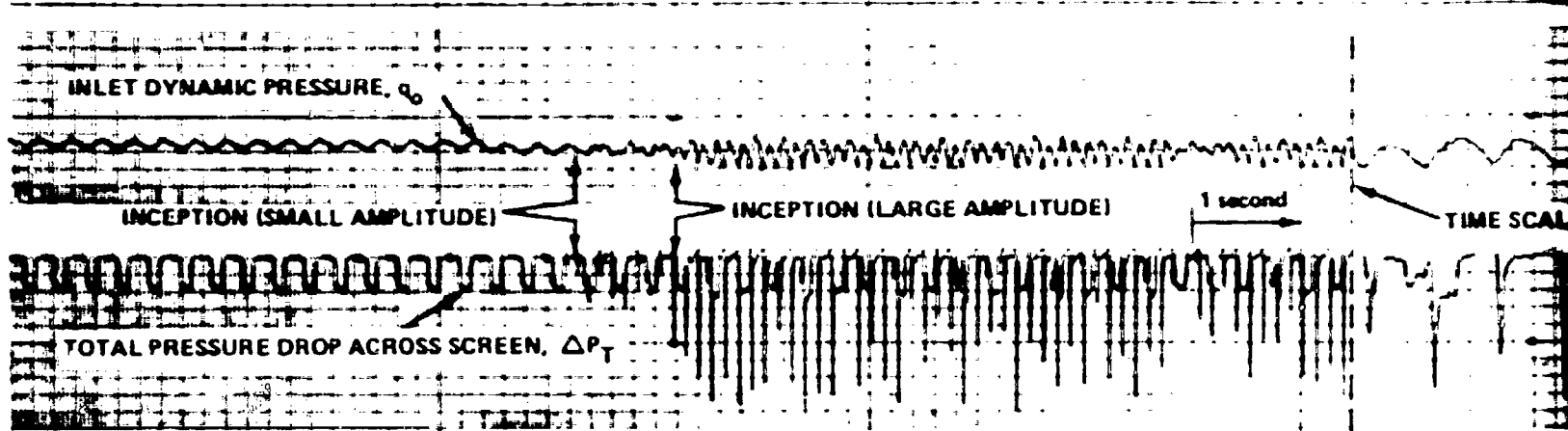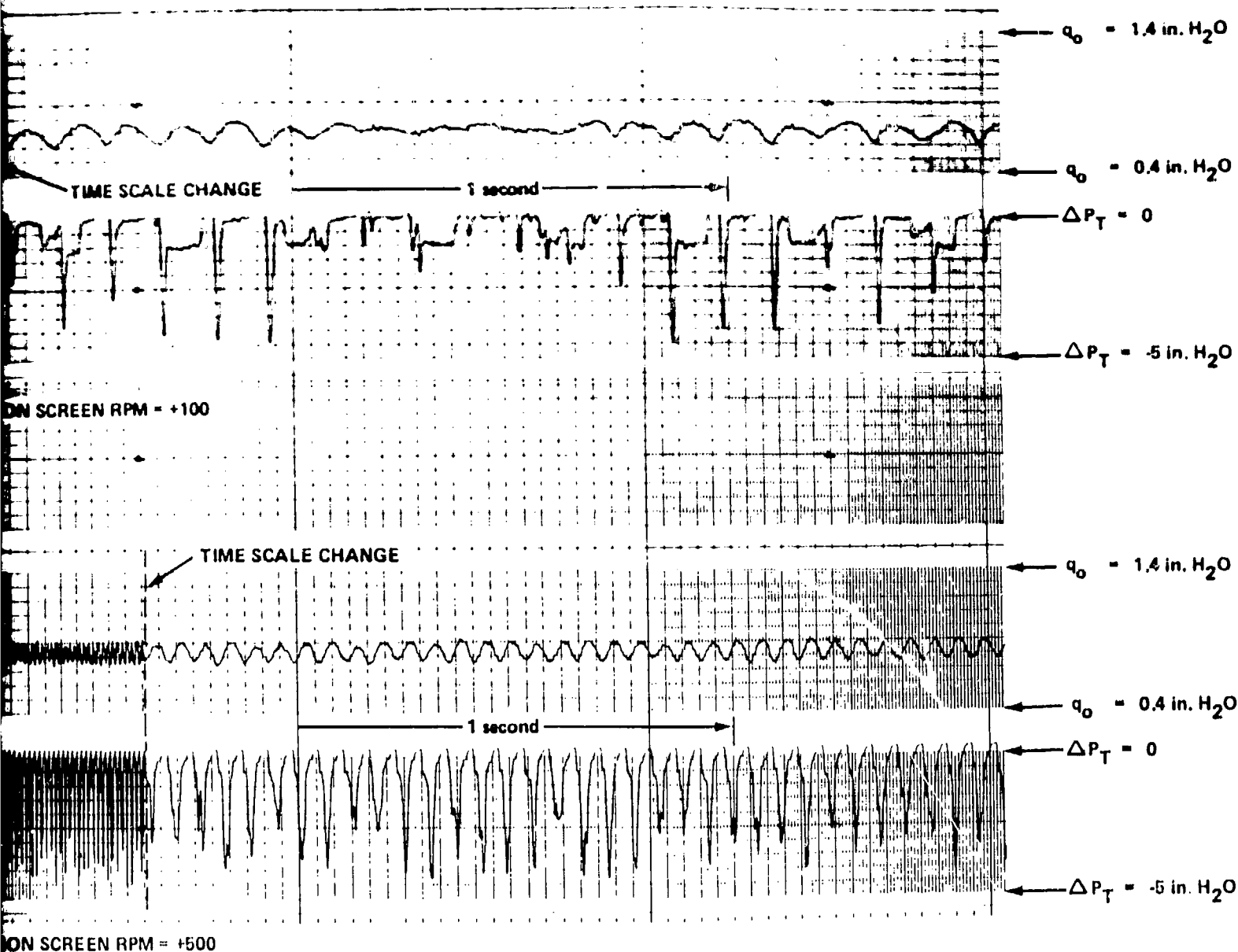
INCEPTION

1 second

TIME SCALE CHANGE

TOTAL PRESSURE DROP ACROSS SCREEN, ΔP_T

a) DISTORTION SCREEN RPM = 100

INLET DYNAMIC PRESSURE, q_0

INCEPTION

1 second

TIME SCALE CHANGE

TOTAL PRESSURE DROP ACROSS SCREEN, ΔP_T

b) DISTORTION SCREEN RPM = 500

INLET DYNAMIC PRESSURE, q_0

INCEPTION

1 second

TIME SCALE CHANGE

TOTAL PRESSURE DROP ACROSS SCREEN, ΔP_T

c) DISTORTION SCREEN RPM = 800

$q_o = 1.4$ in. H_2O

1 second

$q_o = 0.4$ in. H_2O

$\Delta P_T = 0$

$\Delta P_T = 2$ in. H_2O

$q_o = 1.4$ in. H_2O

SCALE CHANGE

1 second

$q_o = 0.4$ in. H_2O

$\Delta P_T = 0$

$\Delta P_T = 2$ in. H_2O

$q_o = 1.4$ in. H_2O

1 second

$q_o = 0.4$ in. H_2O

$\Delta P_T = 0$

$\Delta P_T = 2$ in. H_2O

Figure 24

INCEPTION OF ROTATING STALL WITH DECREASING
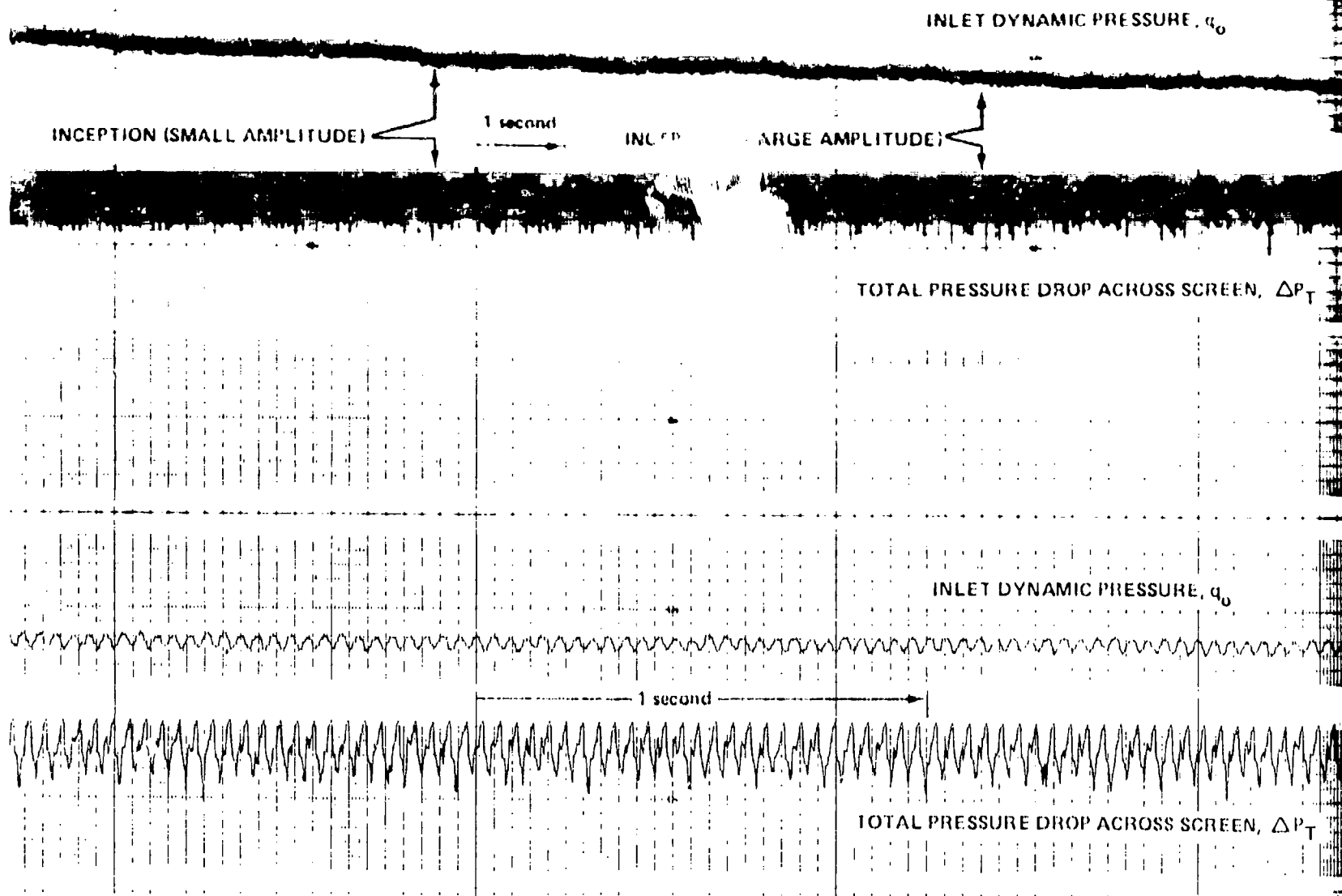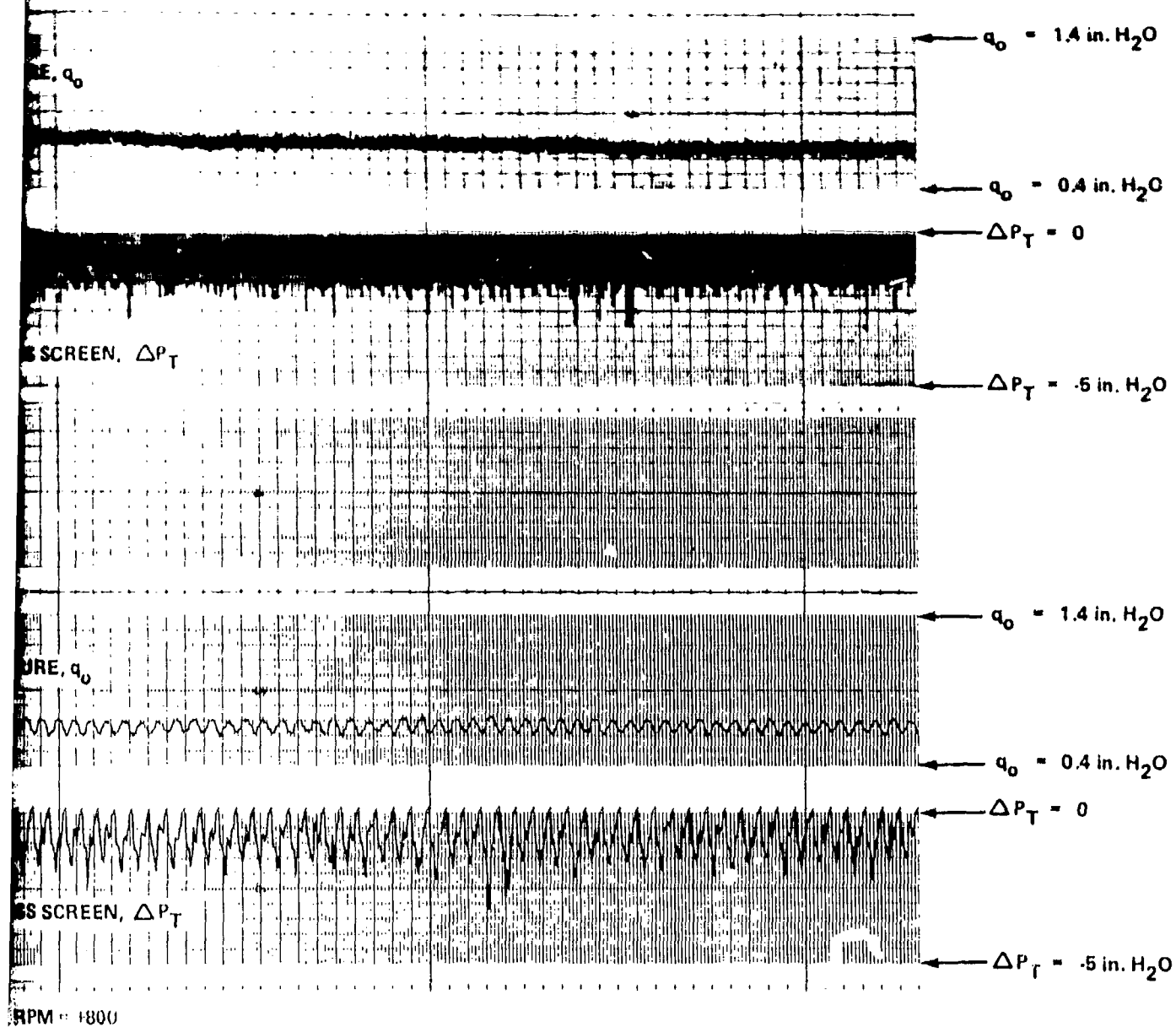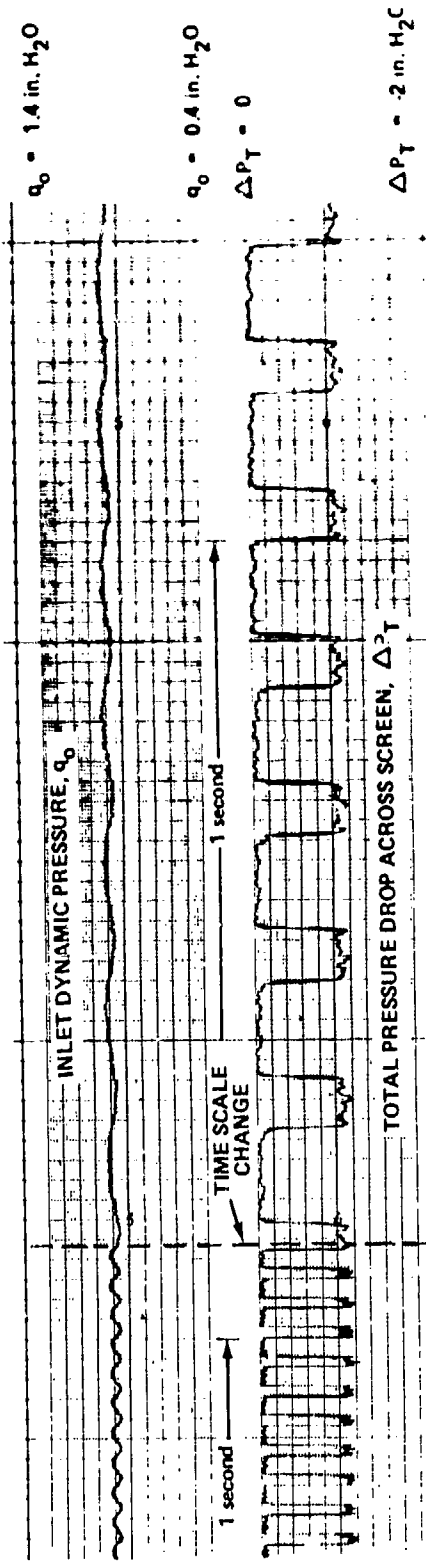INLET DYNAMIC PRESSURE-ROTATING DISTORTION
ROTOR RPM = 1000
DISTORTION ROTATING OPPOSITE TO ROTOR DIRECTION

134

INLET DYNAMIC PRESSURE, q_0

INCEPTION (SMALL AMPLITUDE) INCEPTION (LARGE AMPLITUDE) 1 second TIME SCALE

TOTAL PRESSURE DROP ACROSS SCREEN, ΔP_T

a) DISTORTION SCREEN RPM

INLET DYNAMIC PRESSURE, q_0

INCEPTION (LARGE AMPLITUDE) 1 second

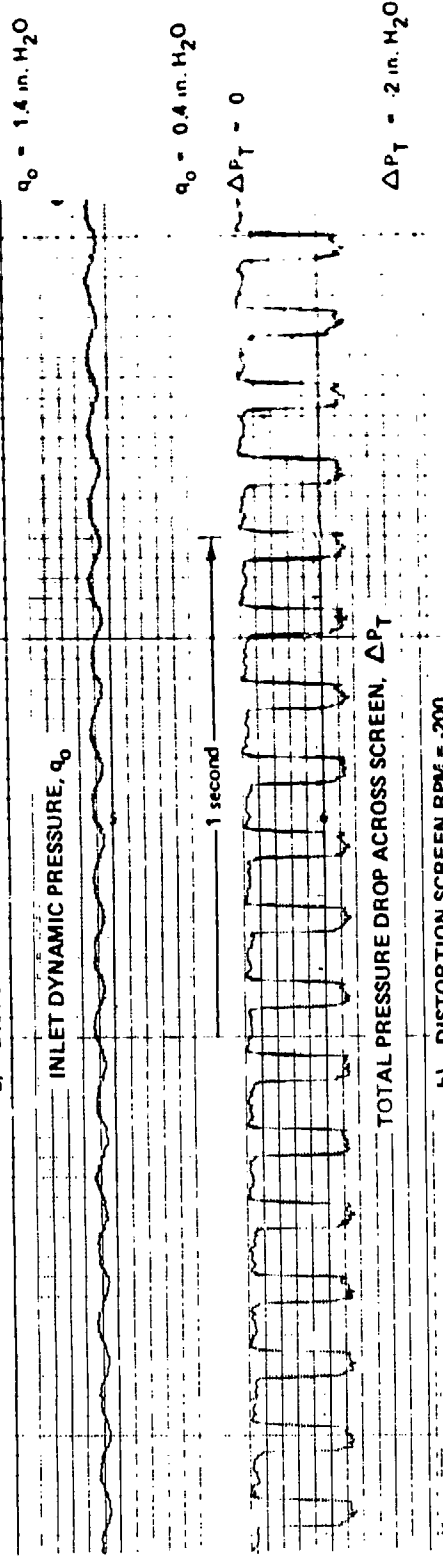TOTAL PRESSURE DROP ACROSS SCREEN, ΔP_T
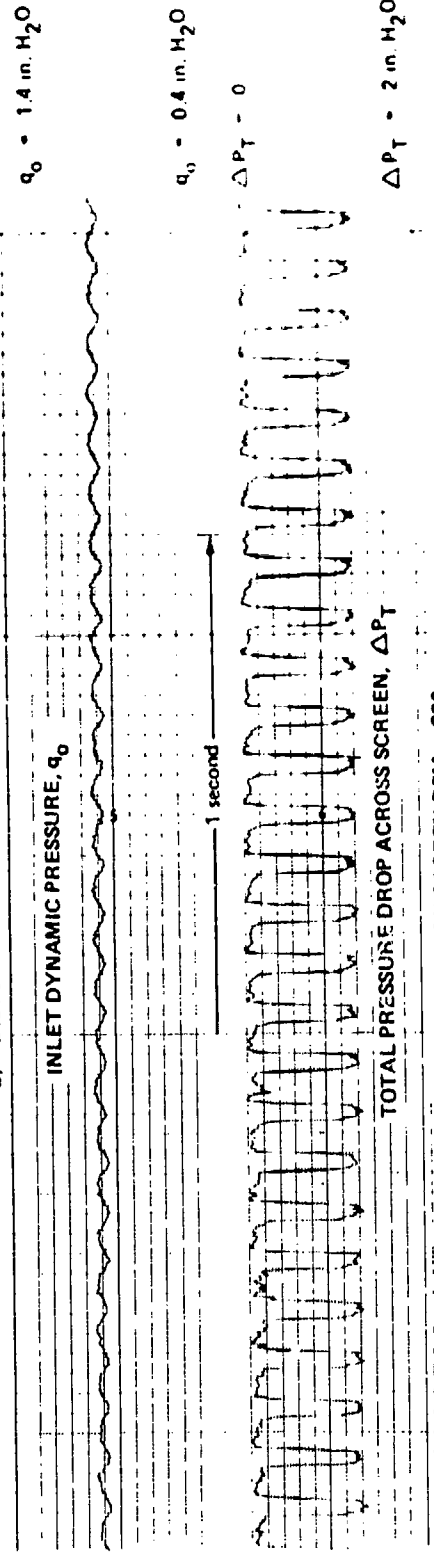
b) DISTORTION SCREEN RPM

Figure 25

INCEPTION OF ROTATING STALL WITH DECREASING
INLET DYNAMIC PRESSURE
ROTATING DISTORTION, ROTOR RPM = 1000
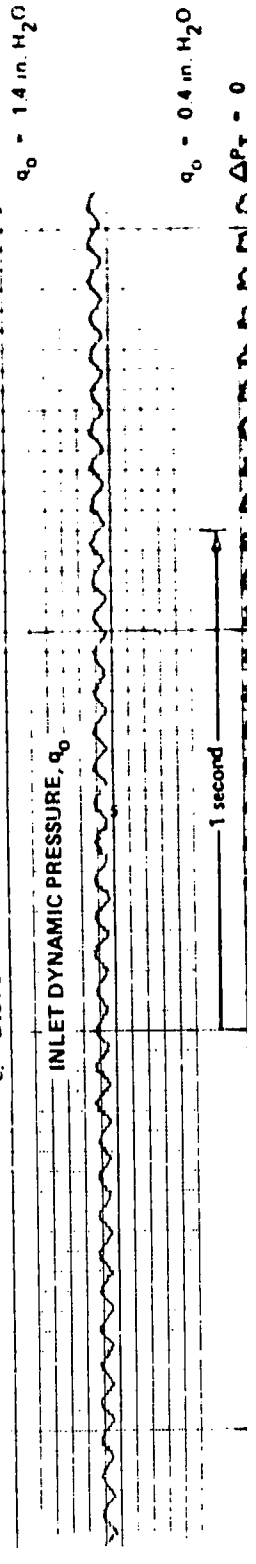DISTORTION ROTATING IN SAME DIRECTION AS ROTOR

135

INLET DYNAMIC PRESSURE, q_o

INCEPTION (SMALL AMPLITUDE)

1 second

INC... ...ARGE AMPLITUDE)

TOTAL PRESSURE DROP ACROSS SCREEN, ΔP_T

INLET DYNAMIC PRESSURE, q_o

1 second

TOTAL PRESSURE DROP ACROSS SCREEN, ΔP_T

c) DISTORTION SCREEN RPM = 1800

$q_o = 1.4$ in. H_2O

$q_o = 0.4$ in. H_2O

$\Delta P_T = 0$

SCREEN, ΔP_T

$\Delta P_T = .5$ in. H_2O

$q_o = 1.4$ in. H_2O

URE, q_o

$q_o = 0.4$ in. H_2O

$\Delta P_T = 0$

S SCREEN, ΔP_T

$\Delta P_T = .5$ in. H_2O

RPM = 1800

Figure 25 (Cont.)

INCEPTION OF ROTATING STALL WITH DECREASING
  INLET DYNAMIC PRESSURE
  ROTATING DISTORTION, ROTOR RPM = 1000
DISTORTION ROTATING IN SAME DIRECTION AS
  ROTOR

a) DISTORTION SCREEN RPM = 100
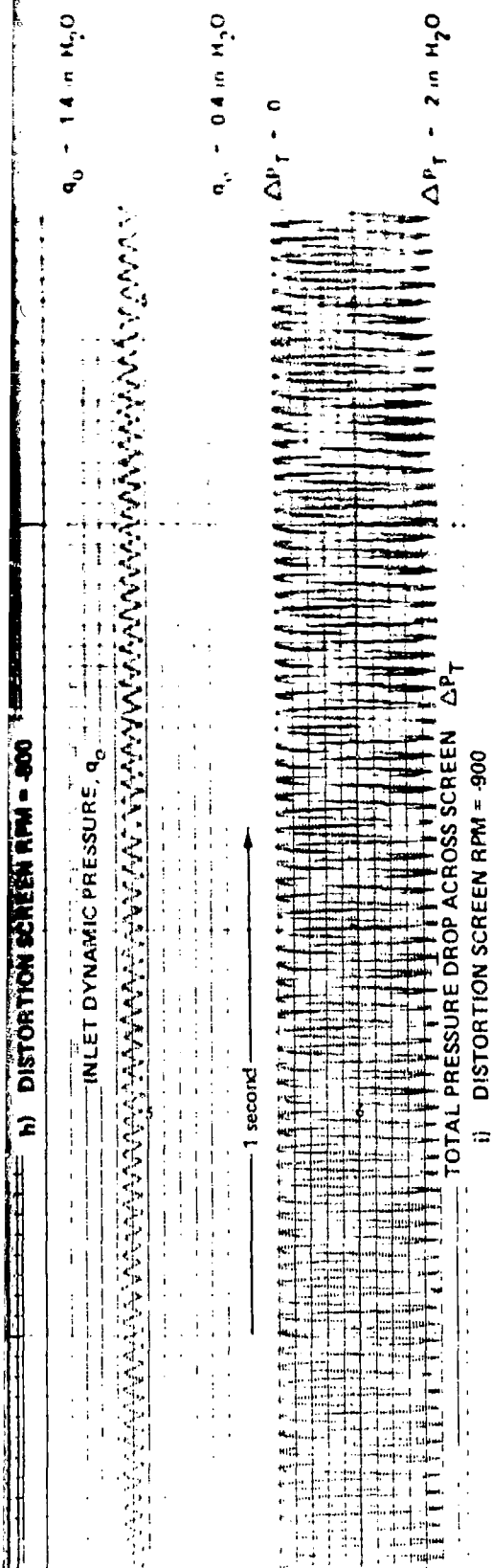
b) DISTORTION SCREEN RPM = 200

c) DISTORTION SCREEN RPM = 300
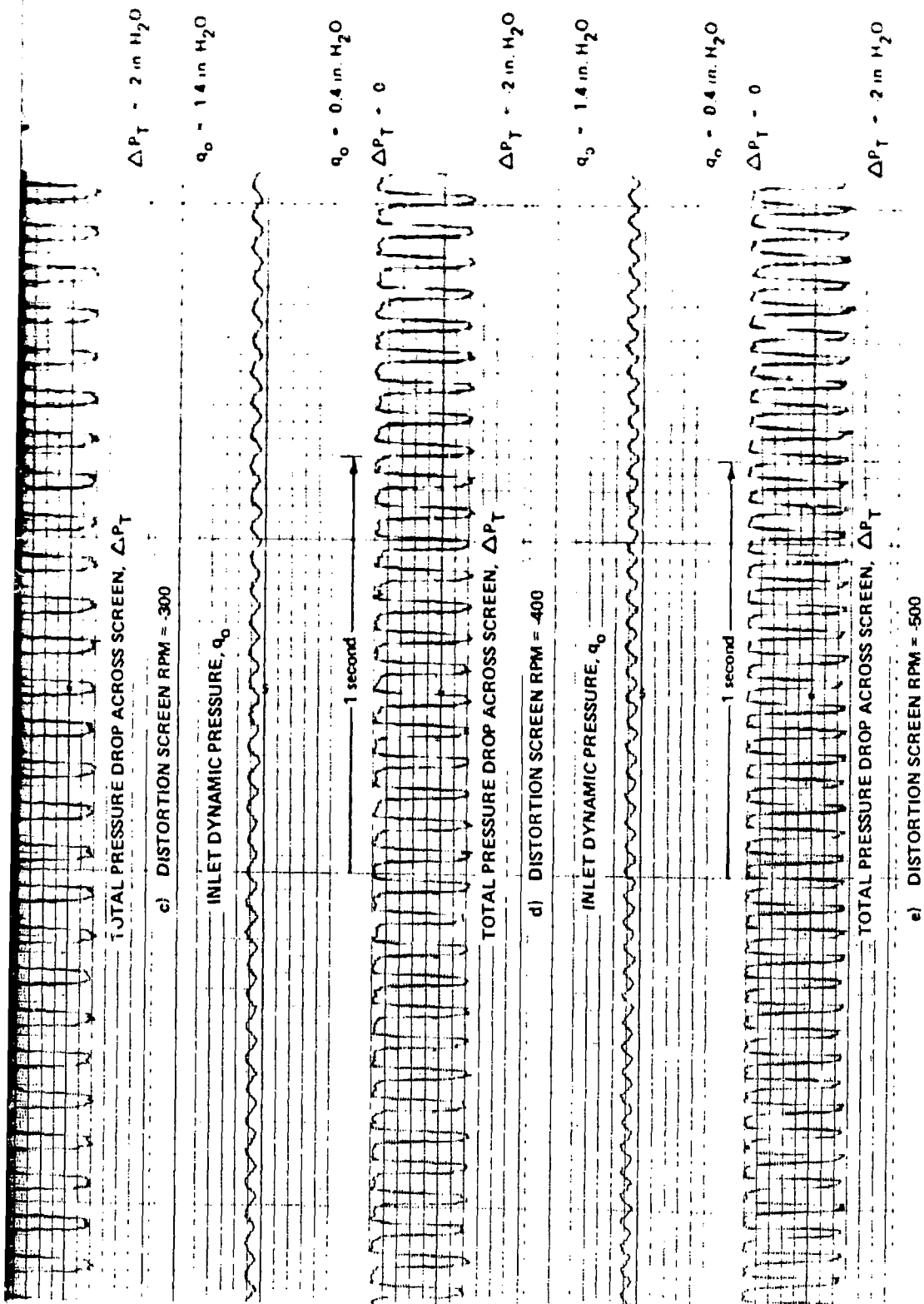
Figure 26

TOTAL PRESSURE DROP ACROSS ROTATING DISTORTION
SCREEN FOR CONSTANT MEAN INLET DYNAMIC
PRESSURE, $\bar{q}_o \approx 1$ IN. H_2O, ROTOR RPM = 1000
DISTORTION ROTATING OPPOSITE TO ROTOR DIRECTION

$q_0 = 14 \text{ in } H_2O$

$q_0 = 0.4 \text{ in } H_2O$

$\Delta P_T = 0$

INLET DYNAMIC PRESSURE, q_0

$\Delta P_T = 2 \text{ in } H_2O$

TOTAL PRESSURE DROP ACROSS SCREEN, ΔP_T

f) DISTORTION SCREEN RPM = 600

1 second

$q_0 = 14 \text{ in } H_2O$

$q_0 = 0.4 \text{ in } H_2O$

$\Delta P_T = 0$

INLET DYNAMIC PRESSURE, q_0

$\Delta P_T = 2 \text{ in } H_2O$

TOTAL PRESSURE DROP ACROSS SCREEN, ΔP_T

g) DISTORTION SCREEN RPM = 700

1 second

$q_0 = 14 \text{ in } H_2O$

$q_0 = 0.4 \text{ in } H_2O$

$\Delta P_T = 0$

INLET DYNAMIC PRESSURE, q_0

$\Delta P_T = 2 \text{ in } H_2O$

TOTAL PRESSURE DROP ACROSS SCREEN, ΔP_T

h) DISTORTION SCREEN RPM = 800

1 second

INLET DYNAMIC PRESSURE, q_0

$q_0 = 14 \text{ in } H_2O$

h) DISTORTION SCREEN RPM = -800

$q_o = 1.4$ in H_2O

INLET DYNAMIC PRESSURE, q_o

$q_s = 0.4$ in H_2O

$\Delta P_T = 0$

1 second

TOTAL PRESSURE DROP ACROSS SCREEN ΔP_T

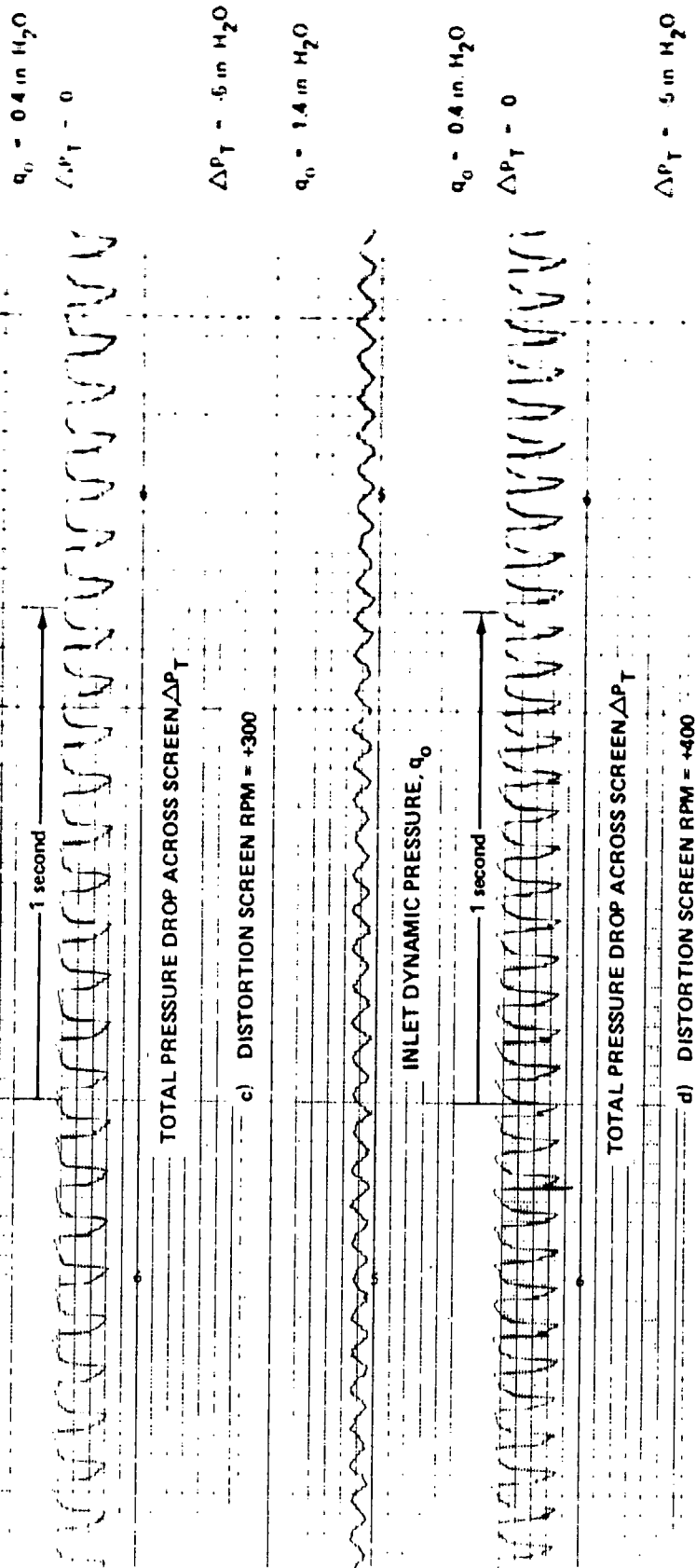$\Delta P_T = 2$ in H_2O

i) DISTORTION SCREEN RPM = -900

Figure 26 (Cont.)

TOTAL PRESSURE DROP ACROSS ROTATING DISTOR-
TION SCREEN FOR CONSTANT MEAN INLET
DYNAMIC PRESSURE, $\bar{q}_o \approx 1$ IN. H_2O, ROTOR
RPM = 1000
DISTORTION ROTATING OPPOSITE TO ROTOR DIRECTION

INLET DYNAMIC PRESSURE, q_o

1 second

TOTAL PRESSURE DROP ACROSS SCREEN ΔP_T

a) DISTORTION SCREEN RPM = +100

INLET DYNAMIC PRESSURE, q_o

1 second

TOTAL PRESSURE DROP ACROSS SCREEN ΔP_T

b) DISTORTION SCREEN RPM = +200

INLET DYNAMIC PRESSURE, q_o

1 second

TOTAL PRESSURE DROP ACROSS SCREEN ΔP_T

c) DISTORTION SCREEN RPM = +300
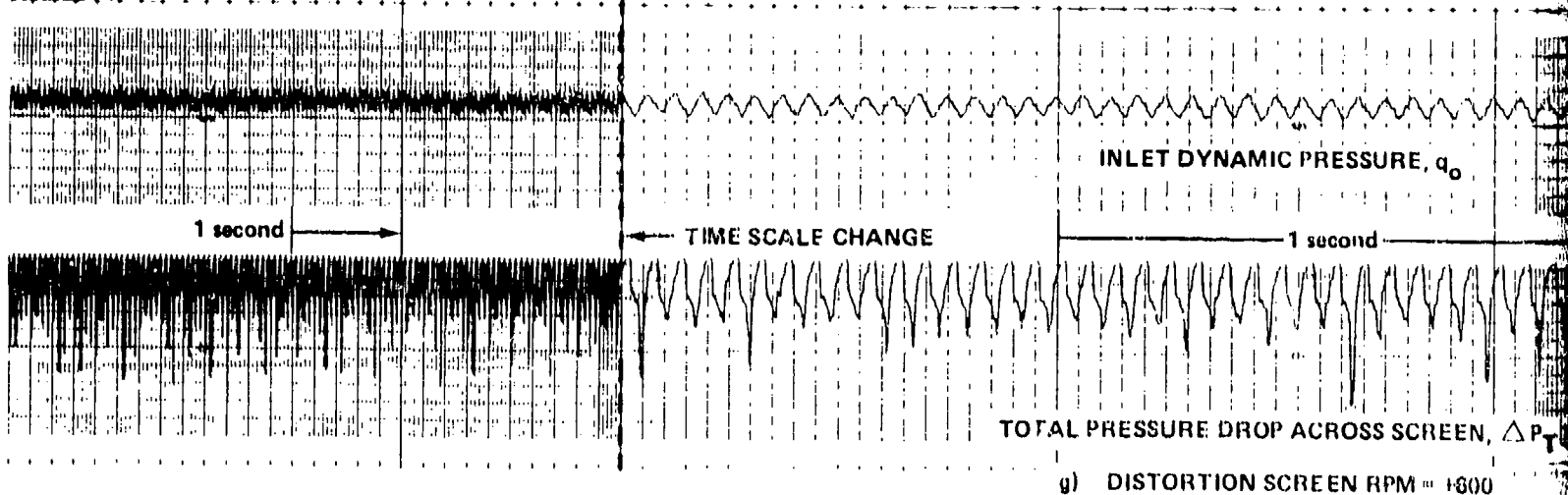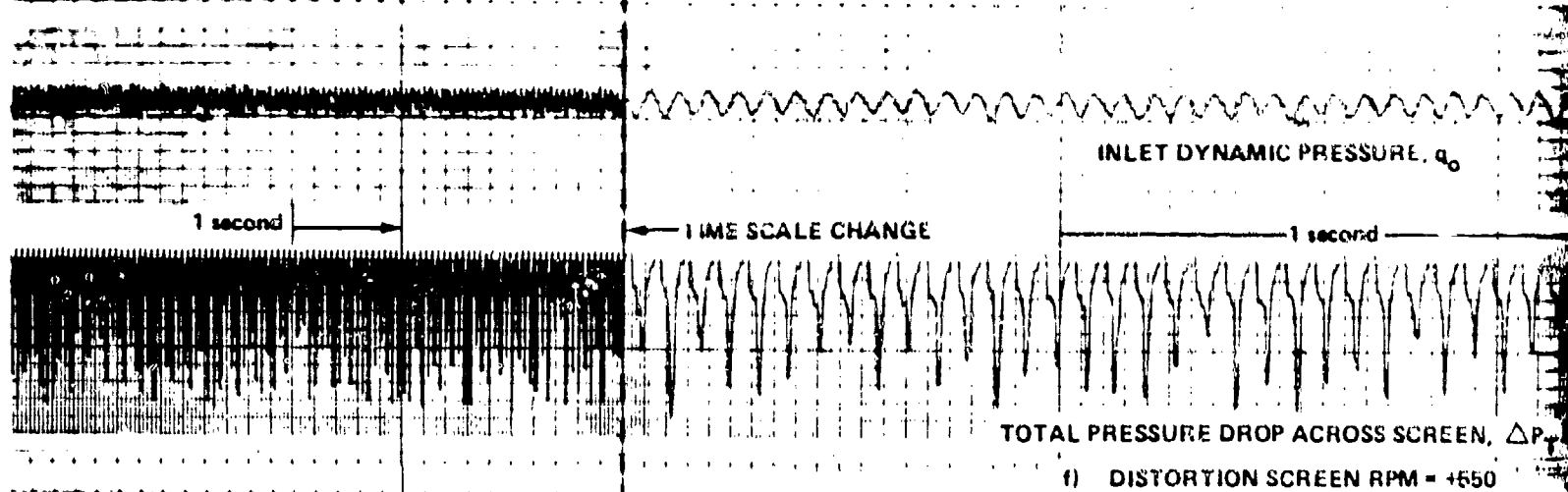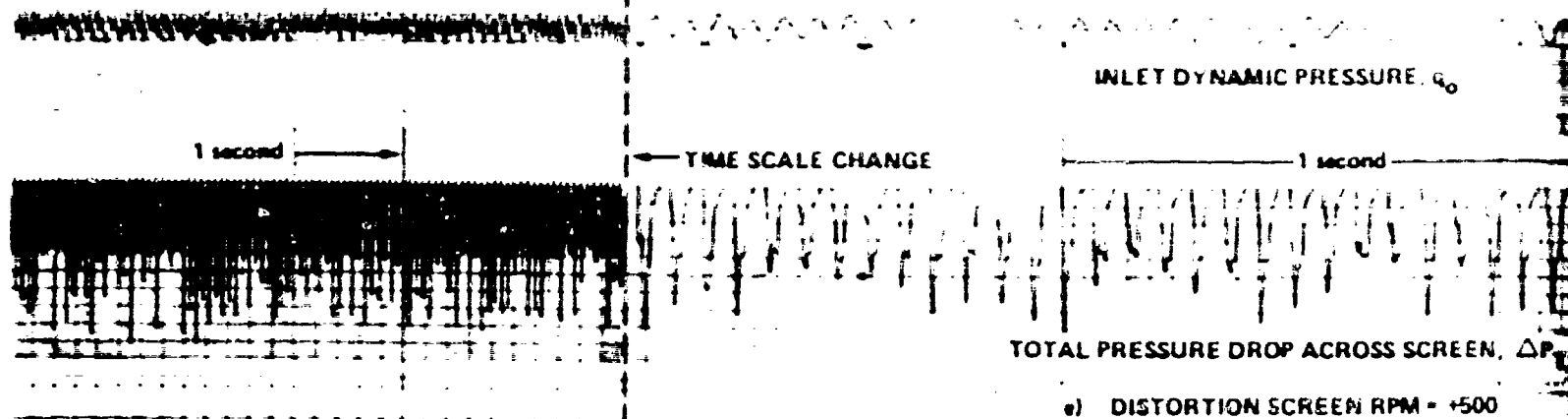
INLET DYNAMIC PRESSURE, q_o

$q_o = 1.4 \text{ in } H_2O$

$q_o = 0.4 \text{ in } H_2O$

$\Delta P_T = 0$

$\Delta P_T = 5 \text{ in } H_2O$

$q_o = 1.4 \text{ in } H_2O$

$q_o = 0.4 \text{ in } H_2O$

$\Delta P_T = 0$

$\Delta P_T = 5 \text{ in } H_2O$

$q_o = 1.4 \text{ in } H_2O$

$q_o = 0.4 \text{ in } H_2O$

$\Delta P_T = 0$

$\Delta P_T = 5 \text{ in } H_2O$

$q_o = 1.4 \text{ in } H_2O$

$q_o = 0.4 \text{ in } H_2O$

$\Delta P_T = 0$

TOTAL PRESSURE DROP ACROSS SCREEN ΔP_T

$\Delta P_T = .6 \text{ in } H_2O$

c) DISTORTION SCREEN RPM = +300

$q_o = 1.4 \text{ in } H_2O$

INLET DYNAMIC PRESSURE, q_o

$q_o = 0.4 \text{ in } H_2O$

$\Delta P_T = 0$

TOTAL PRESSURE DROP ACROSS SCREEN ΔP_T

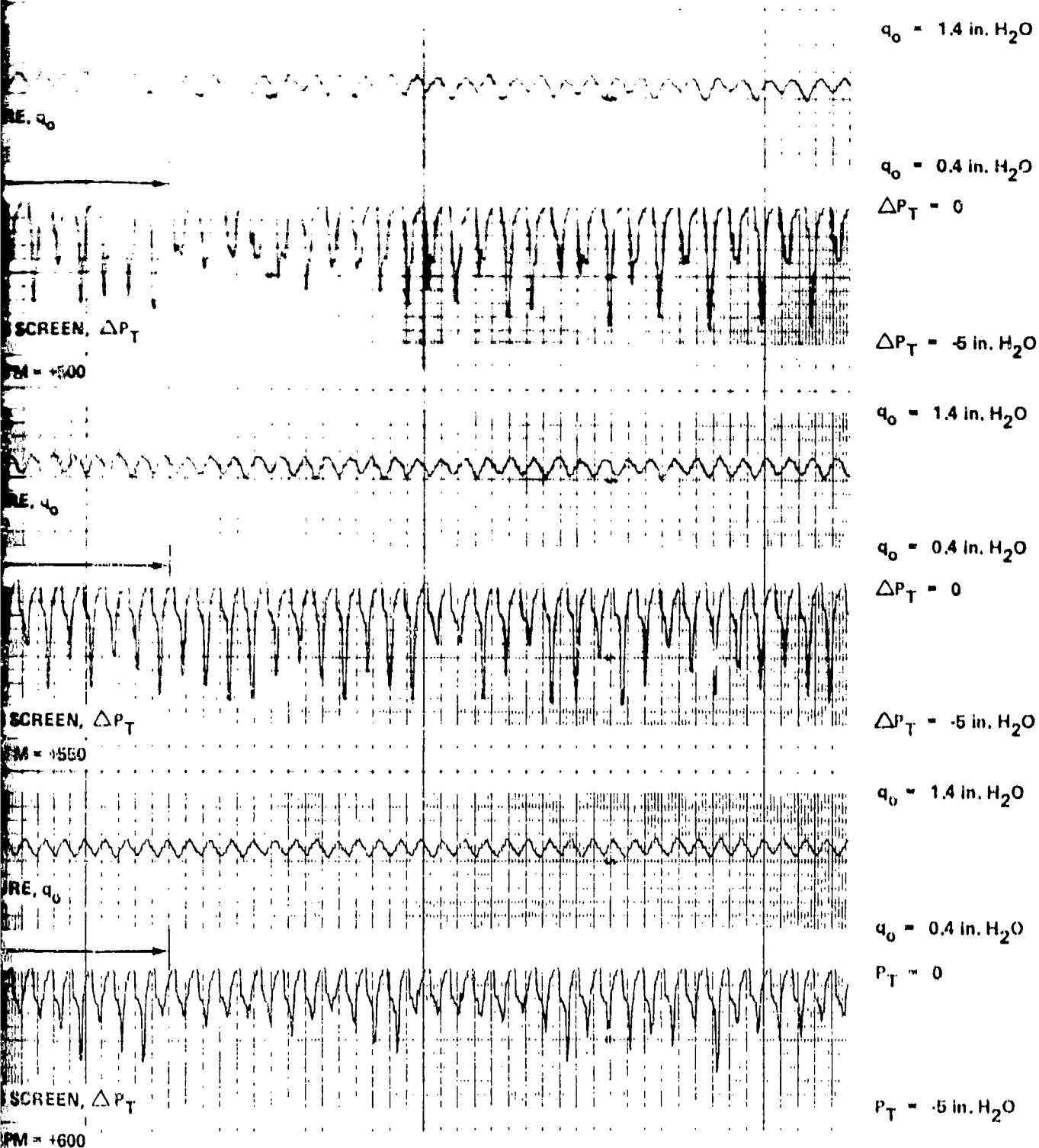$\Delta P_T = .5 \text{ in } H_2O$

d) DISTORTION SCREEN RPM = +400

1 second

Figure 27

TOTAL PRESSURE DROP ACROSS ROTATING DISTORTION
SCREEN FOR CONSTANT MEAN INLET DYNAMIC
PRESSURE, $q_o \approx 1$ IN. H_2O, ROTOR RPM = 1000
DISTORTION ROTATING IN SAME DIRECTION AS ROTOR

189

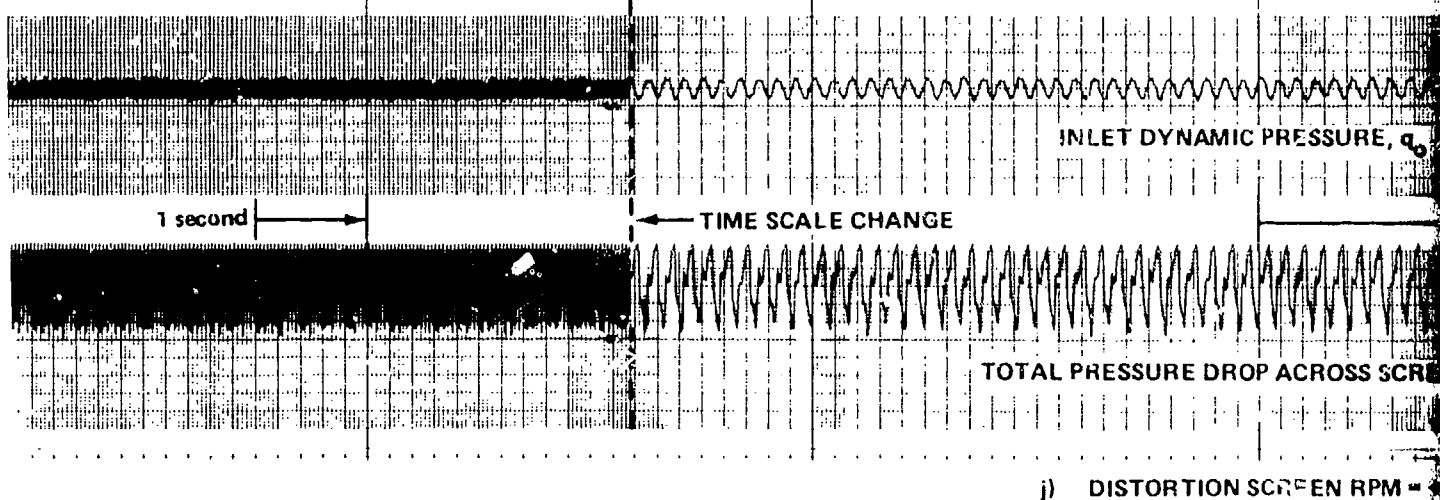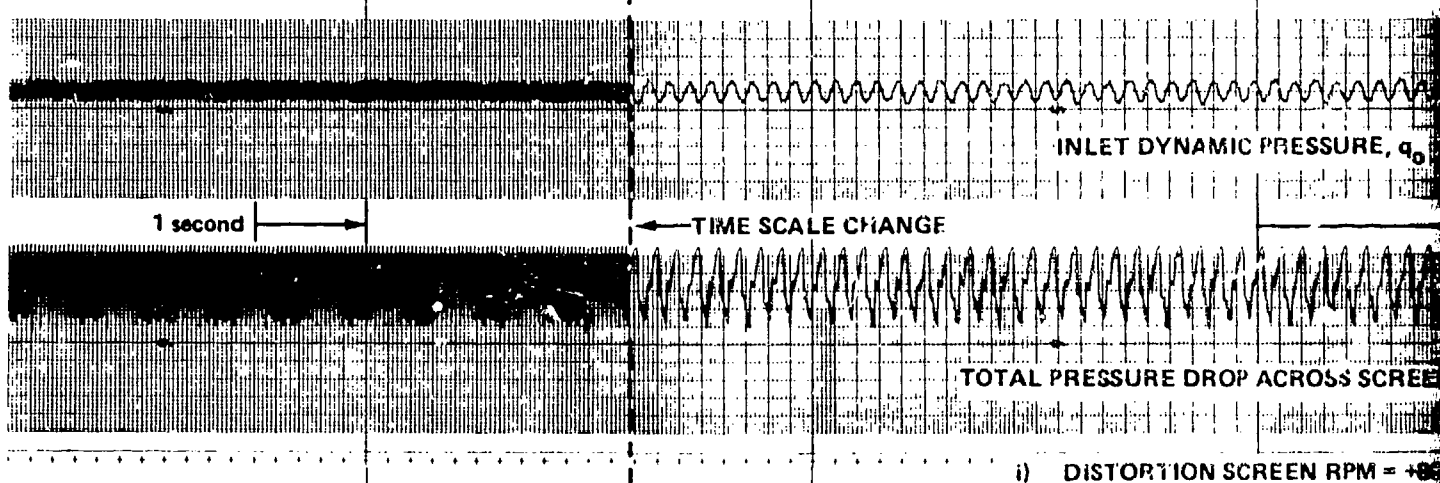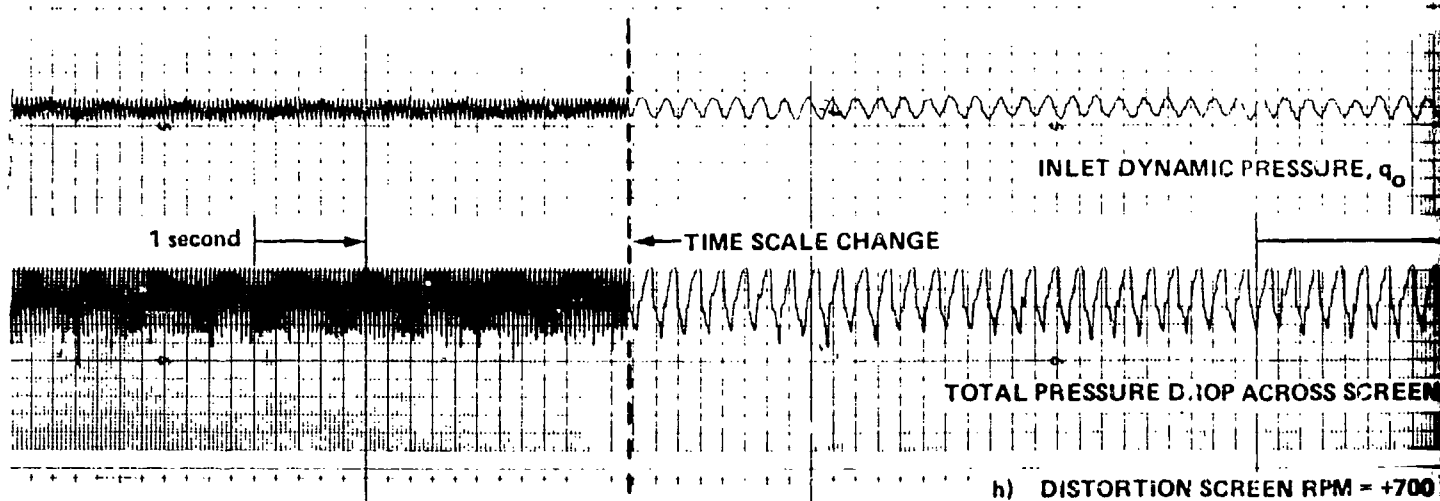INLET DYNAMIC PRESSURE, q_o

1 second ⟶ ⟵ TIME SCALE CHANGE 1 second

TOTAL PRESSURE DROP ACROSS SCREEN, ΔP_T

e) DISTORTION SCREEN RPM = +500

INLET DYNAMIC PRESSURE, q_o

1 second ⟶ ⟵ TIME SCALE CHANGE 1 second

TOTAL PRESSURE DROP ACROSS SCREEN, ΔP_T

f) DISTORTION SCREEN RPM = +550

INLET DYNAMIC PRESSURE, q_o

1 second ⟶ ⟵ TIME SCALE CHANGE 1 second

TOTAL PRESSURE DROP ACROSS SCREEN, ΔP_T

g) DISTORTION SCREEN RPM = +600

RE. q_o

q_o = 1.4 in. H_2O

q_o = 0.4 in. H_2O

ΔP_T = 0

SCREEN, ΔP_T

ΔP_T = -5 in. H_2O

PM = +500

q_o = 1.4 in. H_2O

RE. q_o

q_o = 0.4 in. H_2O

ΔP_T = 0

SCREEN, ΔP_T

ΔP_T = -5 in. H_2O

M = +550

q_o = 1.4 in. H_2O

RE, q_o

q_o = 0.4 in. H_2O

P_T = 0

SCREEN, ΔP_T

P_T = -5 in. H_2O

PM = +600

Figure 27 (Cont.)

TOTAL PRESSURE DROP ACROSS ROTATING DISTORTION
SCREEN FOR CONSTANT MEAN INLET DYNAMIC
PRESSURE, $q_o \approx 1$ IN. H_2O, ROTOR RPM = 1000
DISTORTION ROTATING IN SAME DIRECTION AS ROTOR

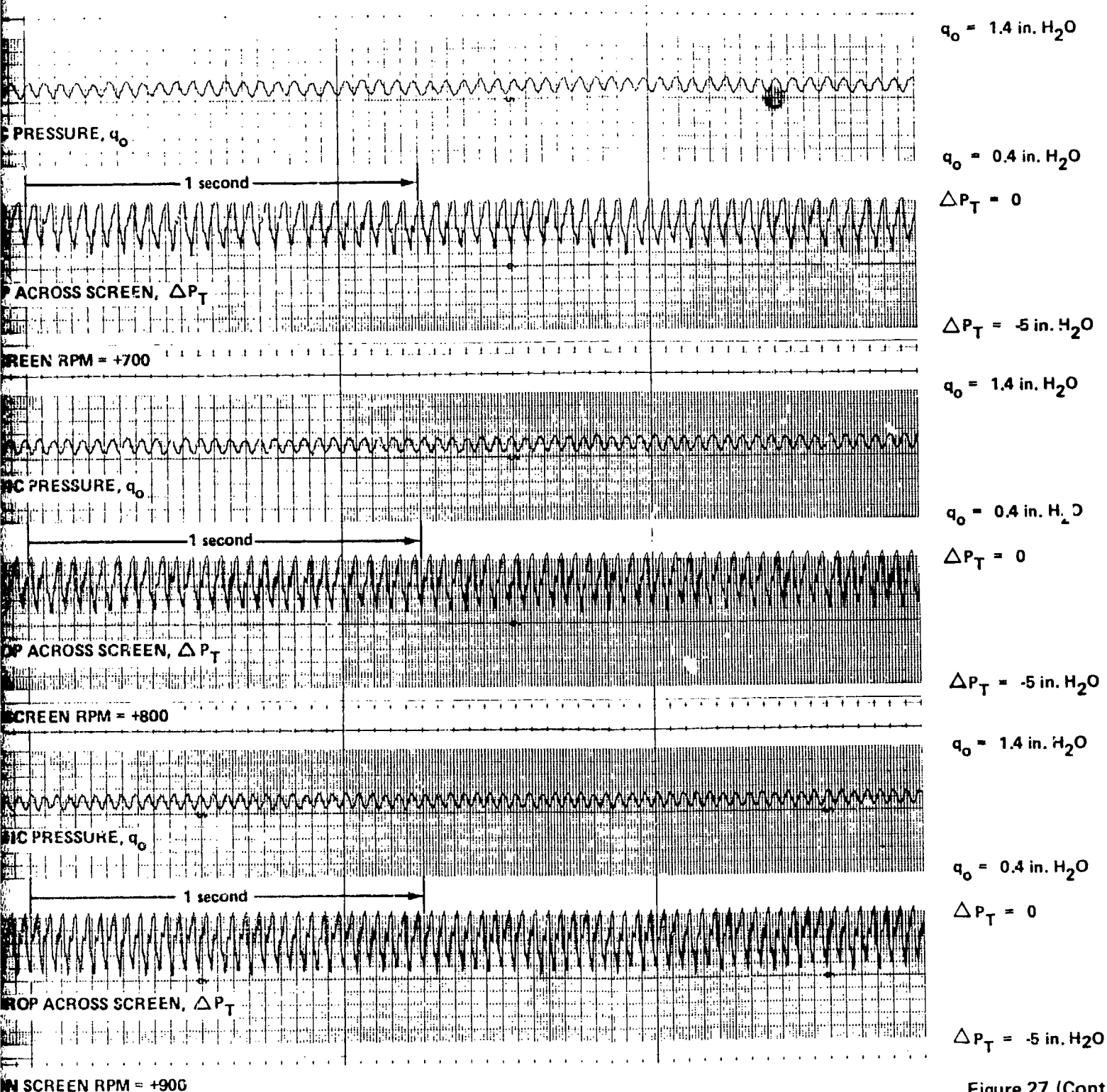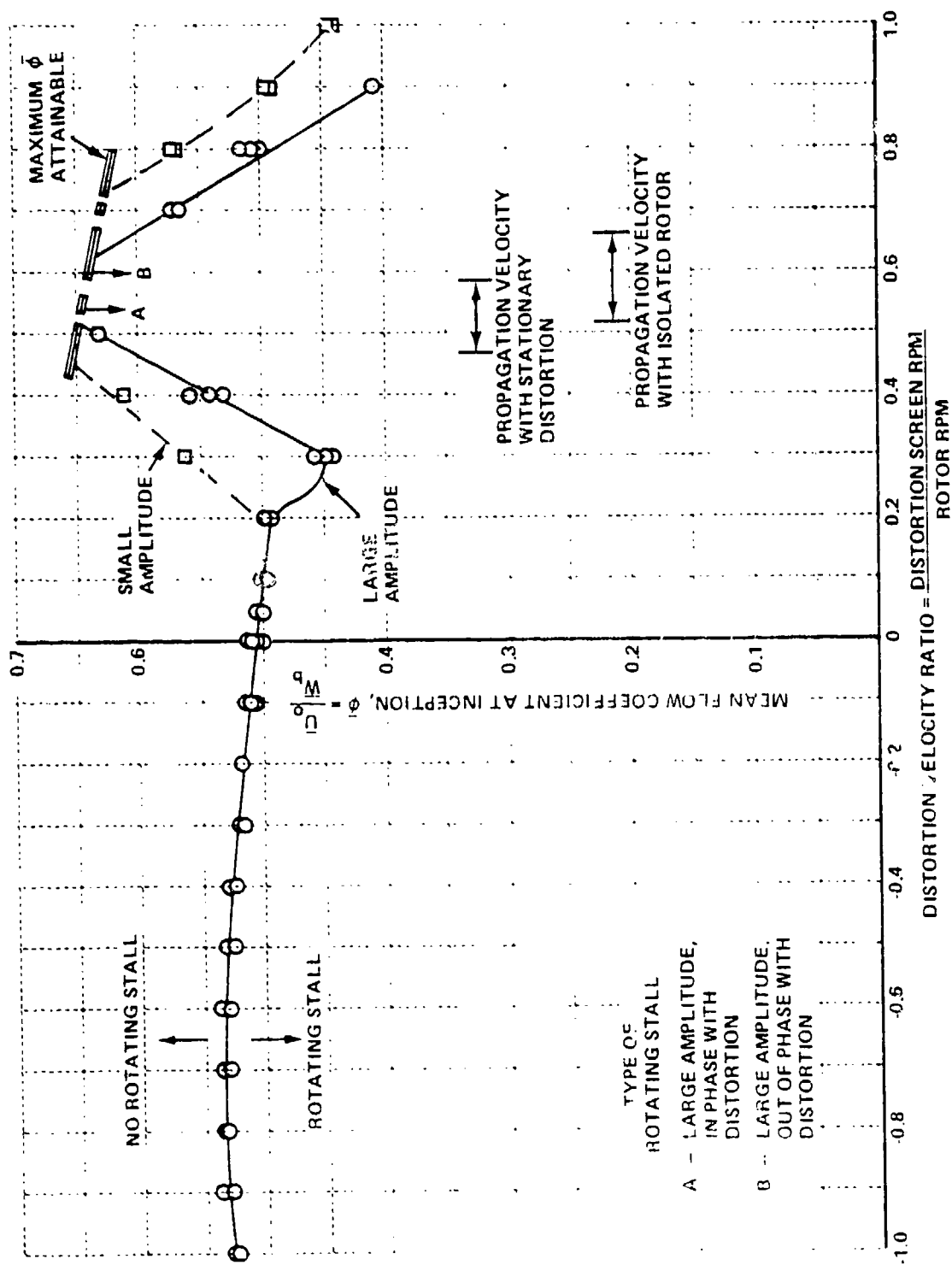INLET DYNAMIC PRESSURE, q_o

1 second ◄—TIME SCALE CHANGE

TOTAL PRESSURE DROP ACROSS SCREEN

h) DISTORTION SCREEN RPM = +700

INLET DYNAMIC PRESSURE, q_o

1 second ◄—TIME SCALE CHANGE

TOTAL PRESSURE DROP ACROSS SCREE

i) DISTORTION SCREEN RPM = +8

INLET DYNAMIC PRESSURE, q_o

1 second ◄—TIME SCALE CHANGE

TOTAL PRESSURE DROP ACROSS SCRE

j) DISTORTION SCREEN RPM =

PRESSURE, q_o

q_o = 1.4 in. H_2O

q_o = 0.4 in. H_2O

$\triangle P_T$ = 0

— 1 second —

ACROSS SCREEN, $\triangle P_T$

$\triangle P_T$ = -5 in. H_2O

REEN RPM = +700

q_o = 1.4 in. H_2O

IC PRESSURE, q_o

q_o = 0.4 in. H_2O

— 1 second —

$\triangle P_T$ = 0

DP ACROSS SCREEN, $\triangle P_T$

$\triangle P_T$ = -5 in. H_2O

SCREEN RPM = +800

q_o = 1.4 in. H_2O

IC PRESSURE, q_o

q_o = 0.4 in. H_2O

— 1 second —

$\triangle P_T$ = 0

ROP ACROSS SCREEN, $\triangle P_T$

$\triangle P_T$ = -5 in. H_2O

N SCREEN RPM = +900

Figure 27 (Cont.)

TOTAL PRESSURE DROP ACROSS ROTATING DISTORTION
SCREEN FOR CONSTANT MEAN INLET DYNAMIC
PRESSURE. $\bar{q}_o \approx 1$ IN. H_2O, ROTOR RPM = 1000
DISTORTION ROTATING IN SAME DIRECTION AS ROTOR

141

Figure 28   EFFECT OF ROTATING DISTORTION ON INCEPTION OF ROTATING STALL
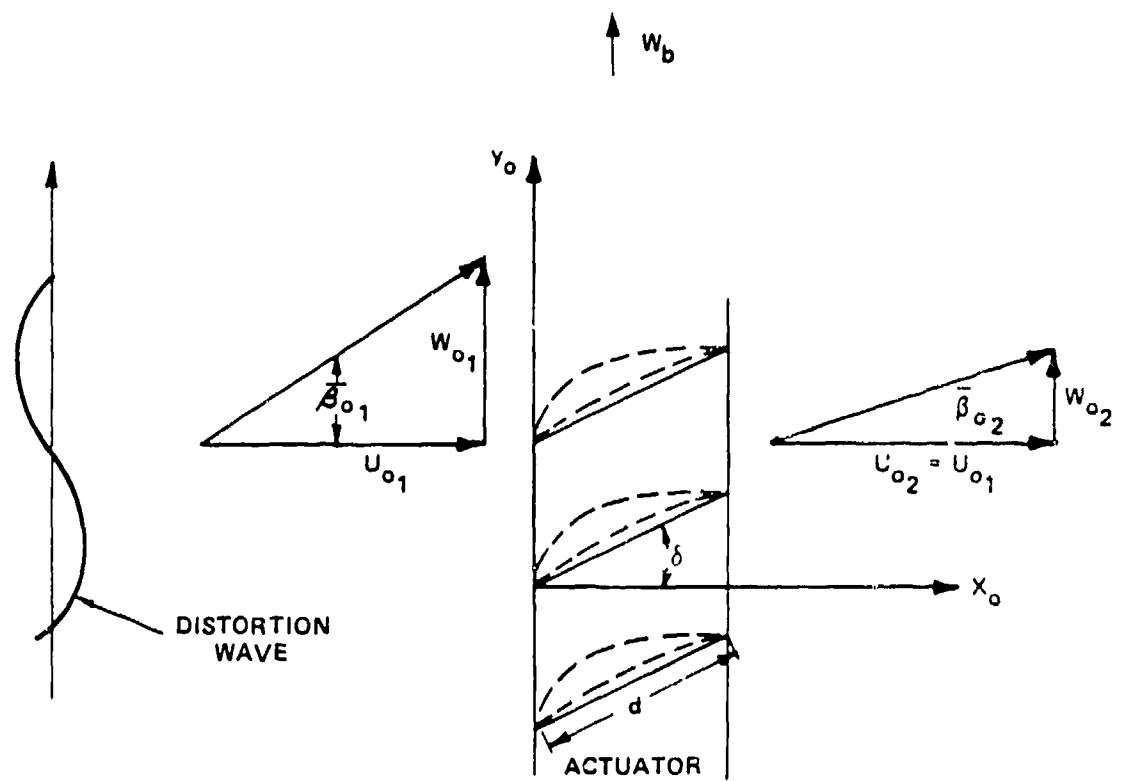
Figure 29   FINITE THICKNESS ACTUATOR MODEL FOR ANALYSIS OF DISTORTION
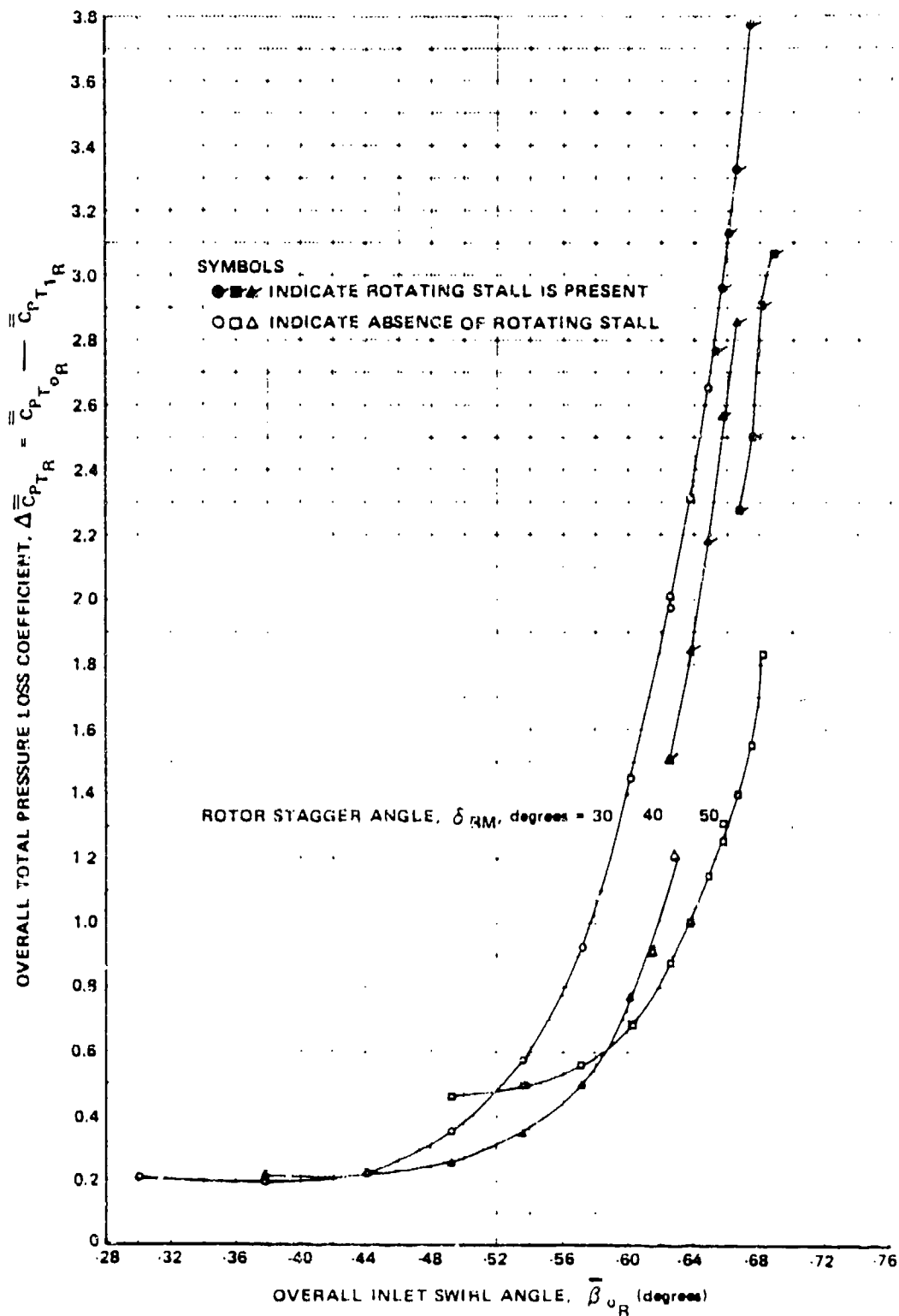
Figure 30   OVERALL TOTAL PRESSURE LOSS THROUGH ROTOR SET NO. 1,
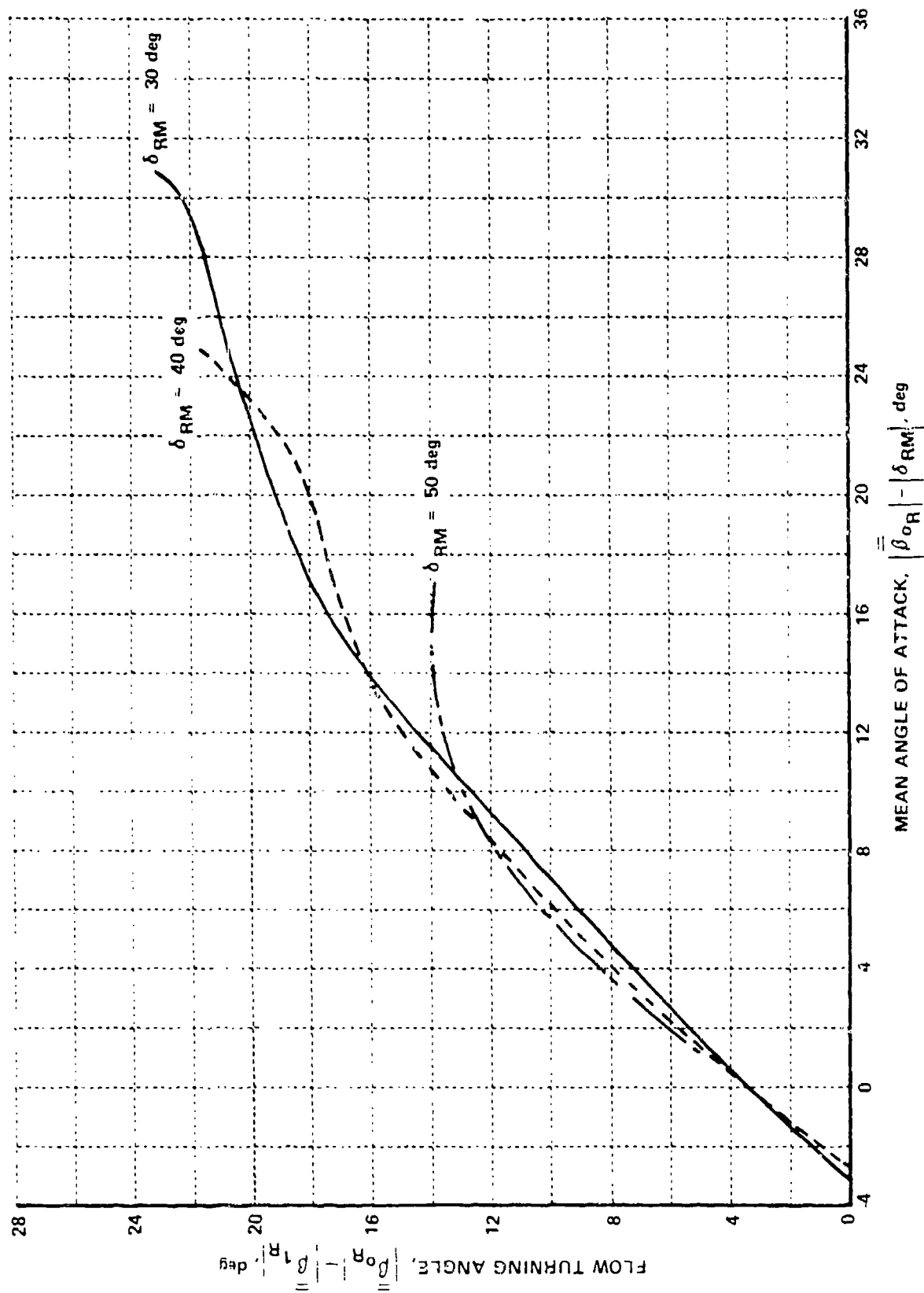COORDINATE SYSTEM RELATIVE TO ROTOR

Figure 31   FLOW TURNING ANGLE PERFORMANCE, ROTOR SET NO. 1 —
VARIOUS ROTOR STAGGER ANGLES, δ_{RM}
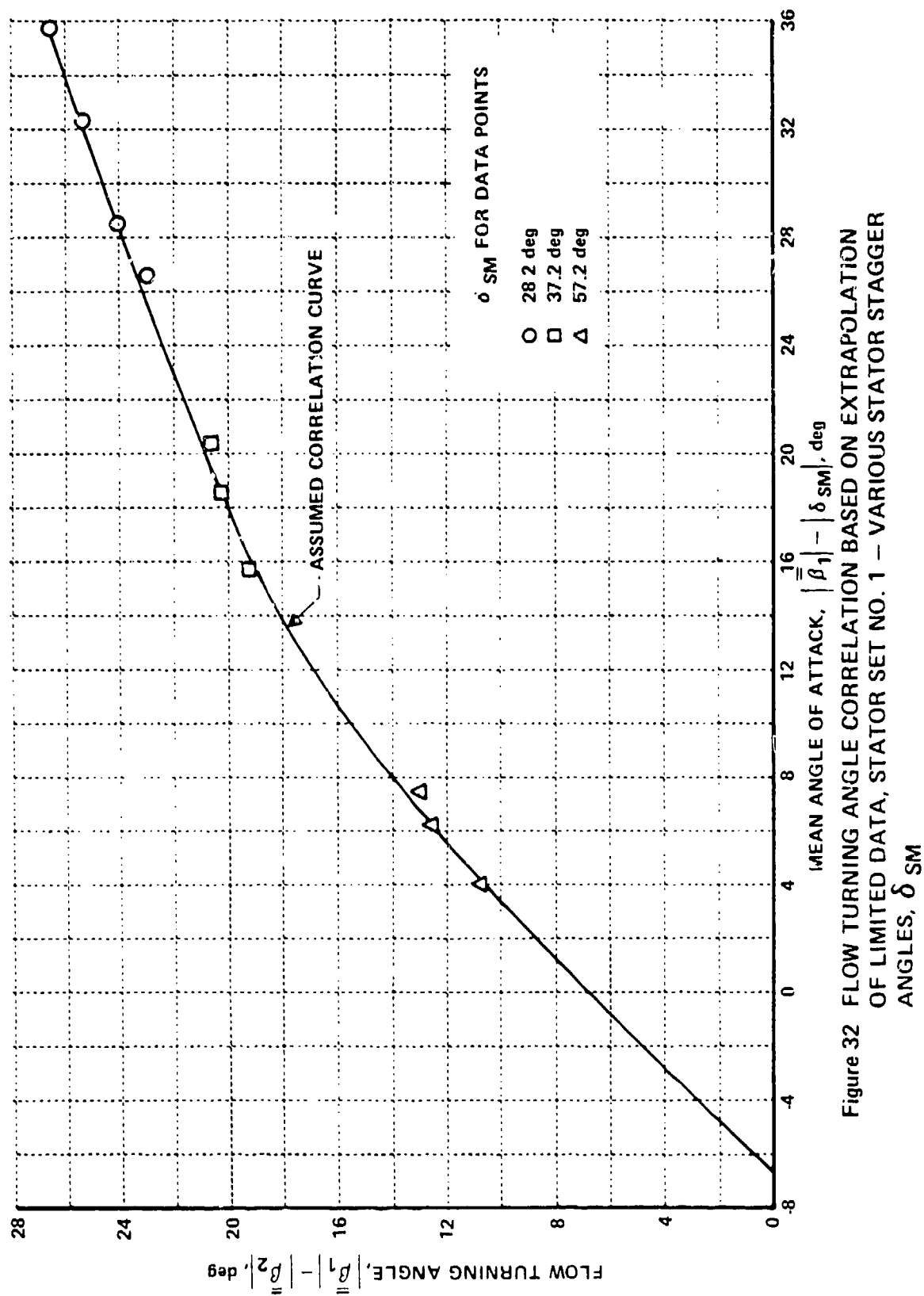
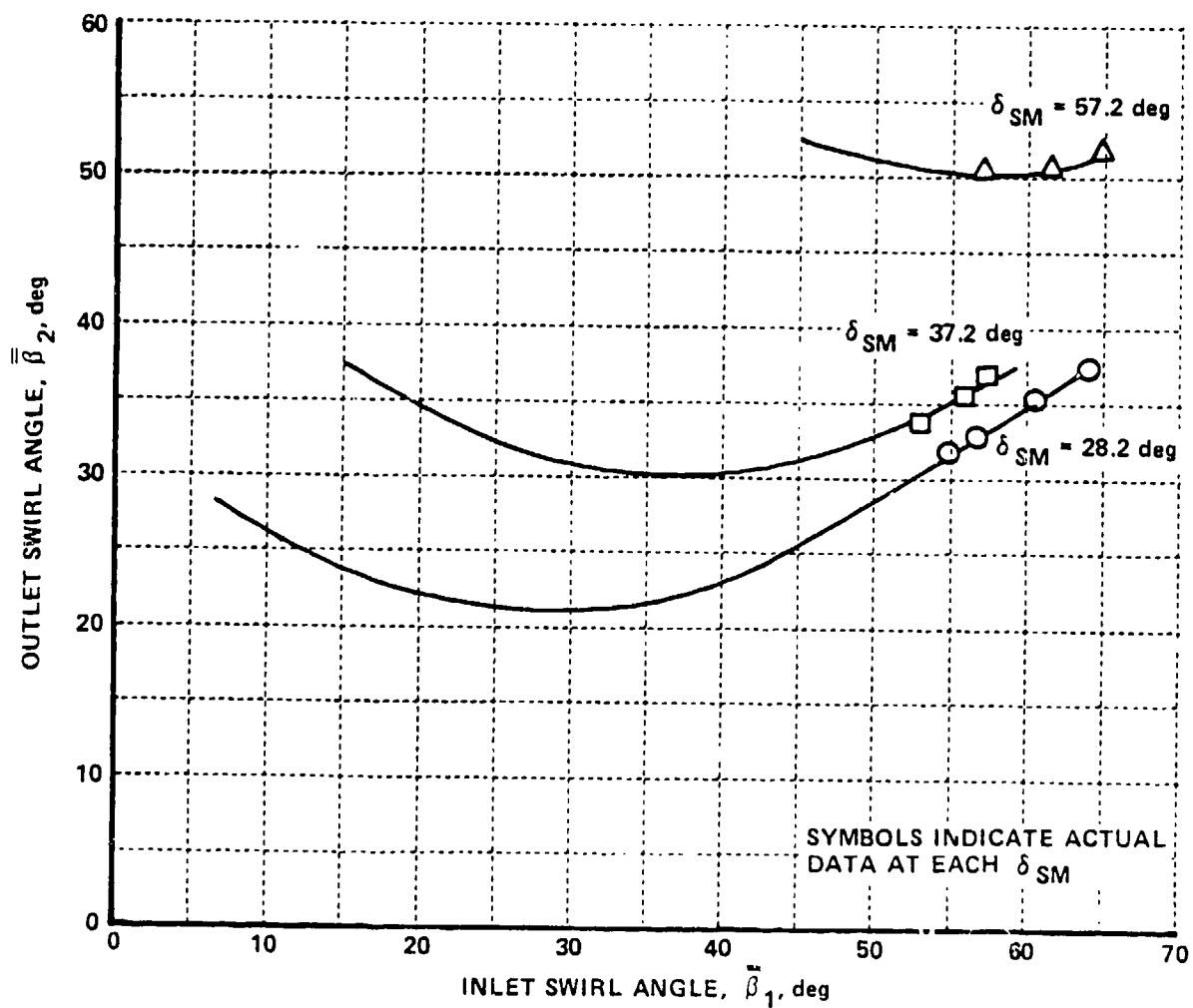Figure 32 FLOW TURNING ANGLE CORRELATION BASED ON EXTRAPOLATION OF LIMITED DATA, STATOR SET NO. 1 — VARIOUS STATOR STAGGER ANGLES, δ_{SM}

Figure 33 FLOW TURNING PERFORMANCE EXTRAPOLATIONS, STATOR SET NO. 1 —
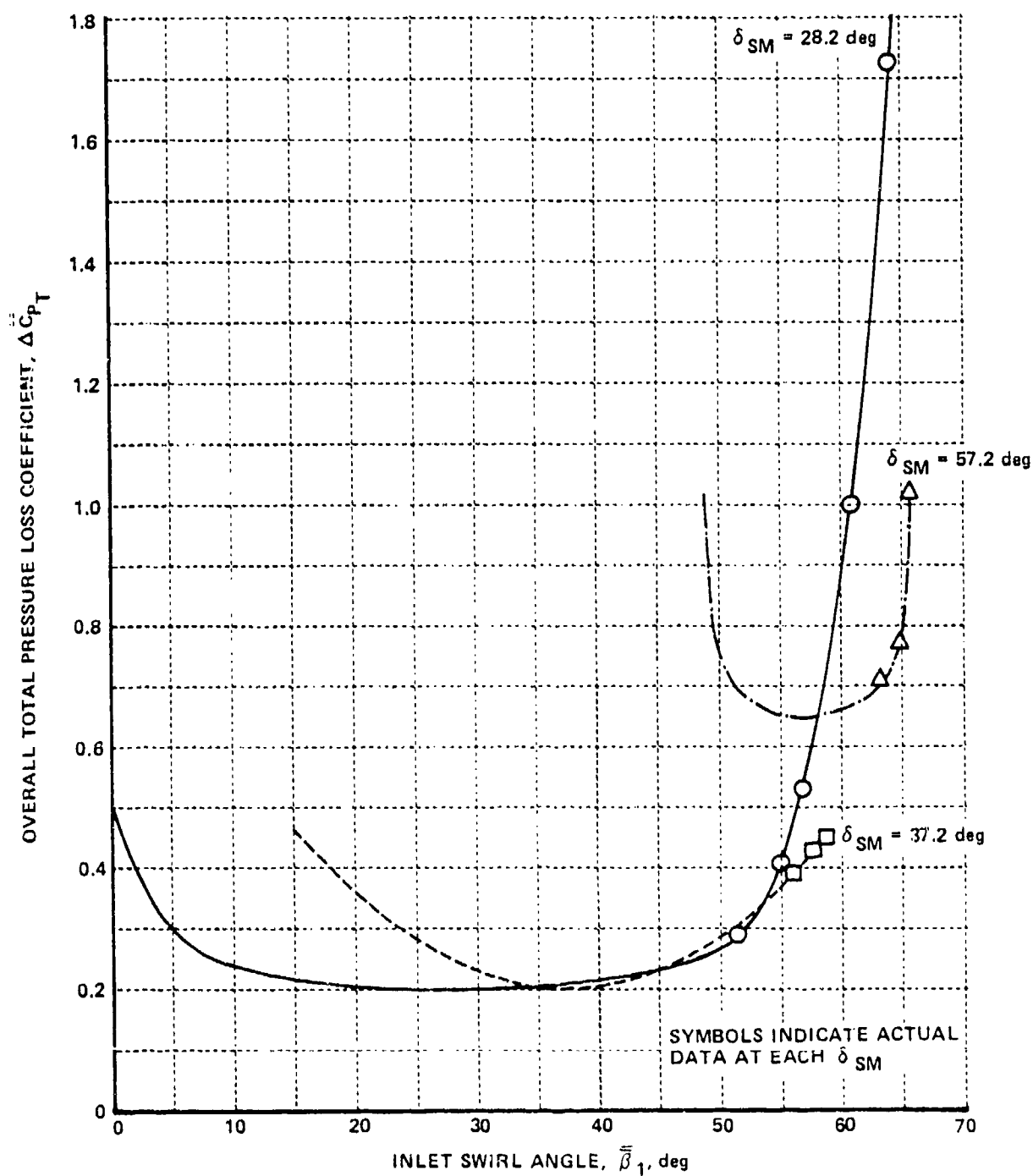VARIOUS STATOR STAGGER ANGLES, δ_{SM}

Figure 34   OVERALL TOTAL PRESSURE LOSS EXTRAPOLATIONS, STATOR SET NO. 1 —
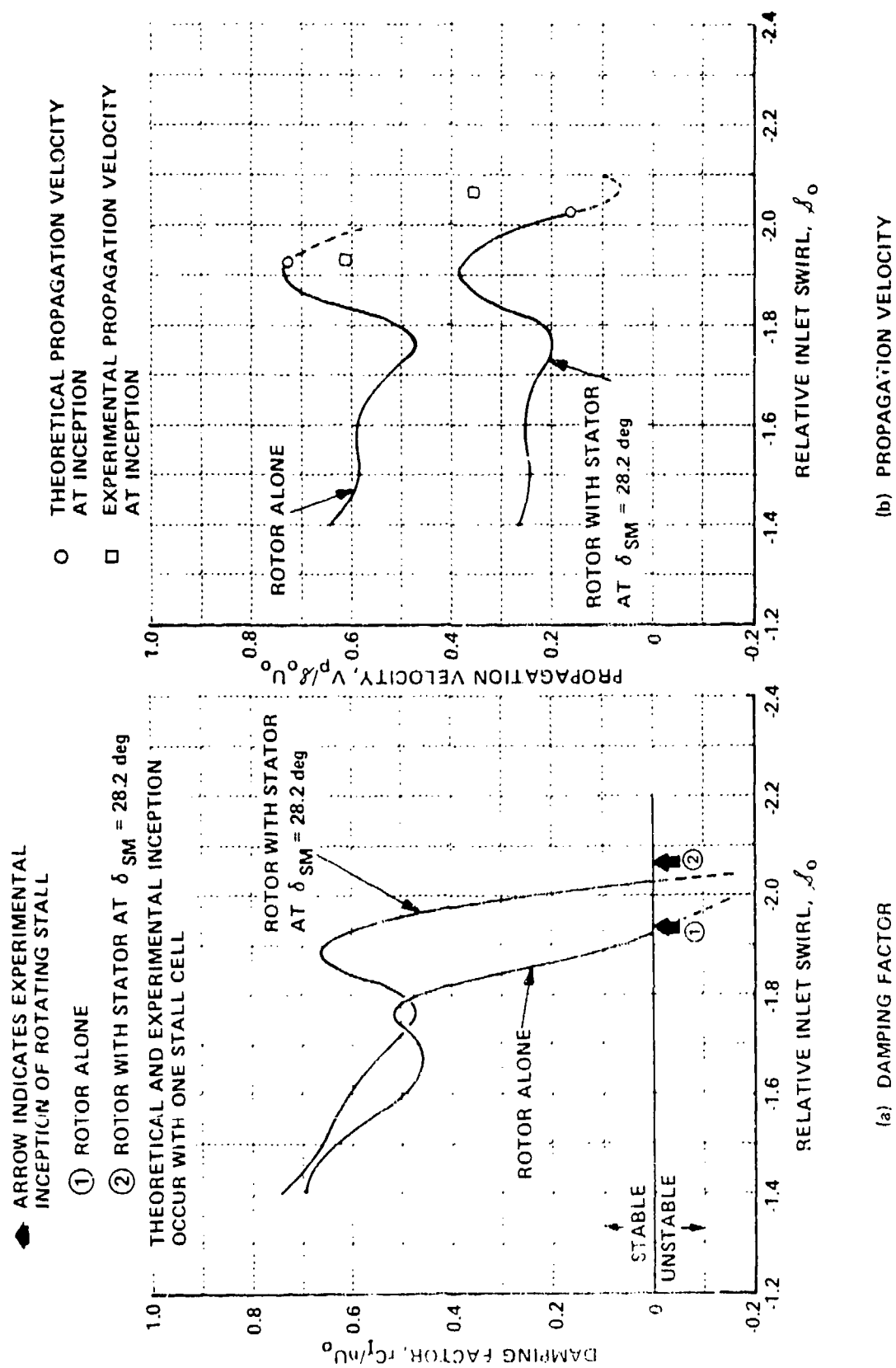VARIOUS STATOR STAGGER ANGLES, δ_{SM}

148

ARROW INDICATES EXPERIMENTAL
INCEPTION OF ROTATING STALL

① ROTOR ALONE

② ROTOR WITH STATOR AT δ_{SM} = 28.2 deg

○ THEORETICAL PROPAGATION VELOCITY
AT INCEPTION

□ EXPERIMENTAL PROPAGATION VELOCITY
AT INCEPTION

THEORETICAL AND EXPERIMENTAL INCEPTION
OCCUR WITH ONE STALL CELL

(a) DAMPING FACTOR

(b) PROPAGATION VELOCITY

Figure 35   THEORETICAL STABILITY CHARACTERISTICS OF STAGE, ROTOR SET NO. 1
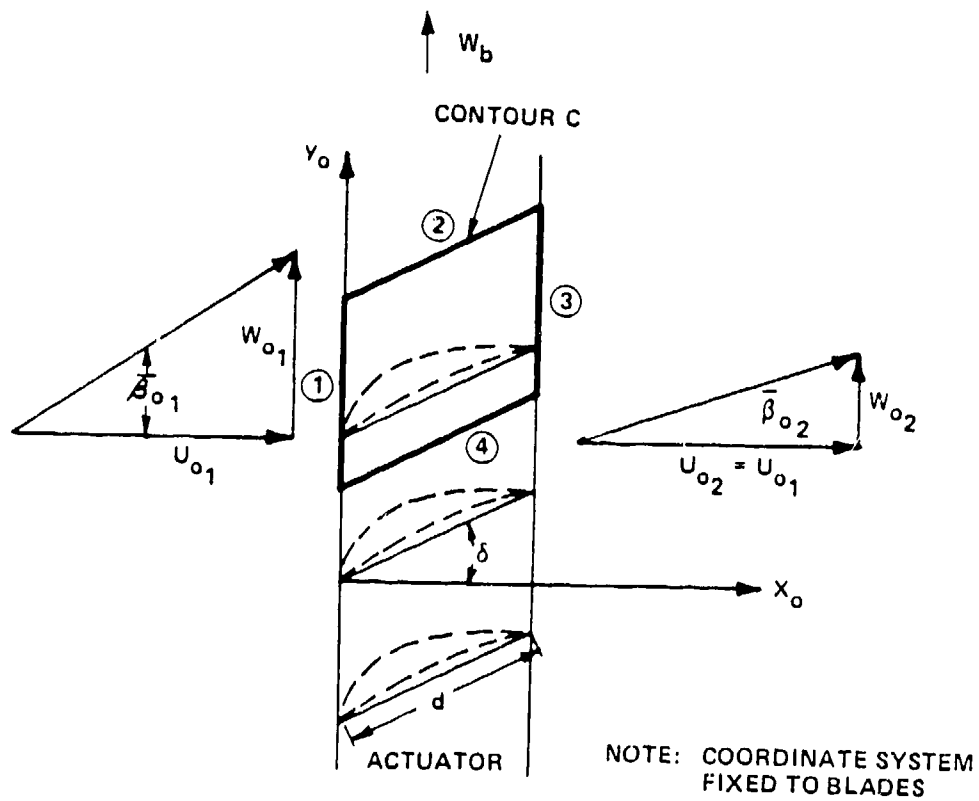AND STATOR SET NO. 1 – ROTOR STAGGER ANGLE, δ_{RM} = 40 deg

110

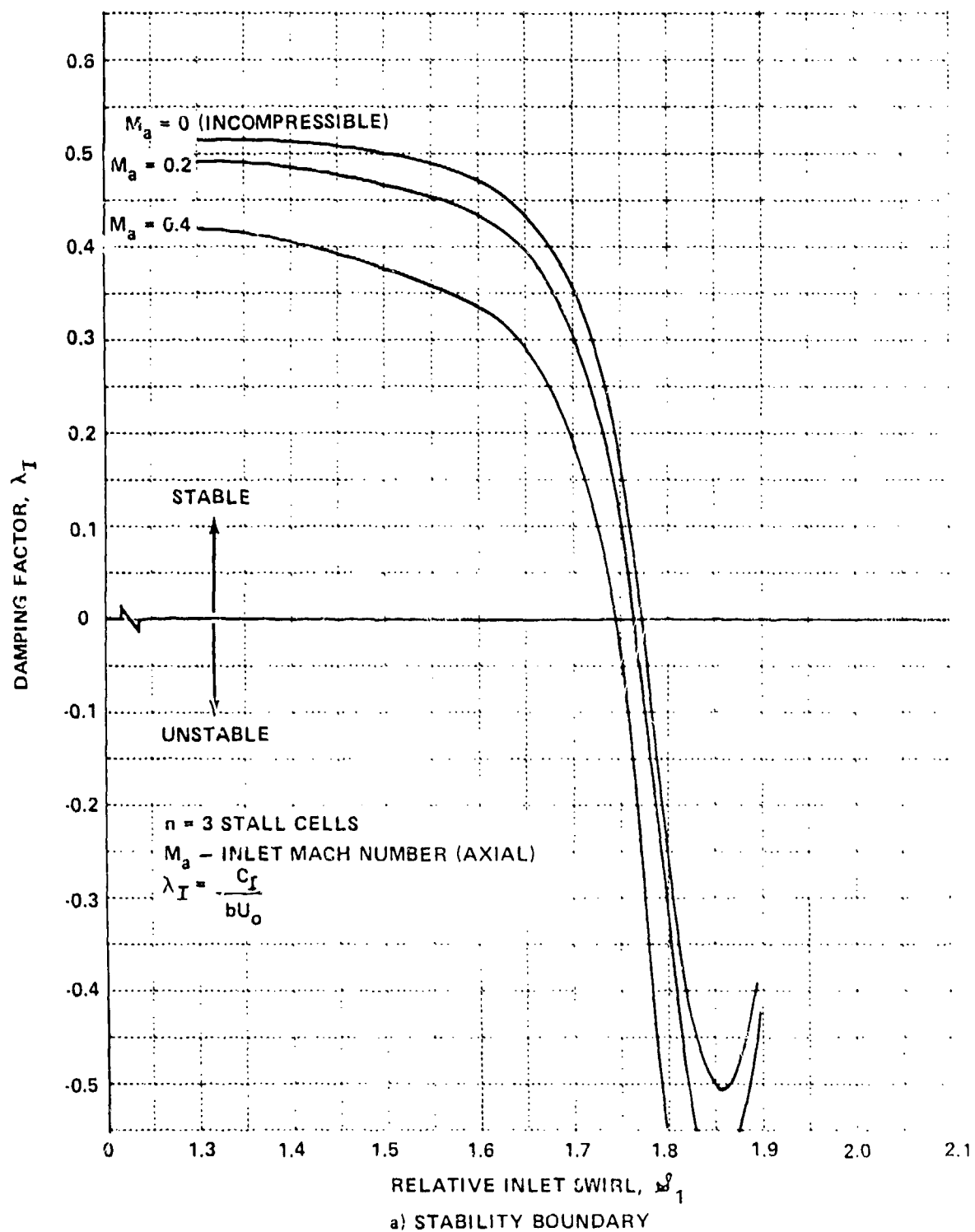Figure 36   FINITE THICKNESS ACTUATOR MODEL FOR COMPRESSIBLE FLOW

Figure 37 COMPRESSIBILITY EFFECT ON STABILITY CHARACTERISTICS FOR
STATOR SET NO. 4 WITH $\varsigma_{SM} = 28.2^o$
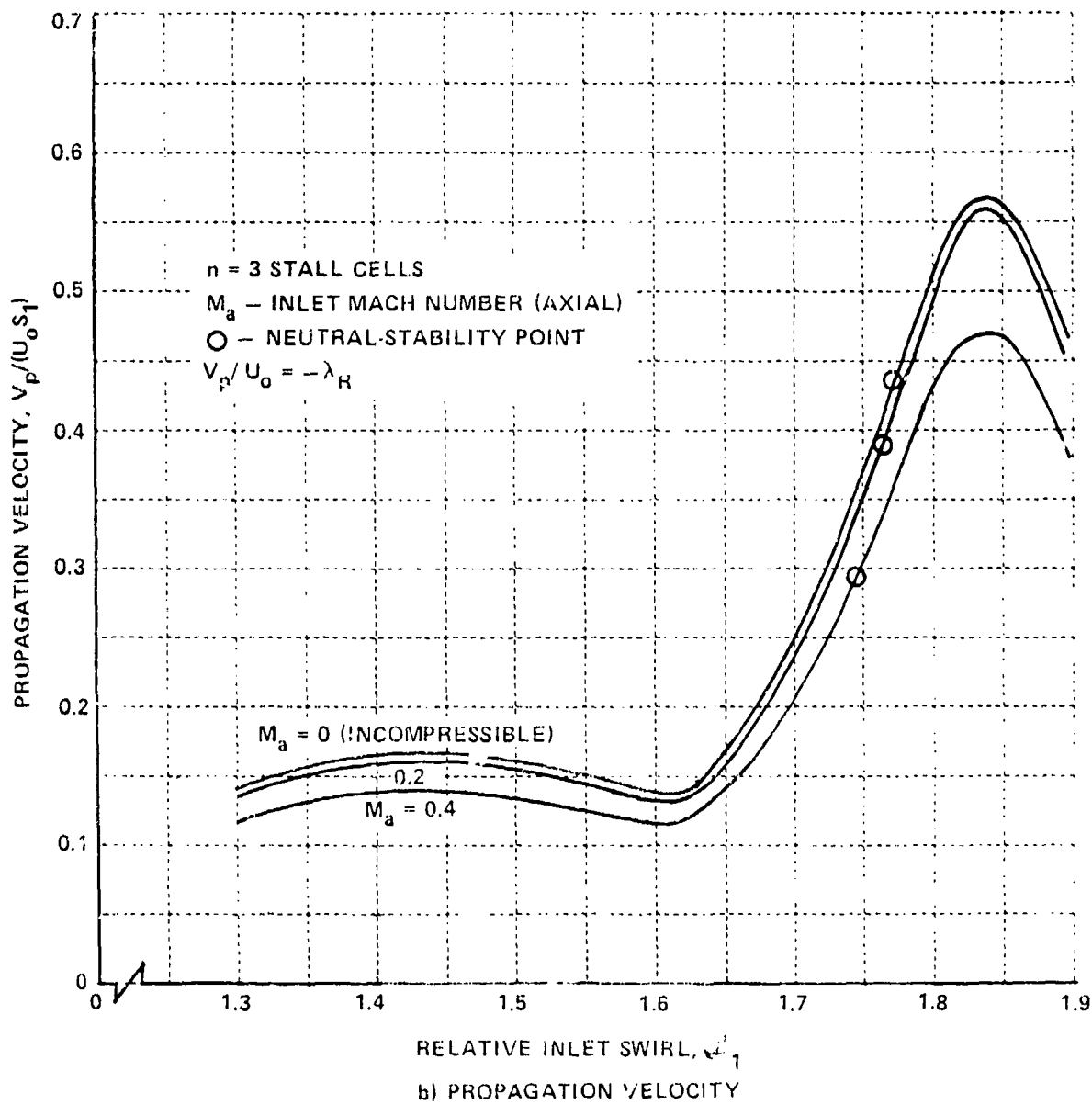
151

b) PROPAGATION VELOCITY

Figure 37 COMPRESSIBILITY EFFECT ON STABILITY CHARACTERISTICS FOR
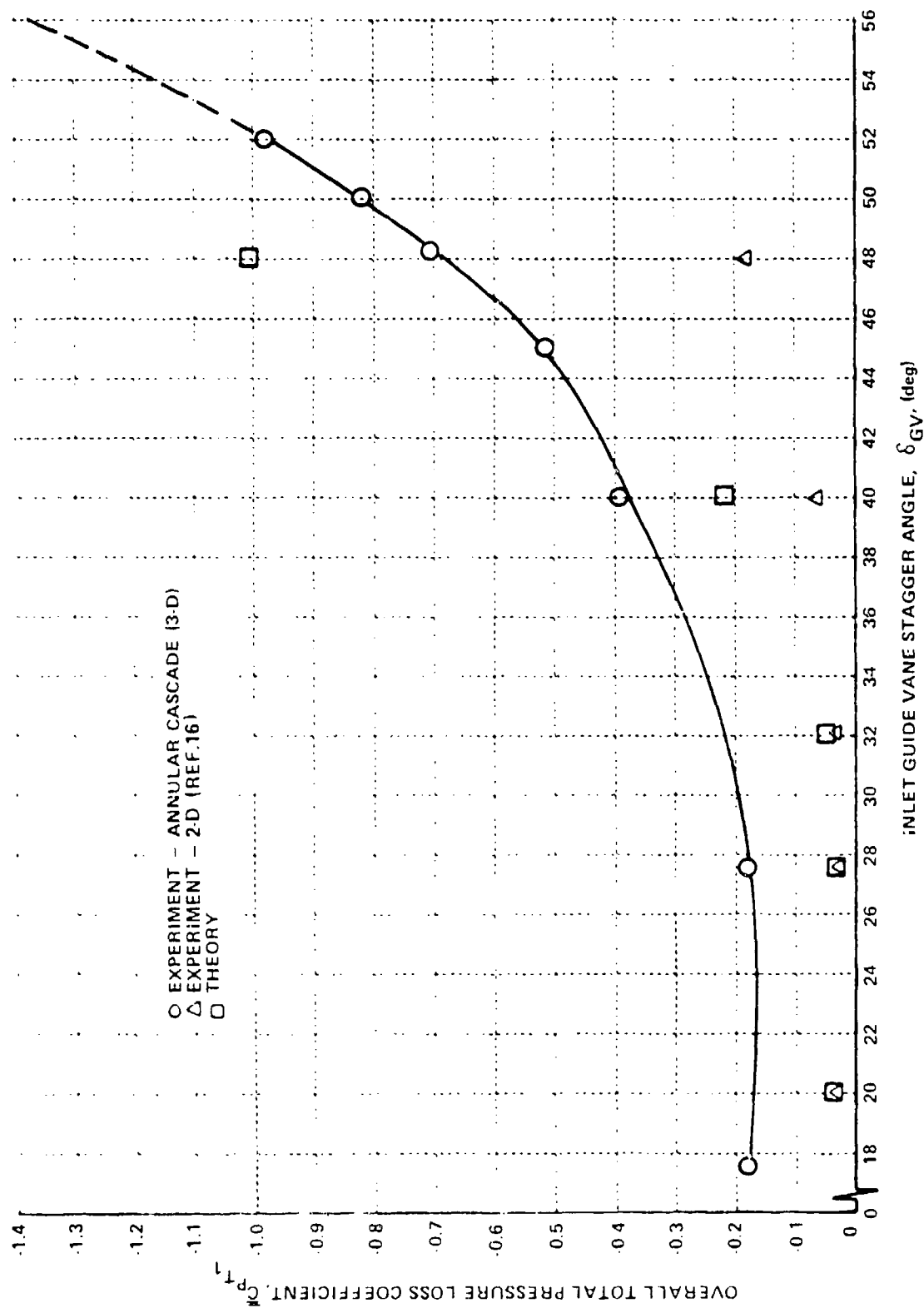STATOR SET NO. 4 WITH $\delta_{SM} = 28.2^\circ$

152

Figure 38 COMPARISON OF THEORETICAL AND EXPERIMENTAL LOSS PERFORMANCE
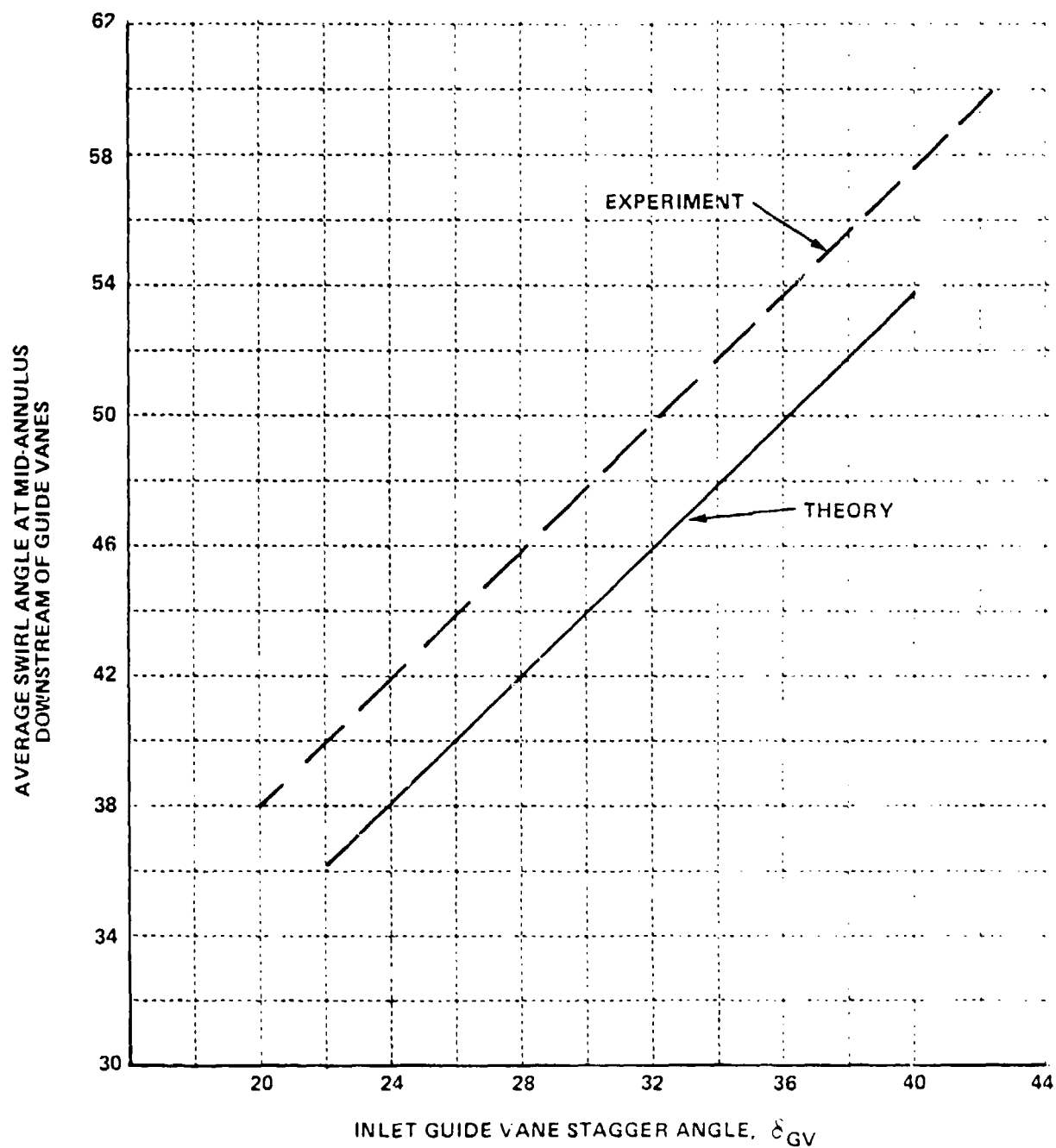FOR STATIONARY INLET GUIDE VANES

153

Figure 39   COMPARISON OF THEORETICAL AND EXPERIMENTAL TURNING
PERFORMANCE OF INLET GUIDE VANES

REFERENCES

1. Ludwig, G.R., Nenni, J.P. and Arendt, R.H., "Investigation of Rotating Stall in Axial Flow Compressors and the Development of a Prototype Rotating Stall Control System", AFAPL-TR-73-45, May 1973.

2. Ludwig, G.R., Nenni, J.P. and Rice, R.S., Jr., "An Investigation of Rotating Stall Phenomena in Turbine Engine Compressors", AFAPL-TR-70-26, May 1970.

3. Langston, C.E.,, "Distortion Tolerance - By Design Instead of By Accident", AME Paper No. 69-GT-115, March 1969.

4. Reid, C., "The Response of Axial Flow Compressors to Intake Flow Distortion", ASME Paper No. 69-GT-29, March 1969.

5. Korn, J.A., "Compressor Distortion Estimates Using Parallel Compressor Theory and Stall Delay", Journal of Aircraft, Vol. 11, No. 9, 584, September 1974.

6. Greitzer, E.M. and Griswald, H.R., "Compressor-Diffuser Interaction with Circumferential Flow Distortion", Paper presented at the Project Squid/AFOSR/VARL Workshop on Unsteady Flows in Jet Engines held at United Aircraft Research Laboratories, July 11 and 12, 1974.

7. Sussman, M.B., "A Remark Concerning Engine-Inlet Distortion", Journal of Aircraft, Vol. 5, No.1, 95, January-February 1968.

8. Rae, W.J., "Three-Dimensional Transonic Flow Through a Compressor Blade Row, In the Nonlinear Small-Disturbance Approximation; Part I Formulation of the Equation", Calspan Report No. AB-5487-A-1, January 1976.

9. Rae, W.J., "Three-Dimensional Transonic Flow Through a Compressor Blade Row, In the Nonlinear Small-Disturbance Approximation; Part II Finite-Difference Solution By a Relaxation Method", Calspan Report No. AB-5487-A-2

10. Marble, F.E., "Three-Dimensional Flow in Turbomachines", Section C of Aerodynamics of Turbine and Compressors, Vol X High Speed Aerodynamics and Jet Propulsion, Princeton University Press, 1964.

11. Wu, T.Y., "Flow Through a Heavily Loaded Actuator Disc", Schiffstechnik Bd. 9 Heft 47, 134, 1962.

12. Oates, G.C., "Actuator Disc Theory for Incompressible Highly Rotating Flows", ASME J. of Basic Engineering, 613, September 1972.

13.   Kerrebrock, J.L.,   "Waves and Wakes in Turbomachine Annuli with Swirl"
        AIAA Paper No. 74-87, January 1974.

14.   Oates, G.C. and Knight, C.J.,   "Throughflow Theory for Turbomachines",
        AFAPL-TR-73-61, 1973.

15.   Oates, G.C. and Carey, C F.,   "A Variational Formulation of the Com-
        pressible Throughflow Problem", AFAPL-TR-74-78, November 1974.

16.   Dunavant, J.C.,   "Cascade Investigation of a Related Series of 6-
        Percent-Thick Guide-Vane Profiles and Design Charts", NACA TN 3959,
        May 1957.